



UNIVERSITY OF  
BIRMINGHAM

# **Zeolites and Other Molecular Sieves for Chromate Remediation**

Rowena Fletcher-Wood

A thesis submitted to The University of Birmingham for  
the degree of Doctor of Philosophy

School of Chemistry  
College of Engineering and Physical Sciences  
University of Birmingham  
December 2014

UNIVERSITY OF  
BIRMINGHAM

**University of Birmingham Research Archive**

**e-theses repository**

This unpublished thesis/dissertation is copyright of the author and/or third parties. The intellectual property rights of the author or third parties in respect of this work are as defined by The Copyright Designs and Patents Act 1988 or as modified by any successor legislation.

Any use made of information contained in this thesis/dissertation must be in accordance with that legislation and must be properly acknowledged. Further distribution or reproduction in any format is prohibited without the permission of the copyright holder.

## **Acknowledgements**

I would like to thank my supervisor Dr Joseph Hriljac for his invaluable support and guidance throughout my research project.

I am also grateful to the other members of the Hriljac group: Evin Chen, Tom Carey, Tim Lucas, Sav Savva, Geoff Cutts, George Day, and Katrina Warrack, for their continuous assistance and collaboration, as well as the other members of the Floor 5 Materials Chemistry group and especially Dr Jackie Deans.

I would also like to thank my collaborators at Sheffield Hallam, Dr Sue Forder and Dr Paul Bingham, and their visiting research students, Robin Gerard, J-C. D'Hollander, and Colin Gorin, who have transformed the nature of my research.

At the University of Birmingham, I am also grateful to Terry Green, Dr Paul Anderson and Dr Simon Cotton for their help with EPR spectroscopy, Dr Zoe Schnepf for her help with TEM, and Professor Frank Berry for his help with Mössbauer spectroscopy.

I am as ever grateful to my friends and family for their support and enthusiasm throughout this venture and, in particular, my husband, Guy, who has battled bravely with my software, and won.

## Abstract

In this thesis, porous solids loaded with redox-active ions were examined for the selective uptake and simultaneous reduction of Cr(VI) from aqueous solution. Results demonstrate that chromium recovery is governed primarily by iron loadings and not structure. Whilst Fe-loaded zeolite X took up 29.1 mg<sub>Cr</sub>/g<sub>sieve</sub>, rising to 33.1 mg<sub>Cr</sub>/g<sub>sieve</sub> after alginate templating to create mesopores, mg<sub>Cr</sub>/mg<sub>Fe</sub> ratios remain constant, *i.e.* templating increases Fe-loadings. Mn(II) ions are less appreciably oxidised than Fe(II) ions: Mn-loaded AlPO-5 shows higher uptakes than Fe-loaded AlPO-5, but lower than the zeolites: ion exchange is crucial to the uptake mechanism.

Fe(II)-loaded molecular sieves were found to be appreciably oxidised (~ 80 %) and sensitive to hydration levels. Promising systems were reduced under hydrogen gas flow at 500 °C demonstrating fine oxidation state control across 0-24 hours. Fe(II) fractions increased, until Fe(0) metal was evolved after 3 hours in Fe-loaded zeolite X and, in some AlPO systems, after 6 hours. Some systems demonstrate oxidation. Metal ions cluster upon all chemical treatments. Trends in chromium uptake with iron oxidation state indicated that only Fe(II) reduces Cr(VI) to Cr(III). As Fe(0) metal loadings increased, Powder X-Ray Diffraction (PXRD) patterns demonstrated a loss in crystallinity compatible with the irreversible breakdown of the molecular sieve upon formation of metal clusters.

Acid treatment, complexation and ion exchange demonstrated viable simultaneous reduction and recycling of Cr viable alongside other toxic metal ions (anions and cations). Three Fe-loaded systems: zeolite X, hydrogen reduced zeolite X and hydrogen reduced AlPO-5 were shown to reduce the chromium content of wastewaters below the WHO recommended limit of 50 µg/l until concentrations of 500 µg/l – the limiting upper expected contamination level. Chromium uptake may be limited by surface contamination. Appreciable leaching of Fe ions produce a secondary waste stream from which zeolite catalysts may be reloaded.

# Index

<b>Chapter 1: Introduction</b>	<b>1</b>
<i>1.1. Role of Cr(VI)</i>	<i>1</i>
<i>1.2. Anion Exchange Materials</i>	<i>3</i>
<i>1.3. Cation Exchange Materials: Zeolites</i>	<i>4</i>
<i>1.4. Proposed Mechanism for Chromate Treatment and its Limitations</i>	<i>7</i>
<i>1.5. Recycling</i>	<i>11</i>
<i>1.6. Aims</i>	<i>12</i>
<b>Chapter 2: Experimental Section</b>	<b>13</b>
<b>2.1. Techniques</b>	<b>13</b>
<i>Schlenk Line</i>	<i>13</i>
<i>Gas Flow Techniques</i>	<i>13</i>
<i>Inert Atmosphere Glove Box</i>	<i>14</i>
<b>2.2. Materials</b>	<b>14</b>
<i>Zeolites – Basic Systems</i>	<i>14</i>
<i>Zeolites – Templated Systems</i>	<i>15</i>
<i>Zeolites – Ion Exchanges</i>	<i>15</i>
<i>AlPOs</i>	<i>16</i>
<i>Chromium Exchanges</i>	<i>17</i>
<i>Reduction</i>	<i>18</i>
<b>2.3. Characterisation</b>	<b>18</b>
<i>X-Ray Diffraction</i>	<i>18</i>
<i>Wavelength Dispersive X-Ray Fluorescence Spectroscopy (WD XRF)</i>	<i>27</i>
<i>X-Ray Photoelectron Spectroscopy (XPS)</i>	<i>33</i>
<i>Electron Paramagnetic Resonance (EPR)</i>	<i>35</i>
<i>Thermogravimetric Analysis (TGA)</i>	<i>37</i>
<i>Inductively Coupled Plasma Mass Spectrometry (ICP)</i>	<i>37</i>
<i>Mössbauer Spectroscopy</i>	<i>38</i>
<i>Ultraviolet-Visible Absorption Spectroscopy (UV-vis)</i>	<i>44</i>
<i>SEM and EDS</i>	<i>46</i>
<i>Transmission Electron Microscopy (TEM)</i>	<i>47</i>
<b>Chapter 3: Effect of Structure Upon Chromium Uptake</b>	<b>49</b>

<b>3.1. Reaction Conditions</b>	<b>49</b>
<i>pH</i>	49
<i>Exposure Conditions</i>	50
<b>3.2. Zeolites - Basic Systems</b>	<b>50</b>
<i>Zeolite A</i>	51
<i>Zeolite X</i>	56
<i>Clinoptilolite</i>	61
<b>3.3. Zeolites – Templating</b>	<b>64</b>
<i>Templated Zeolite X</i>	64
<i>Hierarchically porous ZSM-5 Zeolite</i>	69
<b>3.4. AIPOs</b>	<b>71</b>
<i>AIPO-5</i>	71
<i>AIPO-Fe<sub>23</sub></i>	76
<i>LAU AIPO</i>	82
<b>Chapter 4: Mechanism for Chromium Uptake</b>	<b>84</b>
<b>4.1. Assigning Fe and Mn Sites</b>	<b>84</b>
<i>Colour</i>	84
<i>Mössbauer Spectroscopy</i>	85
<i>EPR Spectroscopy</i>	91
<i>XPS</i>	98
<i>Surface Fouling</i>	102
<b>4.2. Changes upon Cr-exchange</b>	<b>104</b>
<i>Mössbauer spectroscopy</i>	106
<i>EPR Spectroscopy</i>	108
<i>XPS</i>	
<i>Error: Reference source not found</i>	
<b>4.3. Looking at Cr sites</b>	<b>114</b>
<i>XPS</i>	114
<i>UV-vis spectroscopy</i>	116
<i>pH</i>	117
<b>Chapter 5: Effect of Modified Ions Upon Chromium Uptake</b>	<b>119</b>
<b>5.1. Air Exposure</b>	<b>119</b>
<i>Colour</i>	119
<i>Mössbauer Spectroscopy</i>	120
<b>5.2. Reduction</b>	<b>122</b>

<i>Mössbauer Spectroscopy</i>	123
<i>EPR Spectroscopy</i>	131
<i>XRD</i>	133
<i>XRF Spectroscopy</i>	135
<b>5.3. Changes Upon Chromate Exposure</b>	<b>136</b>
<i>Mössbauer Spectroscopy</i>	136
<i>EPR Spectroscopy</i>	138
<b>Chapter 6: Suitability for Application and Recycling</b>	<b>141</b>
<i>6.1. Competitive Ions</i>	141
<i>6.2. Extent of Removal</i>	145
<i>6.3. Chromium Extraction and Recovery</i>	149
<b>Chapter 7: Summary and Conclusions</b>	<b>156</b>
<b>Appendix I</b>	<b>161</b>
<b>Appendix II</b>	<b>163</b>
<b>Bibliography</b>	<b>164</b>



## Chapter 1: Introduction

### 1.1. Role of Cr(VI)

Chromium accumulates in ground and surface waters as two major species, Cr(III) and Cr(VI)(1,2). Cr(III) occurs naturally as a mineral nutrient used by the human body to digest sugars, proteins and fats(3). It is soluble at low pH, but above pH 3.5 it forms a mixture of strongly-bound hydroxy complexes, and neutral  $\text{Cr}(\text{OH})_3^0$  species precipitate(4). Cr(VI), however, rarely occurs naturally, but is discharged into waste water from industrial plants(5,6). In solution, it forms anionic species that are highly pH-dependent. At low pH and high chromium concentrations, dichromate,  $\text{Cr}_2\text{O}_7^{2-}$ , predominates, whilst at pH greater than 6.5 the major form is chromate,  $\text{CrO}_4^{2-}$  (7). Both species are highly water soluble and mobile, making Cr(VI) difficult to extract from water and so increasing the impact of its toxicity and risk of bio-accumulation in plants, and later animals and humans, readily permeating the cell membrane to cause damage inside the body(1,2,8,9). The strongly-oxidising Cr(VI) is 1-2 orders of magnitude more toxic than Cr(III)(5). Eating infected crops or animals leads to the build up of toxic ions in the body. This hazard is especially prominent in China, where population pressure forces the farming of all available land(1). Contact with skin causes localised tissue damage and sometimes powerful burns; cuts and abrasions may heal abnormally or not at all and, left untreated, the skin will suffer ulceration and chronic allergic contact dermatitis. Nasal inhalation provokes acute toxicity, especially respiratory sensitisation, irritation and the formation of ulcers on the nasal septum(10–12). Acute exposure leads to swelling in the trachea and lungs. Ingestion results in nausea, diarrhoea and severe damage to several major organs, including the heart, liver and kidneys. Ulcers form in the stomach and intestines, internal haemorrhages occur and anaemia may arise(11). Exposure to the eyes may produce permanent impairment. Cr(VI) is an International Agency for Research on Cancer (IARC) Group 1 classified carcinogen, with sufficient evidence for effects in humans(13).

Natural dissolved concentrations of chromium in groundwater are typically less than  $10 \mu\text{g/l}$ (14) but, in contaminated areas, concentrations have been known to reach  $300\text{-}500 \mu\text{g/l}$ (15). The World Health Organisation (WHO) recommend a regulatory standard of  $50 \mu\text{g/l}$ (5), which has been adopted by the European Commission as the maximum safe exposure limit in drinking water. The US Environmental Protection Agency (EPA) set an exposure limit of twice this

concentration(7).

Chromium (VI) oxide is a common contaminant waste product of several major industries, most notably in metal refinery, coating of steel and other alloys for corrosion control; however, it is also prevalent in wood, paint and textile industries, printing, leather tanning and as a by-product of processes such as welding(6,9,16,17). 600 tons of sludge are produced by leather tanneries every year, containing 1 g<sub>Cr</sub>/kg. Soil contamination can reach ~2500 mg<sub>Cr</sub>/kg(1). Many sources of chromium are also sources of other heavy metals, in particular cadmium, which complicates remediation strategies by introducing the need to deal with both anionic and cationic ions in solution simultaneously(18).

Its widespread application means that Cr(VI) contamination is an increasing problem. Alternative processes have been developed to assume the role of chromium. However, whilst there may seem to be strong motivation for the elimination of Cr(VI) from industry, technological changeover is retarded by the inconvenience of initial set up. This is exacerbated by the absence of any universal replacement for Cr(VI), even within a distinct industry. The implementation of whole new technologies is demanded. Some materials may replace chromium directly: permanganates are used as dyes and boron compounds for wood treatment, whilst in metal works, cobalt-phosphorus alloys may replace chrome in electroplating. However, these systems are limited, operating only with a few specific materials. Alternative corrosion preventions include electroless nickel plating, Chemical Vapour Deposition (CVD), thermal sprays, explosive bonding, vacuum coating and surface hardening(19). Unfortunately, not only do many of these techniques involve hazardous vapours and corrosive chemicals which still present health risks, but they are often less effective, raising reluctance for their adoption(20).

A number of health and safety regulations are placed upon chromium work, making its application and disposal tedious and expensive. Most chromium is still converted into waste and dumped in landfill sites(1,5). Whilst Cr(VI) does not naturally precipitate out, conversion into Cr(III) can facilitate this. This also reduces the risk of Cr(VI) leaching from dumping sites and re-entering waterways. Most processes involve a two-step reduction to Cr(III) and then physical separation using filtration methods(21). Reduction may be carried out with a variety of electron-donating materials, including H<sub>2</sub>S, Na<sub>2</sub>S<sub>2</sub>O<sub>4</sub>, NaHSO<sub>3</sub>, CaHSO<sub>3</sub>, CaS<sub>5</sub>, SnCl<sub>2</sub>, Fe filings, FeSO<sub>4</sub> and a delafossite photocatalyst(6,22–24). The effectiveness of reduction processes is highly dependent upon the pH and concentration of metal ions; further, the chemicals, which then also need to be extracted, are not cost-effective for low concentration of Cr(VI)(5). Enzymic reduction using natural bacteria, yeast, algae and plants, however, suffers from competition with non-biological reduction pathways and is often slow by comparison(25–27). In addition, it still requires the

presence of a metal such as Fe or Mn or oxidised organic matter to provide electrons. Filtration or sedimentation is carried out by soil washing to chemically or physically separate out Cr-contaminated soil. Chelating agents (such as diphenyl carbazide), surfactants and acids are used to trap chromium and resins; electrokinetics or phytoextraction may then be employed to further concentrate the chromium waste(5). Barrier technologies such as membrane or quartz sand filtration can trap a wide range of contaminants and also work prior to chromate reduction; however, these methods often depend upon groundwater levels and thus may be seasonal(17,28).

Immobilisation, whether or not accompanied by reduction to Cr(III), is still considered the best available technology for chromium remediation(29). The major drawback of this method is the inaccessibility of once-used chromium, which remains under demand from industries. Thus as the scarcity of chromium increases, there is a rising demand for recycling and reintroduction to industrial application.

Not all chromate removal mechanisms involve solidification and disposal in landfill sites. In-situ vitrification (ISV) works by running an electric current through moist soil to seal the metals into a glassy mixture(5). However, this procedure requires a high energy outlay in order to melt the contaminated soil. Phytoremediation, the application of plants for chromium uptake and reduction, successfully removes chromium from soil once they are harvested, but the high chromium produce cannot be consumed. The most promising methods for chromate remediation are sorption and ion exchange processes. These are often carried out with reducing materials such as iron/iron oxide nanoparticles and manganese oxides, which may additionally be supported in clay, sand, soil, graphene nanosheets or zeolite frameworks(5,30–32). Cr(III) is more readily adsorbed than Cr(VI), especially at high pH, where sorption of Cr(VI) is negligible(16). Ion-exchange or surface fouling as  $(\text{Cr, Fe})(\text{OH})_3$  precipitates occurs. Frequently, these solids are then disposed of in landfill sites as before, but the possibility for extraction and remediation exists and reduction to Cr(III) species bypasses the problem of a secondary waste stream(18,33). Cheap and environmentally friendly materials such as activated carbon, seaweed, coconut husk and straw lignin are ideal sorbents(34–40). Biosorption recovers chromium in a form that may be directly supplied to a new industry as a catalyst in organic reactions(41). Whilst this does not feed the continuing demand in existing industries, it presents an effective method for chromium recycling.

## **1.2. Anion Exchange Materials**

Whilst cation exchangers are plenty, there is a distinct lack of good anion exchangers, and targeted removal of  $\text{CrO}_4^{2-}$  is problematic.

FeOOH-loaded anion resin has been shown to efficiently take up phosphate species from solution and relieve eutrophication, whilst some metal organic frameworks (MOFs), actinide borates and layered materials have been suggested for removal of anions including chromates(42–44). However, nanoparticles are vulnerable to oxidation and agglomeration(45). The most promising anionic framework types are those of poorly crystalline layered double hydroxides (LDHs), which incorporate chromate species *via* intercalation chemistry – usually *via* exchange with hydroxide ions(46–48). Guest species and the starting structure may then be recovered *via* mild acid treatment, which makes these materials recyclable at low cost.

LDHs may be expressed with the structural formula  $[M^{z+}_{1-x}M^{3+}_x(OH)_2]^{z+}(X^{n-})_{\zeta/n}.mH_2O$ , where  $z = 2$  and  $M(II) = Ca, Mg, Zn, Ni, Mn, Co$  or  $Fe$ ,  $M(III) = Al, Cr, Mn, Be, Ga, Co$  or  $Ni$  and  $\zeta = x$  in most cases. Values of  $0.1 < x < 0.5$  have been reported. Although LDH intercalation is fast and high capacity, it is rarely selective, driven chiefly by ion exchange or acid-base reactions, although some isomeric preferences have been observed(49). The charge and sterics of framework and intercalates determine the anion packing and layer spacing. Halides, oxyhalides, hydroxides, carbonates, sulfates and silicate anions have thus been assimilated, although the stability of intercalated carbonates is such that further exchange is inhibited and recycling cannot occur(50–55); polymers may be integrated *via in situ* polymerisation of inserted monomers or direct polymer templating during initial synthesis; recently, porphyrins, vitamins and amino acids have been stored in LDHs with the intention of drug transport and selective discharge(49,50,56–60). However, the low pH instability of LDHs has demanded the extensive modification of the materials for this application. LDHs are most useful at a pH between 6.5 and 7.5(61). Below this pH range deintercalation occurs, and above this pH range, obstructive metal hydroxides, lowering the absorption activity of the compound, and competitive phases such as meixnerite are formed.

### 1.3. Cation Exchange Materials: Zeolites

Zeolites were discovered in 1756, when Swedish mineralogist Axel Fredrik Cronstedt observed the release of steam upon heating volcanic rocks(62,63). This discovery prompted the name zeolite derived from the Greek *zeo* (stones) and *lithos* (boiling).

Zeolites were first classified as crystalline aluminosilicates consisting of complete corner-sharing  $[SiO_4]^{4-}$  and  $[AlO_4]^{5-}$  tetrahedra characterised by the  $O/(Al+Si)$  ratio 2(64). Average  $(Si,Al)-O$  distances lie between 1.58 and 1.78 Å and  $O-(Si,Al)-O$  angles are usually within 5 ° of the ideal tetrahedral, such that the polyhedra are only marginally distorted(65). Terminal hydroxyl groups form at the external surfaces and internal defects and may be shown by NMR(66,67).

Si-OH and Al-OH linkages are prone to deprotonation and reprotonation depending on pH, providing positively charged surfaces for pHs in the range 3.0-8.0 and negatively charged surfaces at limiting pHs(68,69).

When linked together, the silicon tetrahedra are electronically neutral, whilst the 3+ valency of aluminium gives rise to -1 charge per Al, producing an anionic framework, which must be compensated for with charge balancing cations(67). The even distribution or ordering of aluminium ions may be studied *via*  $^{27}\text{Al}$  NMR(70,71). This ordering arises because of the charge-forbidden Al-O-Al sequence known as Löwenstein's rule(72).

Numerous exchangeable counter cations may rest in cavities that form at the intersection of one-, two- or three-dimensional  $\sim 3\text{-}10$  Å pores running through the structure. These pores express a flexibility window essential to the large diversity of zeolite structures, and one of the main limitations to predictive structure-determination encountered by computational modelling; distortions to the pores and diffusion aperture result from high sensitivity to cation positions and coordination environments(73,74). Monovalent cations tend to restrict pores to smaller sizes, limiting the access of larger exchange ions. Pores may be tuned to deliver selectivity: the majority of zeolites have environmental applications including water softening by heavy metal extraction and removal of radioactive isotopes(75–82). Often, zeolites may be recycled and reused(35,66,67,75,83). As such, zeolites exhibit uptake *via* both surface adsorption and cation exchange capacity (CEC), such that they are often more effective than uncharged environmentally friendly absorbants such as activated carbon (a crude amorphous graphite) or metal ion composites(7,66,77).

Not only cations, but also neutral species, enter the pore channels and diffuse through the zeolite, allowing for further applications in gas separation, paraffin collection, and pharmaceutical contaminant uptake. Natural chabazite selects for molecules  $< 5$  Å in diameter and, as such, accrues the uncharged pollutant gas  $\text{SO}_2$ , whilst zeolite Y shows significant adsorbence preference for salicylic acid over carbamazepine in pharmaceutical remediation(83–86). Water is found in the cavities of all zeolites. They adsorb moisture from the air until they are heavily hydrated and  $\text{H}_2\text{O}$  makes up a significant portion of their overall mass. Dehydrating zeolites thus produces potent drying agents (*e.g.* for pet litter), although cation exchange may be inhibited(64,73,87). During the dehydration, cations migrate from positions of high coordination to positions of lower coordination, increasing their localisation in the zeolite structure and exerting a stronger influence over pore dimensions, causing the framework to buckle(64). Reversible dehydration may be achieved in all zeolites with no structural damage *via* gradual heating under moderate conditions(73). This allows for better characterisation by diffraction techniques: intensities give readily predictable and

repeatable values and are no longer strongly influenced by sample-specific water distributions.

Naturally occurring zeolite deposits tend to contain a mixture of mineral phases, which may make the selection of properties more difficult. Common tuffs include kaolin, mordenite, chabazite and clinoptilolite(65,82,88–92). Modified natural zeolites or synthetic zeolites are more costly to produce, but exhibit increased selectivity and adsorption capacities(80). Amongst the synthetic zeolites, well-studied structures and framework types include MFI, BEA, and FAU zeolites (FAU includes zeolite X, [Figure 1.1](#)) (92–99). Syntheses are designed to mimic the natural conditions under which zeolites form; different phases are favoured by different Si/Al ratios (where  $\text{Si/Al} \geq 1$ ), and temperatures and heating times, which normally range between 80 and 160 °C, half an hour and a week(74,96). Fly ash waste from coal combustion may be converted into mesoporous zeolites under environmentally benign hydrothermal conditions and with the addition of a caustic reagent(66,96,100–102). ~ 800 million tons are produced a year but only 15 % is recycled. It has a composition similar to that of volcanic rocks, consisting of silicates, aluminates, carbonates, chlorides, sulfates and phosphates which first inspired the conversion in 1985(102,103).

Broader classifications of zeolites or “zeotypes” have incorporated similar structures containing alternative elements at “T sites” such as P, Ge, B, Ga, Be and Zn(98). Aluminium phosphates, or AlPOs (e.g. AlPO-5, [Figure 1.1](#)), consist of tetrahedrally coordinated  $\text{Al}^{3+}$  and  $\text{P}^{5+}$  ions in a 1:1 ratio producing neutral frameworks. These frameworks may be isostructural with zeolites: SAPO-37 is isostructural with faujasite zeolite and  $\alpha$ -berlinite is the AlPO analogue of quartz(104,105). Although frameworks are uncharged, cations such as Fe(III), Mn(II) and Co(II) may be incorporated during the initial synthesis to produce catalytically active reaction centres(106,107). AlPOs are mostly synthesised hydrothermally, although microwave synthesis has been applied to control crystal morphology and improve phase purity(108). These methods mean that ions are usually incorporated in their most stable oxidation state and species such as Fe(II) result from post-synthetic modifications(108,109). Mixed valent Fe(II)/(III) phosphates with three-dimensional open structures have also been produced(110).

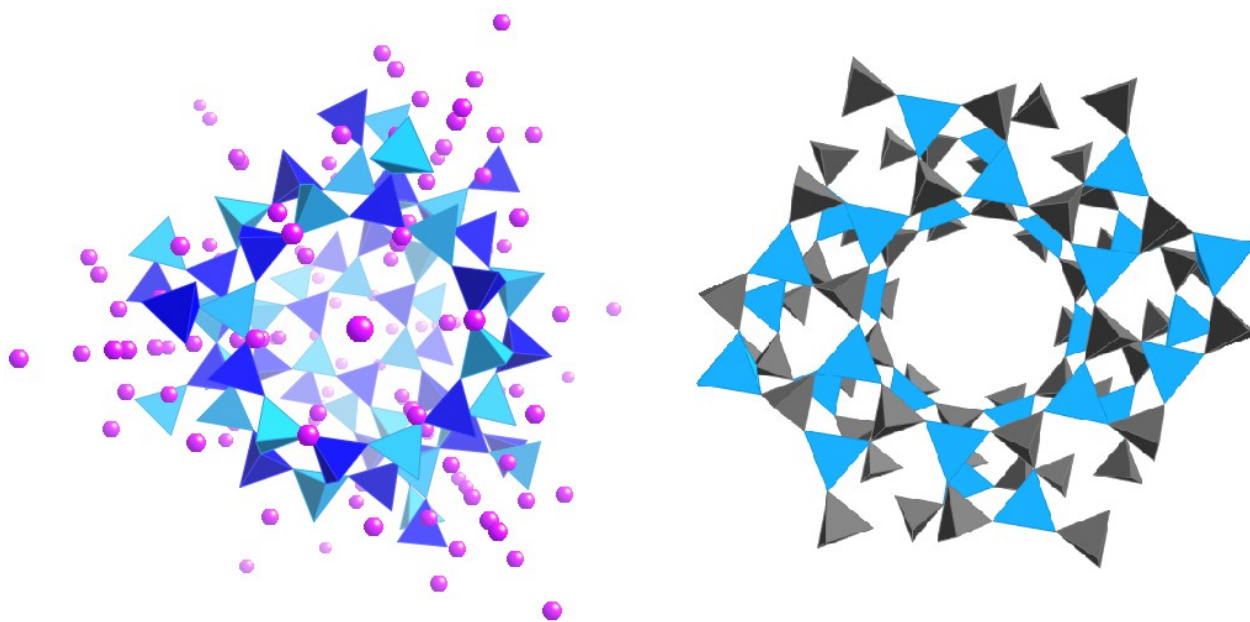


Figure 1.1: Left: zeolite X with intercalated metal ions; right: AlPO-5 neutral framework with no metal ions.

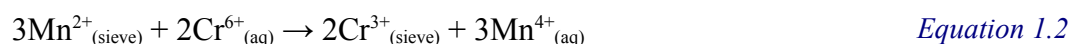
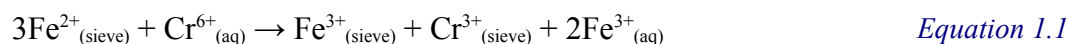
Zeolites have been tuned to exhibit remarkable selectivity towards target systems. Clinoptilolite has been widely studied for the immobilisation of radioactive caesium waste although ion exchange studies have shown Ag(I) and Ba(II) ions compete(82). Similarly, zeolite A shows a strong preference for Ag(I) ions(111). In zeolites X and A, Zn(II) (0.430 nm hydrated radius) is selected preferentially to Cd(II) (0.426 nm hydrated radius): it is proposed that the smaller ions preferentially occupy smaller surface pores of these structures(96). The large size of the 0.461 nm  $[\text{Cr}(\text{H}_2\text{O})_6]^{3+}$  ion makes it polarisable by highly-charged frameworks (*i.e.* those with lower Si/Al ratios and more counter cations in the lattice), such that the ion may deform sufficiently to pass through larger-ring apertures and occupy internal sites(111,112). However, smaller extraframework sites can only be occupied by smaller ions, and narrower pore openings may restrict larger ions with greater hydrated radii(17,113,114). Metal oxides embedded in the pore network establish some shape selectivity and zeolites with a narrower pore size distribution, such as GIS and ANA, are more selective(115,116). These molecular sieves also exhibit transition state selectivity, allowing some reactions to take place and not others, such as isobutane isomerism over H-ZSM-5 zeolite or the selective oxidation of cyclohexane in metal-substituted AlPO-5(116,117).

#### 1.4. Proposed Mechanism for Chromate Treatment and its Limitations

Although zeolites are cation exchangers, some anion uptake has been achieved: natural zeolites have been used to control the fluoride content of drinking water and several metal anions

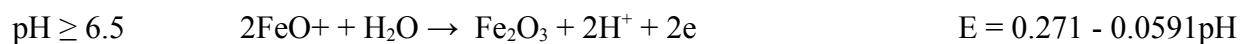
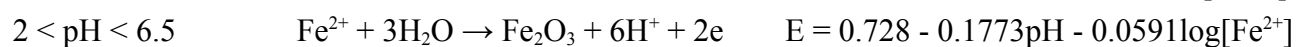
may be sorbed: arsenates, iodides, nitrates, perchlorates, antimonates and chromates, usually on the surface only(41,118–122).  $\beta$ -FeOOH coated silicates that operate only *via* surface adsorption take up 0.076 mg<sub>Cr</sub>/g<sub>sieve</sub> Cr(VI) within 180 minutes at slightly elevated temperatures, whilst Yokoi *et al.* found that Fe(III)-loaded MCM-41 selectively adsorbed up to 95 mg<sub>Cr</sub>/g<sub>sieve</sub> Cr(VI) into the pore network(123). Bacterium-supported zeolite Y achieved chromium loadings of 2.6 mg<sub>Cr</sub>/g<sub>sieve</sub> after 7 days and bacteria were also responsible for initial reduction of Cr(VI) to Cr(III)(9). This bacterial reduction has also been documented elsewhere(21). Ethylenediamine-reduced graphene oxide can also perform this *in situ* reduction and sorption of the resulting cation(28,124). Fe(II)-loaded clinoptilolite has been proposed for a similar mechanism, whereby Cr(VI) binds to the zeolite surface electrostatically at low pH and is afterwards reduced and released or readsorbed as Cr(III)/Fe(III) hydroxides(82). Kiser and Manning have shown that the reduction of Cr(VI) to Cr(III) is successful using Fe(II)-loaded faujasite samples and Figueiredo *et al.* find the presence of iron in all three oxidation states may enhance chromium uptake from solutions containing Cr(VI) species(41,125).

This work proposes the application of redox-active zeolites and aluminium molecular sieves for the *in situ* reduction and uptake of Cr(VI), followed by later extraction and recycling:



Electrochemical Equations are derived from the *Atlas of Electrochemical Equilibria in Aqueous Solutions* have been used to produce the thermodynamic Pourbaix diagram in Figure 1.2 assuming log[concentrations]  $\sim$  0(126). These model the redox reactions that take place across a broad pH range, under the assumption that all ions are in aqueous solution. Thus, results obtained may be seen as a useful guide to the viability of these systems, although the free energy of reactions may vary. Full Pourbaix diagrams from the book that show how Fe(II) is readily oxidised to form hydroxides as pH increases are shown in Appendix I.

**Fe:** Equation 1.3



**Mn:**

Equation 1.4

pH < 4	$\text{Mn}^{2+} + 2\text{H}_2\text{O} = \text{MnO}_2 + 4\text{H}^+ + 2\text{e}$	$1.228 - 0.1182\text{pH} - 0.0295\log[\text{Mn}^{2+}]$
$4 \leq \text{pH} \leq 6$	$\text{Mn}^{2+} + 3\text{H}_2\text{O} = \text{Mn}_2\text{O}_3 + 6\text{H}^+ + 2\text{e}$	$1.443 - 0.1773\text{pH} - 0.0591\log[\text{Mn}^{2+}]$
$6 < \text{pH} < 8$	$3\text{Mn}^{2+} + 4\text{H}_2\text{O} = \text{Mn}_3\text{O}_4 + 8\text{H}^+ + 2\text{e}$	$1.8234 - 0.2364\text{pH} - 0.0886\log[\text{Mn}^{2+}]$
$8 \leq \text{pH}$	$3\text{MnO} + \text{H}_2\text{O} = \text{Mn}_3\text{O}_4 + 2\text{H}^+ + 2\text{e}$	$E = 0.462 - 0.0591\text{pH}$

**Cr:**

Equation 1.5

pH < 7	$2\text{Cr}^{3+} + 7\text{H}_2\text{O} \rightarrow \text{Cr}_2\text{O}_7^{2-} + 14\text{H}^+ + 6\text{e}$	$E = 1.333 - 0.1379\text{pH}$ $- 0.0098\log \frac{[\text{Cr}_2\text{O}_7^{2-}]}{[\text{Cr}^{3+}]^2}$
$7 \leq \text{pH}$	$\text{CrO}_2^- + 2\text{H}_2\text{O} = \text{CrO}_4^{2-} + 3\text{H}^+ + 3\text{e}$	$E = 0.945 - 0.0788\text{pH}$ $+ 0.0197\log \frac{[\text{CrO}_4^{2-}]}{[\text{CrO}_2^-]}$

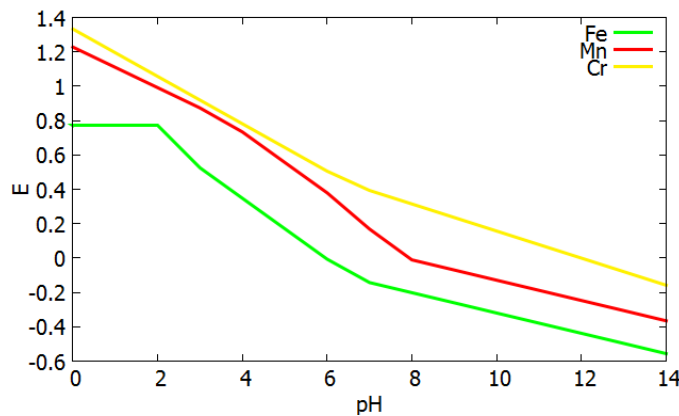


Figure 1.2: Pourbaix thermodynamic diagram: lines for Fe(II) → Fe(III) (Equation 1.3, green), Mn(II) → Mn(IV) (Equation 1.4, red) and Cr(III) → Cr(VI) (Equation 1.5, yellow) across pH.

This project builds upon previous studies that have validated the principle behind the proposed mechanism and aims to select and reduce Cr(VI) to Cr(III) without the use of expensive and potentially toxic organics and biological species. Even benign and reusable bacteria risk disturbing ecosystems if they leach into the environment and thus create their own waste streams. Although iron can be considered a pollutant, it is found naturally in large amounts and has a relatively high WHO limit of 0.3 mg/l, as well as being an essential mineral in the human diet(76). Manganese is also an essential trace mineral, but can be a hazard to aquatic organisms in large quantities and is therefore less preferable than iron for this application. As divalent rather than monovalent ions, Fe(II) and Mn(II) may also assist in opening up the pore network, creating greater accessibility for ion exchange(116).

This work aims to take up Cr(III) whilst avoiding the formation of difficult to recover hydroxides that are regularly dumped in landfill sites. Thus, elucidation of the uptake mechanism is vital to determining the viability of the technique. In order to elucidate mechanism, a detailed study of Fe ion oxidation states, coordination environments and the changes to them upon chromate exposure will be carried out, which has been hitherto unexplored (although Kiser and Manning have studied Cr ions)(125). Crucially, the extent to which Cr ions are reduced and adsorbed by the molecular sieves is of interest. The extent of uptake will be limited by the extent of cation exchange: ions rarely exchange 100 %, producing mixed compounds(127). A range of factors govern this limit: the presence of competing cations and complexing agents, dimensions of the hydrated dissolved species compared to the openings of the zeolite channels, and external surface activity(9,17,76,123,128,129). In the proposed mechanism, a low pH must be maintained to discourage the precipitation of chromium hydroxides. Specific cation exchange capacity may be measured by submerging the sorbent in a saturated solution(96). CEC depends upon the charge capacity (determined by aluminium content), phase purity, pore sizes and access, which may be limited by surface fouling or gatekeeper cations blocking smaller pores(66,73). Surface chemisorption competes with ion exchange through the pore network, which may be identified by non-stoichiometric loadings(89). CEC drops linearly with uptake of Cr(VI) due to surface sorption(90,96,130). In a competitive Cr(VI)/Cd(II) adsorption, Cr(III) hydroxide precipitates fouled the surface and decreased cadmium uptake(82). Lead and copper are chiefly taken up by surface adsorption and the presence of these ions can also affect CEC, eventually deactivating the sorbent(89,131).

In addition to mechanism, this work explores various structures and attempts modifications using templates to optimise systems for maximum chromium uptake. Templates may be employed during synthesis to improve framework crystallinity and direct particular pore dimensions, especially larger pores for enhanced molecular accessibility and relief of pore blockage: templating has generated zeolites with pore sizes from the microporous  $< 20 \text{ \AA}$  to macroporous  $> 500 \text{ \AA}$ (131). In the case of AlPOs, synthesis is profoundly influenced by choice of templates; the templates may afterwards be abstracted by chemical or thermal decomposition (64,132–134).

Common hard templates include triethylamine and other amines, which have been used to expand zeolite A and X pore networks from 4-8  $\text{\AA}$  to  $\sim 20\text{-}30 \text{ \mu m}$  and direct AlPO-5 and AlPO-18 formation, and large quaternary ammonium cations, in particular tetrabutylammonium hydroxide(107,135–140). A mixture of templates will produce varying crystal morphologies(141).

Soft templates differ from these hard templates by a diversity of zeolite-template interactions including but not restricted to van der Waals', hydrogen and covalent bonding. They

may include colloidal silicas (*e.g.* tetraethylorthosilicate and pre-organofunctionalised silica), polymers (*e.g.* polystyrenes, guanidines, dextran) and general surfactants(28,67,142–146). CTAB, cetyl trimethyl ammonium bromide, is a favourite amongst soft templates for introducing porosity(139,147–150).

Unfortunately, many templates are expensive, toxic and time-consuming to synthesise and may increase the likelihood of contamination or impurity phases(151). Other procedures such as dealumination under steam or acid treatment may be employed to obtain mesopores. Steam activation causes the hydrolysis of Al-O bonds and eventual extraction of aluminium from the framework leaving behind site defects and highly siliceous zeolites(94). Alternatively, concentrated nitric acid preferentially dissolves out the aluminium rapidly and thoroughly to give a naked framework that may be shown by the absence of Al-O stretches in infra-red spectroscopy(152–157). Extremely acidic conditions will create a disordered solid and eventually destroy all crystallinity. Siliceous zeolites may readily accept new ions into the framework such as Sn, Ti or Zr, but will not readily ion-exchange; they exhibit tunable acidity, high hydrothermal stability and hydrophobic properties such as adsorption of organic compounds(75,157). This process also removes surface deposits to regain access to the pore network, increasing the surface area(158,159).

## **1.5. Recycling**

This research goes further than previous studies in that it aims to produce a recyclable adsorbent which, whilst retaining Cr(III) in the waste water environment, may afterwards be washed with a specific elutant to free both the chromium and catalyst for reuse. From dealumination, the application of acid for metal extraction is well-recognised, but is accompanied by the unfortunate breakdown of the molecular sieve. Whilst zeolites with a high cation retention capacity are good candidates for chromium uptake, the adsorbed species may then prove difficult to extract, such that careful consideration of the environmental impact of end-of-life destination must be taken into account when selecting potential systems(79,90).

Regeneration has been achieved for a number of systems: Cr(VI)-bound anion resins were regenerated *via* washing with sodium hydroxide and brine and Na-zeolites have been reformed from Zn-exchanged analogues using various solutions, including acetates, carbonates and hydroxide solutions, of which EDTA was found to be the most satisfactory for 6 regeneration cycles, and NaCl for a further 3(5,160). In a two-step process of calcination at 350 °C and surfactant replenishment, sodium zeolite Y was thermally regenerated(86).

## 1.6. Aims

This work explores the application of Fe- and Mn-exchanged molecular sieves zeolites X, A, hierarchially porous ZSM-5, a natural zeolite tuff consisting primarily of clinoptilolite, AIPO-5, a mixed Fe(II)/Fe(III)-loaded AIPO and a LAU framework AIPO for the *in situ* reduction of Cr(VI) to Cr(III) and subsequent uptake into the sieve by an ion-exchange mechanism. [Chapter 3](#) details these systems and the impact of templating upon their crystallinity (characterised by powder x-ray diffraction) and chromium uptake (by x-ray fluorescence spectroscopy). Transmission electron microscopy measurements are used to explore mesoporosity. In [Chapter 4](#), the assignment of Fe and Mn sites before and after treatment with chromium solution is discussed using data gathered from Mössbauer spectroscopic investigations and electron paramagnetic resonance; surface measurements are provided by scanning electron microscope, energy dispersive x-ray spectroscopy and x-ray photoelectric spectroscopy. pH measurements monitor the exchange reaction and the dependence of Cr uptake upon pH is explored. [Chapter 5](#) investigates the aerial oxidation of iron ions loaded into zeolite by Mössbauer spectroscopy; reduction under hydrogen gas flow at elevated temperatures is then employed to reduce Fe(III) species in some systems, which are characterised using techniques already discussed. Chromium uptake and crystallinity are compared. Finally, [Chapter 6](#) explores the impact of competitive ions upon chromium adsorption, measures the extent of removal in solutions of different Cr(VI) concentration and attempts the recovery of Cr(III) and molecular sieves *via* metal ion/surfactant exchanges and acid treatment. X-ray fluorescence spectroscopy and UV-vis spectroscopy are employed.

## Chapter 2: Experimental Section

### 2.1. Techniques

#### *Schlenk Line*

The Schlenk line is used for handling air-sensitive materials under inert nitrogen gas flow or vacuum. It consists of two lines, which may be selected using a double oblique stopcock with greased ground glass joints. This connects to rubber tubing which may be attached to the side arm of a Schlenk flask or fitted with a reversed filter cannula for direct insertion through a rubber septa, e.g. for bubbling nitrogen through a liquid. A Teflon tap on the side arm may be opened or closed to expose the flask to the line. Two oil bubblers are fitted in series between the nitrogen line and open laboratory for the purpose of relieving an overpressure. A trap submerged in a Dewar flask of liquid nitrogen condenses waste gases from the vacuum line and protects the pumping system from solvent damage. Liquid nitrogen training was provided by the School of Chemistry and completed on 30 November 2011.

Deionised water, used as the solvent, is bubbled through with nitrogen for at least 20 minutes before being exposed to chemicals to ensure that it is de-oxygenated to an acceptable standard. To transfer liquids from one Schlenk flask to another, the necks are fitted with rubber septa, which can be pierced with cannulas or filter cannulas (if there is solid in suspension). Nitrogen is passed through the side arms in the direction of flow and an exit needle allows nitrogen relief in the collection flask.

Non-air-sensitive solids and PTFE magnetic stirrer bars may be added by removing the flask cap under nitrogen flow, which excludes air from the vessel. Solid products are filtered using a double-ended filtration flask and stored in an argon-filled glove box over drying beads.

#### *Gas Flow Techniques*

A controlled, reactive atmosphere may be produced by one-directional gas flow over an exposed sample. An alumina boat containing the starting materials sits in an end-capped silica and alumina tube, through which a gas is fed. Flow rate is controlled by adjusting the cylinder regulator

and monitoring the flow through a sulfuric acid bubbler. The tube sits in a tube furnace for heating purposes.

Waste gas is released into a fume hood. An empty flask separates the gas cylinder and acid bubbler to prevent suck back into the cylinder.

### ***Inert Atmosphere Glove Box***

A Saffron Scientific Alpha Anaerobic argon-filled glove box provides a high quality atmosphere for storing and working with air sensitive materials.

Recirculation through molecular sieves and copper catalyst filters remove H<sub>2</sub>O and O<sub>2</sub> respectively, maintaining an atmosphere of ~ 1 ppm oxygen/water. The catalysts are regenerated manually every few months through a process of heating and purging with 1:20 H<sub>2</sub>:N<sub>2</sub> gas. Freshly cut sodium will remain shiny if the atmosphere is clean.

All equipment entering the glove box must be thoroughly dry. Wet zeolite samples are stored over drying beads in a sealed desiccator kept within the glove box and not exposed to the glove box atmosphere for several days. Samples within the glove box are manipulated using a pair of protruding thick butyl rubber gloves.

## **2.2. Materials**

### ***Zeolites – Basic Systems(161)***

Zeolites A and X were synthesised through the combination of sodium aluminate, NaAlO<sub>2</sub> (Fisher Scientific), with sodium silicate, Na<sub>2</sub>SiO<sub>3</sub> (Aldrich), solutions and NaOH (Sigma Aldrich). These solutions are shaken vigorously and warmed in a furnace in polypropylene bottles to crystallise out the zeolites, which are then dried under suction filtration.

To produce 10 g of zeolite X, 1.23 g of NaOH and 5.69 g of sodium aluminate were dissolved in 116 ml of deionised water; this is later combined with 1.23 g of NaOH and 27.08 g of sodium silicate dissolved in 104 ml of deionised water under gentle heat. The sample is stirred for an hour at room temperature and then heated to 90 °C for 20 hours with periodic shaking for the first 3 hours.

To produce 10 g of zeolite A, 1.44 g of NaOH is dissolved in 160 ml of deionised water, which is then divided into two. In one, 16.52 g of sodium aluminate was dissolved, and in the other 30.96 g of sodium silicate under gentle heat. The sample is heated at 99 °C for 5 hours with periodic

shaking. This synthesis was also attempted with 10 % excess aluminate due to the production of zeolite X phase impurities through seeding in the synthesis bottle.

Natural zeolite containing clinoptilolite was supplied by Zoe Maher from the National Nuclear Lab.

### *Zeolites – Templated Systems*

Hierarchically porous ZSM-5 was synthesised using CTAB as a templating agent(139). The aim was to synthesise a zeolite with pore cavities similar to highly chromium-adsorbing MCM-41, but less silaceous, allowing for ion exchange, and with 3 dimensional pore channels. 0.078 g of sodium aluminate was dissolved in 8.24 ml of deionised water, and then stirred for 2 hours with 10.96 g of tetrabutylammonium bromide ( $\geq 98\%$ , Fluka) and 6.2 ml tetraethylorthosilicate ( $\geq 99\%$ , Aldrich). The solution was stood overnight before combining with 1 g CTAB, hexadecyltrimethylammonium bromide,  $C_{19}H_{42}BrN$  ( $\geq 98\%$  Sigma), 7 ml distilled water and 10 g ethanol (Fisher Scientific), stirred for 24 hours and then left overnight to dry. The dried material was then diluted with a little water and placed into a 150 ml Teflon-lined stainless steel autoclave to be heated to 150 °C for 36 hours. The product was filtered and washed, left to dry in air and then calcined at 550 °C for 6 hours to remove the organics.

Zeolite X was templated with CTAB by stirring 1 g into the sodium aluminate solution before combining with sodium metasilicate solution during its synthesis. The same process was used to introduce polymer templates of gelatin, agar and alginates. 1 g each of gelatin G2500 (Sigma), Agar A4550 (Sigma) and alginate LF20/40 (FMC) were dissolved slowly in 9 ml deionised water under gentle heating before stirring into the sodium aluminate solution gradually. Less concentrated solutions of alginates were also prepared: LF20/40 was prepared at 0.1 g:9.9 ml, 0.2 g:9.8 ml and 0.4 g:9.6 ml; alginates GP3350 (FMC) and 180947 (FMC) were also prepared at 0.2 g:9.8 ml. Zeolite products were calcined at 500 °C for 2-6 hours to remove the templates.

### *Zeolites – Ion Exchanges*

**Iron:** Zeolites were exchanged at 2.5 g of zeolite with a source of Fe(II). 3.45 g, a 3-4 fold excess, or a stoichiometric 1.465 g, of green  $FeSO_4 \cdot 7H_2O$  ( $\geq 99\%$  Sigma Aldrich) was used as a standard, whilst 2.475 g of  $FeCl_2 \cdot 4H_2O$  (99+ % Acros Organics) was also effective.  $Fe_2(SO_4)_3 \cdot 5H_2O$  (97 % Acros Organics) was used for one experiment to create an Fe(III) exchanged sample. These solids were dissolved in 125 ml of deionised water under nitrogen gas. The solution was stirred overnight and dried at room temperature under vacuum on the Schlenk line, then later stored in a

desiccator over drying beads in an argon-filled glove box.

Gentle heating of Fe(II)-loaded samples initiated a green → orange transition indicative of oxidation of Fe(II) to Fe(III). Preliminary experiments were carried out within air. However, Benchtop experiments saw the *in situ* oxidation as the green solution browned overnight.

**Manganese:** Samples were prepared on the benchtop by combining 2.455 g of MnCl<sub>2</sub>·4H<sub>2</sub>O (98+ % Sigma Aldrich) with 2.5 g of zeolite in 125 ml of water. The products of these exchanges were white or pale pink.

### *AlPOs*

To produce 10 g of AlPO<sub>4</sub>-5, synthesis was attempted according to the method proposed by Girnus *et al.* 1.73 g of triethylamine (99 % Aldrich) was added dropwise to 3.2 g of 85 % orthophosphoric acid (Fisher Scientific) and 5.83 g deionised water(162). The solution was cooled to 0 °C in an ice bath or over water before the addition of aluminium isopropoxide (Sigma Aldrich) and exchange ion salts. The solution was stirred at room temperature for 2 hours with 0.69 g of HF (Aldrich). Calcium Calgonate gel was kept on hand as a safety precaution against spillages.

The product was crystallised at 180 °C in a 150 ml Teflon-lined stainless steel autoclave in a preheated oven for 6 hours with 74.3 g water. After filtering and washing with water, the crystals were calcined in air at 600 °C overnight. Calcined and uncalcined products were produced (Table 2.1).

*Table 2.1: Preparation details of seven ion-loaded AlPO-5 systems*

Relative ion content/%	Exchange ion	Exchange ion/g	Aluminium isopropoxide/g
0			4.36
5	FeSO <sub>4</sub> ·7H <sub>2</sub> O	0.30	4.140
10	FeSO <sub>4</sub> ·7H <sub>2</sub> O	0.59	3.924
15	FeSO <sub>4</sub> ·7H <sub>2</sub> O	0.89	3.706
20	Fe acetate	0.90	3.488
50	Fe acetate	2.25	2.180
10	MnCl <sub>2</sub> ·4H <sub>2</sub> O	0.512	3.924

AlPO-Fe23, [Fe(II)Fe(III)<sub>0.8</sub>(H<sub>2</sub>O)<sub>2</sub>Al<sub>1.2</sub>(PO<sub>4</sub>)<sub>3</sub>].H<sub>3</sub>O, was synthesised according to the method proposed by L. Peng *et al.*(163). Adjustments were made to the original synthesis in attempts to synthesise a pure product, which was not achieved by these authors.

The “full-sized” reaction mixture consisted of 2.00 g aluminium isopropoxide, 16 ml triethyl glycol (99 % Alfa Aesar), 3.2 g imidazole, C<sub>3</sub>H<sub>4</sub>N<sub>2</sub> (≥ 99 % Sigma Aldrich), 2.8 ml 85 %

orthophosphoric acid and 0.97 g  $\text{FeCl}_2 \cdot 4\text{H}_2\text{O}$ /1.35 g  $\text{FeSO}_4 \cdot 7\text{H}_2\text{O}$ /1.50 g Fe acetate (95 % Acros Organics). The solution was stirred for 1 hour and then heated to  $180 \pm 30$  °C in a 45 ml Teflon-lined stainless steel autoclave for a 1-9 days. In some experiments, the amount of the reaction mixture was adjusted (to a half, third, quarter and sixth of the original) to vary the pressure in the autoclave.

A LAU-zeotype AlPO was synthesised according to the method proposed by Guo *et al.*(164). 0.838 g  $\text{FeCl}_2 \cdot 4\text{H}_2\text{O}$ , 2.18 ml of 85 % orthophosphoric acid, 12 ml triethyl glycol and 2.4 ml deionised water were stirred together for 30 minutes before the addition of 1.6 g of aluminium isopropoxide. The mixture was left stirring in air for a further 4 hours, after which it was combined with 2.69 g of imidazole and heated to 180 °C for 7 days. The product was filtered and dried, finely ground and heated to 100 °C under vacuum for 3 hours, and then 500 °C under inert gas flow for a further 4.5 hours to remove the templates.

### ***Chromium Exchanges***

Chromium ion-exchanges were carried out using a 0.02 M sodium dichromate solution (at least tenfold excess). 0.0745 g of  $\text{Na}_2\text{Cr}_2\text{O}_7 \cdot 2\text{H}_2\text{O}$  (99.5 % Aldrich) was dissolved in 25 ml of deionised water and shaken with 0.5 g of zeolite or AlPO before being allowed to stand overnight. The solid was then collected *via* suction filtration and the liquid mixed with 0.805 g, a 5-fold excess, of  $\text{SnSO}_4$  (95.5 % Alfa Aesar) to reduce the chromium ions to the +3 oxidation state. Tin sulfate solution was kept on hand to treat spillages by reducing carcinogenic Cr(VI) to Cr(III).

The effect of pH was investigated by conducting the exchange in solutions between pH 5 (37 % HCl, Fisher Scientific) and 13, prepared using NaOH as a base. pH was recorded using a calibrated HANNA Instruments pH211 Microprocessor pH Meter.

Mixed metal solutions were prepared at a concentration of 0.02 M for each metal and Fe- or Mn-loaded zeolite X was exchanged overnight in solutions containing two or more of the metals  $\text{CdCl}_2 \cdot 2.5\text{H}_2\text{O}$  (99+ % Acros Organics),  $\text{CuCl}_2 \cdot 2\text{H}_2\text{O}$  (Sigma Aldrich),  $\text{CoCl}_2 \cdot 6\text{H}_2\text{O}$  (Aldrich),  $\text{FeCl}_2 \cdot 4\text{H}_2\text{O}$ ,  $\text{MnCl}_2 \cdot 4\text{H}_2\text{O}$  (98+ % Sigma Aldrich),  $\text{NiCl}_2 \cdot 6\text{H}_2\text{O}$  (98 % Aldrich),  $\text{PbCl}_2$  (98 % Aldrich),  $\text{SnCl}_2 \cdot 2\text{H}_2\text{O}$  (Aldrich),  $\text{ZnCl}_2$  (Fisher Scientific),  $\text{CrCl}_3 \cdot 6\text{H}_2\text{O}$  (Aldrich) and  $\text{Na}_2\text{Cr}_2\text{O}_7 \cdot 2\text{H}_2\text{O}$ . Tin (II) sulfate solution was kept on hand to treat spillages by reducing highly reactive ions to lower oxidation states.

To identify a method by which chromium could be extracted from Cr-exchanged molecular sieves, samples of Cr-loaded zeolite X were ion exchanged with 0.02 M competitive sodium (NaCl, Fisher Scientific), potassium (KI Fisher Scientific), zinc ( $\text{ZnCl}_2$ ), silver ( $\text{AgCl}$ , 99 % Sigma Aldrich)

and barium ( $\text{BaCl}_2 \cdot 2\text{H}_2\text{O}$ , Sigma Aldrich) ions. Experiments on removal *via* complexing with 0.02 M EDTA (99+ % Aldrich) or tri-sodium citrate (Fisons) were also performed. Thirdly, samples were treated overnight with 25 ml of hydrochloric acid solutions at a pH between 0 and 4.5.

### ***Reduction***

In order to increase the proportions of Fe(II) present in the samples and potentially introduce Fe(0) metal, ~ 0.5-1 g of Fe-containing molecular sieve was loaded into a tube furnace in an alumina weighing boat under continuous 90:10  $\text{N}_2:\text{H}_2$  gas flow. They were heated rapidly to 400 or 500 °C and held at that temperature for between 0 and 24 hours, after which the furnace was switched off and they cooled rapidly to room temperature. Samples were removed into air after the furnace had dropped below 40 °C and instantly transferred to a glove box environment. Samples varied in colour between orange and silver grey.

## **2.3. Characterisation**

### ***X-Ray Diffraction***

#### ***Principle***

Electrons produced by a hot tungsten element are accelerated by a potential difference and strike a metal target (usually copper), ionising core 1s electrons. X-rays are emitted when higher energy electrons relax to replace the missing 1s electron, *e.g.* the  $\text{K}\alpha$   $2p \rightarrow 1s$  transition. Only a small fraction of the incident electron energy is converted into x-rays: the rest becomes heat and is quenched in a cooling process to prevent the apparatus from melting.

The x-ray beam is then directed upon a crystal lattice, which acts like a 3D diffraction grating when the wavelength is of the same order of magnitude as the interatomic spacings: approximately 0.5-3 Å.

Crucially, in x-ray diffraction, the electromagnetic wave interacts with electrons belonging to atoms in the structure. Atoms scatter radiation coherently – that is, without modifying the wavelength; this can be seen as an elastic collision. In crystalline solids, diffracted x-ray beams also undergo constructive interference. This is a consequence of the translational symmetry that fundamentally describes a crystal lattice: a periodic array of equivalent structural units that form a

space-filling three-dimensional structure. Atoms may be described as aligned at regular intervals: the waves diffracted from them have short path differences, which leads to constructive interference when these path differences are equal to a whole number of wavelengths. The detector measures the intensity of the beam diffracted by the lattice as a function of  $2\theta$  at fixed wavelength.  $2\theta$  describes the angle between the incident and diffracted beams. The magnitudes of these intensities and the angles at which they occur give information about the elements contained within the lattice and unit cell parameters describing the  $x$ ,  $y$  and  $z$  dimensions ( $a$ ,  $b$ ,  $c$ ) and angles of the repeating unit.

The diffraction of x-rays by crystals was discovered by Max Laue in 1912, who developed a rigorous mathematical derivation to describe constructive interference (Figure 2.1).

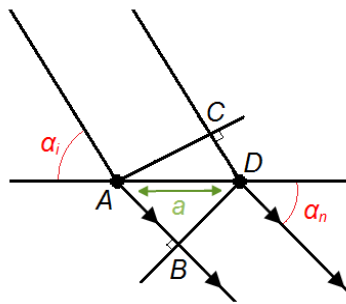


Figure 2.1: Diagram of diffraction angles, origin of Laue equations.

The path difference between diffracted beams is given by

$$AB - CD = a(\cos\alpha_n - \cos\alpha_i) = n_x\lambda \quad \text{Equation 2.1}$$

where  $a$  = interatomic spacing in the  $x$ -direction

$\alpha$  = angle between the  $x$ -axis and  $i$ , incident or  $n$ , diffracted beams

$n$  = an integer

$\lambda$  = wavelength

For constructive interference, scattered beams must be in-phase and so Laue equations satisfied in three dimensions simultaneously:

$$b(\cos\beta_n - \cos\beta_i) = n_y\lambda \quad \text{Equation 2.2}$$

$$c(\cos\gamma_n - \cos\gamma_i) = n_z\lambda \quad \text{Equation 2.3}$$

The requirements for constructive interference may also be described more simply by William Bragg's model, which proceeds from the assumption that planes of atoms reflect x-rays (Figure 2.2).

$$n\lambda = 2d_{hkl}\sin\theta \quad \text{Equation 2.4}$$

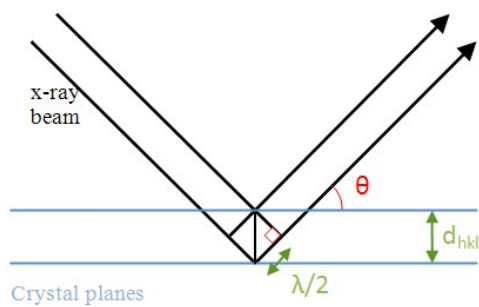


Figure 2.2: Diagram of reflection angles, origin of Bragg equation.

The angles at which peak intensities arise are used to calculate d-spacings, which describe the separations between lattice planes; these are unique to a structure (few d-spacings coincide between different cells) and independent of wavelength. d-spacings are then indexed to yield Miller indices, which label how often a plane cuts an axis per unit cell (Figure 2.3). From these, the unit cell symmetry and lattice parameters,  $a$ ,  $b$ ,  $c$ ,  $\alpha$ ,  $\beta$  and  $\gamma$  are derived.

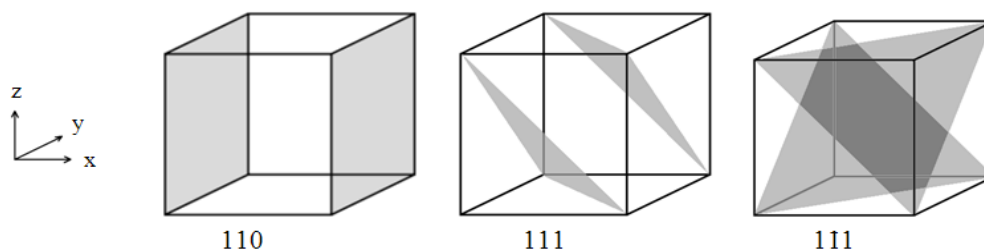


Figure 2.3: Miller planes  $110$ ,  $111$  and  $111$  represented on arbitrary unit cells.

$$\frac{1}{d_{hkl}^2} = \frac{h^2}{a^2} + \frac{k^2}{b^2} + \frac{l^2}{c^2}$$

Equation 2.5

Some  $hkl$  values are systematically absent. These absences arise from the cancellation of an equal number of same-amplitude out-of-phase diffraction beams. They depend upon intra-cell translational symmetry, providing a shortlist of possible space groups.

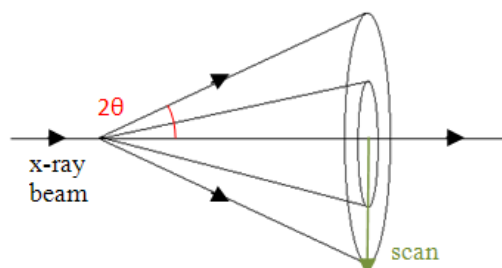


Figure 2.4: Debye-Scherrer PXRD scattering cone of the x-ray beam.

A powder consists of a large number of crystallites  $\sim 10^{-6}$  m in diameter, arranged in random orientations such that some provide lattice planes correctly oriented so as to satisfy Bragg's Law.

In powder x-ray diffraction, the diffracted beam scatters in a cone, such that the incident beam lies along the rotational axis (Figure 2.4). Orientation averaging on the cone means that the intensities are projected into a single dimension and readings between same or similar  $d$  values overlap, giving rise to many fewer peaks than in single crystal diffraction. Extreme preferred orientation can also lower the number of peaks observed in the powder x-ray diffraction pattern.

The intensities of lattice peaks arise from the sum of contributions from different scatterers. Because x-ray diffraction involves the interaction between x-rays and electrons, heavier elements with more electrons scatter more strongly and contribute more to intensity. This can help differentiate between similar structures with the same lattice, but also means that lighter elements may become invisible in the presence of heavier atoms. Intra-structural species like water molecules also contribute to intensity and may further distort intensity information.

Intensity is given by the equation:

$$I_{hkl} = K_e \frac{M_{hkl}}{V^2} |F_{hkl}|^2 Lp \quad \text{Equation 2.6}$$

where  $K_e$  = an experimental constant

$M_{hkl}$  = the multiplicity of the  $hkl$  planes

$V$  = the volume of the unit cell

$|F_{hkl}|^2$  = the structure factor

$Lp$  = Lorentz-Polarisation correction, such that

$$Lp = \frac{1 + \cos 2(2\theta) \cos 2(2\theta_M)}{\sin 2\theta \cos \theta} \quad \text{Equation 2.7}$$

where  $\theta_M$  = the angle of the monochromator

The Lorentz-Polarisation correction depends upon the exact geometry of data collection. The amount of sample in the beam, the detector efficiency and the original intensity of the x-rays are also very important in determining the scale of peak intensities, and these factors are contained within the other terms. However, only two terms, the multiplicity of the planes,  $M_{hkl}$ , and structure factor,  $F_{hkl}$ , contribute to the relative intensities between peaks – *i.e.* they have an  $hkl$  dependence. The contribution of the structure factor dominates, such that the relative intensity of peaks is often reduced to a proportionality:

$$I_{hkl} \propto |F_{hkl}|^2 \quad \text{Equation 2.8}$$

Because of this relationship, only the modulus of the structure factor may be derived from intensity measurements for any given  $hkl$  reflection, which gives rise to a fundamental problem of structure solution in crystallography, known as the phase problem. Electron density cannot be mapped from x-ray diffraction data without first determining the relative phase of each contribution. Direct Methods and the Patterson Method work with large data sets from single crystal measurements such that solutions can in practise be solved – but powder diffraction patterns are still best solved by matching with existing model structures.

The structure factor is a complex term:

$$F_{hkl} = q \cdot \sum_{n=1}^N f_n(\theta) e^{[2\pi i (hx_n + ky_n + lz_n)]} \quad \text{Equation 2.9}$$

or

$$F_{hkl} = q \cdot \sum_{n=1}^N f_n(\theta) [\cos 2\pi (hx_n + ky_n + lz_n) + i \sin 2\pi (hx_n + ky_n + lz_n)] \quad \text{Equation 2.10}$$

where  $q$  = Debye-Waller factor

$f_n$  = the atomic form factor, the scattering power of atom  $n$

However, centrosymmetric crystals possess a centre of inversion such that identical atoms sit at  $\pm (x,y,z)$ , sine terms in the imaginary part cancel, and a real description is left that depends upon the Debye-Waller factor, scattering power of atom  $n$  ( $f_n$ ) and its  $x$ ,  $y$  and  $z$  coordinates:

$$F_{hkl} = q \cdot \sum_{n=1}^N f_n(\theta) \cos 2\pi (hx_n + ky_n + lz_n) \quad \text{Equation 2.11}$$

Destructive interference normally occurs at high scattering angles between x-rays diffracted off different parts of an electron cloud belonging to the same atom, leading to a drop off in intensity and limiting the information that may be extracted from these reflections. The sharpness of this drop off is increased with atomic vibration, which increases the effective size of the electron cloud around an atom and so the extent of destructive interference taking place. Extremely rapid intensity drop off may result from using the wrong geometry, *e.g.* reflection geometry assumes infinite thickness, which is not true for all samples containing very light elements.

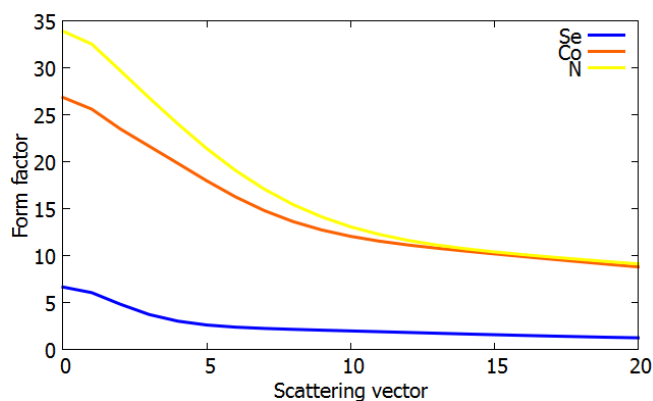


Figure 2.5: Plot of the atomic form factor against scattering vector, showing drop off at increasing angle. Elements: Se, in yellow, Co, in orange, and N in blue.

The Debye-Waller factor,  $q$ , describes the temperature-dependent spread of electron density due to increasing atomic vibration (assuming a rigid body) and static or dynamic positional order. Atomic vibrations which are not temperature-dependent are accounted for by the atomic form factor,  $f_n$ , which is a Fourier transform of the spatial distribution of charge density (assuming spherical atoms). The atomic form factor has a greater influence over the rate of drop off of intensity than the Debye-Waller factor; it is dependent upon the number of electrons in an atom, such that as  $\theta \rightarrow 0$ , the atomic form factor  $\rightarrow$  the total number of electrons,  $Z$ , in the atom (Figure 2.5).

### ***Equipment***

In-house powder x-ray diffraction data were collected on five powder diffractometers.

#### **Bruker D8 ADVANCE**

Routine measurements were carried out in the Bruker D8 ADVANCE diffractometer. Samples were mounted on rotating discs between two pieces of tape and analysed for 28 minutes per sample at a range of 5-70 ° with a step size of 0.019802258. This instrument is run in transmission mode.  $\lambda = 1.5405999 \text{ \AA}$  and the tube operates under a 40 kV/30 mA acceleration. The Vario1 Johansson focusing monochromator produces high-flux Cu K $\alpha$ -1 radiation. Training took place on 6th October 2011.

#### **Bruker AXS D5005**

Routine measurements were carried out in the Bruker AXS D5005 diffractometer. Samples were loaded into a cavity and the surface flattened with a slide and analysed for 25 or 54 minutes per sample at a range of 5-65 ° with a step size of 0.019802258. This instrument is run in reflection mode.  $\lambda = 1.5405 \text{ \AA}$  and the tube operates under a 40 kV/30 mA acceleration, producing Cu K $\alpha$ -1 radiation. Training took place on 29th August 2012.

#### **Bruker D8 ADVANCE capillary**

For zeolite samples, the Bruker D8 ADVANCE and Bruker AXS D5005 give good resolution diffraction peaks, but inaccurate, varying intensities result from the high water and cation content. Instant absorption on exposure to air makes dehydration difficult. Thus, improved XRD patterns were recorded on the Bruker D8 ADVANCE capillary diffractometer after dehydrating the samples over drying beads. Non-heat- and air-sensitive samples were warmed for a few days in air, and temperature- and air-sensitive samples were stored in a desiccator under inert atmosphere for one month before being finely ground and loaded into 0.6-0.7 mm silica capillary tubes. Samples

were analysed for 3-10 hours at a range of 5-70 ° with a step size of 0.019758105. This instrument is run in reflection mode.  $\lambda = 1.5405999 \text{ \AA}$  and the tube operates under a 40 kV/40 mA acceleration, producing Cu K $\alpha$ -1 radiation. Training took place on 9th January 2013.

### **Siemens D5000 capillary**

A changeover of equipment meant that further capillary measurements were run on the Siemens D5000 diffractometer. Samples were prepared and loaded as before, and run in 0.6-0.7 mm silica capillary tubes for 4-8 hours per sample at a range of 10-80 ° with a step size of 0.0154613. This instrument is run in transmission mode.  $\lambda = 1.5406 \text{ \AA}$  and the tube operates under a 40 kV/30 mA acceleration, producing Cu K $\alpha$ -1 radiation. Training took place on 24th May 2013.

### **Bruker D2 PHASER**

The Bruker D2 PHASER operates with a Co rather than a Cu source, and thus does not fluoresce Fe and Mn. Therefore this machine improves the peak to background intensity for samples that causes problems in the routine diffractometers, such as those containing Fe or Mn. This was particularly useful for assessing the crystallinity of zeolites after treatment with competitive metal ions. Samples were loaded into a cavity and the surface flattened with a slide and analysed for 26 minutes per sample at a range of 5-80 ° with a step size of 0.350. This instrument is run in Lynxeye reflection mode.  $\lambda = 1.79026 \text{ \AA}$  and the tube operates under a 30 kV/10 mA acceleration, producing Co K $\alpha$ -1 radiation. Training took place on 18th June 2013.

### ***Analysis(165–167)***

Samples were routinely analysed using Bruker's EVA software for pattern matching and phase identification. d-spacings and peak widths could be extracted and background intensity removed. Rietveld refinement of known trial structures against data gathered from powder x-ray diffraction was carried out using the program GSAS. Although this method requires a predicted structure, it bypasses the problem of resolving intensity into different contributions and, significantly, does not use the integrated intensity of the *hkl* planes as observations, but the profile intensities of every data point. Rietveld refinement may be used to elucidate unit cell parameters, atomic coordinates, site occupancies and phase fractions and can go on to model peak profiles, which are determined by the instrument and imperfections in the material.

The procedure minimises the difference between observed ( $y_i$ ) and calculated ( $y_i^{calc}$ ) data for the  $i^{\text{th}}$  point (after background subtraction) using least squares refinement:

$$S_y = \sum_i w_i (y_i - y_i^{calc})^2 \quad \text{Equation 2.12}$$

where  $S_y$  = the residual function

$w_i = 1/y_i$  (the weighting factor), such that each observed point contributes equally

The refinement is cycled initially a small number of times. Gradually, more variables may be introduced as more parameters are refined. Heavier atoms with more electrons will have a greater influence over the structure, so their positions should be refined first. Peak profile parameters should be refined last so they do not try to account for poor peak positions. By the end of the refinement, all parameters should be refined simultaneously to generate estimates of their reliability. If the original model is not good enough, the refinement will either diverge or lead to a false local minimum.

The most reliable way of monitoring the progress of the refinement is a by-eye assessment of the difference plot. However, it is important to pair this with chemical knowledge: in zeolites, low-angle peak intensities are much more sensitive to the presence of extraframework species, so the scale factor is best matched to high-angle peak intensities, which primarily result from framework species: this may create a plot with a poor low-angle intensity match, demonstrative of the limitations to the model. Thermal parameters may to some degree compensate for this: problems such as negative thermal parameters reflect extraframework species missing from the structural model. Structural parameters such as bond lengths and angles can provide complementary data on whether the model is chemically sensible. However, non-systematic errors in intensities cannot always be accounted for, *e.g.* poor representation of crystal orientations when powder grains are too large.

The profile fit and the shift or standard deviation of minimised  $S_y$  are the most valuable measures of the refinement quality. Residual “R” functions follow the progress of the refinement mathematically to indicate how well the pattern is being accounted for by the structural model. However, these should not be over-interpreted. They map the precision of the refinement, not its accuracy.  $R_p$ , the pattern R factor, and  $R_{wp}$ , the weighted pattern R factor, are the most commonly used.

$$R_p = \frac{\sum |y_i - y_i^{calc}|}{\sum y_i} \quad \text{Equation 2.13}$$

$$R_{wp} = \left[ \frac{\sum w_i (y_i - y_i^{calc})^2}{\sum w_i y_i^2} \right]^{\frac{1}{2}} = \left[ \frac{S_y}{\sum w_i y_i^2} \right]^{\frac{1}{2}} \quad \text{Equation 2.14}$$

A good  $R_{wp}$  should approach the statistically expected R value,  $R_{exp}$ , which describes the collected data quality.

$$R_{\text{exp}} = \left[ \frac{N_o - N_v}{\sum w_i y_i^2} \right]^{\frac{1}{2}} \quad \text{Equation 2.15}$$

where  $N_o$  = the number of observations  
 $N_v$  = the number of parameters

The ratio between these R factors is the “goodness of fit parameter”,  $\chi^2$ , an estimate of the statistical quality of the refinement:

$$\chi^2 = \left( \frac{R_{\text{wp}}}{R_{\text{exp}}} \right)^2 = \frac{S_y}{N_o - N_v} \quad \text{Equation 2.16}$$

As  $R_{\text{wp}}$  approached  $R_{\text{exp}}$ ,  $\chi^2$  approaches 1. However, a low value of  $\chi^2$  close to 1 may not necessarily reflect a good refinement: if a pattern has a high background that has not been subtracted from  $y$  values, much of the intensity will be modelled by the background function and  $R_{\text{wp}}$  will be misleadingly low; similarly, in low-quality patterns where not enough data points have been measured,  $R_{\text{exp}}$  will be very large, minimising  $\chi^2$ .

Not all parameters may be freely refined. In zeolites, Si and Al have the same number of electrons and are thus indistinguishable by x-ray diffraction: relative site occupancies cannot be refined. Site occupancy and thermal parameters are also interdependent as they describe the extent of electron spread: thermal parameters are often fixed at sensible values whilst occupancies are refined.

Peak shape arises as a function of sample and the instrument conditions, varying with  $2\theta$  (Figure 2.6). The peaks are assumed to be made up of a combination of both Gaussian and Lorentzian components:

Gaussian:  $\text{FWHM}^2 = U \tan^2\theta + V \tan\theta + W$  Equation 2.17

Lorentzian:  $\text{FWHM}^2 = X \tan\theta + Y/\cos\theta$  Equation 2.18

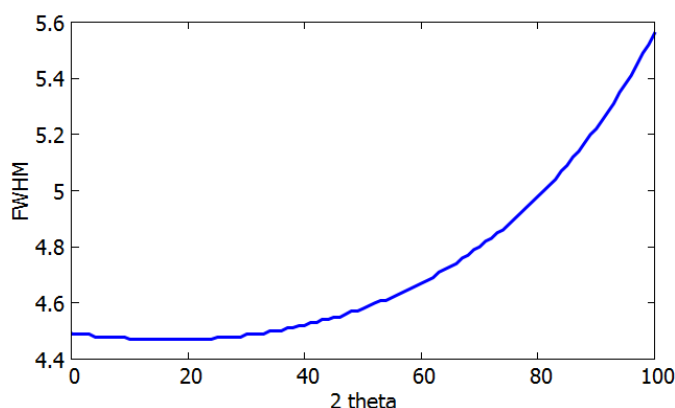
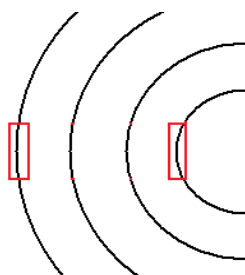


Figure 2.6: Plot of FWHM against  $2\theta$ . The dip or minimum occurs where  $GV$  is negative.

However, the  $2\theta$ -dependence may not account for low angle peak asymmetry, and additional parameters may need to be fitted to describe beam curvature at low  $2\theta$  values (Figure 2.7).



*Figure 2.7:  $2\theta$ -dependence of peak shapes: the red box represents the detector intersecting with the x-ray scattering cone; at low angles, the cone is highly curved, whereas at high angles the cone may be approximated to a straight line such that readings give a more symmetric peak.*

Where Rietveld refinement of known trial structures against data gathered from powder x-ray diffraction is carried out to obtain unit cell parameters, atomic coordinates, site occupancies and phase fractions, Le Bail refinement fits the intensity and profile data gathered from powder x-ray diffraction only, obtaining unit cell parameters. Structural parameters are not included and, as such, the Le Bail does not refine/provide values for atomic coordinates, site occupancies and phase fractions. Le Bail provides a quick refinement that bypasses the problem of fitting peak intensities to electron density provided by the elements in the structure to give accurate unit cell parameters. The accuracy of these parameters may be compromised in Rietveld refinement of zeolites with intensities that are readily perturbed by the presence of water that naturally inhabits the pore network, and may vary wildly from sample to sample and measurement to measurement, giving little or no useful information.

### ***Wavelength-Dispersive X-Ray Fluorescence Spectroscopy (WD XRF)(168,169)***

#### ***Principle***

The principles of x-ray fluorescence are similar to those of x-ray diffraction. Electrons accelerated by an applied voltage strike an anode material, depositing their energy, 1-2 % of which is converted into x-rays. This occurs when high energy electrons relax to replace low energy core electrons ionised by the electron beam.

This x-ray beam falls upon the sample, where the same thing happens. The energy of the incident beam must exceed the characteristic binding energy of inner electrons within the sample to excite characteristic 'secondary' x-ray fluorescences. The fluorescence yield,  $\omega$ , is the probability of

an x-ray resulting per incident pulse. This depends upon atomic number and the electron transition within the element. Light elements have low  $\omega$  values and heavier elements have higher  $\omega$  values, tending towards 1. Due to the limiting factor of the applied voltage, certain binding energies are inaccessible.

Each element possesses characteristic electron binding energies – *i.e.* the energies required to dissociate electrons from different energy levels. This allows for the qualitative and quantitative determination of chemical elements within the sample. Characteristic Rh lines appear in the spectrum from the anode (Figure 2.8), as do Rayleigh and Compton scattering lines, although these are partially removed by a primary beam filter, which optimises the performance of the spectrometer to enhance detection sensitivity for particular groups of elements within a fluorescent energy range. Other additional peaks include “escape peaks”, which arise when the inert gas is ionised by the x-ray beam, emitting its own characteristic x-ray. The measured signal will then be lower than the incident energy by the energy of the new x-ray: for Ar gas, this is  $\sim 3$  eV. For lighter elements such as He, the effect is negligible.

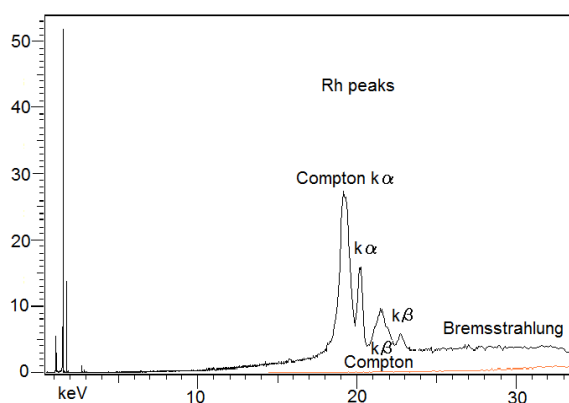


*Figure 2.8: Characteristic Rh lines in the XRF spectrum.*

Not all elements are detected by this technique. The XRF spectrometer does not detect matrix compounds such as oil and polymer films, water, or wax and flux that are used as preparation agents. To account for the presence of these materials, they must be measured and input into the calculations by the user. Passing through materials reduces the intensity of x-rays, especially when heavier elements are present. Those x-rays of lower energy – or longer  $\lambda$  – are absorbed more readily, such that x-rays emitted from light elements are often completely absorbed by the sample. With the Rh anode, everything up to Be may be unseen.

X-ray fluorescence is a good technique for analysing inorganic materials such as geological, environmental and metallurgical compounds. The technique is comparative, using the intensities of reference materials to determine the factor by which the pulse height in counts per second (kcps) of

characteristic elements relates to their concentration in samples. Kcps describes the number of detected photons of a given energy per unit time, *i.e.* how much of the element is “seen” by the spectrometer. A calibration may be used to increase the accuracy of the comparative method. The peak shape for a given spectrometer is fixed as a function of analyser crystal, collimator and spectrometer geometry, such that intensity may be considered independent of peak width (on the order of 0.01 eV) when evaluating elemental concentration.

### ***Equipment***

Experiments were run on the Bruker S8 Tiger 3K X-Ray Fluorescence spectrometer, data compiled using S8 Collector and analysed with Spectra Plus Launcher software. Training took place on 10th October and 13th December 2011.

The S8 Tiger has a 3 kW x-ray tube, operating up to 60 kV and 150 mA. The high applied voltage requires non-conductive, deionized water to cool the tube and anode. The system is fitted with an integrated vacuum pump and the counter runs under methane 10:90 argon gas, whilst the tube operates under He gas for powder and liquid samples. The primary beam filter consists of a 0.2 mm thick Cu filter, which largely absorbs the Rh tube radiation.

Collimators are used to filter out the divergence of the secondary fluorescence reaching the analyser crystals *via* a series of parallel slits set at a specific aperture angle. Collimators with larger apertures select for light elements at low resolution (broad peak width), whilst narrower apertures can detect heavier elements better. The S8 Tiger features a standard collimator with an aperture angle of 0.23 °, such that 0.23 ° describes the limit the spectral energy may diverge from the parallel path without being filtered out.

The fluorescent spectrum consists of a blend of radiation characteristic of the elements present in the sample. The wavelength dispersive XRF spectroscopy relies upon diffraction to resolve the wavelengths of different elements using a series of monochromatic crystals of known d-spacings. Several crystals of different d-spacings must be used in order to cover the angular range for which Bragg's Law holds true (0-90 °) and thus detect the widest spectrum of elements possible. The S8 Tiger is fitted with two lithium fluoride crystals: LiF220, which has a d-spacing of 2.85 Å, and LiF200, which has a d-spacing of 4.03 Å. A pentaerythrite crystal or “PET” has a d-spacing of 8.74 Å and the final crystal, a tungsten/silicon multilayer crystal, XS-55, has the largest d-spacing of 55 Å and can diffract wavelengths of lighter elements, such as magnesium.

The job of the detector is to use Bragg's Law ([Equation 2.4](#)) to calculate the wavelength and measure the intensity at that wavelength. To do this, a goniometer sweeps the emission spectrum,

giving the Bragg angle,  $2\theta$ , for the separated wavelengths. The detection limit is given by,

$$\text{Detection limit} = \frac{3}{m} \sqrt{\frac{I_b}{T_b}} \quad \text{Equation 2.19}$$

where  $m$  = sensitivity of analyte in kcps/mass %

$I_b$  = background intensity of analyte in kcps

$T_b$  = counting time in seconds for background

### *Analysis*

The S8 Tiger may be fitted with three masks of different sizes: 8 mm, 23 mm and 34 mm for detection of samples prepared by different methods. It is important to prepare samples carefully, as inconsistencies in grain size and homogeneity can build errors into the measurement. Surface treatment is more important for heavy matrices and light elements may suffer from poor resolution because of inadequate penetration depths, although a few mm is enough for most samples. Samples may be run as loose powders, liquids, pressed into pellets with wax, or fused into glass beads.

Loose powders and liquids are prepared in plastic holders fitted with stretched Mylar film on the surface exposed to the spectrometer. Liquids are measured in 34 mm sample holders fitted with 3" diameter Mylar films and loose powders are measured in 8 mm sample holders (in order to create sufficient depth) fitted with 2.5" diameter Mylar films after grinding with a pestle and mortar. Chemplex Mylar of 2.5  $\mu\text{m}$  thickness was used; Mylar is made of polyester,  $\text{C}_{10}\text{H}_8\text{O}_4$ , and is a good film material for acidic samples, although not recommended for use with bases. Powder samples may also be pressed into 10 mm pellets using Spectroblend 44  $\mu$  powder wax as a binding agent. They are formed in a pellet press under  $\sim 5$  tonnes of applied pressure.

Fused beads have the advantage of introducing matrix homogeneity by fixing them with a glass flux. They are synthesised by combining a flux with the sample in a 10:1 ratio and heating the solids to 1050  $^{\circ}\text{C}$  in a platinum crucible. Usually 0.35 g of sample are used to make beads suitable for measurement with the 23 mm spectrometer mask. Smaller, 8 mm beads may also be made with smaller quantities of sample. Samples are measured to a depth of  $\sim 0.3 \mu\text{m}$ . To produce the glass, the sample is first heated in a furnace to 500  $^{\circ}\text{C}$  for a few hours to ensure complete oxidation, *i.e.* all elements are in their maximum oxidation state. This ensures there will be no change in composition inside the fused bead furnace. The sample is then ground together with Sigma lithium 66 % meta- ( $\text{LiBO}_2$ ) 34 % tetra- ( $\text{Li}_2\text{B}_4\text{O}_7$ ) borate flux, which melts at 825  $^{\circ}\text{C}$ , and a spatula tip full of Sigma Aldrich ammonium iodide is added as a releasing agent.

A full elemental scan takes 17 minutes to run, whilst calibrations are much faster: 2-7 minutes for zeolites and AlPOs, depending upon the number of elements. Fused bead calibrations are used to obtain more accurate values using the SPECTRA<sup>plus</sup> software. Elements present in the samples are selected and the compositions of reference materials made up for the purpose are entered before they are run against these theoretical values. The calibration curve may then be interpolated when samples of unknown composition are compared (Figure 2.9). This means that the reference materials must be synthesised with compositions across the range of expected mass percentage of the elements appearing in the studied samples.

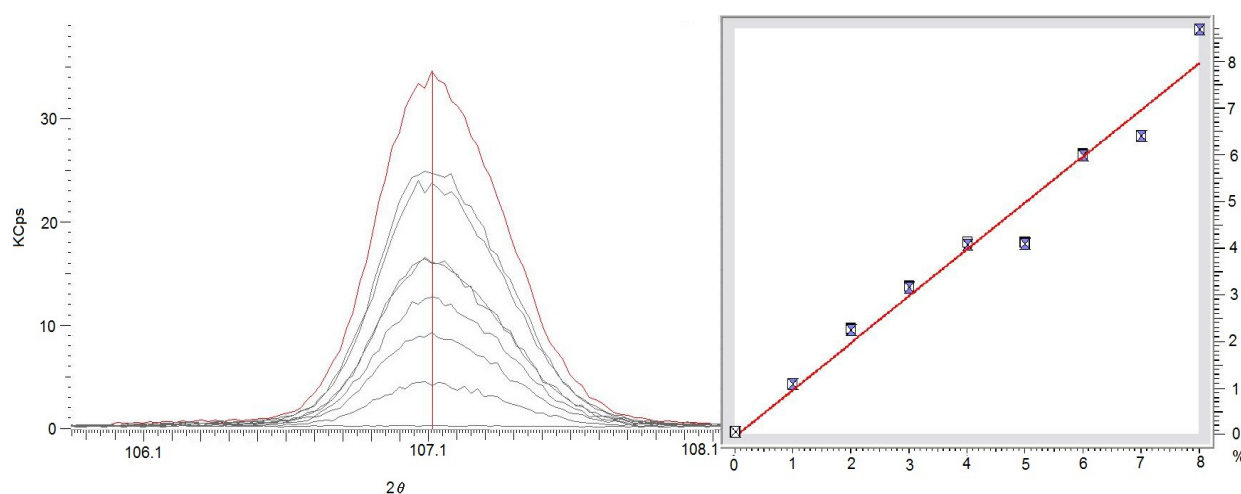


Figure 2.9: Left: calibration curves for chromium peaks in zeolite calibration samples; right: linear correlation between kcps and measured input chromium content in calibration samples.

Usually oxides of the elements are used for making up reference beads. For zeolite and AlPO samples these include  $\text{Al}_2\text{O}_3$ , 99.7 % Sigma Aldrich,  $\text{Cr}_2\text{O}_3$ , 99 % Acros Organics,  $\text{Fe}_2\text{O}_3$ ,  $\geq 99$  % Sigma Aldrich,  $\text{MnO}$ , 99 % Aldrich, and  $\text{SiO}_2$ , Merck (Tables 2.2 and 2.3). Oxides of sodium and phosphorus are unstable, and as such formed *in situ* from sodium carbonate  $\text{Na}_2\text{CO}_3$ , and ammonium phosphate dibasic  $(\text{NH}_4)_2\text{HPO}_4$ , Sigma Aldrich. The solids are gently warmed in an oven prior to weighing to ensure that no water is present that might distort the calibration.

Table 2.2: Calculations of relative zeolite oxide quantities by weight (g) for Fe and Mn calibration fused beads of 0.35 g.

<b>Beads</b>	<b>SiO<sub>2</sub></b>	<b>Al<sub>2</sub>O<sub>3</sub></b>	<b>Na<sub>2</sub>CO<sub>3</sub></b>	<b>Cr<sub>2</sub>O<sub>3</sub></b>	<b>Fe<sub>2</sub>O<sub>3</sub></b>	<b>MnO</b>
<b>Oxide %</b>	<b>33-49</b>	<b>19-33</b>	<b>7-11</b>	<b>0-8</b>	<b>15-25</b>	<b>0</b>
<b>1_Fe</b>	0.2450	0.0950	0.0599	0.0000	0.1250	0.0000
<b>2_Fe</b>	0.2350	0.1038	0.0641	0.0050	0.1188	0.0000
<b>3_Fe</b>	0.2250	0.1125	0.0684	0.0100	0.1125	0.0000
<b>4_Fe</b>	0.2150	0.1213	0.0727	0.0150	0.1063	0.0000
<b>5_Fe</b>	0.2050	0.1300	0.0770	0.0200	0.1000	0.0000
<b>6_Fe</b>	0.1950	0.1388	0.0812	0.0250	0.0938	0.0000
<b>7_Fe</b>	0.1850	0.1475	0.0855	0.0300	0.0875	0.0000
<b>8_Fe</b>	0.1750	0.1563	0.0898	0.0350	0.0813	0.0000
<b>9_Fe</b>	0.1650	0.1650	0.0941	0.0400	0.0750	0.0000
<b>Oxide %</b>	<b>35-55</b>	<b>23.5-38.5</b>	<b>5-10</b>	<b>0-0.5</b>	<b>0</b>	<b>11.5-21</b>
<b>1_Mn</b>	0.2750	0.1175	0.0855	0.0000	0.0000	0.0575
<b>2_Mn</b>	0.2550	0.1325	0.0770	0.0005	0.0000	0.0670
<b>3_Mn</b>	0.2350	0.1475	0.0684	0.0010	0.0000	0.0765
<b>4_Mn</b>	0.2150	0.1625	0.0599	0.0015	0.0000	0.0860
<b>5_Mn</b>	0.1950	0.1775	0.0513	0.0020	0.0000	0.0955
<b>6_Mn</b>	0.1750	0.1925	0.0428	0.0025	0.0000	0.1050

Table 2.3: Calculations of relative AlPO oxide quantities by weight (g) for Fe and Mn calibration fused beads of 0.35 g.

<b>Beads</b>	<b>(NH<sub>4</sub>)<sub>2</sub>HPO<sub>4</sub></b>	<b>Fe<sub>2</sub>O<sub>3</sub></b>	<b>Al<sub>2</sub>O<sub>3</sub></b>	<b>MnO</b>	<b>Cr<sub>2</sub>O<sub>3</sub></b>
<b>Element %</b>	<b>40-60</b>	<b>0-18</b>	<b>22-42</b>	<b>0-15</b>	<b>0-4.5</b>
<b>A1</b>	0.1548	0.0784	0.1168	0.0000	0.0000
<b>A2</b>	0.1373	0.0901	0.1082	0.0000	0.0143
<b>A3</b>	0.1420	0.1135	0.0926	0.0000	0.0020
<b>A4</b>	0.1650	0.0530	0.1256	0.0000	0.0063
<b>A5</b>	0.1653	0.0971	0.0568	0.0000	0.0308
<b>A6</b>	0.1651	0.0633	0.0862	0.0113	0.0241
<b>A7</b>	0.1804	0.0381	0.0796	0.0338	0.0181
<b>A8</b>	0.1936	0.0261	0.1029	0.0232	0.0041
<b>A9</b>	0.2070	0.0127	0.0730	0.0452	0.0121
<b>A10</b>	0.2255	0.0000	0.0661	0.0564	0.0020

## X-Ray Photoelectron Spectroscopy (XPS)(170)

### *Principle*

XPS is a surface-sensitive technique for quantitative characterisation to a typical penetration depth of  $\sim 10$  nm. It involves the irradiation of a material with high energy photoelectrons ( $\sim 1250$ - $1500$  eV), which ionise core electrons. Those within the escape depth are ejected from the sample, filtered through a hemispherical analyser, and their number and the distribution of their kinetic energies are measured to give the XPS spectrum. However, the escape depth is limited to 10 nm and electrons ejected from greater depths have a low probability of exiting the sample surface without undergoing an energy loss event. Their energies are likely to contribute to the broad background signal rather than measurable spectral peaks. The resonances of the peaks, measured as electron binding energies,  $E_{BE}$ , are representative of quantised energy levels and thus may yield information about the surface composition and chemical states of the elements.

$$E_{BE} = h\nu - E_{KE} - \phi \quad \text{Equation 2.20}$$

where  $\phi$  = the work function of the spectrometer

$E_{KE}$  = the kinetic energy of the electrons

Relative shifts give information about oxidation states: positive ions have higher binding energies than the corresponding elements, as their orbitals are e-poor and contracted. Similarly, negative ions have lower binding energies; radii are expanded and electrons held more loosely. Spin orbit coupling may be quantified by the energy difference.

Full width at half maximum (FWHM) also provides information about chemical states: broadening may arise as a consequence of the number or distribution of chemical bonds; it may also represent physical influences such as x-ray damage or charging of the surface. The surface becomes charged when electrons exit a non-conducting sample, causing a potential difference to build up that acts as a retarding field on the ejected electrons. Their kinetic energy is reduced and peaks may be shifted to energies as much as 150 eV lower. Charge compensation during data processing aims to adjust peak positions to compensate for this effect, usually by reference to calibration peaks, such as carbon impurities from the instrument.

XPS is a quantitative technique: the number of measured electrons of a given binding energy is proportional to the number of surface species. Atomic concentrations can be estimated within 10 %, but measurements are highly repeatable: *i.e.* data are precise, but not accurate. Relative quantities in atomic percentages are highly comparable, but not absolute quantities: the repeatability

of measurements depends upon the operating mode of the instrument and is susceptible to variation. Sample preparation can also affect intensities; rough surfaces might create a modulation in sample depth and thus evidence may exist for an element at high kinetic energies which is absent at low kinetic energies because electrons resulting from those transitions did not escape the sample. This might occur with Fe2p and 3p transitions. The most reliable atomic percentage will then belong to the peak of highest energy and intensity.

To determine atomic percentages, relative sensitivity factors, (RSFs) and degeneracy must be taken into account. RSFs are only accurate for homogeneous materials, but are fair approximations for most solids. Integrated intensities determine the ratio of spin states, *e.g.*  $S = \frac{1}{2}$  (RSF = 5.6,  $2S+1 = 2$ ) and  $S = \frac{3}{2}$  (RSF = 10.8,  $2S+1 = 4$ ), so for ionisation of the Fe2p levels: ratio 1:2.

Other peaks may also be observed. Auger peaks occur when a high energy electron drops into a lower energy vacancy and an electron with kinetic energy corresponding to the energy difference is released. Satellite peaks come from data collected using a non-monochromated x-ray source and are offset from the standard spectral lines by the energy difference between the x-ray spectrum and the anode source. Because Auger peaks are independent of the spectrometer, these do not show satellite peaks. Plasmon peaks arise from surface scattering of incident electrons. Peak sharpness depends upon the sample structure: sharper peaks arise from metallic structures, whilst those from compounds such as oxides can be very broad and contribute to the background.

### ***Equipment***

Data were collected on the  $K\alpha$ 1486 X-Ray Photoelectric spectrometer from the NEXUS Nanolab with the help of Dr Naoko Sano at Newcastle University. This spectrometer operates with an Al  $K\alpha$  source of energy 1486.68 eV and resolution of 50  $\mu\text{m}$ . Samples were prepared to a maximum thickness of 20mm, the depth at which only 5 % of photoelectrons are ejected from the surface, and loaded into the ultra-high vacuum analysis chamber before being exposed to an electron beam. A controlled electrostatic field deflects emerging spectral electrons according to their velocity and records the output as an electrical pulse at the detector.

Data were peak fitted and analysed using the Casa XPS Processing Software and compared to values found on the National Institute of Standards and Technology (NIST) database(170). The background comprises of electrons of high energy which have lost some of that energy through scattering events. The unpredictable nature of these events makes background estimation inexact, such that peak intensities will always contain uncertainties, even without problems such as peak

overlap. Lines are modelled as a combination of Gaussian and Lorentzian components with symmetric and asymmetric parts; pairs of peaks may be modelled separately or together. The fit is limited by existing information on the sample: if this is not taken into account, the fit will have no physical meaning.

### ***Electron Paramagnetic Resonance (EPR)(171)***

#### ***Principle***

Electron Paramagnetic Resonance (or Electron Spin Resonance) is an analytical technique for exploring species with unpaired electrons, typically transition metal ions. It may elucidate coordination environments and is especially useful for  $d^5$  systems such as Fe(III) and Mn(II). Although it is not applicable to the wide range of materials without unpaired electrons, this limitation allows for highly specific probing in some very complex systems.

Under an applied magnetic field of strength  $B_0$ , the magnetic moment of the unpaired electron aligns parallel or anti-parallel to the field:  $m_s = \pm 1/2$ . The energy of these components due to the Zeeman effect is directly proportional to the strength of the applied magnetic field.

$$E = m_s g \mu_B B_0 \quad \text{Equation 2.21}$$

where  $g$  = the g-factor

$\mu_B$  = the Bohr magneton

Thus, the energy difference between the states for unpaired, free electrons is given by the resonance condition: the energy of an emitted or absorbed photon that initiates a transition between spin states.

$$\Delta E = g \mu_B B_0 = h\nu \quad \text{Equation 2.22}$$

The technique works by exciting the sample to flip the unpaired electron spin. The magnetic field increases until the energy difference between states is equal to the energy of the applied photon beam and degeneracy is lifted; unpaired electrons may move freely between states. However, more electrons lie in the lower energy state ( $m_s = - 1/2$ ) than the upper energy state ( $m_s = + 1/2$ ), as given by the Maxwell-Boltzmann distribution:

$$\frac{n_u}{n_l} = e^{\left(\frac{-E_u - E_l}{k_B T}\right)} = e^{\left(\frac{h\nu}{k_B T}\right)} \quad \text{Equation 2.23}$$

where  $n$  = number of electrons in a given state

$u$  and  $l$  denote upper and lower energy levels respectively

$k_B T$  = the Boltzmann temperature in Kelvin

At room temperature,  $n_u/n_l \sim 0.998$ . Net absorption of energy occurs upon irradiation, and it is this which is scanned to give the EPR spectrum.

For a free electron, the g-factor is given simply by the *electron* g-factor,  $g = g_e$ . However, spin-orbit coupling perturbs the electron spin magnetic moment. The magnitude of the difference provides information about influences on the angular momentum of the electron orbital, which depends upon the symmetry of the ion.

$$g = g_e(1 - \sigma) \quad \text{Equation 2.24}$$

where  $\sigma$  = the shielding constant, and may be positive or negative

Coupling to nuclear spins gives rise to hyperfine coupling in the spectrum; the electron spin levels split into  $2I + 1$  sub-levels, seen on the spectrum by splitting of the resonance line. An increasing number of nuclei lead to increasing complexity, which is eventually quenched if the sample is saturated with too many unpaired electron spins.

The discrete energy levels may be represented by eigenvalue equations and thus the total energy may be mapped by the Hamiltonian operator,  $\hat{H}$ , with first approximation:

$$\hat{H} = \beta \mathbf{H} g \mathbf{S} + D[S_z^2 - \frac{1}{3}S(S+1)] + E(S_x^2 + S_y^2) \quad \text{Equation 2.25}$$

where  $\beta$ ,  $D$  and  $E$  are constants

$S$ ,  $S_z$  and  $S_y$  = total, z and y spins respectively

If  $D = E = 0$ , then a  $g \approx 2$  absorption line is observed for simple cubic systems. When  $E \approx 0$ , but  $D > 0.4 \text{ cm}^{-1}$ ,  $\lambda$  (the ratio  $E/D$ )  $\approx 0$  and peaks are seen at  $g_{\parallel} = 2$  and  $g_{\perp} = 6$ . This demonstrates a system with strong axial symmetry. When  $D \approx 0$ , but  $E \neq 0$ ,  $\lambda \rightarrow 1/3$ . A characteristic  $g = 4.29$  represents rhombic distortion.

### ***Equipment***

Experiments were run on the Bruker EMX EPR Spectrometer using BioSpin collection software and WinEPR analysis. The EPR spectrometer has a typical sensitivity of 10-12 moles of electron spins at room temperature; this depends upon the incident photon frequency, settings of the spectrometer and sample size. Electromagnetic radiation to flip the spin is generated by either varying the frequency of incident photons under a fixed magnetic field, or, as in this case, varying the magnetic field under a fixed photon frequency. This frequency usually falls within the microwave region of the spectrum  $\sim 9$ -10 GHz and  $B_0$  is  $\sim 0.35$  T.

Training was completed on 1st December 2011.

### ***Thermogravimetric Analysis (TGA)***

#### ***Principle***

Thermogravimetric analysis is an analytical technique to sensitively determine the weight loss of a ~ 30 mg sample under programmed heating in a controlled atmosphere. The experiment relies upon the volatility of one component in the sample, which is then lost as a function of temperature to give a weight loss curve in percentage by mass. In the zeolite samples being studied, this component is water.

The amount of water per formula unit may be calculated given a known composition of the compound under study, which is why TGA is often paired with mass spectrometry. It also means that TGA is complementary to XRF spectroscopy.

#### ***Equipment***

TGA data were collected from the Netzsch STA 449 F1 Jupiter thermal analyser using the Netzsch-Proteus measurement and analysis suite, which can take samples up to 1400 °C. In these experiments, samples were recorded at 900 °C in specially fitted alumina crucibles pre-warmed to desorb moisture. Training was completed on 31st October 2011.

### ***Inductively Coupled Plasma Mass Spectrometry (ICP)***

#### ***Principle***

Thermogravimetric Inductively Coupled Plasma Mass Spectrometry (ICP) is a method of quantifying the elemental content of a material. ICP typically spans nine orders of magnitude and can resolve concentrations down to parts per trillion (ppt).

The machine operates an electromagnetic coil with rapidly oscillating field that causes electrons to accelerate to and fro. Exposed to an argon gas flow, the oscillating electrons ionise the argon atoms. When the rate of electron removal equals the rate of electron-Ar<sup>+</sup> recombination, the gas forms a hot conducting plasma ~ 6,000-10,000 K. This plasma will freeze dry, dissociate and ionise samples introduced as an aerosol, creating positively charged ions that are filtered into the mass spectrometer and scanned across a mass-to-charge ration range. An electron multiplier amplifies the pulse and detects the charged particles. Each isotope is measured separately. Most

elements can be measured, but those, such as Cl, which form negatively charged ions, may be difficult.

### ***Equipment***

Samples were measured on an Agilent 7500ce instrument with Octopole reaction system (ORS) capable of multielement determinations. The plasma runs with an RF power of 1500 W. Precision varies with element, concentration and matrix, but was < 5 % for the measurements recorded here. Chromium was recorded at molecular mass 52 and iron at molecular mass 56. Each sample was measured four times, compared to known measurement standards, and averaged. The detection limits are 0.02 and 0.05 ppb for Cr and Fe respectively. Samples were exposed to the ICP as liquids and introduced via a Miramist nebuliser.

### ***Mössbauer Spectroscopy(172–175)***

#### ***Principle***

Mössbauer spectroscopy is an analytical technique used to examine the magnetic properties, valence state and coordination polyhedron occupied by iron ions or other Mössbauer active species. Significantly, it is a non-destructive technique, which makes it applicable for probing valuable samples and artefacts, such as the moon rock samples brought to Earth, or probed on site by robots. It works by probing nuclear energy levels: the spacings between which are determined by the interactions between the nucleus and its immediate environment, *i.e.* the number and behaviour of surrounding electrons – its chemistry.

A nucleus experiencing a change in energy through absorption or emission must recoil to conserve its momentum.

$$E_{\gamma} = E_0 - E_R \quad \text{Equation 2.26}$$

where  $E_{\gamma}$  = energy of  $\gamma$  ray

$E_0$  = energy of transition

$E_R$  = recoil energy

However, when the recoil energy is less than the gap between vibrational levels of the lattice, there is a probability,  $f$ , of no vibrational excitation: that is, recoilless emission. The crystal

absorbs the momentum (its large mass giving a minute  $E_R$ ) and the nucleus does not recoil (Figure 2.10). This is the Mössbauer effect. In solids,  $f$  is high enough to make Mössbauer spectroscopy possible.

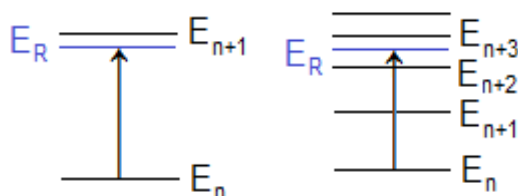


Figure 2.10: Transitions in vibrational energy levels of the lattice (IR: 6-8 orders of magnitude  $> \gamma$ ). Recoilless emission occurs when the recoil energy,  $E_R$  is less than spaces between energy levels (left),  $E_R < \Delta E$ , whereas when the energy levels are more closely packed (right), a transition may occur and recoil is observed.

For a given temperature, the fraction of recoilless emission,

$$f = e^{-k_y^2 \langle x^2 \rangle} \quad \text{Equation 2.27}$$

where  $k_y$  = the wavenumber of the emitted gamma ray

$\langle x^2 \rangle$  = the average of the squared displacement of the probe nucleus

To record a Mössbauer spectrum, a source is moved towards and away from a detector at constant acceleration (Synchrotron Mössbauer keeps the source stationary and oscillates the sample). Changes of fractions of mm/s relative to the speed of the gamma rays ( $3 \times 10^{11}$  mm/s) produce tiny observable energy shifts. As a result, the energy scale is measured in mm/s. This is a technique with high energy resolution.

$$\frac{\Delta E}{E_o} = \frac{v}{c} = \frac{10^{-3}}{10^8} \quad \text{Equation 2.28}$$

$^{57}\text{Fe}$ -Mössbauer spectroscopy is the most common and comprises more than half of the Mössbauer literature: in particular, the ease of distinguishing between Fe(II) and Fe(III) allows a rich and extensive exploration of the chemistry of iron-containing compounds. A source of radioactive  $^{57}\text{Co}$  is used in Fe-Mössbauer spectrometers, embedded in Rh or Cu to limit line-broadening.  $^{57}\text{Co}$  decays to  $^{57}\text{Fe}$ , an unstable product that gives off a gamma ray (along with other types of energy). This may be absorbed by other  $^{57}\text{Fe}$  nuclei in the sample. Typically,  $^{57}\text{Fe}$  constitutes 2 % of natural iron.

Differences in source and sample local environments produce differences in the nuclear energy levels and  $s$  electron densities, giving a transmission spectrum with a shift away from zero

velocity. This is known as the isomer shift, IS.

As the number of species in the coordination polyhedron around an Fe-centre decreases, so does the shielding of 4s electrons: bonding interactions are very similar, such that shielding effects dominate – and so the nucleus is affected and the isomer shift decreases (Figure 2.11). Thus octahedral Fe species have bigger isomer shifts than tetrahedral Fe species. Similarly, Fe(II) ions, with more electrons shielding the nucleus, have larger positive isomer shifts than Fe(III) ions. Small distortions to the symmetry of the coordination sphere are unlikely to affect the isomer shift, but more radical alterations will produce an affect. Some tetrahedral environments may have very large isomer shifts and become difficult to distinguish from octahedral environments. In a totally spherically symmetric Fe(II) environment, the degeneracy of the orbitals is such that there is no electric field gradient or ligand field splitting, and the spectrum shows a singlet. One example is the perovskite  $\text{RbFeF}_3$ ; however, this is very rare and isomer shifts usually follow recognisable patterns.

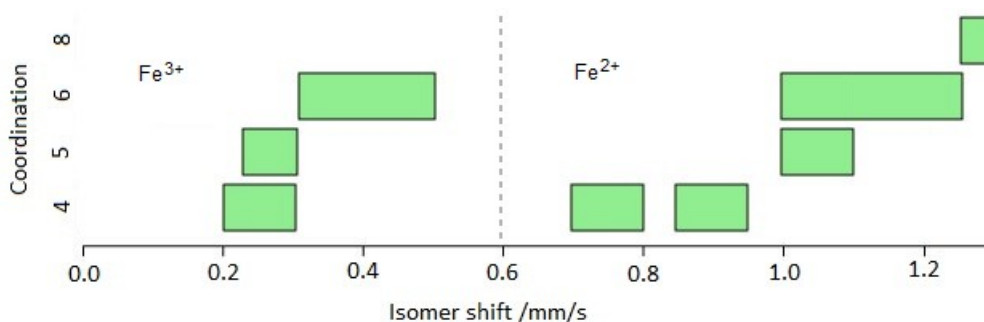


Figure 2.11: Recognisable isomer shift distributions for 4-, 5-, 6- and 8-coordinated Fe(III) and Fe(II) ions.

Magnetic splitting is seen in a Mössbauer spectrum when an effective magnetic hyperfine field at the nucleus interacts with the magnetic moment of the nucleus, such that the degeneracy of nuclear energy levels is lost. Fe(0) metal forms eight spectral lines, of which two are forbidden, giving a sextet centred about 0 mm/s (*i.e.* it shows no isomer shift). The spacing between peaks is determined by the magnetic field  $B$ , usually  $\sim 33$  T.

A non-spherical charge distribution produces a nuclear quadrupole moment, which interacts with the electric field gradient to generate quadrupole splitting, QS, of nuclear energy levels from  $I = 3/2$  into  $m_1 = \pm 3/2$  and  $m_1 = \pm 1/2$  (where  $I = \text{spin}$  and  $m_1 = \text{the magnetic quantum number}$ ). The quadrupole splitting is a measure of asymmetry, and is seen as doublets on the spectrum corresponding to  $m = \pm 3/2$  ( $I = 1/2$  has no quadrupole moment). The midpoint is the isomer shift. The magnitude of the interaction is given by the peak separation (Figure 2.12)(175). The nuclear environment is determined by the numbers of electrons, anions, any magnetic ordering and the symmetry surrounding the nucleus. A  $d^6$  configuration for Fe(II) ions is much more asymmetric than a high spin  $d^5$  configuration, and so experiences a bigger quadrupole splitting.

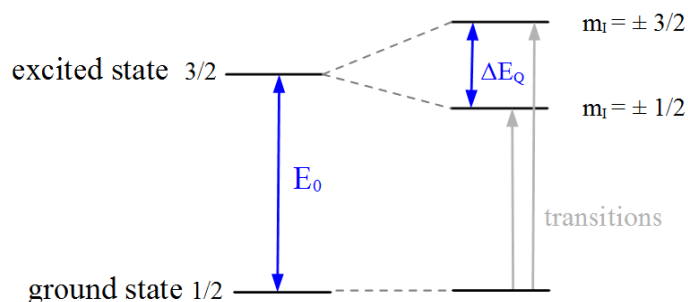


Figure 2.12: Energy level diagram showing transitions between ground and excited states: not to scale

Mössbauer spectroscopy is temperature sensitive. Studying the quadrupole splitting parameter at low temperatures can expose low-lying electronically excited states in partially-filled orbitals. At low temperature, distinct environments resolve and peak intensity may be improved, whilst at high temperature, processes such as electron exchange speed up, interchanging oxidation states give a time-averaged single environment with increasingly sharp peaks as  $T$  increases. High, low and intermediate spin compounds are distinguishable by Mössbauer spectroscopy. For some compounds, spin state even changes with temperature, and may be carefully monitored and explored *via* Mössbauer techniques.

### Equipment

Transmission  $^{57}\text{Fe}$  Mössbauer spectroscopy was performed on a constant acceleration Wissel spectrometer in the Materials and Engineering Research Institute at Sheffield Hallam University, with the assistance of S. Forder and P. Bingham. A  $^{57}\text{Co}$  source was used and experiments run at room temperature, usually across a velocity range of  $\pm 6$  mm/s.

The mass of each absorber (material sample) was calculated to give good resolution Mössbauer Spectroscopy: the agreed Fe loading is  $\sim 2$  mg/cm<sup>2</sup> (see Appendix II). The sample was then weighed roughly and combined with sufficient graphite powder (99.9995 % Alfa Aesar) to fill a Mössbauer absorber disc of 1.5 cm diameter and  $\sim 1$  mm thickness. For air sensitive samples, these were prepared in the glove box and subsequently sealed using Araldite glue. Non-air-sensitive samples were sealed between two pieces of Scotch tape.

To calculate the sample mass in a 1.5 cm diameter disc:

$$\text{Area} = \pi r^2 = 1.77 \text{ cm}^2 \quad \text{Equation 2.29}$$

$$\frac{2 \text{ mg Fe}}{1 \text{ cm}^2} = \frac{3.53 \text{ mg Fe}}{1.77 \text{ cm}^2} \quad \text{Equation 2.30}$$

$$M_{\%} = 100 \cdot \frac{M_{\text{Fe}}}{M_{\text{tot}}} = \frac{3.53 \text{ mg}}{M_{\text{disc}}} \quad \text{Equation 2.31}$$

where  $M_{\%}$  = Fe mass %

$M_{Fe}$  = mass of Fe in a sample

$M_{tot}$  = total sample mass

$M_{disc}$  = sample mass to go in disc

Finally,  $M_{disc}$  is then multiplied by the expected number of distinct Fe species (*i.e.* the predicted number of doublets + sextets) to allow more sample to be used and give good counting statistics. Samples were usually between 10 and 60 mg.

X-Ray Fluorescence Spectroscopy (XRF) provides an  $M_{\%}$ , but this value does not account for framework oxygen nor water. Using the formula for the molecular sieves, Si (zeolites) or P (AlPOs) mole percentage may be used to estimate the mole percentage of framework oxygen and thus normalise the mass percentage of Fe to take into account XRF-invisible O (as shown in  $\text{mg}_{Cr}/\text{g}_{sieve}$  calculations, [Appendix II](#)). To account for water in the systems, TGA data for water by percentage mass may be used to make a further, simple correction to the data.

### *Analysis(176)*

As the constant acceleration spectrometer scans the sample between  $\pm$  velocity limits, it sweeps the energy spectrum twice. Therefore, before the spectrum is fitted, it must be folded across the mirror line between the two sets of data. This has the effect of doubling the counting statistics to provide better quality data and allowing the measurement of zero velocity at the midpoints of the spectra relative to the calibration of  $\alpha$ -Fe.

Lorentzian multiplet powder analysis was used to fit peaks, with the assistance of R. Gerard, J-C. D'Hollander, C. Gorin, S. Forder and P. Bingham. This analysis selects singlets, doublets or sextets corresponding to paramagnetic states or sites with magnetic hyperfine fields (in paramagnetic materials the hyperfine field  $\sim 0$  T and fewer parameters are needed to describe the spectrum). Hyperfine interactions are treated as static and modelled by a static Hamiltonian with only time-independent interactions. A more complex RECOIL analysis could take into account dynamic effects.

Unlike the Voigt analysis, the analysis used contains only Lorentzian and no Gaussian components, which means that it cannot accommodate for inhomogenous line broadening due to thickness or crystal effects. This assumption is valid because the sample mass was calculated to give a suitable concentration of  $^{57}\text{Fe}$  per unit area,  $n_a$ , where the Mössbauer thickness,  $t_a$  is given by

$$t_a = f_a n_a \sigma_0 \quad \text{Equation 2.32}$$

$f_a$  = absorber recoilless fraction

$\sigma_0$  = resonant absorption cross-section

Differences in Mössbauer thickness should therefore be negligible between samples.

Singlets are fitted with an isomer shift (IS in mm/s), half width at half maximum of the peak, HMHM ( $w_+$  in mm/s) and area ( $A$  in counts mm/s, but can be displayed as percentage adsorption). Doublets are fitted with the same parameters, plus quadrupole splitting (QS in mm/s) and ratios of low to high velocity area and peak width ( $A_-/A_+$  and  $w_-/w_+$ ). For magnetic states, the first approximation is used such that the quadrupole shift is very small ( $QS \rightarrow 0$  mm/s) compared the Zeeman splitting ( $z = 33$  T for this set up). HWHM ( $w_3$ ) is given as the highest intensity peak and ratios are also calculated  $A1/A3$ ,  $A2/A3$ ,  $w1/w3$  and  $w2/w3$ . Usually these are not refined.

This model does not fix the width, but to be physically sensible, the Lorentzian HWHM must be greater than the Heisenberg natural line width of the nuclear transition:  $0.21$  mm/s  $\pm$   $0.02$  mm/s. In the case of substantial deviation below this limit, this parameter was fixed.

$\chi^2$  values quoted for Mössbauer spectroscopy are calculated in a similar way to those for Rietveld refinement of PXRD data(177,178). The procedure minimises the difference between observed ( $y_i$ ) and calculated ( $y_i^{calc}$ ) data for the  $i^{\text{th}}$  point. The residual function is calculated the same way as in XRD (Equation 2.12), but the Mössbauer  $\chi^2$  calculation contains an extra term in the minimisation sum,  $1/y_i^{calc}$ .

$$\chi^2 = \sum_i \frac{w_i (y_i - y_i^{calc})^2}{y_i^{calc}} \quad \text{Equation 2.33}$$

where  $w_i = 1/y_i$  (the weighting factor), such that each observed point contributes equally

As the difference between  $y_i$  and  $y_i^{calc}$  increases, so does the value of  $\chi^2$ . At the limit of this equation,  $y_i = y_i^{calc}$ , and thus  $y_i - y_i^{calc} = 0$ ,  $\chi^2 \geq 0$ .

In Rietveld refinement, the  $\chi^2$  is then given by the residual function divided by the number of degrees of freedom, *i.e.* the difference between the number of observations ( $N_o$ ) and the number of parameters ( $N_v$ ), limiting  $\chi^2$  to  $\geq 1$  (Equation 2.16). This can also be calculated in Mössbauer spectroscopy fitting to give a reduced  $\chi^2_r$ . However, typically it is  $\chi^2$ , rather than  $\chi^2_r$ , which is quoted in the fit.

$$\chi_r^2 = \frac{\chi^2}{N_o - N_v} \quad \text{Equation 2.34}$$

The minimisation procedure is iterative and requires starting parameters to be estimated. A good fit will therefore try a range of different sensible starting parameters to eliminate the problem of resolving only local minima. At each iteration, inversion of the the covariance matrix is used to

obtain errors as variances (squares), which are quoted in RECOIL with 95 % confidence. Because  $\chi^2$  relies upon minimising the differences between observed data points and the fitted line, poor quality data with very few data points can give misleadingly low errors, and it is always important to assess the quality of the fit by eye.

### *Ultraviolet-Visible Absorption Spectroscopy (UV-vis)*

#### *Principle*

The Beer-Lambert Law describes how the absorbance of ultraviolet or visible light by molecules or ions is directly proportional to the concentration of absorbing species for a fixed path length.

$$\frac{I}{I_0} = 10^{-\epsilon cl}$$

*Equation 2.35*

where  $I$  = intensity of transmitted light

$I_0$  = intensity of incident light

$\epsilon$  = extinction coefficient of absorber

$c$  = molar concentration

$l$  = path length through absorber

Ultraviolet visible spectroscopy can identify transition metal ions, conjugated aromatic compounds and biological macromolecules by their characteristic spectra, and estimate their concentrations. It is usually carried out in solution, but can work for solids too. When these species absorb light, electrons are excited to low-lying higher energy unoccupied molecular orbitals. The HOMO-LUMO gap determines the wavelength of light that is absorbed (the smaller the gap, the longer the wavelength). These species are usually coloured (Figure 2.13).

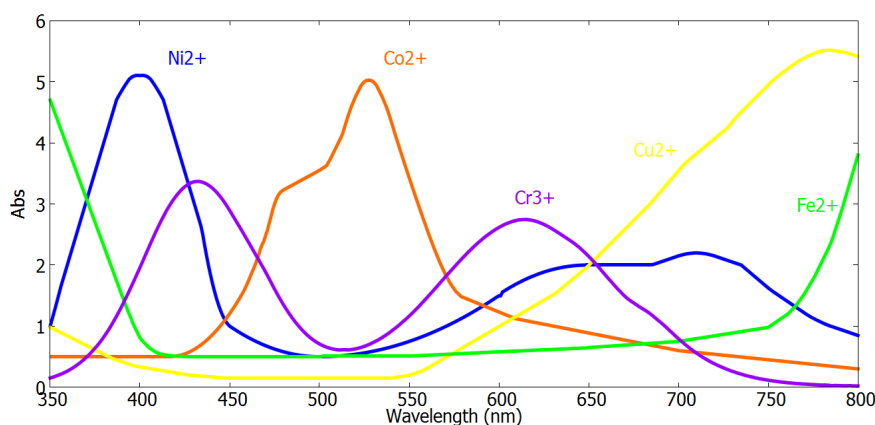


*Figure 2.13: d-d transitions in the UV-vis spectrum for Ni(II), Co(II), Cu(II), Cr(III) and Fe(II) ions.*

d-electrons are easily excited between electronic states. The d-d transitions are determined by selection rules:

$$\text{Spin rule:} \quad \Delta S = 0 \quad \text{Equation 2.36}$$

$$\text{Laporte rule:} \quad \Delta l = \pm 1. \quad \text{Equation 2.37}$$

The magnitude of the HOMO-LUMO gap and thus the wavelength of the transition is highly sensitive to (a) oxidation state:  $\Delta$  increases with increasing charge, (b) the size of the metal ion:  $\Delta$  increases down the period table, and (c) ligands: number, geometry ( $\Delta_t > \Delta_o$ ) and nature (spectrochemical series) (Figure 2.14).

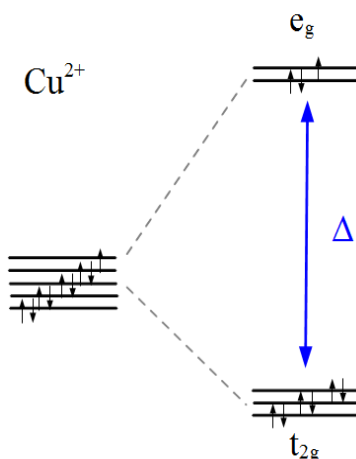


Figure 2.14: Cu(II):  $\Delta \sim 800 \text{ nm}$ , yellow light is absorbed and these solutions are blue.

### Equipment

Ultraviolet visible absorption spectra were obtained on a Cary 5000 NIR supplied with a tungsten halogen source of visible light and deuterium arc UV source. The Cary 5000 has a limiting UV-vis resolution  $< 0.05 \text{ nm}$  and covers a wavelength range of 175-3300 nm.

Scans were run at room temperature across a scan range of 200-800 nm. Solution samples were run in a 3 ml cuvette at a dilution up to 1 in 125. In the set up, light from the bulb travels through a dispersion device and incident wavelengths are selected using an aperture before being directed through the sample to a detector on the other side. Solid samples were prepared by pressing into a plate cavity and run using a Praying Mantis attachment. The Praying Mantis focusses the incident beam onto the solid and the diffuse reflection light onto the detector using a series of mirrors. Baseline scans of water, acid or NaCl were run to provide a background that was subtracted from sample measurements. CarywinUV was used to run the scans and convert the data into CSV files for plotting in spreadsheet software.

## ***Scanning Electron Microscopy and Energy Dispersive X-Ray Spectroscopy (SEM and EDS)***

### ***Principle***

The Scanning Electron Microscope (SEM) scans across the surface of a solid sample with a narrow, focussed beam of high energy electrons. The incident beam strikes the surface to a penetration depth of 1-2  $\mu\text{m}$  and excites atoms in their ground states. Secondary electrons are emitted, leaving an inner core electron hole, which is filled by the relaxation of a higher energy electron. An x-ray is emitted of equal energy to the difference between the shells and characteristic of the element. The number and energy of x-rays, primary reflected electrons and secondary electrons is measured. High resolution SEM electron micrographs are produced based on the number of secondary electrons that strike a position on the detector, showing sample morphology.

EDS determines elements present at the sample surface, their distribution and their relative ratios. Qualitative analysis is carried out through the detection of backscattered electrons. The extent to which primary electrons are reflected and scattered is determined by atomic number, and so contrast in the images is representative of electron density, or  $Z$ . These images tend not to be as high quality as SEM images. However, the x-rays produced are also characteristic of the elements from which they originate, and may be used for quantitative elemental analysis once sorted into distinct energies by the energy dispersive detector.

### ***Equipment***

SEM and EDS measurements were recorded on a Philips XL-30 SEM with Oxford Isis EDS with the help of Paul Stanley at the Centre for Electron Microscopy, Metallurgy and Materials, University of Birmingham. This SEM is fitted with a lanthanum hexaboride,  $\text{LaB}_6$ , filament and operates under an acceleration voltage of 30 kV to a resolution limit of 3.5 nm. The samples are mounted onto a  $50 \times 50$  mm sample stage and viewed with a NordlysS camera. Non-conducting samples are finely coated with carbon or gold in advance. The Oxford Isis EDS can detect elements from Na; x-rays originating from lower-energy transitions are absorbed by the Be window in the detector and, as such, elements such as oxygen are EDS invisible.

## ***Transmission Electron Microscopy (TEM)***

### ***Principle***

Transmission electron microscopy operates on the same principles as the visible light microscope, but at a much higher resolution. In a visible light microscope, the maximum resolution,  $R_{max}$ , is limited by the wavelength:  $400 \leq \lambda \leq 700$  nm.

$$R_{max} = \frac{\lambda}{2 n \sin \alpha} \quad \text{Equation 2.38}$$

where  $2 n \sin \alpha$  = the aperture

The wavelength of electrons is determined by their speed, so accelerating an electron beam produces a shorter wavelength and thus allows more detailed images. In a TEM, electrons may approach the speed of light,  $c$ . Thus the wavelength is given by the de Broglie equation corrected for relativistic effects:

$$\lambda_e = \frac{h}{\sqrt{2 m_0 E \left(1 + \frac{E}{2 m_0 c^2}\right)}} \quad \text{Equation 2.39}$$

where  $h$  = Planck's constant

$m_0$  = rest mass of an electron

$E$  = the energy of the accelerated electron

Electrons are generated by an emission source, usually a tungsten filament or LaB<sub>6</sub> source and accelerated through the vacuum by a potential. Because the electrons are negatively charged, they cannot pass through glass: instead, they are focussed onto the screen by a series of electromagnetic lenses, which have a flexible angle for beam convergence, allowing manipulation of the resolution. Electrons are converted into light to form an image on the fluorescent screen, CCD camera or photographic film. On the captured images, lighter areas represent sites of greater electron penetration through the sample, thus providing structural, textural and morphological information. An  $R_{max}$  of  $\sim 0.2$  nm means that fine detail such as rows of atoms may even be resolved.

### ***Equipment***

TEM images were collected on the JEOL JEM-2100 LaB<sub>6</sub> TEM with INCA EDS system at the Centre for Electron Microscopy, Metallurgy and Materials, University of Birmingham with the help of Dr Zoe Schnepf. In order for electrons to pass through, samples must be prepared ultra thin: this is known as electron transparency. Samples were prepared in ethanol solution to a by-eye

concentration and dispersed by submersion in a Branson 2510 ultrasonic bath before dropping onto a carbon-coated copper TEM grid.

## Chapter 3: Effect of Structure Upon Chromium Uptake

Within this chapter, the synthesis of several basic molecular sieves is recorded and the potential for these systems to take up chromium measured using XRF spectroscopy. Structures are characterised using PXRD, SEM imaging and TGA. Rietveld and Le Bail refinements are performed on PXRD data to obtain unit cell parameters and impurity phase fractions where possible. The pH of solution both before and after chromate exposure is examined. Modifications to morphology and mesoporosity are attempted on potential systems for chromate remediation, through the use of various templates, and these systems are then probed using TEM.

### 3.1. Reaction Conditions

#### *pH*

When Cr(VI) is reduced by Fe(II), a decrease in pH is expected as Cr(III)/Fe(III) oxyhydroxides precipitate out (or are consumed by surface adsorption onto molecular sieves); however, where reduction takes place in acidic conditions, protons will be consumed and pH should increase(8). In zeolites, Cr(III) and Fe(III) remain partially within the pore network and are not free ions in solution; further, ready ion exchange between protons in solution and charge balancing cations occurs as a matter of course; some hydrolysis of the framework will also take place, especially at low pH. As such, a pH rise is expected upon Cr(VI) treatment due to non redox processes. Rios Reyes *et al.* report that “pH increase is almost unavoidable in removal of heavy metals by zeolite” (17).

The literature reports working pH ranges from acidic to neutral in removal of heavy metals by zeolites(82). On the one hand, the more acidic the solution, the greater the dissolution of the sieve framework, on the other, and Mohan and Pittman Jr found that, on activated carbons, the optimal pHs for Cr(III) and Cr(VI) uptake respectively were 5.0 and 2.0: a pH between these values is preferable(7). Other groups reported heavy metal redox experiments between pH 4.0 and 4.5, the normal range for water containing minerals: as such, pH was not routinely adjusted in this work(5,89). Illustrative measurements were taken of solution pH before and after mixing with redox-active molecular sieves (Table 3.1).

*Table 3.1: pH changes upon ion exchange: pH values of 0.02 M sodium dichromate solution initially (immediately after mixing with the molecular sieves) and finally, 24 hours later.*

Sample type	pH Cr <sub>sol</sub> initial	pH Cr <sub>sol</sub> final
Zeolite A	9.75	9.81
	9.75	9.97
Zeolite X	6.01	6.93
Fe zeolite X	4.00	4.50
	4.59	5.88
Mn zeolite X	5.02	5.86
Clinoptilolite	4.80	4.00
Fe-AlPO-5	4.50	4.40
	4.25	4.01
	4.14	4.09
	4.27	4.26
Mn-AlPO-5	4.81	5.2

### ***Exposure Conditions***

When Cr(VI) solutions are exposed to samples of redox active molecular sieves, they must have a concentration and exposure time in excess of that required to reach equilibrium, such that maximum loading capacities are obtained. Since 0.02 M is a limiting safe concentration, sodium dichromate was prepared at 0.02 M for testing with samples. Xing *et al.* report the attainment of equilibrium within 30 minutes for the adsorption of Pb(II) and a cationic dye, whilst longer reports are more common: 120 minutes for saturation of Pb(II) in zeolite Y and 180 minutes for 58.9 % Cr(VI) uptake into  $\beta$ -FeOOH(28,77,89); arsenate exposure by kaolin natural zeolite took place for 2, 7 and 12 hours (88). In this work, samples were exposed for 24 hours unless otherwise stated.

### **3.2. Zeolites - Basic Systems**

Zeolites A and X were selected for initial investigation on the basis of their pore sizes and cation retention capacities. Natural zeolite containing mostly clinoptilolite was also explored for its high ion exchange capacity, although phase pure synthetic zeolites may be more cation selective.

### ***Zeolite A***

Zeolite A is posed as a viable candidate zeolite for selective Cr(III) ion exchange because of its high absorbent capacity. It has pores of 4-5 Å, large enough to accommodate the hydrated  $\text{Cr}(\text{H}_2\text{O})_6^{3+}$  species with diameter 4.61 Å(90). However, phase pure synthesis of LTA framework zeolite A proved difficult to achieve repeatedly, and seeding of zeolite X regularly took place in the synthesis bottle. Rietveld refinement using GSAS was employed to assess the phase fractions of several zeolite A samples with zeolite X impurities (Table 3.2, Figure 3.1).

*Table 3.2: Phase fractions derived from Rietveld refinement using GSAS of samples of zeolite A with zeolite X impurities. The goodness of fit is given by  $\chi^2$  values.*

<b>Sample</b>	<b>Phase fractions A /%</b>	<b>Phase fractions X /%</b>	<b><math>\chi^2</math></b>
<b>(a)</b>	70.4 (6)	30 (1)	2.245
<b>(b)</b>	97.10 (2)	2.9 (6)	1.830
<b>(c)</b>	68.5 (5)	31.5 (9)	1.916
<b>(d)</b>	99.874 (4)	0.12577 (0)	1.139

Zeolite A is fitted to the cubic space group  $Pm-3m$ , which treats each Si/Al site as a 50:50 blend of the two ions. A 12 Å cell model was selected and model weighted Le Bail refinement used to best fit the powder diffraction patterns of samples of zeolite A both before and after exposure to Fe, Mn and Cr ions (Table 3.3).

*Table 3.3: Zeolite A cell parameters derived from Le Bail refinement using GSAS of a variety of samples of zeolite A with zeolite X impurities. The goodness of fit is given by  $\chi^2$  values.*

<b>Sieve</b>		<b><math>a</math> /Å</b>	<b><math>\chi^2</math></b>
<b>Parent</b>	<b>Pre-Cr treatment</b>	12.2522 (2)	1.654
	<b>Post Cr-treatment</b>	12.2443 (4)	1.486
<b>Fe zeolite</b>	<b>Pre-Cr treatment</b>	12.125 (1)	1.385
	<b>Post Cr-treatment</b>	12.129 (2)	1.086
<b>Mn zeolite</b>	<b>Pre-Cr treatment</b>	12.2048 (2)	1.511
	<b>Post Cr-treatment</b>	12.179 (8)	2.738

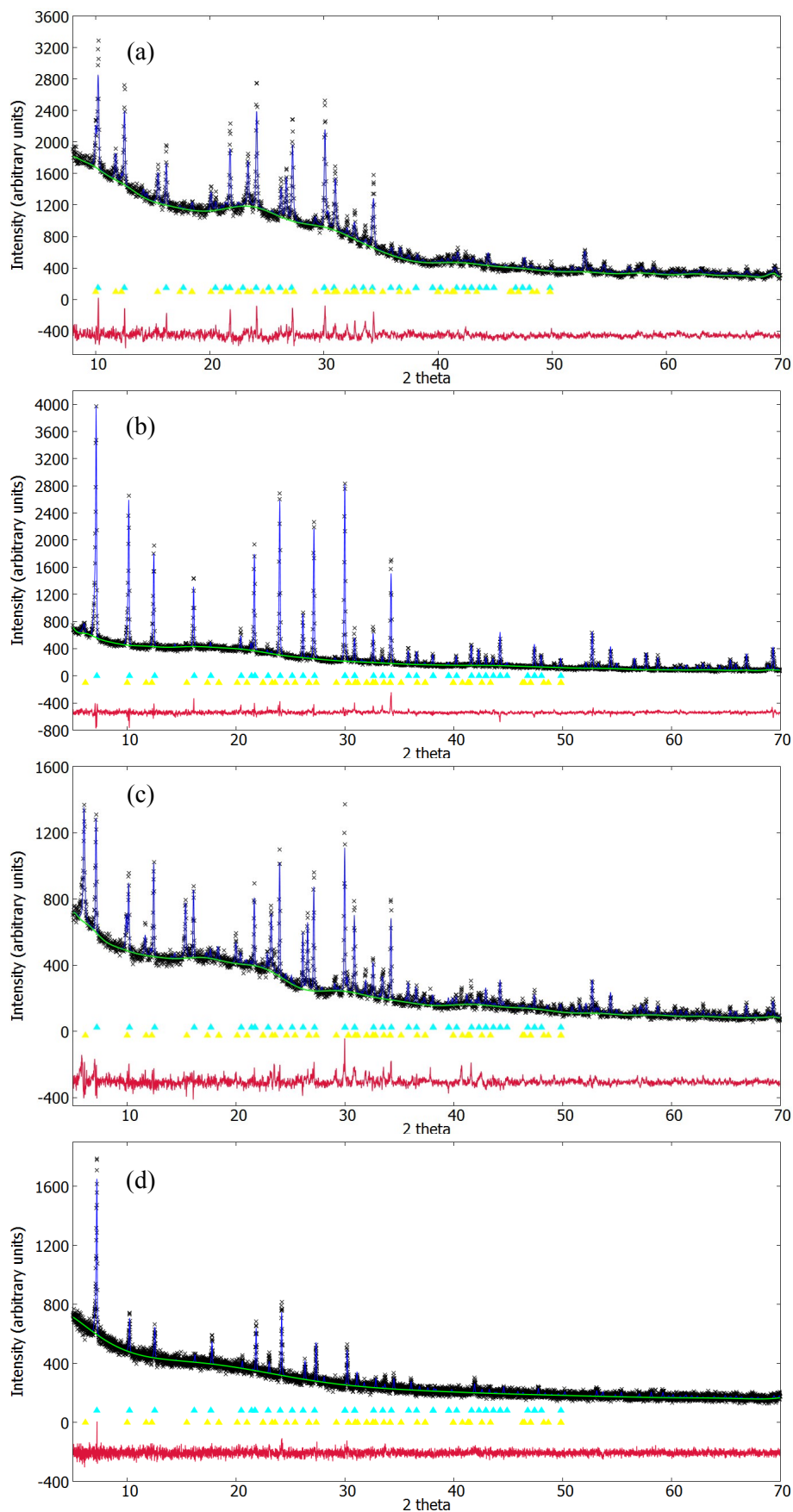


Figure 3.1: Rietveld refinement of samples (a), (b), (c) and (d), respectively. Data are represented by black crosses, background by a green line, the fit with a blue line and the residual is presented below in red. Turquoise markers represent the zeolite X phase and yellow markers the zeolite A phase.

Some claim that looking at cell parameters can help determine whether ion exchange has taken place, when lattice parameters may increase slightly as the zeolite opens up to allow the ready transport of ions through the pore network(179). However, other processes such as framework substitutions result in much larger increases in lattice parameters(180). Here, if anything, a contraction occurs that may be due to the presence of small, more highly-charged ions or merely variation between samples, such as hydration levels, and errors in peak positions.

Upon ion exchange, changes in cation positions occur, which may lead to variations in electron density and possibly structural degradation as pores flex. In the PXRD pattern, changes to electron density are reflected by fluctuations in peak intensities, whilst degradation of crystallinity may be seen as an increase in amorphous background intensity and increases in the full widths at half maximum (FWHM) of peaks as zeolite grains decrease in size. In order to determine whether any degradation of crystallinity is taking place upon ion exchange with Fe, Mn, and Cr, the EVA software was used to obtain d-spacings and FWHM of the first three peaks in the PXRD patterns of samples containing zeolite A (Table 3.4, Figure 3.1). Results show that, on the contrary, peak breadths narrow, shrinking to half the value of the FWHM for the parent zeolite: this is especially noticeable for Fe-loaded zeolite X and Mn-loaded zeolite X before treatment with Cr and indicates aggregation of the zeolite grains, forming larger particles. The errors on these data are equal to half the step size used on the diffractometers to gather the data, *i.e.* 0.01 to 1 sf for both the D8 ADVANCE and capillary diffractometers.

*Table 3.4: d-spacings and full widths at half maximum (FWHM) of zeolite A peaks ( $\text{\AA}$ ) from a variety of samples. The uncertainty in the data is equal to half the step size used on the diffractometers, *i.e.* 0.01 to 1 sf.*

		<b>Peak 1</b>	<b>Peak 2</b>	<b>Peak 3</b>
<b>Zeolite A</b>	<b>d spacing</b>	12.49 (1)	8.77 (1)	7.14 (1)
	<b>FWHM</b>	0.14 (1)	0.16 (1)	0.15 (1)
<b>Cr-treated zeolite A</b>	<b>d spacing</b>	12.44 (1)	8.74 (1)	7.13 (1)
	<b>FWHM</b>	0.12 (1)	0.11 (1)	0.13 (1)
<b>Fe-loaded zeolite X</b>	<b>d spacing</b>	12.32 (1)	8.69 (1)	7.05 (1)
	<b>FWHM</b>	0.07 (1)	0.08 (1)	0.09 (1)
<b>Mn-loaded zeolite X</b>	<b>d spacing</b>	12.49 (1)	8.88 (1)	7.14 (1)
	<b>FWHM</b>	0.09 (1)	0.08 (1)	0.079 (1)
<b>Cr-treated Mn-loaded zeolite X</b>	<b>d spacing</b>	12.35 (1)	8.68 (1)	7.08 (1)
	<b>FWHM</b>	0.14 (1)	0.08 (1)	0.10 (1)
<b>Cr-treated Fe-loaded zeolite X</b>	<b>d spacing</b>	12.63 (1)	8.88 (1)	7.56 (1)
	<b>FWHM</b>	0.10 (1)	0.10 (1)	0.10 (1)

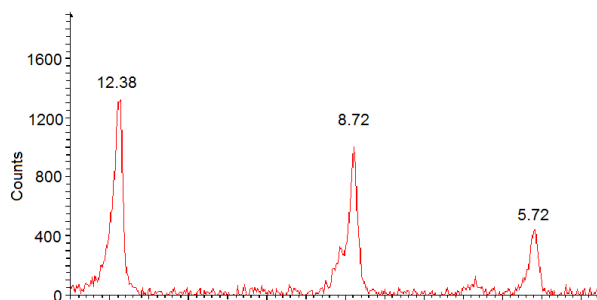


Figure 3.2: Image of the first three peaks of sample (d) of zeolite A with d-spacings marked in Å.

Scanning Electron Microscope images allow the long-range morphology of the zeolite to be examined. Images of zeolite A show clusters of ball-like crystals of diameter  $\sim 0.5 \mu\text{m}$ ; the limiting resolution of SEM made it impossible to observe any greater detail (Figure 3.3).

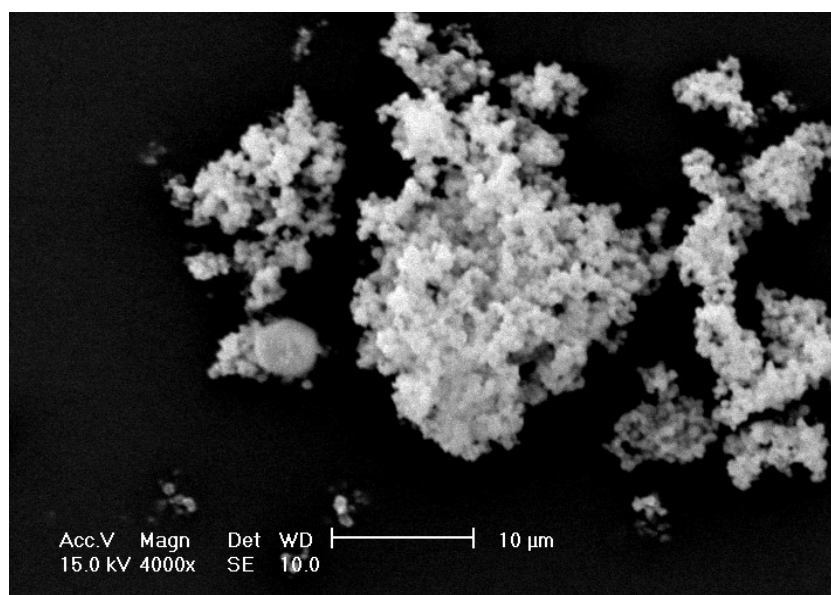


Figure 3.3: SEM image of one sample of zeolite A with zeolite X impurities.

TGA indicates a 26 % mass loss upon heating one air-exposed Fe-containing sample consisting of 68 % zeolite A and 32 % zeolite X (sample (c), Figure 3.4). This is likely to be due to water. However, a small event seen at  $\sim 600 \text{ }^\circ\text{C}$  is characteristic of dehydroxylation: the additional removal of terminal hydroxides at the zeolite surface. On page 59, TGA finds a comparable water content for a sample consisting of 100 % zeolite X: this implies that the water capacity of zeolites A and X is similar. Thus, for the typical zeolite A formula  $\text{Na}_{12}\text{Al}_{12}\text{Si}_{12}\text{O}_{48}\cdot x\text{H}_2\text{O}$ ,  $x \sim 33$ . This is comparable to literature values: Breck *et al.* measure an  $x$  value of 27(181).

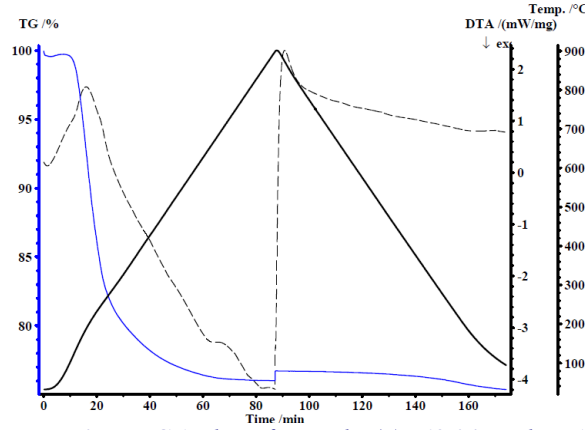


Figure 3.4: TGA plot of sample (c), 68 % zeolite A, 32 % zeolite X.

The formula of zeolite A may be calculated using the measurements of composition derived from XRF spectroscopy data of ~ 100 % zeolite A (Table 3.5) because elemental ratios measured by XRF spectroscopy,  $E_{XRF}$ , are proportional to the elemental ratios in the formula unit,  $E_{formula}$ . In order for charges to balance, the sodium zeolite composition takes the form  $Na_{12}Al_{12}Si_{12}O_{48} \cdot xH_2O$ .

$$\frac{Si_{XRF}}{Al_{XRF}} = y = \frac{Si_{formula}}{Al_{formula}} \quad \text{Equation 3.1}$$

$$\rightarrow y \cdot Al_{formula} = Si_{formula} \quad \text{Equation 3.2}$$

$$Si_{formula} + Al_{formula} = 24 = (y + 1) Al_{formula} \quad \text{Equation 3.3}$$

When other charge balancing cations are found in the system, the number per formula unit may be calculated for known oxidation states such that, for a given metal, M:

$$\frac{M_{XRF}}{Na_{XRF}} = n = \frac{M_{formula}}{Na_{formula}} \quad \text{Equation 3.4}$$

$$Al_{formula} = Na_{formula} + M_{formula} \times ox. \text{ state} \quad \text{Equation 3.5}$$

Thus, for M = Fe(II)/Mn(II) (oxidation state = +2), Equation 3.5 may be rearranged to:

$$Al_{formula} - Na_{formula} = 2M_{formula} \quad \text{Equation 3.6}$$

$$n \cdot Na_{formula} = M_{formula} \quad \text{Equation 3.7}$$

$$Al_{formula} = (2n + 1) \cdot Na_{formula} \quad \text{Equation 3.8}$$

Thus, in the Fe-loaded material (for a theoretical 100 % Fe(II)), Si/Al = 1.01 and Fe/Na = 2.01  $\rightarrow Fe_{4.8}Na_{2.4}Al_{12}Si_{12}O_{48} \cdot xH_2O$ . And in the Mn-loaded material (for a theoretical 100 % Mn(II)), Si/Al = 0.97 and Mn/Na = 1.64  $\rightarrow Mn_{4.6}Na_{2.8}Al_{12}Si_{12}O_{48} \cdot xH_2O$ . After chromate exposure, a

mixture of ion oxidation states is assumed to exist, such that charge balancing calculations become non-trivial: partitioning bulk and excess surface metal species is arbitrary. Values of Si/Al and M/Na are given in Table 3.5, determined by XRF spectroscopy from calibrated fused beads, which record an uptake of 20.3 mg<sub>Cr</sub>/g<sub>sieve</sub> by the Fe-loaded sample of phase pure zeolite A, whilst uptake by parent material Na- and Mn-zeolite A is negligible.

Table 3.5: XRF spectroscopy data from calibrated fused beads of sample (d) 99.874 (4) % zeolite A, 0.12577 (0) % zeolite X, where M = Fe or Mn.

Sieve		Si/Al	M/Na	M/Si	mg <sub>M</sub> /g <sub>sieve</sub>	mg <sub>Cr</sub> /g <sub>sieve</sub>
<b>Parent</b>	<b>Pre-Cr treatment</b>	1.12	-	0	0	0
	<b>Post Cr-treatment</b>	1.02	-	0	0	0
<b>Fe zeolite</b>	<b>Pre-Cr treatment</b>	1.01	2.01	0.39	111.3	0
	<b>Post Cr-treatment</b>	1.05	2.85	0.25	76.4	20.3
<b>Mn zeolite</b>	<b>Pre-Cr treatment</b>	0.97	1.64	0.39	106.9	0
	<b>Post Cr-treatment</b>	1.36	1.14	0.13	45.4	0

### *Zeolite X*

Although zeolite X has a lower absorbent capacity than zeolite A due to a higher Si/Al ratio,  $1 < \text{Si/Al} < 1.5$ , and so fewer charge balancing cations resting in the pore cavities, it has larger pores of  $\sim 8 \text{ \AA}$ , making it a good candidate for Cr(III) selective uptake, even after distortion(96,182). It forms an FAU framework, distinct from zeolite A.

Model-weighted Le Bail refinement was used to ascertain the unit cell parameters for zeolite X, which was fitted to cubic space group  $Fd-3$ . Zeolite X forms across a range of Si/Al ratios and no long-range order of Si and Al atoms exists. Le Bail refinement was selected to obtain unit cell parameters in order to bypass the problem of fitting peak intensities that are readily perturbed by the presence of water.  $a$  parameters for zeolite X were obtained both before and after Fe, Mn and Cr introduction, using samples that all derived from the same starting material. The calculated parameters in Table 3.6 have a high level of repeatability, to two or three decimal places. Synthesis was also uncomplicated, with phase pure zeolite X forming readily under the reaction conditions. Like those of zeolite A, these parameters imply a contraction upon initial ion exchange, due to accompanying changes in pore dimensions, or natural variation between samples.

*Table 3.6: Zeolite X cell parameters derived from Le Bail refinement using GSAS. The goodness of fit is given by  $\chi^2$  values.*

Sieve		$a / \text{\AA}$	$\chi^2$
Parent	Pre-Cr treatment	24.9051 (5)	2.504
	Post Cr-treatment	24.8288 (3)	1.818
Fe zeolite	Pre-Cr treatment	24.860 (2)	1.270
	Post Cr-treatment	24.8559 (9)	1.164
Mn zeolite	Pre-Cr treatment	24.8458 (5)	1.315
	Post Cr-treatment	24.8522 (5)	1.298

To determine whether any degradation of crystallinity is taking place upon ion exchange, EVA software was used to obtain d-spacings and full widths at half maximum (FWHM) of the first three peaks in the PXRD patterns of samples of zeolite X both before and after Fe, Mn and Cr ion exposure (Table 3.7). The errors on these data are equal to half the step size used on the diffractometers to gather the data, *i.e.* 0.01 to 1 sf for both the D8 ADVANCE and capillary diffractometers. Results suggest that variations in peak breadths and positions are not significant, particle aggregation is not observed, and crystallinity is maintained.

*Table 3.7: d-spacings and full widths at half maximum (FWHM) of zeolite X peaks ( $\text{\AA}$ ). The uncertainty in the data is equal to half the step size used on the diffractometers, *i.e.* 0.01 to 1 sf.*

		Peak 1	Peak 2	Peak 3
Zeolite X	<b>d spacing</b>	14.57 (1)	8.88 (1)	5.74 (1)
	<b>FWHM</b>	0.07 (1)	0.06 (1)	0.07 (1)
Cr-treated zeolite X	<b>d spacing</b>	14.56 (1)	8.87 (1)	5.73 (1)
	<b>FWHM</b>	0.08 (1)	0.08 (1)	0.09 (1)
Fe-loaded zeolite X	<b>d spacing</b>	14.67 (1)	8.90 (1)	5.74 (1)
	<b>FWHM</b>	0.08 (1)	0.07 (1)	0.08 (1)
Mn-loaded zeolite X	<b>d spacing</b>	14.69 (1)	8.91 (1)	5.75 (1)
	<b>FWHM</b>	0.10 (1)	0.10 (1)	0.08 (1)
Cr-treated Fe-loaded zeolite X	<b>d spacing</b>	14.59 (1)	8.87 (1)	5.73 (1)
	<b>FWHM</b>	0.09 (1)	0.09 (1)	0.09 (1)
Cr-treated Mn-loaded zeolite X	<b>d spacing</b>	14.45 (1)	8.83 (1)	5.71 (1)
	<b>FWHM</b>	0.07 (1)	0.07 (1)	0.08 (1)

To ensure that ion-exchange of zeolite X is readily repeatable without degradation of structure or introduction of competing phases, the PXRD patterns of four samples derived from the same parent zeolite X are compared in Figure 3.5. These patterns show that, other than variations in peak intensity due to water content, patterns do not suggest structural differences between samples.

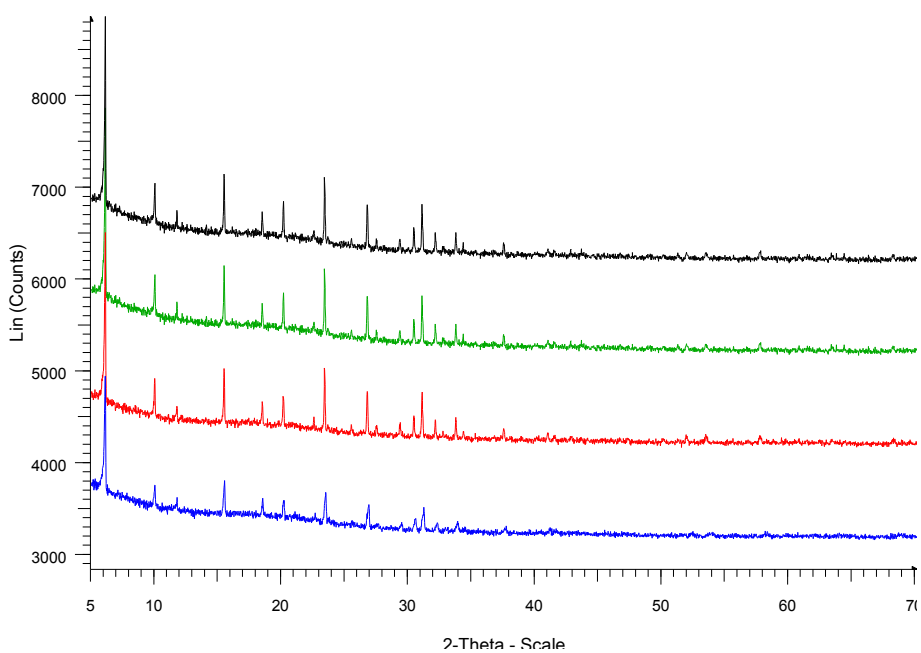


Figure 3.5: PXRD patterns of four samples of Fe-loaded zeolite X that were separately ion exchanged from the same zeolite X starting material.

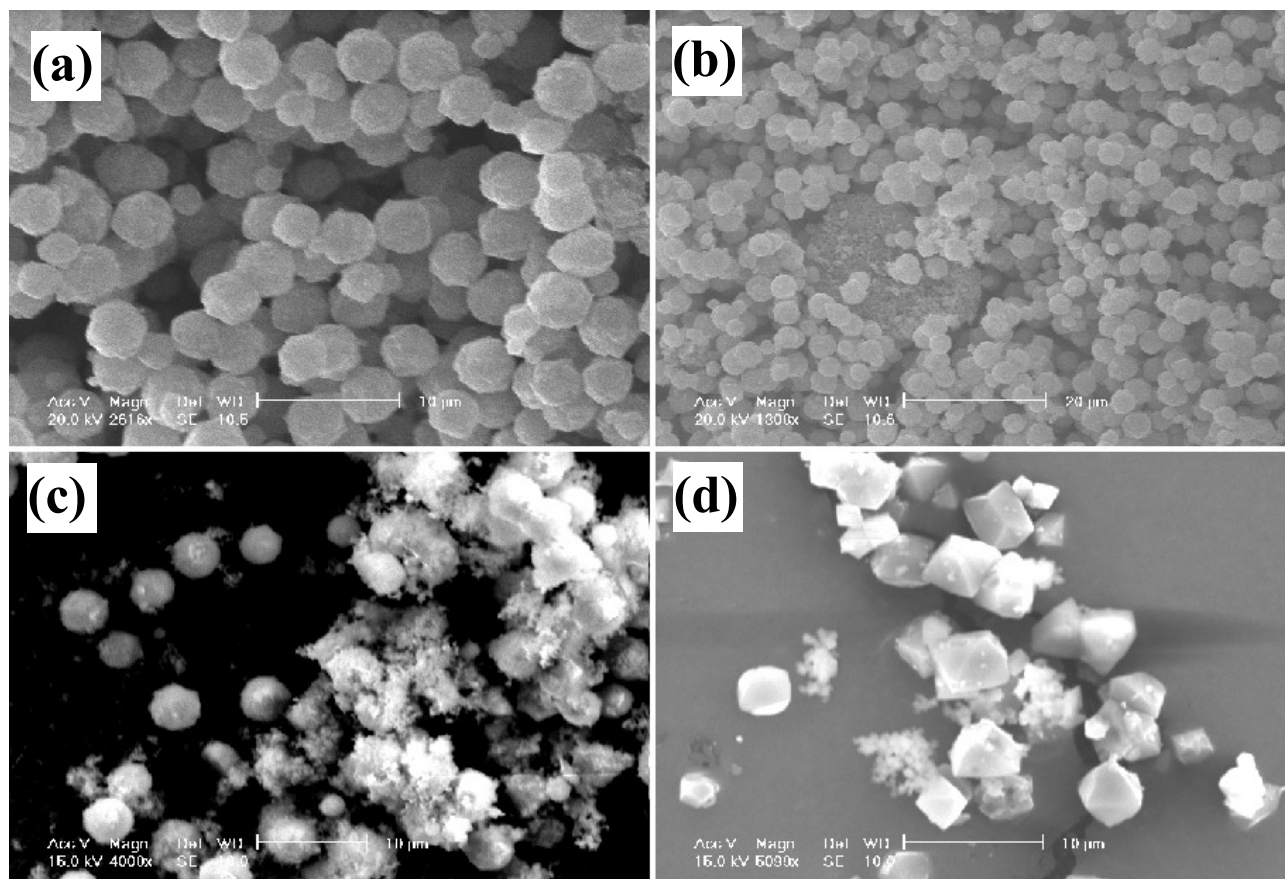


Figure 3.6: SEM images of zeolite X samples: (a) non-ion-exchanged zeolite X; (b) non-ion-exchanged zeolite and larger contaminant particles; (c) non-ion-exchanged zeolite and inter-crystal "fluff"; (d) Mn-loaded zeolite X showing prismatic crystals.

Scanning Electron Microscope images allow the long-range morphology of the zeolite to be examined. Images of zeolite X samples show clusters of ball-like crystals of diameter  $\sim 4 \mu\text{m}$  surrounded inter-crystal impurities in the form of and large oxide particles and fine "fluff". The crystal morphology may be better observed in one Mn-exchanged sample. Figure 3.6 (d) shows the prismatic form of the zeolite crystals.

TGA indicates that 24-27 % of the mass of air-exposed zeolite X is comprised of water. Two Fe-loaded zeolite X samples were measured (Figure 3.7). The majority of the mass loss may be attributed to water, although small events seen at  $\sim 500^\circ\text{C}$  are characteristic of dehydroxylation: the additional removal of terminal hydroxides at the zeolite surface. Since the typical formula of zeolite X is  $\text{Na}_{86}\text{Al}_{86}\text{Si}_{106}\text{O}_{384}\cdot x\text{H}_2\text{O}$  (where  $\text{Si}/\text{Al} = 1.23$ ),  $x$  may be determined by the TGA data, such that here,  $x \sim 248.5$ .

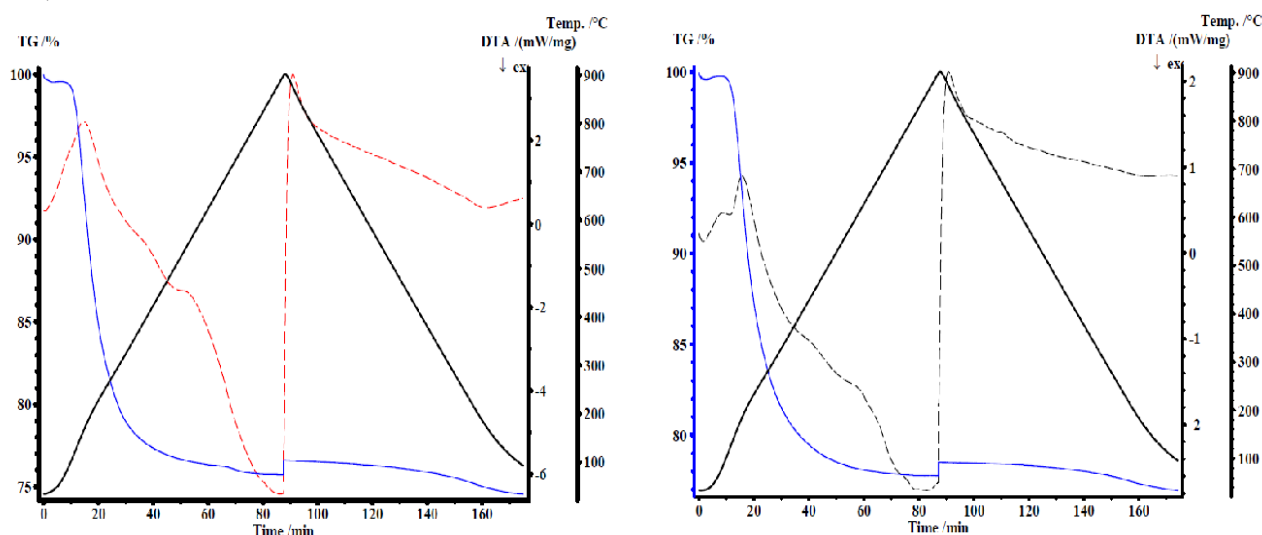


Figure 3.7: TGA plots of two Fe-loaded zeolite X samples.

The exact formula of zeolite X may be calculated using the measurements of composition derived from XRF spectroscopy data (Table 3.8) because elemental ratios measured by XRF spectroscopy,  $E_{\text{XRF}}$ , are proportional to the elemental ratios in the formula unit,  $E_{\text{formula}}$  (Equation 3.4). In order for charges to balance, the sodium zeolite composition takes the form  $\text{Na}_x\text{Al}_x\text{Si}_{192-x}\text{O}_{384}\cdot x\text{H}_2\text{O}$ , such that:

$$\text{Si}_{\text{formula}} + \text{Al}_{\text{formula}} = 192 = (y+1) \text{Al}_{\text{formula}} \quad \text{Equation 3.9}$$

where  $y$  is defined in Equation 3.6

Thus in the parent material zeolite X,  $\text{Si}/\text{Al} = 1.49 \rightarrow \text{Na}_{77}\text{Al}_{77}\text{Si}_{115}\text{O}_{384}\cdot 245\text{H}_2\text{O}$ .

When other charge balancing cations are found in the system, the number per formula unit may be calculated for known oxidation states using Equation 3.7, where  $M = \text{Fe(II)}/\text{Mn(II)}$ . For a mixture of these metal ions,  $M = M_{\text{tot}}$ , the total numbers of metal ions: relative proportions of Fe(II) and Mn(II) may then be assessed using:

$$r = \frac{\left(\frac{Fe}{Si}\right)}{\left(\frac{Mn}{Si}\right)} = \frac{Fe_{formula}}{Mn_{formula}} \quad \text{Equation 3.10}$$

$$M_{tot} = Fe_{formula} + Mn_{formula} = (r + 1) Mn \quad \text{Equation 3.11}$$

A single metal does not always possess all the optimal properties to perform a role in chemistry. Molecular sieves containing a mixture of metal ions have been reported in the literature(77,117). However, since when Na is ion exchanged for Fe or Mn, the exchange is not complete, *i.e.* efficiency decreases by the time Cr(VI) is introduced due to Na contamination, mixed ion systems risk greater penalties due to competition during their introduction.

In the Fe-loaded material (for a theoretical 100 % Fe(II)), Si/Al = 1.59 and Fe/Na = 1.09 → Fe<sub>25.4</sub>Na<sub>23.2</sub>Al<sub>74</sub>Si<sub>118</sub>O<sub>384</sub>.248H<sub>2</sub>O. In the Mn-loaded material (for a theoretical 100 % Mn(II)), Si/Al = 1.33 and Mn/Na = 1.06 → Mn<sub>27.9</sub>Na<sub>26.2</sub>Al<sub>82</sub>Si<sub>110</sub>O<sub>384</sub>.252H<sub>2</sub>O. And in the mixed ion Fe- and Mn-loaded material, Si/Al = 1.61, M/Na = 1.63, Fe/Si = 0.20 and Mn/Si = 0.17 → Fe<sub>15.3</sub>Mn<sub>13.0</sub>Na<sub>17.4</sub>Al<sub>74</sub>Si<sub>118</sub>O<sub>384</sub>.249H<sub>2</sub>O. After chromate exposure, a mixture of ion oxidation states is assumed to exist, such that formula calculations become non-trivial. Values originate from Table 3.8, XRF spectroscopy data from calibrated fused beads, which record that Fe-, Mn-, and FeMn-loaded samples of zeolite X will take up 29.1, 0.5 and 16.3 mg<sub>Cr</sub>/g<sub>sieve</sub> respectively, whilst uptake by parent material Na-zeolite X is negligible. Uptake of chromium by both Fe- and Mn-loaded zeolite X is higher than that of zeolite A, implying that the zeolite A structure is less suitable for Cr ion uptake. The mixed ion loaded zeolite X recorded a chromium uptake between that of pure Fe- and Mn-loaded samples, despite a lower Na content, implying that chromium recovery is strongly influenced by the choice of redox-active ion.

Table 3.8: XRF spectroscopy data from calibrated fused beads of zeolite X, where M = Fe or Mn, and uncalibrated fused beads of zeolite X, where M = Fe+Mn (existing calibrations measure Fe OR Mn content rather than both).

Sieve	Si/Al	M/Na	M/Si	mg <sub>M</sub> /g <sub>sieve</sub>	mg <sub>Cr</sub> /g <sub>sieve</sub>
<b>Parent</b>	<b>Pre-Cr treatment</b>	1.49	-	0	0
	<b>Post Cr-treatment</b>	1.53	-	0	0
<b>Fe zeolite</b>	<b>Pre-Cr treatment</b>	1.59	1.09	0.31	106.3
	<b>Post Cr-treatment</b>	1.59	0.93	0.27	90.1
<b>Mn zeolite</b>	<b>Pre-Cr treatment</b>	1.33	1.06	0.25	83.4
	<b>Post Cr-treatment</b>	1.35	0.79	0.14	49.0
<b>Fe-Mn zeolite</b>	<b>Pre-Cr treatment</b>	1.61	1.63	0.17 (Mn) 0.20 (Fe)	61.1(Mn) 76.8(Fe)
	<b>Post Cr-treatment</b>	1.42	0.38	0.10 (Mn) 0.13 (Fe)	34.0(Mn) 44.4(Fe)

The lattice parameter,  $a$ , for Na-loaded zeolite X is consistent with the Si/Al ratio derived from XRF spectroscopy data (Table 3.8).  $a$  is directly proportional to the number of Al ions in the unit cell of the pure Na-loaded zeolite X, due to longer Al-O than Si-O bond lengths, as given in Equation 3.12 and Figure 3.8(111):

$$a = \frac{1.66656}{1 + \text{Si}/\text{Al}} + 24.191 \quad \text{Equation 3.12}$$

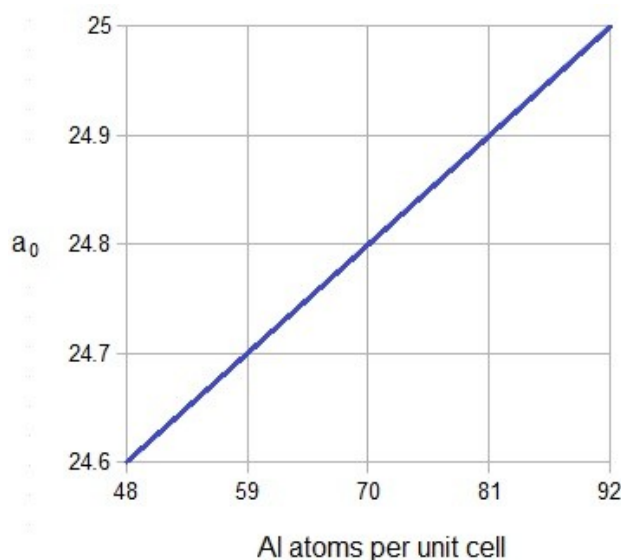


Figure 3.8: Linear relationship between cell parameter  $a$  and number of Al atoms in the unit cell.

Four different Fe-loaded zeolite X samples were prepared as fused beads and their elemental compositions recorded using XRF spectroscopy against a calibration. The mean average Si/Al, Fe/Na, Fe/Si and  $\text{mg}_M/\text{g}_{\text{sieve}}$  ratios were determined and are presented in Table 3.9 beside deviations. These deviations identify the range of error associated with XRF spectroscopic measurements and suggest that similar samples may be synthesised reliably. Si/Al ratios consistently rest at the high end of the range  $1 < \text{Si}/\text{Al} < 1.5$ .

Table 3.9: Mean average XRF spectroscopy data from calibrated fused beads of four Fe-loaded zeolite X samples with deviations in brackets.

Sieve	Si/Al	Fe/Na	Fe/Si	$\text{mg}_M/\text{g}_{\text{sieve}}$
Fe zeolite pre-Cr treatment	1.51 (14)	0.91 (17)	0.27 (5)	92.1 (15.3)

### *Clinoptilolite*

Natural zeolite samples are often impure. Fractions of phases are idiosyncratic to each sample; for example, Concepcion-Rosabal *et al.* found 70 % clinoptilolite, 5 % mordenite, 15 %

anorthite and 10 % quartz in one sample, whilst the natural sample of Ates *et al.* consisted of 30 % clinoptilolite, 40 % mordenite, 10 % quartz, 10 % feldspar and 5 % clay(183,184). The sample referred to here as “clinoptilolite” is chiefly composed of a heulandite zeolite structure, fitting the formula  $(\text{Na,K,Ca})_{1-1.5}\text{Al}_2\text{Si}_7\text{O}_{18}\cdot 6\text{H}_2\text{O}$  and C1 space group as determined by Koyama and Takeuchi, and against which PXRD data is refined in this work(185). PXRD patterns of the sample both before and after ion exchange with Fe, Mn and Cr were used to obtain Rietveld refinements against the data (Figure 3.9, Table 3.10). An increase in cell parameters upon Fe- and Mn-exchange might represent some cell expansion. However, given the poor quality of the data, very little can be determined except for the presence of two phases: clinoptilolite contaminated with mordenite. Poor data quality can be evaluated through inspection of the plot.

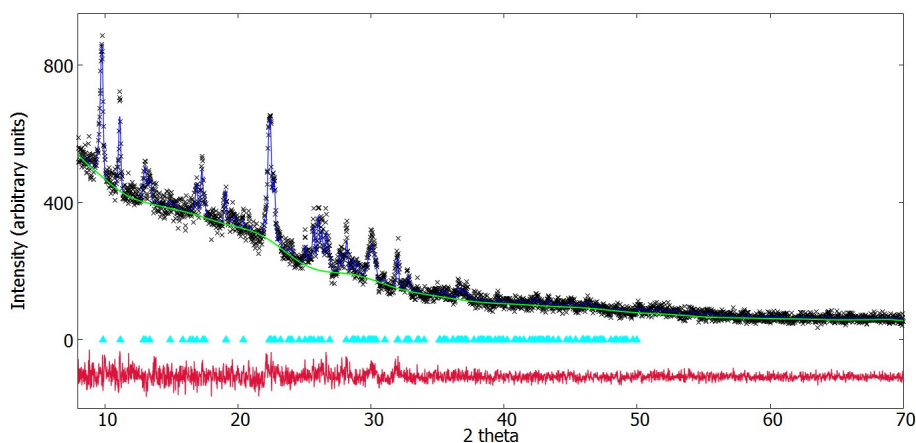


Figure 3.9: Rietveld refinement of one sample of natural zeolite containing clinoptilolite. Data are represented by black crosses, background by a green line, the fit with a blue line and the residual is presented below in red. Turquoise markers represent the clinoptilolite phase.

Table 3.10: Phase fractions and clinoptilolite cell parameters derived from Rietveld refinement using GSAS of a natural clinoptilolite zeolite sample with mordenite impurities. The goodness of fit is given by  $\chi^2$  values.

Clinoptilolite		Clino phase /%	Mordenite phase /%	$a / \text{\AA}$	$b / \text{\AA}$	$c / \text{\AA}$	$\chi^2$
Parent	Pre Cr-exposure	78.4 (4)	22 (2)	17.601 (6)	17.893 (8)	7.382 (2)	1.615
	Post Cr-exposure	85.1 (3)	15 (2)	17.608 (6)	17.878 (7)	7.382 (2)	1.493
Fe	Pre Cr-exposure	85 (1)	15 (3)	17.633 (6)	17.864 (9)	7.397 (3)	1.268
	Post Cr-exposure	85 (2)	15 (4)	17.648 (6)	17.895 (1)	7.395 (3)	1.132
Mn	Pre Cr-exposure	74.0 (3)	26 (1)	17.634 (4)	17.926 (4)	7.394 (2)	1.836
	Post Cr-exposure	77 (2)	23 (2)	17.675 (5)	18.012 (7)	7.409 (2)	1.467

Samples of natural zeolite that contain mixtures of phases and several different charge-balancing cations often demonstrate a blend of different crystal morphologies and diversity of pore sizes, making them poorly cation selective. However, easy access to the network means that

clinoptilolite phase typically exhibits a high ion exchange capacity(84). In this sample, high Si/Al ratios of  $\sim 5$  (Table 3.11) correspond to a lower cation content than the formulaic ratio of 3.5, and thus limit chromium loading, *i.e.* a larger mass of zeolite is required for the same theoretical maximum loading, and the clinoptilolite phase compares badly with synthetic analogues. Chromium uptake was tested in both Fe- and Mn-loaded natural clinoptilolite zeolite samples *via* XRF spectroscopy data from calibrated fused beads: 13.5 and 0.6  $\text{mg}_{\text{Cr}}/\text{g}_{\text{sieve}}$  were adsorbed respectively (Table 3.11).

Table 3.11: XRF spectroscopy data from calibrated fused beads of natural zeolite containing clinoptilolite, where  $M = \text{Fe}$  or  $\text{Mn}$ . Uncalibrated fused bead data were also recorded to provide relative Na, K and Ca quantities to give accurate  $\text{mg}_M/\text{g}_{\text{sieve}}$  and  $\text{mg}_{\text{Cr}}/\text{g}_{\text{sieve}}$  values.

Sieve		Si/Al	M/Na	M/Si	$\text{mg}_M/\text{g}_{\text{sieve}}$	$\text{mg}_{\text{Cr}}/\text{g}_{\text{sieve}}$
Fe zeolite	Pre-Cr treatment	5.00	0.93	0.06	35.8	0
	Post Cr-treatment	4.99	0.91	0.07	38.5	13.5
Mn zeolite	Pre-Cr treatment	4.86	0.50	0.03	17.2	0
	Post Cr-treatment	4.75	0.39	0.02	12.9	0.6

TGA of the non-ion-exchanged parent material indicates that 11 % of the mass of air-exposed zeolite is comprised of water (Figure 3.10). Although this measurement shows a smooth weight loss curve corresponding to uncomplicated loss of one type of small molecule only, Concepcion-Rosabal *et al.* report a two-step profile for Fe-exchanged natural clinoptilolite zeolite sample under heat treatment, where loss of water species occurs at 100 °C, followed by a “sharp endothermic response” at 140 °C attributed to the decomposition of occluded Fe sulfate within the pore network(183).

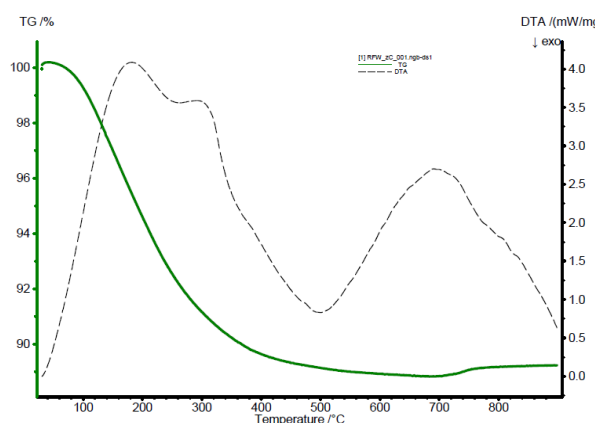


Figure 3.10: TGA plot of natural zeolite containing clinoptilolite.

### Summary

Structural characterisation of zeolites is complicated by the presence of water, which

perturbs peak intensities; although dehydration is viable, since these systems are destined to be used in aqueous environments, and aggregation of particles may occur not only upon ion exchange, as seen in PXRD results, but also upon dehydration, invalidating the method.

### 3.3. Zeolites – Templating

Zeolite templating offers the opportunity to introduce mesoporosity and so increase the surface area and accessibility of the sieve pores. This provides the potential for increased surface adsorption and ion exchange. Cho *et al.* report elevated molecular diffusion in the mesoporous sample over a microporous zeolite(186).

#### *Templated Zeolite X*

Attempts were made to template zeolite X samples by introducing 10 % CTAB, 10 % gelatin G2500, 10 % agar A5440 or 2 % of three kinds of alginate (LF20/40, GP3350 and 180947) at the synthesis stage, before calcining to remove any blockages from the pore network. A lower percentage of alginate template was used because it forms a much more viscous gel. “10 %” template refers to a mass of prepared gel equal to 10 % of the projected theoretical yield of untemplated zeolite. This templating approach is supported by reports in the literature of high uptake in materials with open, porous structures, such as the adsorption of 95 mg<sub>Cr</sub>/g<sub>Sieve</sub> of Cr(VI) ions by Fe(III)-loaded MCM-41(124).

PXRD showed that no loss of structure resulted from the introduction of template materials. EVA software was used to obtain d-spacings and full widths at half maximum (FWHM) of the first three peaks in the PXRD patterns of templated samples of zeolite X both before and after Fe, Mn and Cr ion exposure. Table 3.12 summarises this data as mean averages for d-spacings and FWHMs for each peak. The errors on the data that were averaged are equal to half the step size used on the diffractometers to gather the data, *i.e.* 0.01 to 1 sf, but mean deviations are given in brackets, which often exceed this error value.

Table 3.12: Mean average *d*-spacings and full widths at half maximum (FWHM) of templated zeolite X peaks compared with the mean average *d*-spacings and FWHM of untemplated zeolite X peaks (Å). The uncertainty in the data is equal to half the step size used on the diffractometers, i.e. 0.01 to 1 sf, but deviations, given in brackets, often exceed this.

Zeolite X samples	Peak 1		Peak 2		Peak 3	
	d-spacing	FWHM	d-spacing	FWHM	d-spacing	FWHM
<b>Untemplated</b>	14.59 (12)	0.08 (2)	8.88 (4)	0.08 (2)	5.73 (2)	0.08 (1)
<b>CTAB</b>	14.60 (6)	0.11 (4)	8.88 (2)	0.07 (1)	5.73 (2)	0.13 (6)
<b>Gelatin G2500</b>	14.59 (3)	0.09 (0)	8.87 (2)	0.08 (1)	5.74 (1)	0.09 (0)
<b>Agar A5440</b>	14.60 (2)	0.09 (2)	8.88 (2)	0.08 (1)	5.74 (0)	0.08 (1)
<b>Alginate LF20/40</b>	14.58 (0)	0.08 (0)	8.87 (2)	0.08 (0)	5.72 (0)	0.09 (1)
<b>Alginate GP3350</b>	14.54 (2)	0.09 (3)	8.85 (2)	0.08 (2)	5.72 (1)	0.08 (0)
<b>Alginate 180947</b>	14.53 (4)	0.08 (2)	8.85 (1)	0.08 (1)	5.72 (2)	0.08 (1)

Results suggest that peak widths and positions are not significantly affected by the introduction of templates; indeed, the largest deviation belongs to the first peak of the untemplated sample.

Zeolite X cell parameters were obtained by model-weighted Le Bail refinement both before and after exposure to Fe, Mn and Cr ions (Table 3.13). Le Bail refinement bypasses the problem of fitting peak intensities that are readily perturbed by the presence of water in the pore network. Data suggest that cell parameters are not significantly perturbed.

Table 3.13: Templated zeolite X cell parameters derived from Le Bail refinement using GSAS. The goodness of fit is given by  $\chi^2$  values. Original, untemplated values from Table 3.6 are given below in brackets.

Sieve	<i>a</i> / Å	$\chi^2$
<b>Parent</b>	Pre-Cr treatment 24.8461 (4) 24.9051 (5)	1.412
	Post Cr-treatment 24.9302 (8) 24.8288 (3)	1.692
<b>Fe zeolite</b>	Pre-Cr treatment 24.8566 (9) 24.860 (2)	1.271
	Post Cr-treatment 24.855 (2) 24.8559 (9)	1.136
<b>M zeolite</b>	Pre-Cr treatment 24.8173 (8) 24.8458 (5)	1.329
	Post Cr-treatment 24.8922 (8) 24.8522 (5)	1.09

SEM images of samples of templated zeolite X do not appreciably differ from the untemplated zeolite X. LF20/40 alginate templated zeolite X (Figure 3.12) demonstrated more clustering of zeolite particles than its untemplated parent material (Figure 3.6).

TEM imaging was used to investigate samples of 2 % templated alginate LF20/40 zeolite X, 10 % gelatin and 10 % agar templated zeolite X, to discover whether these contained mesopores and, if so, whether they were an appropriate size to select for Cr(III) (Figure 3.11). TEM imaging reveals that although some changes occur upon gelatin and agar templating, such as the break up of

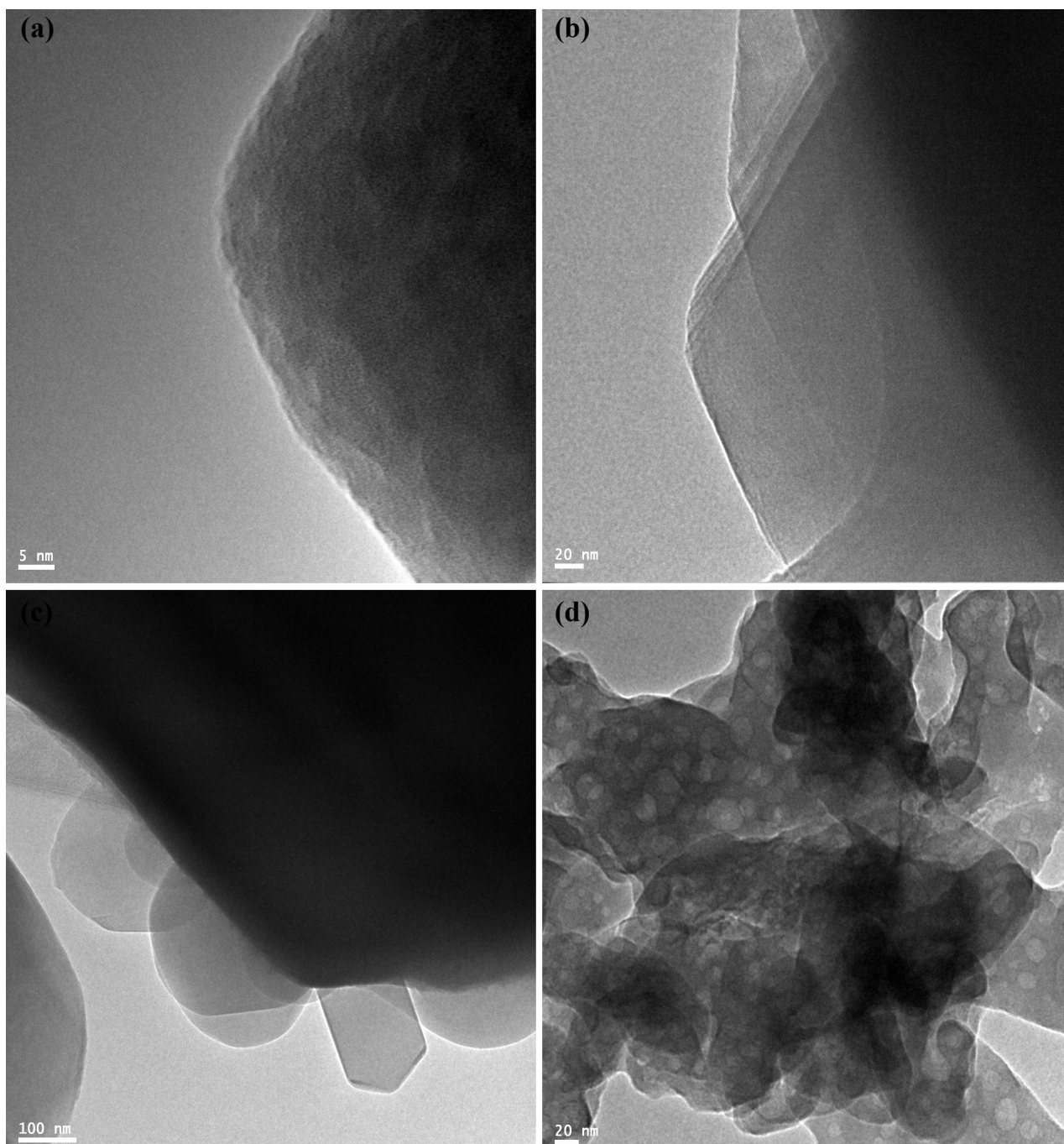


Figure 3.11: TEM images of templated zeolite X samples: (a) untemplated zeolite X; (b) 10 % G2500 gelatin templated zeolite X; (c) 10 % agar A4550 templated zeolite X; (d) 2 % alginate LF20/40 templated zeolite X, with mesopores.

larger crystals into smaller components, layer sliding and separation of differently-shaped crystals (Figure 3.11 (c)), no mesoporosity is introduced and samples largely compare to the untemplated zeolite X. Sodalite layers are visible in Figure 3.11 (b). However, distinct mesopores are formed throughout 2 % alginate LF20/40 templated zeolite X (Figure 3.11 (d)), sized between ~ 4 and 20 nm.

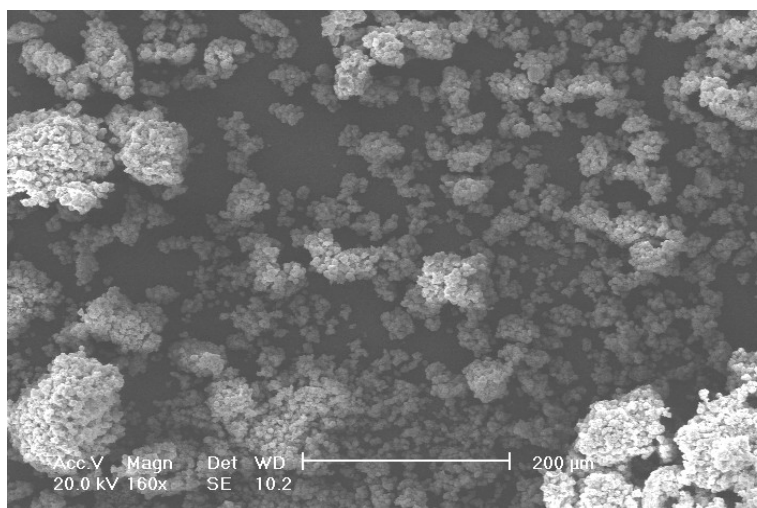


Figure 3.12: SEM image of non-ion-exchanged 2 % alginate LF20/40 templated zeolite X.

XRF spectroscopy data were gathered from calibrated fused beads of Fe-, Mn- and Cr-treated samples of templated zeolite X in order to determine whether templating had increased chromium uptake – likely where mesopores were of the correct proportions to select for Cr(III). Data is presented in Tables 3.14-3.16.

Table 3.14: XRF spectroscopy data from calibrated fused beads of 10 % CTAB templated zeolite X, where  $M = Fe$  or  $Mn$ .

Sieve	Si/Al	M/Na	M/Si	mg <sub>M</sub> /g <sub>sieve</sub>	mg <sub>Cr</sub> /g <sub>sieve</sub>	
Fe zeolite	Pre-Cr treatment	1.47	0.93	0.21	74.3	0
	Post Cr-treatment	1.47	0.82	0.21	73.2	12.3
Mn zeolite	Pre-Cr treatment	1.40	1.02	0.23	77.6	0
	Post Cr-treatment	1.39	0.92	0.22	74.4	0.6

Table 3.15: XRF spectroscopy data from calibrated fused beads of 10 % gelatin G2500 templated zeolite X, where  $M = Fe$  or  $Mn$ .

Sieve	Si/Al	M/Na	M/Si	mg <sub>M</sub> /g <sub>sieve</sub>	mg <sub>Cr</sub> /g <sub>sieve</sub>	
Fe zeolite	Pre-Cr treatment	1.50	0.84	0.25	87.1	0
	Post Cr-treatment	1.49	0.90	0.25	85.8	19.7
Mn zeolite	Pre-Cr treatment	1.45	1.00	0.26	88.8	0
	Post Cr-treatment	1.43	1.03	0.25	85.2	0.6

Table 3.16: XRF spectroscopy data from calibrated fused beads of 10 % agar A4550 templated zeolite X, where M = Fe or Mn.

Sieve		Si/Al	M/Na	M/Si	mg <sub>M</sub> /g <sub>sieve</sub>	mg <sub>Cr</sub> /g <sub>sieve</sub>
Fe zeolite	Pre-Cr treatment	1.54	0.83	0.27	93.8	0
	Post Cr-treatment	1.50	0.75	0.25	85.2	19.1
Mn zeolite	Pre-Cr treatment	1.47	1.03	0.27	92	0
	Post Cr-treatment	1.45	0.84	0.23	80.4	0.6

Table 3.17: XRF spectroscopy data from calibrated fused beads of 2 % alginate LF20/40 zeolite X, where M = Fe or Mn.

Sieve		Si/Al	M/Na	M/Si	mg <sub>M</sub> /g <sub>sieve</sub>	mg <sub>Cr</sub> /g <sub>sieve</sub>
Fe zeolite	Pre-Cr treatment	1.56	1.05	0.33	112.6	0
	Post Cr-treatment	1.54	1.15	0.34	108.2	33.1
Mn zeolite	Pre-Cr treatment	1.49	1.34	0.35	115.6	0
	Post Cr-treatment	1.47	1.33	0.31	104.6	4.3

Table 3.18: XRF spectroscopy data from calibrated fused beads of 2 % alginate GP3350 templated zeolite X, where M = Fe or Mn.

Sieve		Si/Al	M/Na	M/Si	mg <sub>M</sub> /g <sub>sieve</sub>	mg <sub>Cr</sub> /g <sub>sieve</sub>
Fe zeolite	Pre-Cr treatment	1.56	0.43	0.23	77.4	0
	Post Cr-treatment	1.57	0.45	0.21	72.3	18.3
Mn zeolite	Pre-Cr treatment	1.51	0.41	0.19	65.7	0
	Post Cr-treatment	1.50	0.40	0.18	62.3	1.2

Table 3.19: XRF spectroscopy data from calibrated fused beads of 2 % alginate 180947 templated zeolite X, where M = Fe or Mn.

Sieve		Si/Al	M/Na	M/Si	mg <sub>M</sub> /g <sub>sieve</sub>	mg <sub>Cr</sub> /g <sub>sieve</sub>
Fe zeolite	Pre-Cr treatment	1.50	0.76	0.30	99.1	0
	Post Cr-treatment	1.51	0.80	0.26	87.1	19.6
Mn zeolite	Pre-Cr treatment	1.50	0.79	0.24	81.1	0
	Post Cr-treatment	1.44	0.71	0.22	76.0	1.2

Chromium uptake is mostly lower than the value of 29.1 mg<sub>Cr</sub>/g<sub>Fe-sieve</sub> in untemplated Fe-loaded zeolite X (Table 3.8), whilst Mn-loaded zeolite X uptake remains similar and low. In the 10 % CTAB-templated Fe-loaded zeolite X sample, the decrease in chromium uptake is particularly pronounced, dropping to 12.3 mg<sub>Cr</sub>/g<sub>Fe-sieve</sub>. This might imply that integration of CTAB is successful, but that the template was not removed *via* calcination, leading to pore blocking. Alginate LF20/40 templating, however, records a significant *increase* in Fe/Mn-loading and correspondingly higher chromium uptake for both systems; this is in agreement with the TEM observations of mesoporosity. Samples were prepared with half (1 %) and twice (4 %) the quantity of alginate

LF20/40 at the synthesis stage in order to compare with the original 2 % alginate LF20/40-templated sample (Table 3.17).

*Table 3.20: XRF spectroscopy data from calibrated fused beads of 1 %, 2 % and 4 % alginate LF20/40 templated zeolite X, where M = Fe or Mn.*

Sieve		Si/Al	M/Na	M/Si	mg <sub>M</sub> /g <sub>sieve</sub>	mg <sub>Cr</sub> /g <sub>sieve</sub>
Fe-Cr	1 %	1.50	0.74	0.25	84.1	25.2
	2 %	1.54	1.15	0.34	108.2	33.1
	4 %	1.56	0.77	0.22	76.3	17.2
Mn-Cr	1 %	1.47	0.81	0.22	77.6	0.6
	2 %	1.47	1.33	0.31	104.6	4.3
	4 %	1.44	0.85	0.24	80.6	0.6

These data suggest that the 1 % and 4 % alginate templated Fe-loaded zeolite X were not as successful at chromium uptake as the original 2 % alginate templated sample, due to lower initial Fe-loadings. The Fe-loaded 4 % alginate templated sample records a lower Fe-loading and thus lower chromium uptake than both the 1 % alginate templated sample and untemplated sample (Table 3.8), suggesting that chromium recovery is governed primarily by ion loadings and not structure. The Mn-loaded samples similarly demonstrate lower ion-loadings for 1 % and 4 % alginate templating than for 2 % alginate templating. Uptake in the Mn-loaded 1 % and 4 % alginate templated zeolite X is indistinguishable from that of the untemplated zeolite X. Thus, structural modifications that facilitate higher chromium uptake are those which prioritise suitability for loading and retaining Fe(II) and Mn(II) ions, not Cr(III). It is possible that when higher levels of template are introduced, aggregation of template particles occurs such that mesoporosity is not introduced or pores are too large to select for 2.12 Å Fe(II) ions(129). This may also have occurred in gelatin and agar samples. At lower levels of template, dispersion may be more successful, forming mesopores of an appropriate size. The more of these, the higher the uptake. Table 3.17 suggests that 2 % alginate LF20/40 sits in the “sweet spot” between two limits.

### ***Hierarchically porous ZSM-5 Zeolite***

The hierarchially porous ZSM-5 zeolite, Hp-ZSM-5, is an MFI framework type zeolite synthesised using a CTAB template. PXRD shows that the synthesised sample has not fully crystallised: the formation of early ZSM-5 peaks may be observed (Figure 3.13). A longer crystallisation period is required to prepare this material.

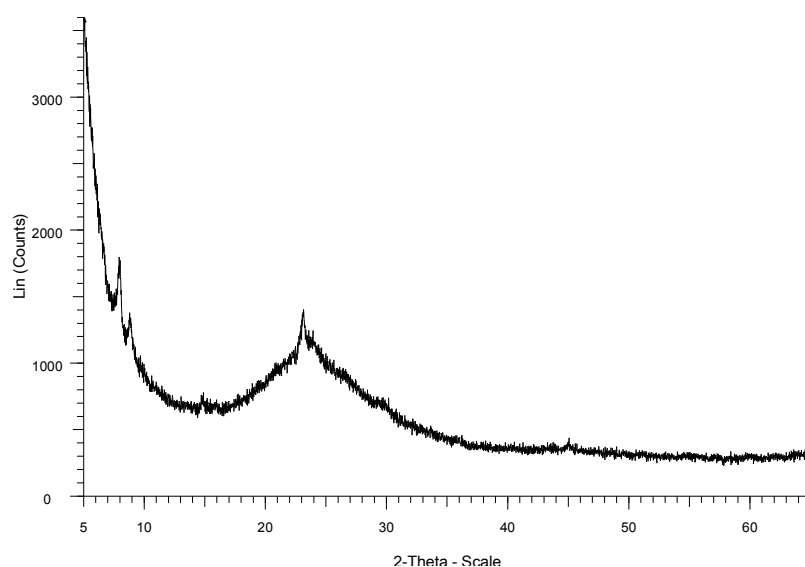


Figure 3.13: PXRD pattern of Hp-ZSM-5 zeolite, showing the poor quality of the pattern.

Although mesoporosity introduced by CTAB is expected to facilitate uptake, Hp-ZSM-5 has a much higher Si/Al ratio than zeolites X and A and thus significantly lower cation capacity (Table 3.21). For this reason, ion exchange was unable to achieve high Fe or Mn loadings and Fe-loaded Hp-ZSM-5 only took up  $7.19 \text{ mg}_{\text{Cr}}/\text{g}_{\text{sieve}}$ , whilst chromium uptake by Mn-loaded Hp-ZSM-5 was negligible (Table 3.21).

Table 3.21: XRF spectroscopy data from calibrated fused beads of Hp-ZSM-5 zeolite, where M = Fe or Mn.

Sieve		Si/Al	M/Na	M/Si	$\text{mg}_{\text{M}}/\text{g}_{\text{sieve}}$	$\text{mg}_{\text{Cr}}/\text{g}_{\text{sieve}}$
Fe zeolite	Pre-Cr treatment	28.5	2.30	0.03	14.8	0
	Post Cr-treatment	35.8	3.16	0.03	12.0.	7.19
Mn zeolite	Pre-Cr treatment	33.3	-	0.02	8.9	0
	Post Cr-treatment	27.0	0.31	0.01	3.3	0

Not only was chromium uptake lower in Hp-ZSM-5 than in untemplated zeolites, but TGA indicated that 42 % of the mass of air-exposed Hp-ZSM-5 is comprised of water or other volatile components (Figure 3.14), such that  $\text{mg}_{\text{Cr}}/\text{g}_{\text{sieve}}$  values are necessarily less competitive. This result highlights one of the inherent difficulties in comparing the remediation effectiveness of samples. Whilst  $\text{mg}_{\text{Cr}}/\text{g}_{\text{sieve}}$  is a valid and widely accepted measure of uptake, samples of some materials such as activated carbon, which have large, porous volumes, high surface areas, and very low molecular weights, exhibit misleadingly high values.

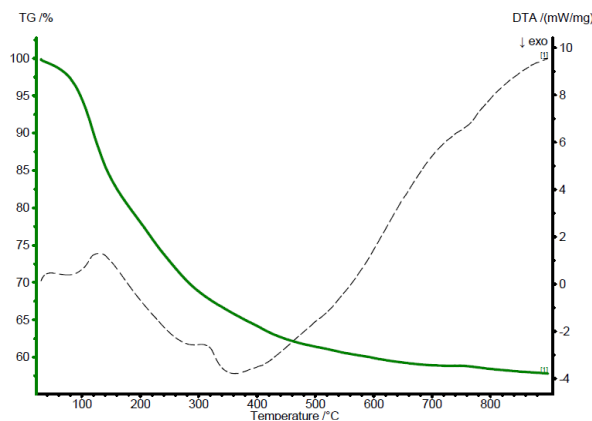


Figure 3.14: TGA plot of Mn-loaded Hp-ZSM-5 zeolite.

### Summary

Alginate templating creates mesopores in the zeolite X structure, increasing Fe uptake and so Cr uptake such that  $29.1 \text{ mg}_{\text{Cr}}/\text{g}_{\text{sieve}} \rightarrow 33.1 \text{ mg}_{\text{Cr}}/\text{g}_{\text{sieve}}$  in Fe-loaded zeolite X, and  $4.6 \text{ mg}_{\text{Cr}}/\text{g}_{\text{sieve}} \rightarrow 0.5 \text{ mg}_{\text{Cr}}/\text{g}_{\text{sieve}}$  in Mn-loaded zeolite X. Consistent  $\text{mg}_{\text{Cr}}/\text{mg}_{\text{Fe}}$  ratios show that chromium recovery is governed primarily by ion loadings and not structure.

### 3.4. AIPOs

Synthesis of several AIPO systems was attempted. Fe(II)- and Mn(II)-loaded AIPO-5, a mixed Fe oxidation state AIPO of formula  $[\text{Fe(II)Fe(III)}_{0.8}(\text{H}_2\text{O})_2\text{Al}_{1.2}(\text{PO}_4)_3] \cdot \text{H}_3\text{O}$ , referred to as AIPO-Fe23, and an Fe(II)-loaded LAU framework AIPO were explored(163). Since these frameworks are charge neutral, ions are introduced at the synthesis stage with the aim of integrating them into the framework where their oxidation states and thus redox activity may then be manipulated.

#### AIPO-5

AIPO-5 has an AFI framework structure containing a 1D channel of 0.73 nm diameter and is attributed the hexagonal space group  $P6cc(162)$ . However, lower symmetry models have been proposed that bypass the unfavourable linear geometry of one oxygen atom in the  $P6cc$  model and account for peak splitting observed at high resolution(104,187).

Several attempts were made to prepare AIPO-5 samples with different quantities of Fe(II) and Mn(II) (Table 3.22). Fe(II) and Mn(II) substitute for aluminium, so the extent of substitution is

given as a percentage, *e.g.* 10 % Fe(II) – with 90 % Al(III). No samples of phase pure AlPO-5 were obtained, and competitive  $\alpha$ -berlinite, the AlPO analogue of quartz, and an orthorhombic cristobalite AlPO<sub>4</sub> phase were identified(188). Table 3.22 gives the phase fractions estimated using Rietveld refinement on calcined samples. Uncalcined samples were not Rietveld refined: templates resting within the structure influence electron density distributions, such that they must be included in Rietveld refinement, complicating it. Table 3.23 gives the cell parameters estimated using a model-weighted Le Bail refinement on both calcined and uncalcined samples. The Le Bail method was chosen in order to obtain accurate unit cell parameters that bypass the problem of fitting peak intensities that are readily perturbed by the presence of water in the pore network. Given the quality and resolution of data, the P6<sub>cc</sub> space group provides a sufficiently good fit to obtain useful cell parameters, and is simple to refine because it contains few parameters.

Several research groups have now synthesised AlPO-5 under microwave conditions(162,189,190). Varying reaction conditions affects crystal purity, size and homogeneity. Optimal conditions of 800 W power, 180 °C and short reaction times (< 1 hour) were identified(137). At higher temperatures, larger AlPO-5 crystals are synthesised, but their crystallinity is compromised. If reaction times are too short (*e.g.* 60 s) and temperatures too low (*e.g.* 160 °C), the target product may not be produced, or unreacted starting materials remain in solution. Attempts were made to synthesise samples of 20 % Fe(II)-loaded AlPO-5 under microwave conditions, including one templated with 2 % alginate LF20/40 (Tables 3.22 and 3.23).

*Table 3.22: Phase fractions derived from Rietveld refinement using GSAS of samples with the target phase AlPO-5 with berlinite and cristobalite impurities. The goodness of fit is given by  $\chi^2$  values.*

Sieve	Phase fractions AlPO-5 /%	Phase fractions cristobalite /%	Phase fractions berlinite /%	$\chi^2$
0 % ions	23.5 (6)	20.7 (5)	55.8 (3)	2.557
5 % Fe	0	0	100	5.601
10 % Fe	0	0	100	5.784
15 % Fe	63.9	12.2 (2)	24	4.727
20 % Fe	80 (2)	0	20 (8)	5.443
50 % Fe	61 (7)	14.7 (9)	24 (1)	1.842
10 % Mn	23 (3)	37 (12)	40 (2)	2.068
20 % Fe (microwave)	53 (1)	46.7 (7)	0	1.331
20 % Fe 2 % alginate (microwave)	0	0	100	1.666

Table 3.23: AlPO-5 cell parameters derived from Le Bail refinement using GSAS of samples with the target phase AlPO-5 with berlinite and cristobalite impurities. The goodness of fit is given by  $\chi^2$  values.

AlPO-5		$a / \text{\AA}$	$b / \text{\AA}$	$\chi^2$
0 % ions	Uncalcined	13.615 (2)	8.498 (1)	1.363
	Calcined	13.702 (3)	8.541 (1)	2.581
15 % Fe	Uncalcined	13.54 (1)	8.34 (3)	3.282
	Calcined	13.191 (7)	8.602 (4)	2.314
20 % Fe	Uncalcined	13.679 (1)	8.4870 (9)	4.569
	Calcined	13.728 (2)	8.381 (1)	5.443
50 % Fe	Uncalcined	13.503 (6)	7.995 (7)	4.803
	Calcined	13.10 (2)	8.61 (2)	1.867
10 % Mn	Uncalcined	13.597 (6)	8.62 (2)	2.490
	Calcined	13.690 (4)	8.784 (2)	3.623
20 % Fe (microwave)	Uncalcined	13.683 (3)	8.524 (2)	1.712
	Calcined	13.48 (1)	8.37 (1)	1.121

The quality of fits varied widely between samples (Figure 3.15).

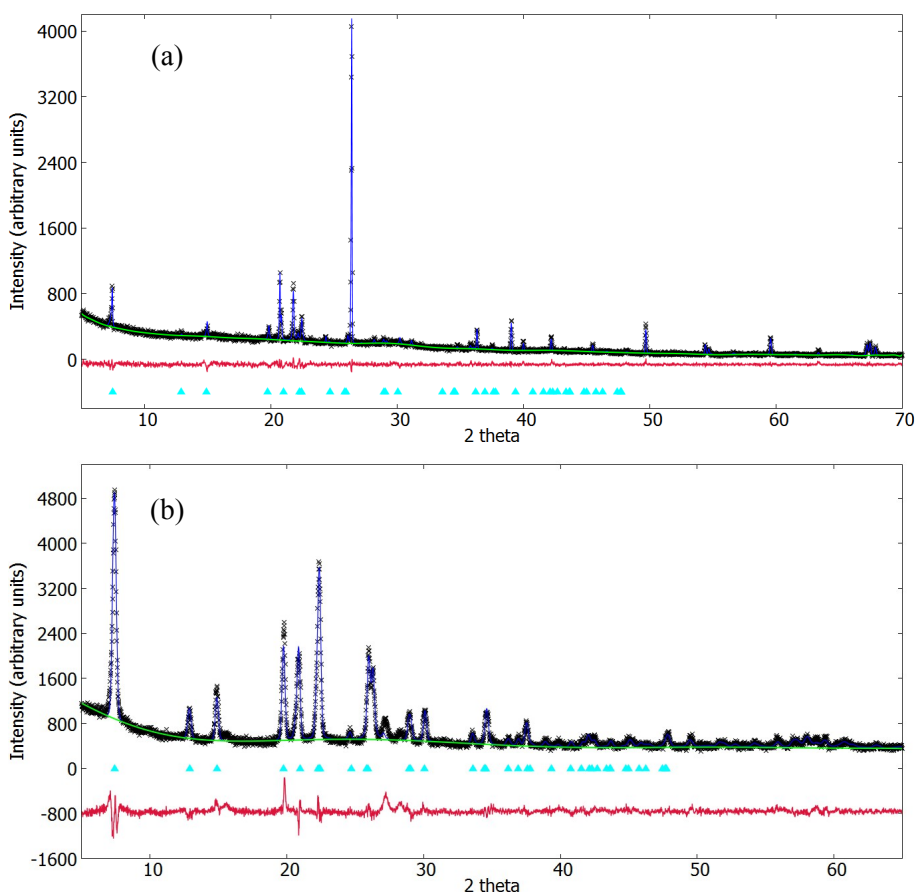
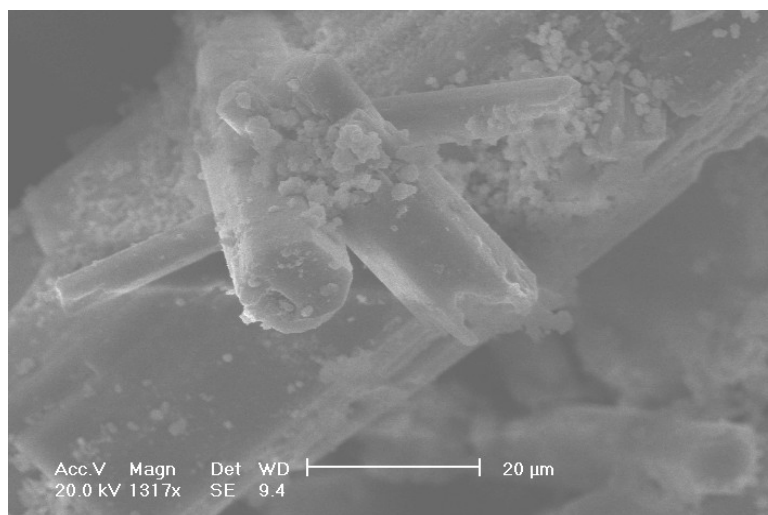


Figure 3.15: Le Bail refinement of samples (a) 0 % ion-doped uncalcined, and (b) 20 % Fe-doped uncalcined. Data are represented by black crosses, background by a green line, the fit with a blue line and the residual is presented below in red. Turquoise markers represent the AlPO-5 phase.

Phase fractions suggest that  $\sim 20\%$  doping is most likely to evolve the desired phase, whilst smaller amounts drive the evolution of a competitive berlinite phase. Cell parameters vary widely. Observable expansions of the unit cell are typical for successful inclusion of metal ions into the AlPO framework; however, the errors found between cell parameters here are large(117,191). In most samples, correlation between uncalcined and calcined sample cell parameters is adequate to justify using only the more easily refined calcined samples to determine phase fractions.

Scanning Electron Microscope images allow the long-range morphology of the AlPO to be examined. Images of AlPO-5 show rod-like hexagonal crystals  $\sim 10\ \mu\text{m}$  in diameter and varying lengths from at least  $20\ \mu\text{m}$  (Figure 3.16) in agreement with the observations of Cardile *et al.*, who additionally noted the presence of lozenge-shaped particles, which they assigned to amorphous impurity phases(192).



*Figure 3.16: SEM image of 20 % Fe-exchanged sample containing 80 % AlPO-5, 20 % berlinite.*

TGA indicates that  $< 1\%$  of the mass of one air-exposed, calcined 10 % Mn-loaded AlPO-5 is comprised of water (Figure 3.17 (b)). However, when an uncalcined 10 % Fe-loaded sample was measured, an 8 % weight loss was observed: some variation on the plot suggest that templating materials may also have been lost (Figure 3.17 (a)). Since the typical formula of AlPO-5 is  $\text{AlPO}_{4-x}\text{H}_2\text{O}$ ,  $x$  may be determined by TGA, such that here,  $x \sim 0.005$  and the mass of templates constitutes  $\sim 7.6\%$  of the AlPO-5 mass.

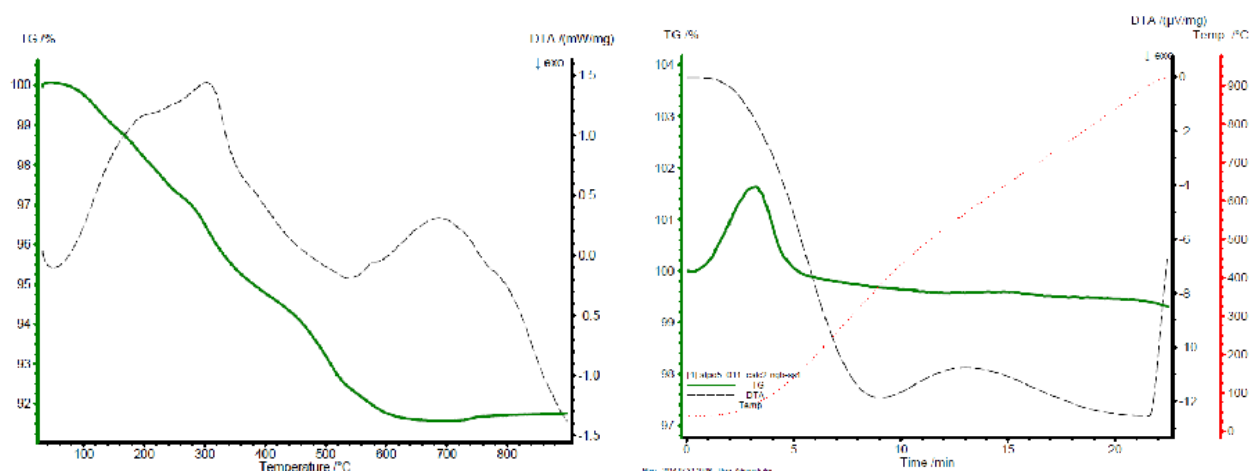


Figure 3.17: TGA data of samples containing AlPO-5: (a) uncalcined 10 % Fe-loaded, (b) calcined 10 % Mn-loaded.

Calibrated XRF spectroscopy data were gathered from representative samples formed into fused beads (Table 3.24). Calcined 10 % Fe-, 20 % Fe- and 10 % Mn-loaded samples of AlPO-5 took up 1.2, 0.5 and 2.3  $\text{mg}_{\text{Cr}}/\text{g}_{\text{sieve}}$  respectively, whilst uncalcined 10 % Fe-, 20 % Fe- and 10 % Mn-loaded samples of AlPO-5 will take up 1.9, 0.6 and 3.3  $\text{mg}_{\text{Cr}}/\text{g}_{\text{sieve}}$  respectively. Uptake is lower in the uncharged AlPO-5 systems than for anionic aluminosilicate zeolites, towards which metal ions are electrostatically attracted. Framework positions are also harder to access and harsher conditions are required to introduce metals. Although differences are small, Mn-loaded samples recorded higher uptakes than Fe-loaded samples, possibly because Mn is less likely to have been oxidised under the synthesis conditions. After calcination, all Fe is likely to be non-redox active Fe(III). Uptake by calcined, Fe(III)-loaded samples may be attributed solely to surface adsorption. Noticeably, the 20 % Fe-loaded samples, which are 80 % AlPO-5 and 20 % berlinite, did not take up any significant amount of chromium, whilst 10 % Fe-loaded samples, which are 100 % berlinite, did take some up. The 10 % Mn-loaded samples, 23 % AlPO-5, 37 % cristabiolite and 40 % berlinite, took up the most (Table 3.24). Uptake may not be driven by the AlPO-5 phase.

0.5-0.6  $\text{mg}_{\text{Cr}}/\text{g}_{\text{sieve}}$  was measured for materials which had not yet been exposed to chromate solution. Since no Cr content is anticipated in these samples, these numbers suggest that a baseline chromium content is measured for the AlPOs by XRF, *i.e.* a systematic error, probably arising in the calibration, such that values are likely to be quoted 0.5-0.6  $\text{mg}_{\text{Cr}}/\text{g}_{\text{sieve}}$  higher than the actual content.

Table 3.24: XRF spectroscopy data from calibrated fused beads of AIPO samples. The 10 % Fe AIPO consists of 100 % berlinite phase; the 20 % Fe AIPO consists of 80 % AIPO-5 and 20 % berlinite phases; and the 10 % Mn AIPO consists of 23 % AIPO-5, 40 % berlinite and 37 % cristobalite phases (Table 3.22). M = Fe or Mn. The numbers marked in red should be 0 and represent the zero error.

Sieve		Al/P	M/P	mg <sub>M</sub> /g <sub>sieve</sub>	mg <sub>Cr</sub> /g <sub>sieve</sub>
Uncalcined 10 % Fe AIPO	Pre-Cr treatment	1.01	0.13	49.5	0.5
	Post Cr-treatment	1.04	0.12	48.4	1.9
Calc 10 % Fe AIPO	Pre-Cr treatment	1.04	0.13	50.8	0.5
	Post Cr-treatment	0.85	0.16	68.6	1.2
Uncalcined 20 % Fe AIPO	Pre-Cr treatment	1.00	0.09	34.3	0.6
	Post Cr-treatment	1.06	0.08	30.1	0.6
Calcined 20 % Fe AIPO	Pre-Cr treatment	1.05	0.05	19.7	0.5
	Post Cr-treatment	1.05	0.05	18.0	0.5
Uncalcined 10 % Mn AIPO	Pre-Cr treatment	1.04	0.12	44.9	0.6
	Post Cr-treatment	0.97	0.13	51.3	3.3
Calcined 10 % Mn AIPO	Pre-Cr treatment	1.10	0.12	43.9	0.5
	Post Cr-treatment	1.11	0.12	43.6	2.3

The XRF spectroscopic data for chromium uptake by microwave samples was similar to those prepared hydrothermally (Table 3.25). The introduction of additional 2 % alginate LF20/40 template leads to 100 % berlinite product and an increased uptake of chromium on the uncalcined but not the calcined sample. This may be tentatively attributed to adsorption onto the template.

Table 3.25: XRF spectroscopy data from calibrated fused beads of microwave synthesised 20 % Fe-loaded AIPO samples. consisting of 53 % AIPO-5 and 47 % cristobalite phases (untemplated sieve), and 100 % berlinite phase (10 % templated sieve), (Table 3.19). M = Fe or Mn. The numbers marked in red should be 0 and represent the zero error.

Sieve		Al/P	M/P	mg <sub>M</sub> /g <sub>sieve</sub>	mg <sub>Cr</sub> /g <sub>sieve</sub>
Untemplated	Uncalcined pre Cr-treatment	0.80	0.29	117.7	0.7
	Uncalcined post Cr-treatment	0.84	0.27	107.2	1.5
	Calcined post Cr-treatment	0.84	0.27	108.5	1.6
10 % templated	Uncalcined pre Cr-treatment	0.87	0.21	85.1	0.6
	Uncalcined post Cr-treatment	0.91	0.21	84.7	7.0
	Calcined post Cr-treatment	0.94	0.22	85.4	1.2

### AIPO-Fe23

“AIPO-Fe23” is an Fe(II)- and Fe(III)-containing LAU open-framework aluminium phosphate belonging to C2c space group and comprised of distorted FeO<sub>4</sub>(H<sub>2</sub>O)<sub>2</sub> octahedra, having the formula [Fe(II)Fe(III)<sub>0.8</sub>(H<sub>2</sub>O)<sub>2</sub>Al<sub>1.2</sub>(PO<sub>4</sub>)<sub>3</sub>].H<sub>3</sub>O(137,163). The original paper by Peng *et al.*

records the synthesis of a mixed phase product, of which 15 % of the iron belongs to purple-red rhombus crystals separated out under an optical microscope – AlPO-Fe23(163). This sieve is of interest because of its potential for supplying redox-active Fe(II) ions and the challenge of phase pure synthesis. Varying reaction times, temperature, pressure, pH and the ratios of reactants allows for systematic phase condition investigation and crystal morphology control. This has been well documented for other AlPO systems and was attempted here. Although phase pure synthesis was not successful, results of the investigation are discussed.

Cell parameters are provided in Table 3.26: Rietveld refinement against an Fe(II) chloride sample prepared by heating to 180 °C for 5 days at the maximum capacity of the reaction vessel (*i.e.* highest available pressure)(163).

*Table 3.26: AlPO-Fe23 cell parameters derived from Rietveld refinement using GSAS of a sample prepared using Fe(II) chloride at a maximum vessel fill and heating to 180°C for 5 days. Comparison to literature values.*

Parameter	Values Obtained	Literature Value
$a / \text{\AA}$	13.67(1)	13.320(1)
$b / \text{\AA}$	10.301(4)	10.210(1)
$c / \text{\AA}$	8.657(4)	8.8412(9)
$\beta / ^\circ$	107.37(5)	108.590(2)

Phase fractions could not be produced as the main competing phase or mixture of phases was not identified using the EVA software Search and Match function, but several AlPO or phosphate hydrates showed similar patterns. A simulation of phase pure AlPO-23 is shown in Figure 3.18. The original paper makes no effort to identify competing crystal phases or investigate the conditions under which they form.

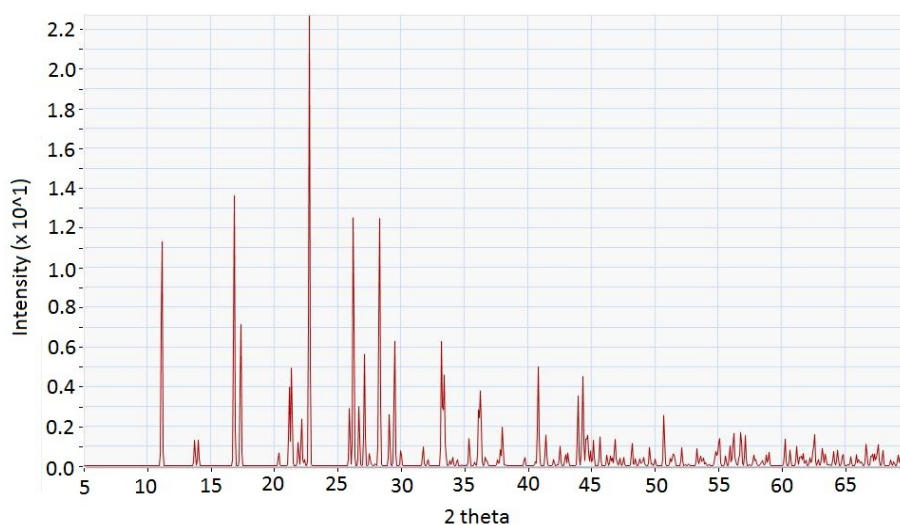


*Figure 3.18: Simulated PXRD pattern of the AlPO-23 phase using CrystalMaker software.*

Inspection across PXRD data showed substantial differences in phase proportions and peak intensities, even between samples prepared under the same reaction conditions (Figure 3.19). Variations in peak intensities could be due to the presence of water that naturally inhabits the pore network.

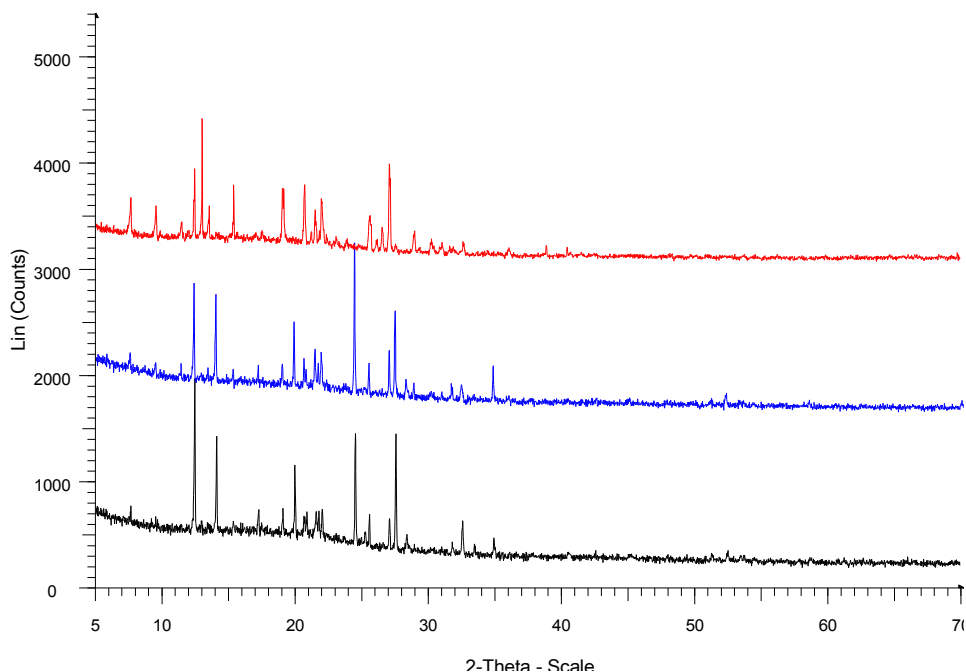


Figure 3.19: PXRD patterns of three samples with the target phase AlPO-Fe<sub>23</sub> that were separately prepared under the same conditions: using Fe(II) chloride starting material and a full vessel, heating to 180 °C for 5 days.

The desired AlPO-Fe<sub>23</sub> phase was synthesised in the majority of prepared samples. Samples prepared with Fe(II) chloride, Fe(II) sulfate and Fe(II) acetate all produced the target product and same impurity phases. As a result of variations in phase proportions, no preferable Fe(II) source could be identified.

Pressure in the reaction vessel was controlled by filling the autoclave by different amounts.

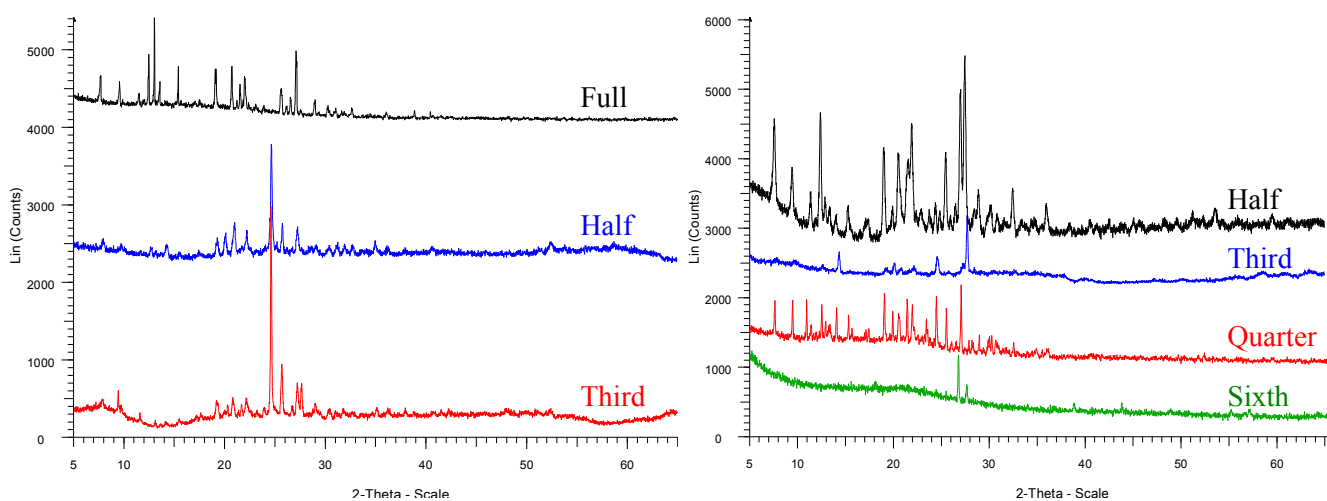
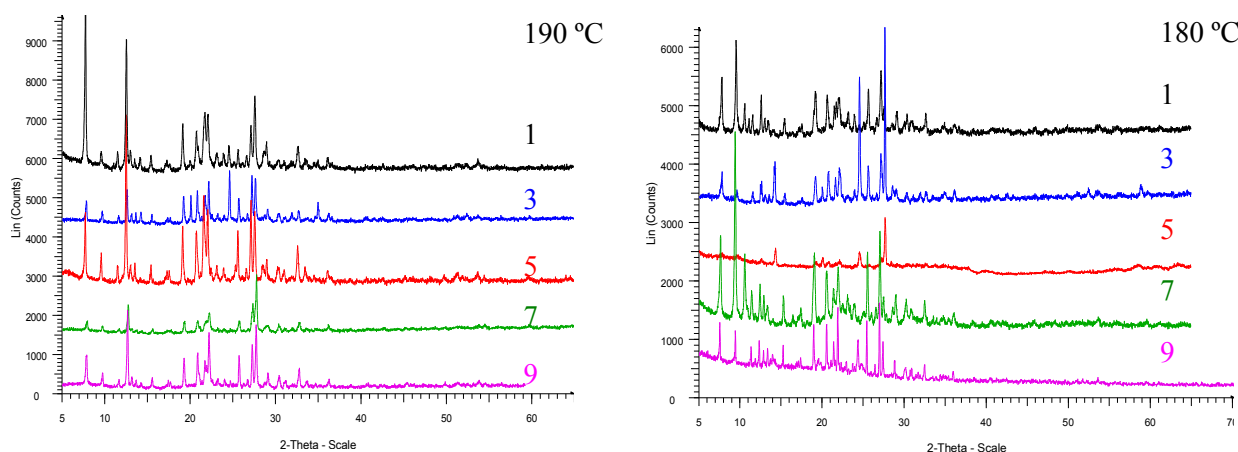


Figure 3.20: PXRD patterns of samples with the target phase AlPO-Fe<sub>23</sub> prepared under the same conditions except for vessel fill. Left: samples prepared from Fe(II) chloride at full (black), half (blue) and third (red) filled vessels. Right: samples prepared from Fe(II) acetate at half (black), third (blue), quarter (red) and sixth (green) filled vessels. All samples were prepared by heating to 180 °C for 5 days.

Normally, a maximum fill of 50 % allows for the vaporisation of solvents and development of hydrothermal pressure during reaction without warping the Teflon liner. In these experiments, smaller volumes, discussed as fractions of the maximum fill, have been explored to assess their impact on phase development. Examining a range of samples prepared from both Fe(II) chloride and Fe(II) acetate starting materials, [Figure 3.20](#) suggests that samples with a lower pressure (lower fill) demonstrated increased amorphous character and more competing phases: a higher pressure reaction condition is preferable for the formation of AlPO-Fe23.

To vary reaction times, samples were heated for between 1 and 9 days (with 5 days in the original synthesis). Two temperatures, 180 °C and 190 °C, are compared across this series ([Figure 3.21](#)). All samples were prepared from Fe(II) acetate starting material at a lower vessel pressure, one third of the maximum capacity.



*Figure 3.21: PXRD patterns of samples with the target phase AlPO-Fe23 prepared under the same conditions except for reaction time: heating a mixture prepared with Fe(II) acetate to 190 °C (left) or 180 °C (right) and at one third of the vessel fill. Reaction times were 1 (black), 3 (blue), 5 (red), 7 (green) and 9 (pink) days from top to bottom.*

These results suggest that the proportions of competing phases do not vary in any systematic way across the heating range 1-9 days. The samples prepared at 180 °C, however, seem to be generally richer in the target phase than their analogues at 190 °C, suggesting that a lower synthesis temperature is favoured. As such, a slightly higher temperature (200 °C) and a lower temperature (150 °C) were compared ([Figure 3.22](#)). The 200 °C was prepared with Fe(II) chloride at half the vessel capacity whilst the 150 °C sample was prepared with Fe(II) acetate at quarter the vessel capacity. Both samples were heated for 5 days. Whilst the target phase readily forms across all heating times at 190 °C, at 200 °C only trace amounts of AlPO-Fe23 form; the pattern is dominated by the formation of AlPO<sub>4</sub>-20, a cubic aluminium phosphate which does not appear as an impurity phase in any other patterns. Lowering the temperature to 150 °C renders the evolution of more competing phases with decreased peak intensities and poor quality crystallinity.

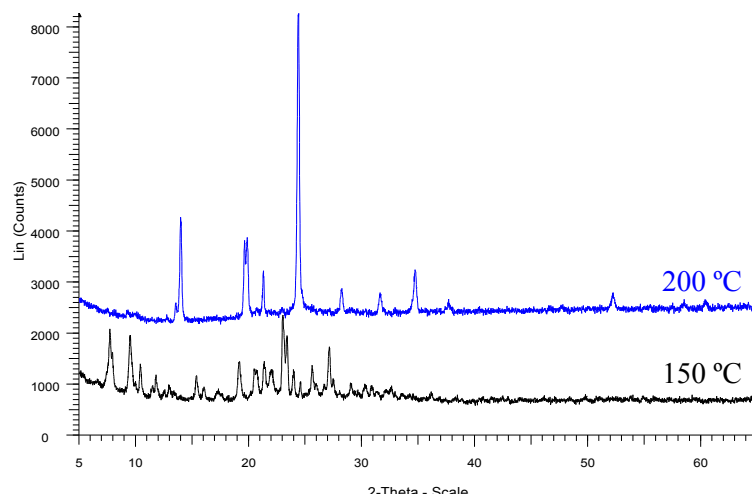


*Figure 3.22: PXR D patterns of two samples with the target phase AlPO-Fe<sub>23</sub> prepared at high and low temperatures: 200 °C for 5 days, from Fe(II) chloride at half the vessel fill (blue) and 150 °C for 5 days, from Fe(II) acetate at quarter the vessel fill (black).*

Microwave synthesis of AlPO-Fe<sub>23</sub> was not successful; although small amounts of the target phase formed, conditions favoured formation of the main competing phase/s and an amorphous phase, especially with longer heating times of 4 rather than 0.5 hours. PXR D patterns were very poor quality, with a number of missing peaks and a high background, especially at low angle.

SEM images were taken of one sample with the target phase AlPO-Fe<sub>23</sub> prepared using Fe(II) acetate and heating to 190 °C for 3 days at one third the maximum capacity of the reaction vessel. The images show plate-like crystals of ~ 5-60 μm in diameter clustered together into larger particles on the order of 100 μm (Figure 3.23).

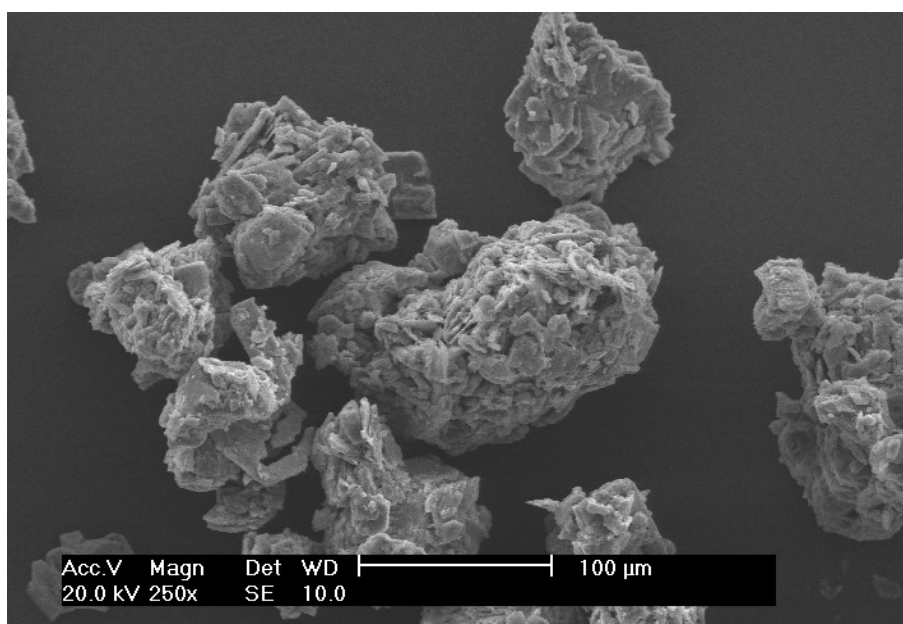


*Figure 3.23: SEM image of one sample with the target phase AlPO-Fe<sub>23</sub>, prepared using Fe(II) acetate and heating to 190 °C for 3 days at one third fill.*

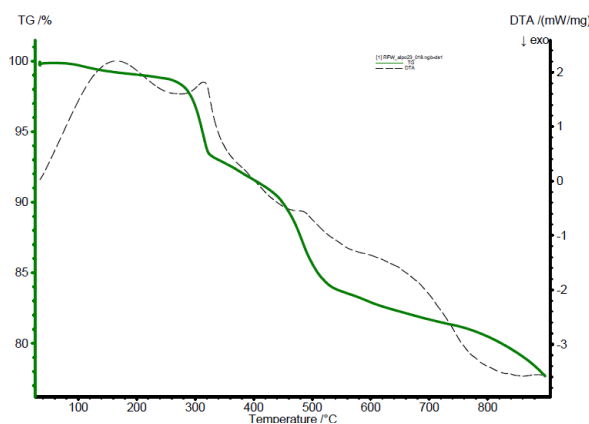


Figure 3.24: TGA plot of sample with the target phase AlPO-Fe<sub>23</sub>, prepared using Fe(II) acetate and heating to 180 °C for 2 days at one third fill.

One sample with the target phase AlPO-Fe<sub>23</sub> demonstrated a 22 % loss in mass under TGA. Inspection of the plot identifies three weight loss steps: 7 %, 10 % and 5 %. Different species were given off and thus the loss cannot all be attributed to water (Figure 3.24). Likely contributors include the imidazole template, ammonia from cations in the templates and acetates from the anions accompanying reactant iron (Figure 3.24). The original paper reported a one-step weight loss of 12.5 % from manually separated AlPO-Fe<sub>23</sub> crystals and noted an absence of ammonium ions occluded in the pores: the additional weight loss may be attributed to breakdown of impurity phases.

XRF spectroscopy data were collected from calibrated fused beads of two samples with the target phase AlPO-Fe<sub>23</sub>: sample 1 was prepared by heating with Fe(II) acetate to 190 °C for 3 days at a third the maximum vessel capacity; sample 2 was prepared by heating with Fe(II) acetate to 180 °C for 9 days at a third the maximum vessel capacity (Table 3.27). Chromium uptake was barely significant above background levels and not appreciably different between the two samples.

Table 3.27: XRF spectroscopy data from calibrated fused beads of two samples with the target phase AlPO-Fe<sub>23</sub>. Sample 1 was prepared by heating to 190 °C for 3 days and sample 2 was prepared by heating to 180 °C for 9 days. Both were prepared from Fe(II) acetate and filled one third of the vessel capacity. The numbers marked in red should be 0 and represent the zero error.

Sieve		Al/P	Fe/P	mg <sub>Fe</sub> /g <sub>sieve</sub>	mg <sub>Cr</sub> /g <sub>sieve</sub>
Sample 1	Pre-Cr treatment	0.58	0.22	85.8	0.5
	Post Cr-treatment	0.68	0.24	90.9	0.7
Sample 2	Pre-Cr treatment	0.65	0.21	79.0	0.6
	Post Cr-treatment	0.71	0.22	80.8	0.8

### LAU AIPO

A LAU-zeotype AIPO was prepared according to the method proposed by Guo *et al.*, who claim that the sample with empirical formula  $(C_3N_2H_5)_8(Fe_8Al_{16}P_{24}O_{96})$  is Fe(II)-substituted despite harsh de-templation conditions(164). This material is sensitive to the synthesis method, competing with other phases. PXRD of the sample refinement using GSAS suggested a three-phase pattern in agreement with the patterns reported in the literature (Figure 3.25). Rietveld refinement against the data was performed with the same Co-APO-LAU model with  $C2c$  space group used by the authors and the most common impurity, Fe-APO-CJ50 (Table 3.28)(193). The third phase was identified using EVA Search and Match software and fitted the structure of an ammonium cyclooctaphosphate  $((NH_4)_8P_8O_{24} \cdot 3H_2O)$ (194).

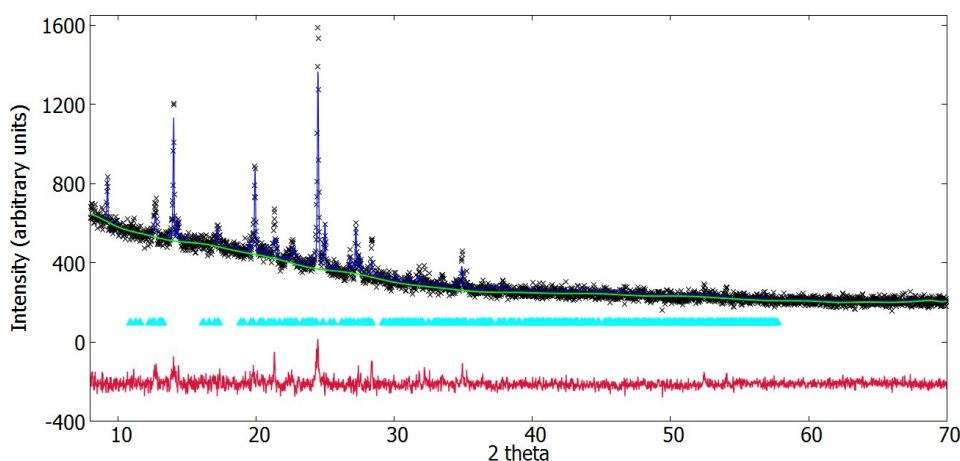


Figure 3.25: Rietveld refinement of one non-chromate-exposed calcined sample with the target LAU-zeotype AIPO phase and Fe-APO-CJ50 and ammonium cyclooctaphosphate impurities. Data are represented by black crosses, background by a green line, the fit with a blue line and the residual is presented below in red.

Cell parameters suggest some cell expansion occurs upon Cr-exposure as pore channels expand to allow the ready transport of ions through the network. The quality of PXRD of the LAU AIPO was compromised by exposure to chromate solution.

Table 3.28: Phase fractions and LAU-zeotype AIPO cell parameters derived from Rietveld refinement using GSAS of one sample with a target LAU-zeotype AIPO phase and Fe-APO-CJ50 and ammonium cyclooctaphosphate impurities. The goodness of fit is given by  $\chi^2$  values.

LAU AIPO	LAU AIPO phase %	Fe APO-CJ50 phase %	$(NH_4)_8P_8O_{24} \cdot 3H_2O$ phase %	$a / \text{\AA}$	$b / \text{\AA}$	$c / \text{\AA}$	$\chi^2$
Pre-Cr exposure	49.7 (8)	12 (1)	37.4 (8)	14.667 (3)	12.952 (4)	15.092 (4)	1.641
Post-Cr exposure	53 (1)	0	47 (1)	14.701 (6)	12.972 (9)	15.215 (8)	1.407

TGA of the LAU AIPO suggests three distinct weight loss steps (Figure 3.26). Guo *et al.* report a 0.5 % weight loss between 300 and 473 K corresponding to water, followed by a 15.0 % weight loss up to 1073 K corresponding to the removal of imidazole templates(164). Figure 3.26 indicates a total weight loss of ~ 15 %, in agreement with this report, and ~ 1 % weight loss < 200 °C due to water. However, the third weight loss step remains unaccounted for: it is possible that it corresponds to the decomposition of one of the impurity phases.

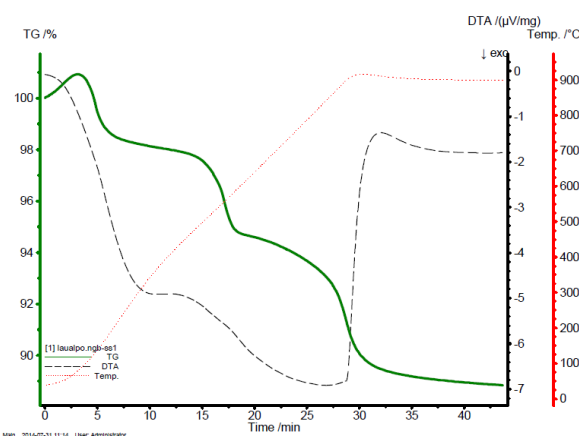


Figure 3.26: TGA plot of one sample with the target LAU-zeotype AIPO phase and Fe-APO-CJ50 and ammonium cyclooctophosphate impurities.

XRF spectroscopy data were collected from calibrated fused beads of LAU AIPO, which measure only 0.8 mg<sub>Cr</sub>/g<sub>sieve</sub>, despite a high Fe loading (Table 3.29). This implies that at least some oxidation of Fe(II) to Fe(III) has taken place, rendering the sieve non-redox active.

Table 3.29: XRF spectroscopy data from calibrated fused beads of samples with the target LAU-zeotype AIPO phase, and Fe-APO-CJ50 and ammonium cyclooctophosphate impurities, where M = Fe or Mn.

Sieve	Al/P	Fe/P	mg <sub>Fe</sub> /g <sub>sieve</sub>	mg <sub>Cr</sub> /g <sub>sieve</sub>
Pre Cr-treatment	0.67	0.36	130.2	0.5
Post Cr-treatment	0.65	0.38	132.3	0.8

These numbers are in agreement with Guo *et al.* who report a 1:1 ratio of (M + Al)/P (1.03 and 1.03 here) and 1:2 ratio of M/Al (0.53 and 0.57 here)(164). These correspond to the empirical formulae (C<sub>3</sub>N<sub>2</sub>H<sub>5</sub>)<sub>6.2</sub>(Fe<sub>8.6</sub>Al<sub>16.2</sub>P<sub>24</sub>O<sub>96</sub>) and (C<sub>3</sub>N<sub>2</sub>H<sub>5</sub>)<sub>6.9</sub>(Fe<sub>9</sub>Al<sub>15.7</sub>P<sub>24</sub>O<sub>96</sub>) respectively for pre and post Cr-treatment samples.

### Summary

Uncharged AIPO frameworks cannot ion exchange so demonstrate lower chromium uptakes than zeolites. A baseline systematic error on XRF measurements of chromium content (~ 0.5 mg<sub>Cr</sub>/g<sub>sieve</sub>) exists in the calibration. AIPO-Fe23 is difficult to form, with the target phase favoured at higher pressures and 150 < T < 200 °C.

## Chapter 4: Mechanism for Chromium Uptake

This chapter employs XPS, Mössbauer and EPR spectroscopies to explore the oxidation states and coordination environments of iron and manganese ions present in selected molecular sieves from Chapter 3 and thus conclude the limitations to the use of these materials. The selected techniques allow for comparison between bulk and surface properties. The presence and distribution of surface fouling counter ions are investigated using EDS and attempts are made to treat the surface to reduce fouling. Systems loaded with Fe(III) rather than Fe(II) metal ions are prepared and their capacity for chromium uptake compared for the purpose of determining mechanistic steps that relate to the surface of the molecular sieves. A brief experiment studies pH dependence of chromium uptake. Some effort is made to determine chromium oxidation states and site symmetries compared with measurements in the literature.

### 4.1. Assigning Fe and Mn Sites

The metals found in molecular sieves may take one of three forms: framework ions, extraframework charge-compensating ions or agglomerates housed within the pore channels or adsorbed onto the external surface. In order to accurately determine the Fe and Mn oxidation states and coordination environments, EPR and Mössbauer spectroscopies were employed.

A large increase in XRD parameters between parent and ion-doped samples is usually indicative of framework substitutions, but smaller indistinct changes may be attributed to expansion of the framework upon ion exchange to allow the ready transport of ions through the pore network(180). Framework substitution may also be observed by changes in relative peak heights in well-dehydrated samples. If samples are not sufficiently dehydrated, variations in relative peak heights between samples may exceed these changes due to introduction of ions into framework positions. It is possible that surface agglomerates may be detected by XRD(195).

### *Colour*

Colour is a clear initial indicator of chemistry, but can also be misleading. The colour of a compound loaded with metal ions may differ depending upon the metal identity, its oxidation state and its location in the structure, *e.g.* whether it is framework or extraframework. In the literature, it is concluded that white samples of Fe-exchanged AlPOs contain negligible quantities of

extraframework ions, with Fe primarily in framework positions(196). Upon calcination, Fe framework substituted zeolites changed colour from white to pale brown(197).

Of the samples synthesised in this work, structures prepared with Fe(II) both during initial synthesis and ion exchanged post synthesis were green in colour, implying the presence of redox-active Fe(II) species in extraframework positions. Mn(II)-loaded structures were either pale pink (AlPOs with Mn introduced during the synthesis step) or pale brown (zeolites with Mn introduced post synthesis *via* ion exchange): these colours imply Mn(II) compounds with structural differences between them. However, these indicators do not exclude the presence of other metal species in different sites or with different oxidation states, *e.g.* Fe(III), and indeed sometimes the conclusions drawn from colour information may be inaccurate.

### ***Mössbauer Spectroscopy***

The most useful technique for probing oxidation state and coordination environment of iron ions in a material is Mössbauer spectroscopy. Whilst Mössbauer cannot clearly distinguish between framework, extraframework and occluded species, hyperfine parameters may give an indication of sensible coordination assignments(198,199). In zeolites and AlPOs, framework species would be tetra- rather than octahedral unless coordinated to additional water molecules within the pore network. Mössbauer spectroscopy parameters are distinct numbers that may be readily interpreted *via* comparison to similar systems (Figure 2.11). Most of the time, parameters fall close to model values and are not ambiguous to assign.

Air-exposed Fe-loaded zeolite X (Figure 4.1 (a), Table 4.1) was best fitted to two Lorentzian doublets, corresponding to one octahedral Fe(III) and one octahedral Fe(II) site, with  $\chi^2 = 0.643055$ . Whilst other zeolite and phosphate systems have produced spectra best fitted to one Fe(III) and *two* octahedral Fe(II) environments (one more and one less distorted) there is no physical justification for assuming two octahedral Fe(II) environments in these samples(200,201). The fitted peaks corresponded to Fe(II)/Fe(III) ions coordinated to both oxygen atoms from the zeolite framework and interstitial water molecules. In an air-exposed system where Fe ions were introduced post synthesis *via* ion exchange, only octahedral species are anticipated, as observed. Results demonstrate the extent to which iron ions introduced to the system undergo spontaneous aerial oxidation. The linewidth for Fe(II) is broad at 45 mm/s, implying a distribution of coordination environments greater than those of Fe(III). It is possible that Fe(III) is largely occluded on the surface or exists as oxides within the pore network, whilst Fe(II) ions coordinate to water molecules: flexible Fe-O<sub>water</sub> bonds lend distortion to the system and thus produce higher quadrupole

splitting parameters. The Fe(III) linewidth also narrows, but less significantly.

The spectrum of a dehydrated Fe-loaded zeolite X was fitted to two Lorentzian doublets corresponding to octahedral Fe(II) and Fe(III) sites with  $\chi^2 = 1.23464$  (Figure 4.1 (b), Table 4.1). Although site populations are unchanged upon dehydration, a significant increase is seen in the linewidth and quadrupole splitting parameters for Fe(II). This corresponds to a narrower range of more distorted Fe(II) environments, consistent with a loss of water molecules from around Fe(II). Supporting these conclusions, the Fe(II) linewidth narrows upon dehydration (Table 4.1) and must be fixed at 0.21 mm/s to prevent it from dropping below the natural linewidth of iron.

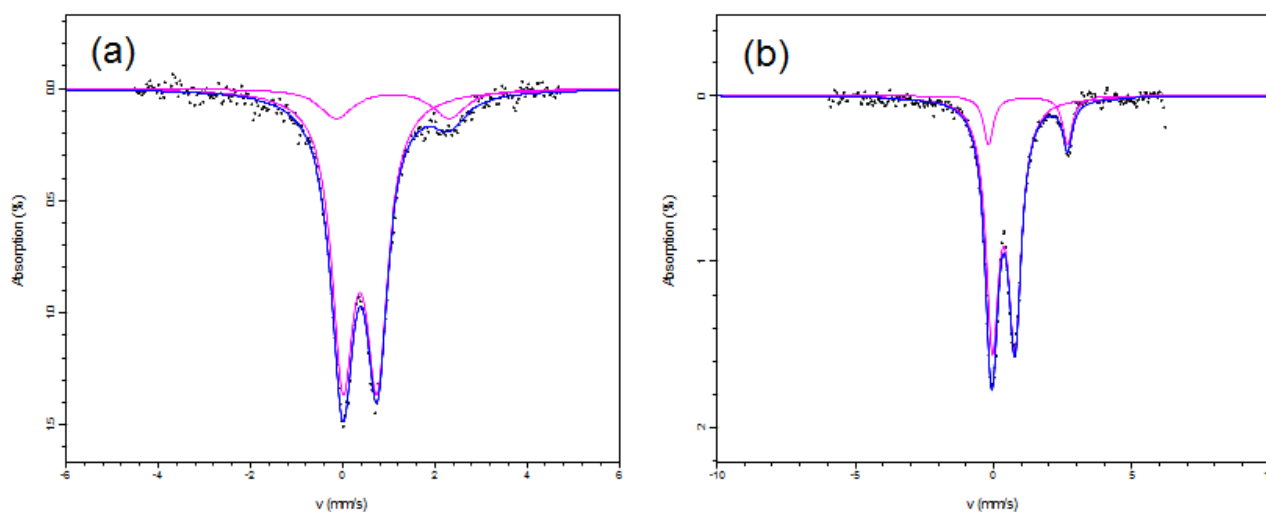


Figure 4.1: Mössbauer spectra of (a) hydrated air-exposed Fe-loaded zeolite X, and (b) dehydrated Fe-loaded zeolite X.

Table 4.1: Mössbauer parameters of hydrated air-exposed Fe-loaded zeolite X,  $\chi^2 = 0.643055$ , and dehydrated Fe-loaded zeolite X,  $\chi^2 = 1.23464$ . Fixed (unrefined) parameters are marked with \*. Uncertainties are calculated using the covariance matrix. The uncertainty in the natural linewidth of Fe is  $\pm 0.02$  mm/s; values quoted beyond 2 dp are included only to show precision uncertainties.

Zeolite X	Species	Peak	Site population /%	IS /mm/s	QS /mm/s	Linewidth / mm/s
Hydrated	Octahedral Fe (III)	Doublet	86 (2)	0.378 (8)	0.74 (1)	0.286 (9)
	Octahedral Fe (II)	Doublet	14 (4)	1.09 (9)	2.44 (18)	0.45 (12)
Dehydrated	Octahedral Fe (III)	Doublet	86 (1)	0.371 (6)	0.81 (1)	0.278 (8)
	Octahedral Fe (II)	Doublet	14 (1)	1.26 (2)	2.86 (5)	0.21*

One air-exposed Fe-exchanged sample, consisting of 70 % zeolite A and 30 % zeolite X (Table 3.2) was also studied by Mössbauer spectroscopy. The spectrum was best fitted to two Lorentzian doublets, octahedral Fe(II) and Fe(III) (19 % and 81 % respectively), with  $\chi^2 = 0.654635$  (Figure 4.2, Table 4.2). Within error, these site populations are comparable to those of pure zeolite X. However, narrower linewidths and lower quadrupole splitting parameters suggest a narrower distribution of coordination environments and less distorted coordination spheres,

consistent with the restrictions imposed on ion environments by the smaller pore cavities of zeolite A (A 4-5 Å, X ~ 8Å). These restrictions could also explain the lower chromium uptake of zeolite A than X (Tables 3.5 and 3.8) despite similar Fe(II) loadings, *i.e.* structural restrictions.

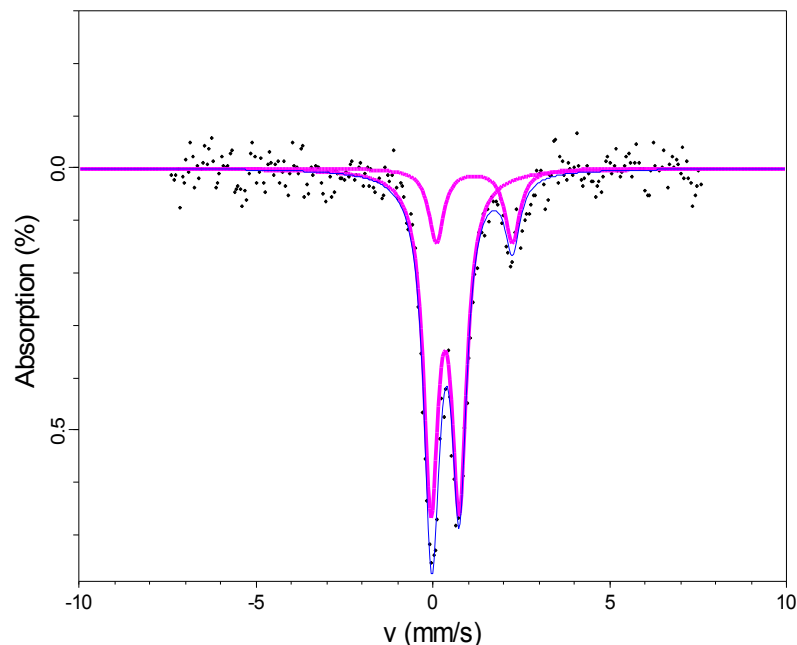


Figure 4.2: Mössbauer spectrum of hydrated air-exposed Fe-loaded zeolite, of 70 % A and 30 % X.

Data were not of sufficient quality to accurately distinguish between zeolite X and A environments for each iron species (Fe(II) and Fe(III)), and a fit with four Lorentzian doublets would have provided parameters carrying a large error. The distribution of environments overlaps between zeolites.

Table 4.2: Mössbauer parameters of hydrated air-exposed Fe-loaded zeolite, of 70 % A and 30 % X,  $\chi^2 = 0.654635$ . Uncertainties are calculated using the covariance matrix. The uncertainty in the natural linewidth of Fe is  $\pm 0.02$  mm/s.

Species	Peak	Site population /%	IS /mm/s	QS /mm/s	Linewidth /mm/s
Octahedral Fe (III)	Doublet	81 (5)	0.35 (2)	0.80 (3)	0.25 (2)
Octahedral Fe (II)	Doublet	19 (6)	1.18 (7)	2.15 (14)	0.25 (10)

A sample of natural zeolite containing clinoptilolite was best fitted to two Lorentzian doublets, Fe(II) and Fe(III) (23 % and 77 % respectively), with  $\chi^2 = 0.655869$  (Figure 4.3, Table 4.3). Although these data suggest higher populations in Fe(II) sites than zeolites X and A, the data is lower in quality such that errors are larger and parameters less trustworthy.

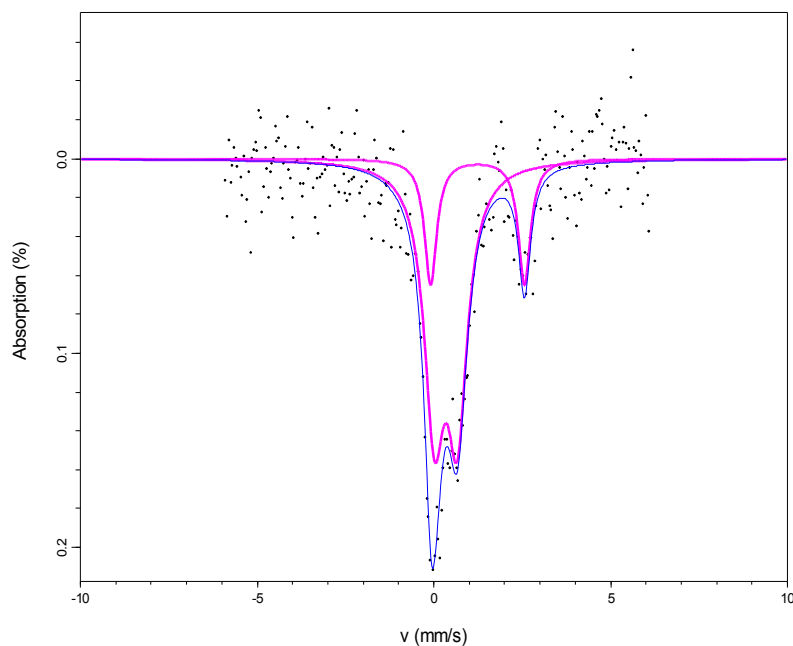


Figure 4.3: Mössbauer spectrum of hydrated air-exposed Fe-loaded natural zeolite containing clinoptilolite.

Table 4.3: Mössbauer parameters of hydrated air-exposed Fe-loaded natural zeolite containing clinoptilolite,  $\chi^2 = 0.655869$ . Uncertainties are calculated using the covariance matrix. The uncertainty in the natural linewidth of Fe is  $\pm 0.02$  mm/s.

Species	Peak	Site population /%	IS /mm/s	QS /mm/s	Linewidth /mm/s
Octahedral Fe (III)	Doublet	77 (10)	0.34 (6)	0.65 (9)	0.35 (8)
Octahedral Fe (II)	Doublet	23 (9)	1.24 (8)	2.66 (15)	0.21 (10)

Narrow linewidths suggest that ions are not distributed across a range of sites, but exist in distinct coordination environments. The very low quadrupole splitting parameter of the Fe(III) doublet is consistent with a highly symmetrical environment and rigidly contained ions: some of these may correspond to Fe ions present in the parent natural clinoptilolite zeolite sample before the ion exchange modification. Naturally occurring Fe may be locked into inaccessible sites in the pore network, where it is coordinated to oxygen atoms both in framework sites and belonging to water molecules. Alternatively, Fe species may be present as occluded oxides, sulfates, acetates or chlorides, depending upon the counter ions present in the starting materials and extent of aerial exposure. Concepcion-Rosabal *et al.* identified the presence of Fe(II) and Fe(III) sulfates in natural clinoptilolite samples *via* Mössbauer spectroscopy when prepared with iron sulfates, but did not observe chloride occlusions for those samples prepared with iron chlorides(183). The ratio  $\text{mg}_{\text{Cr}}/\text{mg}_{\text{Fe}}$  in the natural zeolite sample is 0.35 (Table 3.11, Equation 4.4), similar to the ratio in zeolite X (0.32) (Table 3.8). This implies that chromium uptake is dependent upon iron content and that Fe ions are available to facilitate uptake. Sulfate ions are not considered a significant

hindrance(41).

There is a possibility of framework substitutions amongst AIPO systems, for which the transition metals were incorporated during synthesis. Framework species are distinguished by tetrahedral environments with isomer shifts  $< 0.3$  mm/s, although the observation of an increasing tetrahedral signal upon dehydration implies that some framework positions may be obscured by higher coordination to extraframework water molecules (Figure 2.11). Equally, the reported limiting framework substitution of  $\sim 3\%$  Fe may be unreliable(107,192). In addition, the site of substitution is hard to assign. Although the majority view is that iron substitutes inhomogeneously for aluminium, Prakash *et al.* have proposed the phosphorus site, claiming that specific site analysis better supports this assignment, in contrast with bulk analysis(202). This has not been conclusively disproved.

One uncalcined air-exposed 20 % Fe-loaded AIPO consisting of 80 % AIPO-5 was best fitted to one Lorentzian doublet corresponding to octahedral Fe(III) with  $\chi^2 = 1.3812$  (Figure 4.4, Table 4.4). Whilst Brükner *et al.* fitted AIPO-5 to two octahedral Fe(III) sites, one more and one less distorted, that did not provide a good fit for this data(107). Iron is fully oxidised under the hydrothermal reaction conditions, even before the sample undergoes calcination. The narrow linewidth suggests a narrow distribution of coordination environments; *i.e.* all Fe exists in similar environments, most likely octahedrally coordinated to oxygen atoms from the zeolite framework and interstitial water molecules. Tetrahedral framework positions with additional Fe-O<sub>water</sub> coordinations cannot be ruled out. However, where as much as 25 % of the zeolite mass comprises of water,  $< 1\%$  of the mass of air-exposed AIPO-5 is water (Figure 3.17 (b)).

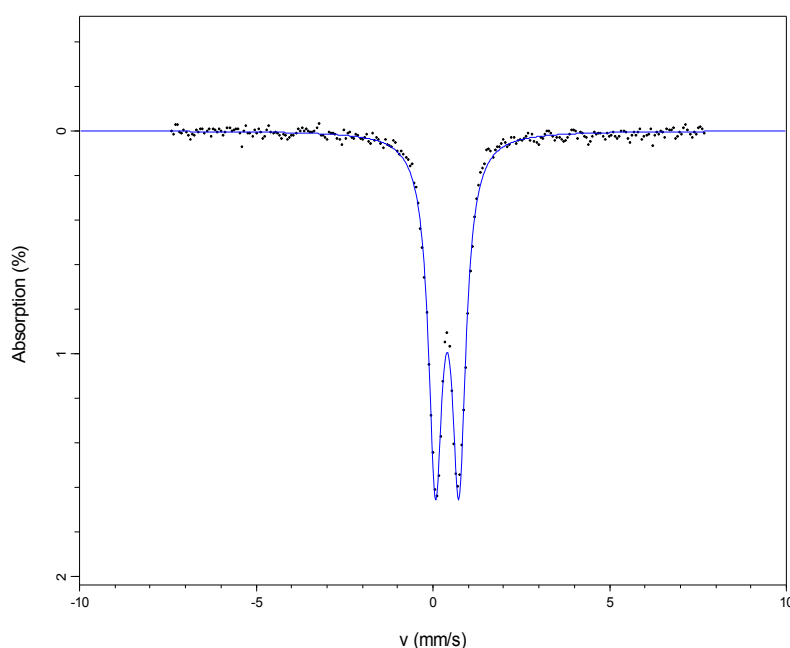


Figure 4.4: Mössbauer spectrum of one uncalcined air-exposed 20 % Fe-loaded sample containing 80 % AIPO-5.

Table 4.4: Mössbauer parameters of one uncalcined air-exposed 20 % Fe-loaded AIPO consisting of 80 % AIPO-5,  $\chi^2 = 0.643055$ . Uncertainties are calculated using the covariance matrix. The uncertainty in the natural linewidth of Fe is  $\pm 0.02$  mm/s: values quoted beyond 2 dp are included only to show precision uncertainties.

Species	Peak	Site population /%	IS /mm/s	QS /mm/s	Linewidth /mm/s
Octahedral Fe (III)	Doublet	100	0.402 (3)	0.665 (5)	0.235 (4)

Two air-exposed Fe(II)-loaded AIPO samples with the target phase AIPO-Fe23 were studied by Mössbauer spectroscopy. Sample (a) was prepared using Fe(II) acetate amongst the starting materials and heating to 190 °C for 3 days at one third the maximum capacity of the reaction vessel. Sample (b) was prepared similarly, but heated to 180 °C for 9 days. The spectra were fitted to two Lorentzian doublets, corresponding to Fe(III) and Fe(II) species.  $\chi^2$  values were 12.832 and 0.679687 respectively (Figure 4.5, Table 4.5). These values may reflect the quality of the background fit. Whilst some literature reports indicate that hydrothermal reaction conditions fully oxidise the AIPO materials they studied, the Mössbauer spectroscopy recorded here shows conclusively that samples with the target phase AIPO-Fe23 do contain Fe(II) in large fractions, in agreement with the cited paper(163,203). An optimal number of peaks cannot be determined because of the unidentified nature of the impurity phases in these species, and as such only one Fe(II) and one Fe(III) have been introduced. However, very narrow linewidths, especially for Fe(III) species which, left unfixed, drop well below the natural linewidth of iron, and low isomer shift and quadrupole splitting parameters imply the possibility of tetrahedral Fe species within the AIPO framework.

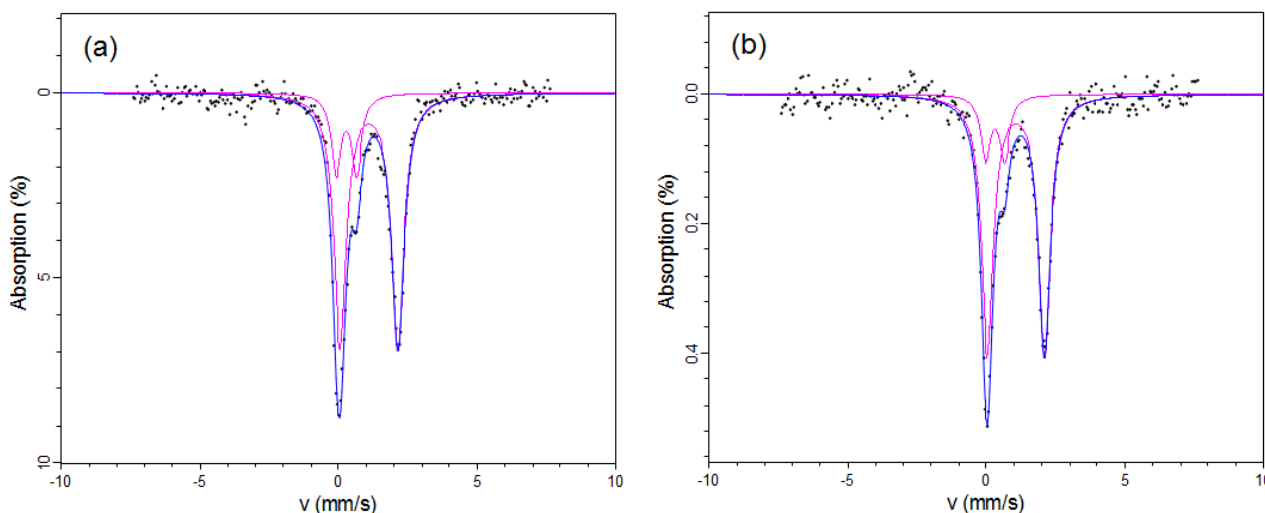


Figure 4.5: Mössbauer spectra of two air-exposed samples with the target phase AIPO-Fe23: (a) prepared with Fe(II) acetate and heated to 190 °C for 3 days at one third the vessel fill; (b) prepared with Fe(II) acetate and heated to 180 °C for 9 days at one third the vessel fill.

Table 4.5: Mössbauer parameters of two air-exposed samples with the target phase AlPO-Fe23: (a) prepared with Fe(II) acetate and heated to 190 °C for 3 days at one third the vessel fill,  $\chi^2 = 12.832$ ; (b) prepared with Fe(II) acetate and heated to 180 °C for 9 days at one third the vessel fill,  $\chi^2 = 0.679687$ . Fixed (unrefined) parameters are marked with \*. Uncertainties are calculated using the covariance matrix. The uncertainty in the natural linewidth of Fe is  $\pm 0.02$  mm/s: values quoted beyond 2 dp are included only to show precision uncertainties.

Sample	Species	Peak	Site population /%	IS /mm/s	QS /mm/s	Linewidth /mm/s
(a)	Fe (III)	Doublet	19.7 (5)	0.294 (7)	0.73 (1)	0.21*
	Fe (II)	Doublet	80.4 (9)	1.104 (2)	2.082 (5)	0.271 (4)
(b)	Fe (III)	Doublet	17 (2)	0.33 (7)	0.68 (15)	0.21*
	Fe (II)	Doublet	83 (4)	1.07 (2)	2.06 (4)	0.26 (2)

### EPR Spectroscopy

For species to be EPR active, they must be spin dilute. Where the concentration of EPR-active species is too high, the unpaired electrons couple between atoms and the signal is suppressed. The critical concentration depends upon the separation between ions and the presence of any effects such as clustering. The Fe-Fe separation may be easily estimated, assuming a uniform distribution of ions, as the cube root of the volume occupied by each ion, and predicts whether a sample has the potential for EPR activity. The volume occupied by each iron atom is calculated in m<sup>3</sup>:

$$V = \frac{Mr}{1000 \cdot d \cdot q \cdot A_r} \quad \text{Equation 4.1}$$

where  $d$  = density, 1.93 g/cm<sup>3</sup> for zeolite X

$Mr$  = molecular/atomic mass, 55.845 g/mol for Fe

$q$  = quantity of Fe in mg<sub>Fe</sub>/g<sub>sieve</sub>

$A_r$  = Avogadro's number,  $6.023 \times 10^{23}$

As a rule of thumb, species with separations  $> 10$  Å should be spin dilute. Table 4.6 suggests that Fe species in the framework have the potential to be spin dilute, assuming an even distribution. Thus any EPR spectra where hyperfine splitting is absent and a broad exchange signal at  $g \sim 2$  occurs is probably indicative of clustered ions rather than of proximity due to high loadings.

Table 4.6: Fe inter-ion distances calculated from Fe-loadings in  $\text{mg}_{\text{Fe}}/\text{g}_{\text{sieve}}$  using Equation 4.5.

Sieve	$q / \text{mg}_{\text{Fe}}/\text{g}_{\text{sieve}}$	$V / 10^{-26} \text{ m}^3$	Inter-ion distance / Å
Zeolite X before Cr exchange	2.09	2.30	28.4
Zeolite X after Cr exchange	1.69	2.84	30.5

Spectra are measured with an intensity scale against magnetic field (B). The precise g-value depends upon the frequency of the spectrometer, but may be calculated from B using the formula:

$$g = 714.484 \nu/B \quad \text{Equation 4.2}$$

where  $\nu$  is frequency in GHz

B is magnetic field in G

There is some disagreement in the literature on the appropriate attribution of EPR signals to ionic symmetry. However, the signal at  $g \sim 2$  is universally assigned to non-framework Fe(III) in symmetrical octahedral environments(81,147). Observations of the concentration dependence of the  $g \sim 2$  signal have led to the interpretation of electron exchange interactions between clustered Fe(III) ions in oxides formed at medium Fe loadings(202,204–206). The signal at  $g = 6$  is usually interpreted as Fe(III) ions in axially distorted environments(207). Where the  $g = 6$  signal is split, axial symmetry is imperfect. The signal at  $g = 4.3$  meanwhile, has been traditionally attributed to isolated Fe(III) ions in rhombically distorted tetrahedral framework positions in zeolites and AlPOs(81,147,179). Some variation in the peak position occurs: where the environment is more distorted, the peak may be observed at lower field. However, many authors firmly believe that the presence of the  $g = 4.3$  signal is not, by itself, adequate evidence for the presence of framework iron species, although it is “a necessary consequence of such a presence”, and could also be attributed to isolated Fe(III) ions in rhombically distorted *octahedral* environments(180,192,204–206). These conclusions are supported by the comparison between hydrated and dehydrated Fe-containing samples (Figure 4.6): a mixture of peaks appears in hydrated samples around  $4.4 < g < 2.4$ , which coalesce into a single  $g = 4.2$  peak upon dehydration. The dehydration conditions are sufficient to generate tetrahedrally coordinated extraframework Fe, rigidly bound to framework oxygens, but not to exclude water from the zeolite altogether. Thus dehydration drives ions into localised positions and lowers their coordination number. Mn(II) ions may exhibit coordination numbers as low as three when fully dehydrated and bound only to zeolite framework oxygen atoms(99). The mixture of signals strongly implies a distribution of symmetry environments and coordinations to water

molecules which, upon their removal, is simplified to a more distorted, more narrowly distributed coordination environment(205).

Noticeably, these Fe-loaded zeolite X samples (Figure 4.6) display no hyperfine splitting. This is not unexpected given the relative abundance of  $^{57}\text{Fe}$ . Hyperfine coupling arises from coupling between electron and nuclear spins, such that the electron spin levels split into  $2I + 1$  sub-levels, seen on the spectrum by splitting of the resonance line. Natural iron comprises of just 2.119 % of spin  $I = \frac{1}{2}$   $^{57}\text{Fe}$ , whilst  $^{56}\text{Fe}$  comprises 91.7 %, but has no nuclear spin ( $I = 0$ ) and thus is not EPR active. Thus the absence of hyperfine splitting does not inform us whether or not ions are clustered, although some exchange interactions are likely to occur, since ions will not be distributed completely homogeneously as assumed in calculations. Migration of cations may occur upon dehydration, increasing the probability of clusters.

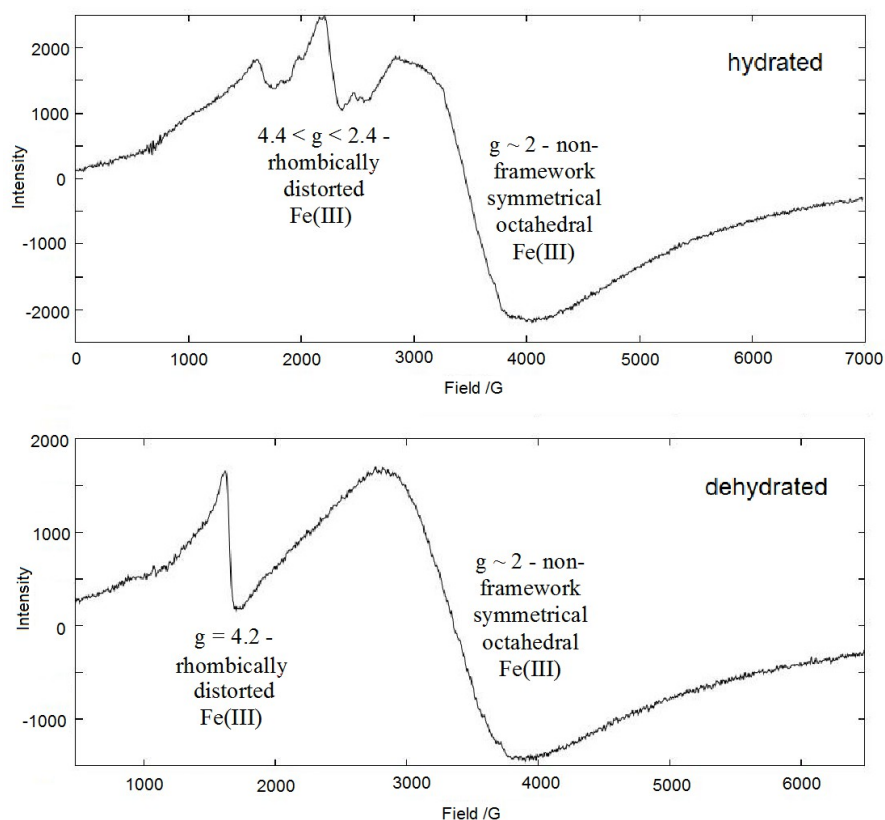


Figure 4.6: EPR spectra of top: hydrated air-exposed Fe-loaded zeolite X,  $\nu = 9.794445$  GHz; bottom: dehydrated Fe-loaded zeolite X,  $\nu = 9.795356$  GHz.

In contrast, manganese comprises 100 %  $^{55}\text{Mn}$ , which has a spin  $I = \frac{5}{2}$ , and thus readily demonstrates hyperfine splitting, producing six characteristic lines. However, Mn(II) ions are rarely homogeneously distributed, clusters lead to exchange interactions that suppress signal and the hyperfine splitting may not be observed, even at very low loadings. Some researchers have specifically prepared additional samples with lower Mn(II) loading ( $< 0.1$  %) for the purpose of

EPR investigation(208,209). In Figure 4.7, the spectrum of one Mn-loaded sample of zeolite X was recorded both before and after dehydration. The hyperfine lines are observed before dehydration, but disappear after dehydration, consistent with reports in the literature(202). These signals at  $1.9 < g < 2.2$  are assigned to Mn(II) framework/extraframework ions in undistorted cubic environments(210–212). The spin lattice relaxation times for Mn(III) are very fast and, as a consequence, these species are not EPR active.

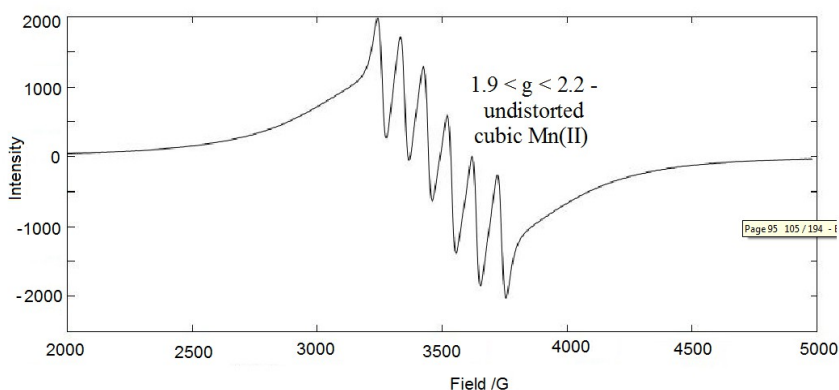


Figure 4.7: EPR spectrum of hydrated air-exposed Mn-loaded zeolite X,  $\nu = 9.794678$  GHz.

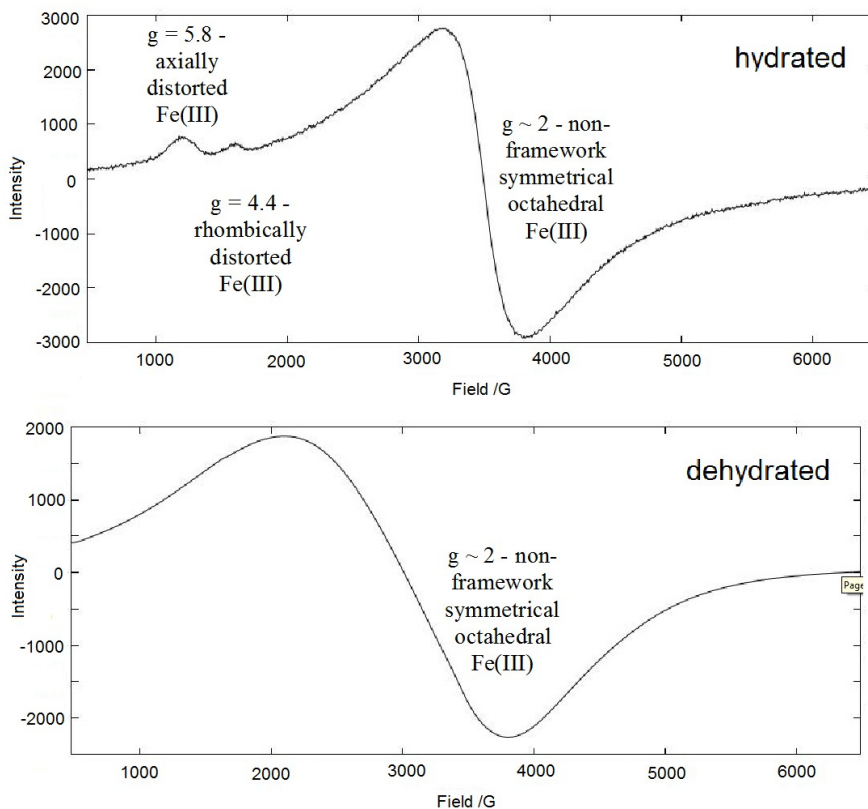


Figure 4.8: EPR spectra of Fe-loaded sample (c) from Table 3.2, which comprises of 68 % zeolite A and 32 % zeolite X. Top: hydrated air-exposed,  $\nu = 9.797449$  GHz; bottom: dehydrated,  $\nu = 9.795378$  GHz.

Fe-loaded sample (c) from Table 3.2, which comprises of 68 % zeolite A and 32 % zeolite X was measured both before and after dehydration (Figure 4.8). In agreement with the narrower Mössbauer linewidths and lower quadrupole splitting parameters (Table 4.2), in the  $g > 2$  region there are only two distinct environments: rhombically distorted  $g = 4.4$  and axially distorted  $g = 5.8$ , agreeing with the conclusions made earlier on page 87: a narrower distribution of coordination environments exists.

The EPR spectrum in Figure 4.8 might justify a Mössbauer spectrum fit with more than one Fe(III) environment, although evidence does not support the attribution of the additional sites to zeolite X and thus assignment remains ambiguous. Neither does it indicate an appropriate fit for Fe(II) species, since Fe(II) sites are rarely seen on EPR spectra. Upon dehydration,  $g > 2$  signals are suppressed and exchange broadening effects dominate the spectrum (Figure 4.8)(213).

The splittings observed in the EPR spectrum of a natural zeolite sample containing clinoptilolite were chaotic and ambiguous, probably perturbed by the presence of other metals naturally occurring in the zeolite (Figure 4.9; close up of the  $g \sim 2$  range inset).

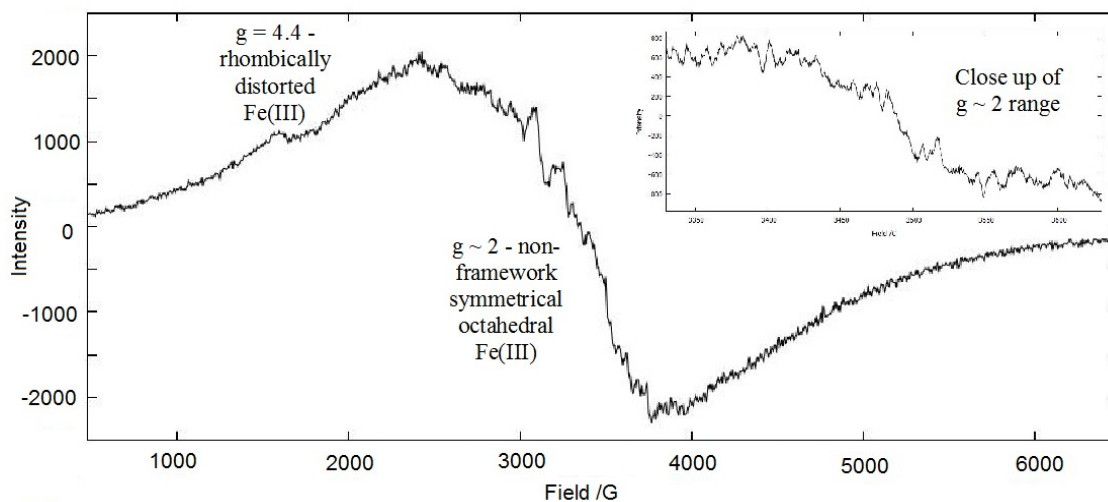


Figure 4.9: EPR spectrum of a hydrated air-exposed natural zeolite sample containing clinoptilolite,  $\nu = 9.794143$  GHz.

Uncalibrated XRF spectroscopy of the solid powder was used to identify contaminant metals present in the sample. In Table 4.7, ten different metals are identified and their  $M/Si$  and  $mg_M/g_{sieve}$  ratios provided. Possible EPR active species include Fe(III), Ti(I)/Ti(III) and Mn(II)/Mn(IV). In particular, Mn(II) is a common impurity to which EPR is highly sensitive.

Also observable on the EPR spectrum of the natural zeolite is the presence of a small peak  $g = 4.4$ , corresponding to rhombically distorted environments. The presence of just one peak is consistent with the low water content measured by TGA (Figure 3.10) and narrow linewidths found

in Mössbauer spectroscopy (Table 4.3): a narrow distributions of sites is likely. EPR does not quantify the extent of the distortion.

*Table 4.7: XRF spectroscopic measurements of trace elements in uncalibrated powder samples of natural zeolite containing clinoptilolite, where M = the trace elements.*

Trace element	M/Si	mg <sub>M</sub> /g <sub>Sieve</sub>
Na	0.07	18.01
Ca	0.05	23.18
K	0.05	22.18
Fe	0.02	13.95
Sr	0.01	6.60
Mg	0.01	3.16
P	0.01	3.08
Ti	0.00	1.20
Mn	0.00	0.67
Rb	0.00	0.18
Zn	0.00	0.13

XRF spectroscopy can also determine sulfur content and thus, *via* Fe/S ratio, the extent of occluded sulfates. In the uncalibrated Fe-loaded natural zeolite containing clinoptilolite, an Fe/S mole ratio of 26.3 indicates that very little of the iron forms occluded sulfur compounds. This corresponds to a maximum 3.8 % Fe(II) sulfates and 96.2 % isolated framework-coordinated ions or 5.7 % Fe(III) sulfates and 94.3 % isolated framework-coordinated ions. As such, the  $g = 4.4$  EPR spectroscopy signal can, with confidence, be assigned to an Fe(III) site coordinated to framework oxygens within the pore network. Additional signals observed elsewhere at  $g = 6$  and  $g = 13$  have been assigned to Fe(III) surface species, but were not observed in these spectra(81,214).

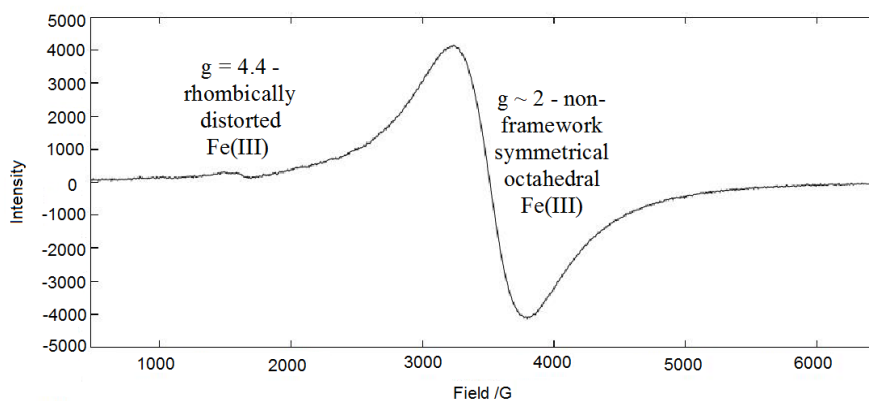


*Figure 4.10: EPR spectrum of hydrated air-exposed 20 % Fe-loaded sample containing 80 % AlPO-5,  $\nu = 9.794580$  GHz.*

Mössbauer indicates that all the iron in Fe-loaded AIPO-5 sample is Fe(III), but does not distinguish framework from extraframework sites. In Figure 4.10, the EPR spectrum of an uncalcined 20 % Fe-loaded AIPO sample, consisting of 80 % AIPO-5, a broad peak at  $g = 4.4$  distinguishes isolated Fe(III) centres present in the pore network.

In the EPR spectrum of 10 % Mn-loaded 23 % AIPO-5 phase samples, inhomogeneity was sufficiently high to suppress hyperfine splitting at  $g \sim 2$ . Broad peaks suggest that exchange interactions take place between neighbouring ions. No  $g = 4.3$  signal is seen in either calcined or uncalcined 10 % Mn-loaded 23 % AIPO-5 phase, only a dip in the trough of the  $g \sim 2$  signal that disappears upon calcination (Figure 4.11). In Mn(II)-loaded AIPO-5 samples reported elsewhere, post-synthetic reaction procedures (such as calcination) have been shown to drive ion migration and clustering, resulting in spin saturation, loss of structure and hyperfine line broadening(208).

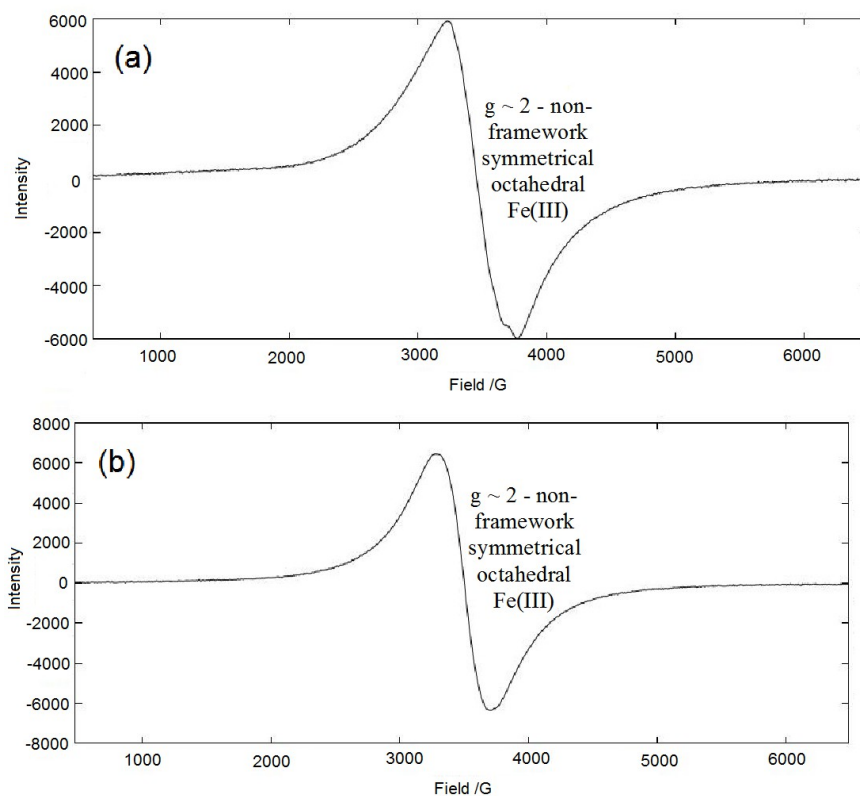


Figure 4.11: EPR spectra of hydrated air-exposed 10 % Mn-loaded sample containing 23 % AIPO-5 with berlinite and cristobalite impurities: (a) uncalcined,  $\nu = 9.794326$  GHz and (b) calcined,  $\nu = 9.794304$  GHz.

Four samples with the target phase AIPO-Fe23 prepared under different conditions were explored using EPR spectroscopy (Figure 4.12). Samples (a) and (b) are identical to those for which Mössbauer spectroscopy was performed (Figure 4.5, Table 4.5) and were prepared from Fe(II) acetate by heating to 190 °C for 3 days and 180 °C for 9 days respectively, at one third the maximum capacity of the reaction vessel. In these samples, some hyperfine splitting was observed around  $g \sim 2$ . This is likely to be due to trace contaminants such as Mn(II). Hyperfine splitting was

not observed in samples (c) and (d). These samples were prepared by (c) heating an Fe(II) chloride sample to 180 °C for 5 days at the maximum capacity of the reaction vessel, and (d) heating an Fe(II) acetate sample to 180 °C for 3 days at one third the maximum capacity of the reaction vessel. In all the samples, signals at  $\sim g = 4.3$  distinguish octa- or tetrahedral Fe(III) ions in an isolated rhombically distorted environment (Figure 4.12: (a)  $g = 4.2$ , (b)  $g = 4.4$ , (c)  $g = 4.4$  (weak), and (d)  $g = 4.3$ ). In sample (c), other signals are seen in the  $g > 2$  region. The shapes of these signals indicate that some originate from the same source, and others elsewhere. The low water content of  $< 1\%$  of total mass (Figure 3.17) suggests that these are not due to several Fe- $O_{\text{water}}$  coordinations. Regularly shaped repeating ridges are likely to be the result of impurity phases. The peaks at high  $g$  values  $> 20$  have elsewhere been interpreted as ferromagnetically coupled Fe(II) species, which are rarely observed in EPR spectra(215). However, the spectrum cannot be more clearly interpreted because of the level of complication and weakness of signals.

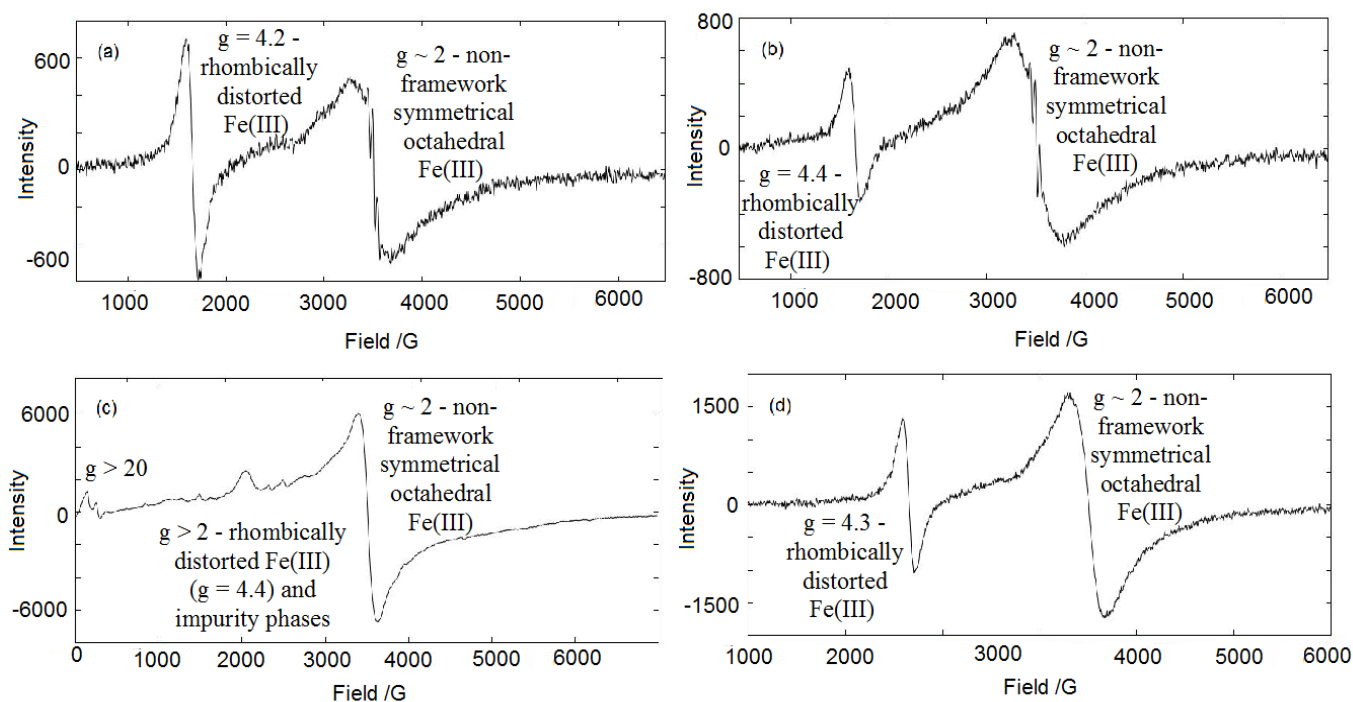


Figure 4.12: EPR spectra of four samples with the target phase AlPO-Fe<sub>23</sub>, (a) prepared with Fe(II) acetate by heating to 190 °C for 3 days at one third the vessel fill,  $\nu = 9.794802$  GHz, (b) prepared with Fe(II) acetate by heating to 180 °C for 9 days at one third the vessel fill,  $\nu = 9.794794$  GHz, (c) prepared with Fe(II) chloride by heating to 180 °C for 5 days at the maximum vessel fill,  $\nu = 9.794232$  GHz, and (d) prepared with Fe(II) acetate by heating to 180 °C for 3 days at one third the vessel fill,  $\nu = 9.794589$  GHz.

EPR spectroscopy of a calcined LAU Fe-containing AlPO gave only a broad  $g \sim 2$  signal. There was no indication of any framework species.

### XPS

XPS measurements were taken of a representative range of samples both before and after

exchange with chromate solution in order to examine ion oxidation states at the external surface. These data are useful for comparison with bulk analysis by Mössbauer spectroscopy, EPR spectroscopy and XRF spectroscopy. Looking at the quantity and oxidation states of Fe at the external surface can guide an interpretation of the Cr uptake mechanism and distinguish the target reaction from surface adsorption which neglects to reduce toxic Cr(VI) to less harmful Cr(III) – a vital distinction in the remediation process.

Table 4.8 gives the peak binding energies ( $B_e$ s) of the relevant elements as provided by the internal database of the CasaXPS fitting software(170). Spectra were calibrated to C 1s = 285.0 eV, which is consistent with the values contained within the NIST database. As such, the true binding energies are 1 eV higher than the values represented in Table 4.8. After Table 4.8, all  $B_e$ s are quoted as true, corrected values. The Relative Sensitivity Factor (RSF) takes into account the multiplicity of the orbital ( $2S + 1$ ) and the *specific elemental response* to electronic probing. Thus peak areas are a function of RSF and must be corrected by dividing through by the RSF before direct comparison.

*Table 4.8: Peak binding energies ( $B_e$ s) of the relevant elements as provided by the internal database of the CasaXPS fitting software and National Institute of Standards and Technology (NIST) database, alongside relative sensitivity factors of relevant orbitals.*

Peak	Casa XPS $B_e$ /eV	NIST database $B_e$ /eV	RSF
C 1s	284	285	11.17
O 1s	532	533	2.93
Fe 2p <sub>3/2</sub>	710	711	10.8
Fe 2p <sub>1/2</sub>	723	724	5.6
Mn 2p <sub>3/2</sub>	641	642	9.17
Mn 2p <sub>1/2</sub>	652	653	4.74
Cr 2p <sub>3/2</sub>	575	576	7.69
Cr 2p <sub>1/2</sub>	584	585	3.98

The *electron binding energy*, *i.e.* the chemical shift upon a change in oxidation state of 1 unit, is usually on the order of  $\sim 1$  eV; however, it depends upon the identity of the element and its oxidation state. That is, as the positive charge on a metal increases, it becomes increasingly difficult to remove further electrons; across the transition metal series, a higher nuclear charge leads to more contracted ions and so more strongly bound equivalent electrons: electron binding energies follow the same pattern as ionisation energies:

$$B_e(\text{Fe}^{3+}) > B_e(\text{Fe}^{2+}) > B_e(\text{Fe}^0)$$

*Equation 4.3*

$$B_e(\text{Fe}^{n+}) > B_e(\text{Mn}^{n+}) > B_e(\text{Cr}^{n+}) \quad \text{Equation 4.4}$$

The energy difference between Fe(III) and Fe(II) is  $\sim 0.85$  eV. Tables 4.9 and 4.10 give the average binding energies for Fe 2p and Mn 2p peaks respectively. The chemical shift is the difference between the binding energies of the ions and those of the elements (see Table 4.8).

*Table 4.9: Corrected Fe 2p  $B_e$ s for samples of Fe-loaded zeolite X and chemical shifts away from element binding energies as provided in Table 4.8.*

Sample	Average $B_e$ 2p <sub>3/2</sub> /eV	Average $B_e$ 2p <sub>1/2</sub> /eV	Chemical shift /eV
Mesoporous Fe zeolite X	713	726	2
Non-air-exposed Fe zeolite X	714 $\pm$ 0.7	728 $\pm$ 1.5	3-4
Air-exposed Fe zeolite X	713 $\pm$ 0.5	727 $\pm$ 0.6	2-3

No data are listed for Fe-loaded AIPO samples containing AIPO-5, because the Fe 2p peaks were indistinguishable. Thus the concentration at the external surface is not sufficiently high to be detected *via* XPS. There is no deviation on the mesoporous Fe zeolite X average  $B_e$  as only one suitable measurement was obtained.

*Table 4.10: Corrected Mn 2p  $B_e$ s for samples of Mn-loaded zeolite X and AIPO containing 23 % AIPO-5, 40 % berlinite and 37 % cristobalite impurity phases, and chemical shifts away from element binding energies as provided in Table 4.8.*

Sample	Average $B_e$ 2p <sub>3/2</sub> /eV	Average $B_e$ 2p <sub>1/2</sub> /eV	Chemical shift /eV
Mesoporous Mn zeolite X	646 $\pm$ 1.5	658 $\pm$ 1.7	4-5
Air-exposed Mn zeolite X	646 $\pm$ 1.8	658 $\pm$ 1.8	4-5
Mn-AIPO containing AIPO-5	644 $\pm$ 0.2	656 $\pm$ 0.6	2-3

The quality of data from Fe- and Mn-containing samples is poor, with a deviation up to  $\sim 2$  eV between repeat measurements of a given sample. The chemical shift away from the elemental standard is a function of both the formal oxidation state of the element *and* its local chemical environment. For Fe- and Mn-containing molecular sieves, the chemical environment dominates: this may be surmised by both the variation and the magnitude of the observed shifts, which are larger than would be expected for standard oxidation states such as +3 and +2. Electron-transfer processes, common amongst transition metals, account for the observed asymmetry in peak position and area. This data supports the conclusions of Mössbauer spectroscopy (page 85) and EPR spectroscopy (page 91): a distribution of chemical environments and oxidation states exists at the external surface as well as in the bulk.

Assuming both Fe(II) and Fe(III) are present in the Fe-containing samples, the spectra may be fitted with either one broad peak describing the distribution of environments, or two peaks representing the Fe(II) and Fe(III) distributions. This second model is a good fit to one air-exposed Fe-loaded zeolite X measurement, giving consistent Fe  $2p_{3/2}/2p_{1/2}$  ratios for both Fe(II) and Fe(III). However, not only does the other air-exposed Fe-loaded zeolite X measurement not fit the Fe(II)/Fe(III) model well, this sample is air-exposed and so unlikely to contain large amounts of surface Fe(II) where the non-air-exposed samples (which do not fit the model) do not (see Figure 4.13). More likely, oxidation has narrowed the distribution of environments compared with the non-air-exposed samples, allowing for a simpler fit. This conclusion is supported by broad line widths (FWHM) of Fe  $2p \sim 3.8$  eV, 4.5 times the Fe(II) to Fe(III) chemical shift (C  $1s$  line widths are  $\sim 2.9$  eV and O  $1s \sim < 3$  eV). Linewidths for the air-exposed Fe-loaded zeolite X sample are narrower. Figures 4.13 and 4.14 fit the Fe(II)/Fe(III) and one Fe models equally.

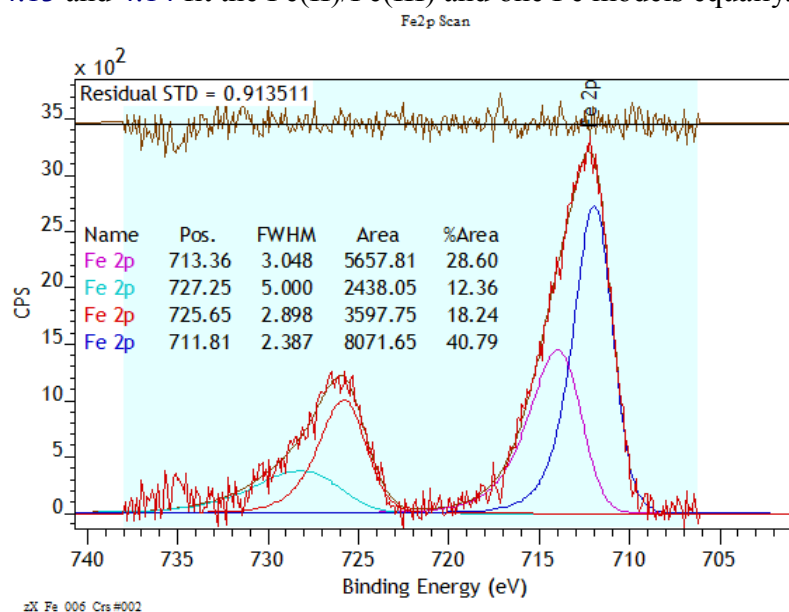


Figure 4.13: XPS spectrum of hydrated air-exposed Fe-loaded zeolite X. Ratios of peaks: Fe (II) (blue/red): 41 %,  $2p^{3/2}/2p^{1/2} = 2.31$ ; Fe (III) (pink/cyan): 59 %,  $2p^{3/2}/2p^{1/2} = 2.24$ .

Small changes in chemical environment and oxidation state are seen as equally small chemical shifts. The power to resolve between peaks is limited by the analyser resolution and peak widths. The extent of broadening is governed by the lifetime of the final state, the extent of scattering of the incident radiation and temperature. In these data, linewidths are sufficiently broad as to preclude any sensible assignment of oxidation states. Larger chemical shifts observed between manganese-containing samples suggest that a higher oxidation state coexists, consistent with the proposed  $Mn(II) \leftrightarrow Mn(IV)$  equilibrium.

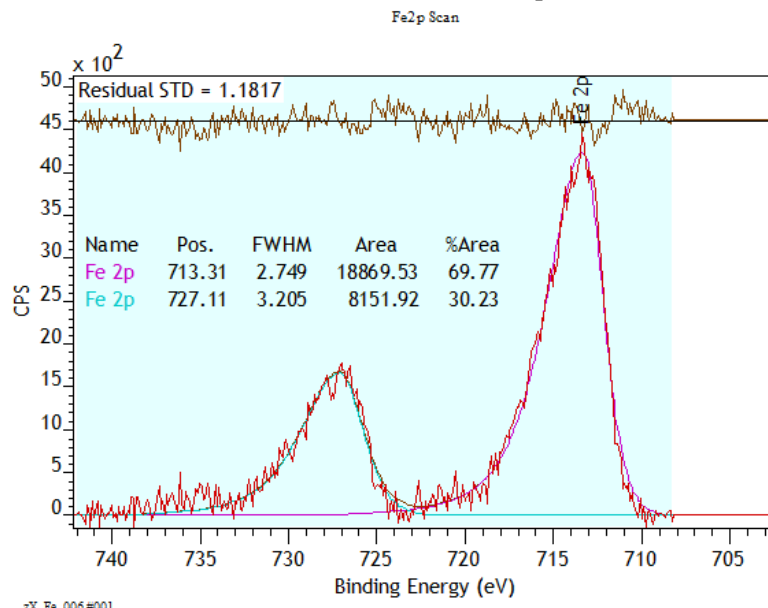


Figure 4.14: XPS spectrum of hydrated air-exposed Fe-loaded zeolite X. Ratios of peaks: Fe (III) (pink/cyan): 100 %,  $2p^{3/2}/2p^{1/2} = 2.31$ .

### Surface Fouling

Kim and Keane describe a “magic number” maximum Na exchange capacity for zeolite Y (68 %), such that if the number of exchanged metal ions exceed this capacity, they must be occupying smaller cages which do not readily accommodate them(76). However, this model does not account for surface fouling, nor the huge influence non-charge-balancing chemisorbed metal ions may exercise over the adsorption properties of the modified material. The adsorption capacity of zeolite Y has been significantly increased by loading iron oxide particles into micropores, and all uptake mechanisms involving activated carbon proceed by or competitively with surface adsorption(28,130). Thus, in order to evaluate the influence of the surface adsorption mechanism in chromium uptake, two zeolites, one parent sample of X and one mesoporous alginate-templated sample of X were prepared with Fe(III) sulfate and subsequently treated with chromate solution. XRF spectroscopy was used to compare the uptake to that of the samples prepared with Fe(II) sulfate (Table 4.12). A total loss of structural integrity is observed with both samples upon Fe(III) exchange. This can perhaps be explained by the tendency of Fe(III) ions to agglomerate, resulting in higher loadings and aggregation into particles, the size of which may exceed the pore diameters of the zeolite, rupturing the structure(81). Data in Table 4.11 supports the conclusion that higher Fe(III) loadings break down the structure.

Table 4.11: XRF spectroscopy data from calibrated fused beads of samples of hydrated air-exposed Fe(III)-loaded zeolite X, both templated and untemplated. All Fe = Fe(III).

Sieve		Si/Al	Fe/Na	M/Si	mg <sub>Fe</sub> /g <sub>sieve</sub>	mg <sub>Cr</sub> /g <sub>sieve</sub>
Fe(III)-zeolite X	Pre-Cr treatment	2.93	16.57	0.85	275.3	0
	Post Cr-treatment	3.12	30.62	0.76	253.2	20.9
Mesoporous Fe(III) zeolite X	Pre-Cr treatment	2.89	18.84	0.83	270.8	0
	Post Cr-treatment	3.08	52.95	0.86	276.3	13.2

These higher Fe-loadings do not drop significantly upon exposure to chromate solution, and subsequent Cr-loadings are low despite higher initial Fe-loadings. No evidence for ion exchange is therefore detected. These results are compatible with the conclusion that an adsorption-only mechanism is inadequate to explain chromium uptake by the Fe(II)-loaded zeolites.

Surface fouling by sulfates is recognised to take place when FeSO<sub>4</sub> is introduced to zeolite systems, even after extensive washing, whilst this does not occur with FeCl<sub>2</sub> precursors. Increasing the Fe loading decreases the surface area and pore volumes and Ates *et al.* report the formation of haematite above Fe concentrations of 2 % as observed by x-ray diffraction methods(184). Inamura *et al.* observe the aggregation of ferric oxides in Fe-zeolite Y after lengthy Fe-exposure (it is important to note that the competing mechanism depends not only upon surface species, but also upon extracted framework species that occlude in the pore channels as oxides)(216). Some ions are not readily introduced to zeolite frameworks: Hey reports the breakdown of zeolite frameworks upon FeCl<sub>3</sub>, AlCl<sub>3</sub> and ZnCl<sub>2</sub> exchange and Morice and Rees upon all Fe(II) exchanges and Fe(NO<sub>3</sub>)<sub>3</sub> after prolonged exposure(64,217).

Four further samples were prepared from the same parent zeolite with the aim of minimising surface contamination (Table 4.12). Two were prepared by exchange with Fe(II) sulfate and two with Fe(II) chloride. The exchange was carried out for just one hour. After preparation, one sulfate and one chloride prepared sample were washed briefly with water, and one of each with pH 1.12 nitric acid in order to remove surface species, increase surface area and facilitate access to the pore network(128,158,159). These measures were necessary as it has been suggested that well dispersed surface species may form bonds of comparable strength to those in the bulk and prove difficult to remove(195,208).

Results suggest that decreasing the Fe(II) excess during exchange does not significantly affect Fe-loadings, whilst the shorter exchange time of 1 hour rather than 24 hours slightly decreases the Fe-loadings and washing with nitric acid significantly decreases Fe-loadings. Cr uptake remained proportional to Fe loadings at ~ 0.32 mg<sub>Cr</sub>/mg<sub>M</sub>, dropping to lower values only for the Fe(II) chloride exchanged samples (0.29 and 0.23 mg<sub>Cr</sub>/mg<sub>M</sub> for water and acid washed samples

respectively) (see Table 4.13).

*Table 4.12: XRF spectroscopy data from calibrated fused beads of hydrated air-exposed Fe-loaded zeolite X prepared under differing conditions, as detailed.*

Fe:Na	Fe source	Time exchange /hrs	Washed in air with		Si/Al	Fe/Na	Fe/Si	mg <sub>Fe</sub> /g <sub>sieve</sub>	mg <sub>Cr</sub> /g <sub>sieve</sub>
1:1	FeSO <sub>4</sub>	24	water	Pre-Cr treatment	1.67	1.21	0.27	97.5	0
				Post Cr-treatment	1.61	1.01	0.28	93.6	29.8
3.5:1	FeSO <sub>4</sub>	1	water	Pre-Cr treatment	1.67	0.72	0.14	72.6	0
				Post Cr-treatment	1.57	0.67	0.23	79.7	24.5
3.5:1	FeSO <sub>4</sub>	1	pH1.12 nitric acid	Pre-Cr treatment	1.54	0.65	0.15	57.2	0
				Post Cr-treatment	1.51	0.53	0.15	54.6	17.6
3.5:1	FeCl <sub>2</sub>	1	water	Pre-Cr treatment	1.58	0.69	0.22	77.4	0
				Post Cr-treatment	1.57	0.82	0.26	87.7	24.4
3.5:1	FeCl <sub>2</sub>	1	pH1.12 nitric acid	Pre-Cr treatment	1.53	0.45	0.13	47.0	0
				Post Cr-treatment	1.48	0.45	0.14	49.8	11.5

### **Summary**

Upon dehydration, the number of environments detected by Mössbauer and EPR spectroscopies narrow, validating the peak fittings to a distribution of water-coordinated sites, despite sulfate surface species. Mn ions are distributed evenly before chromium exchange, but cluster afterwards. XPS could not distinctly resolve iron and manganese oxidation states in order to determine levels of surface oxidation. Low density zeolite samples may have been too thin.

Chromium uptake may proceed via physisorption (surface binding), chemisorption (chemical surface adsorption) or ion exchange. Low uptakes into non-redox active Fe(III)-loaded AlPO-5 systems indicates ion exchange is crucial.

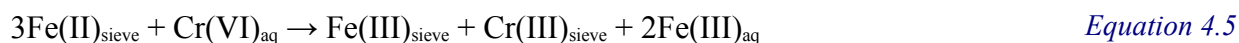
### **4.2. Changes upon Cr-exchange**

mg<sub>Cr</sub>/mg<sub>M</sub> was calculated for a range of samples in order to assess their ion exchange efficiency and support estimates of pre-Cr-treatment oxidation state fractions (Table 4.13).

Table 4.13:  $mg_{Cr}/mg_M$  values from XRF spectroscopy data from calibrated fused beads of hydrated air-exposed Fe-loaded zeolite X prepared under differing conditions, as detailed.

Sieve					$mg_{Cr}/mg_M$
Metal source	Metal excess	Templating	Exchange time /hrs	Washing	
<b>Mn (II) chloride</b>	<b>3-4</b>	-	<b>24</b>		0.00
		<b>1 %</b>			0.01
		<b>2 %</b>			0.04
		<b>4 %</b>			0.01
<b>Fe (II) sulfate</b>	<b>3-4</b>	-	<b>24</b>	<b>water</b>	0.32
		<b>1 %</b>	<b>24</b>		0.30
		<b>2 %</b>	<b>24</b>		0.31
		<b>4 %</b>	<b>24</b>		0.23
	<b>1</b>	-	<b>1</b>	<b>water</b>	0.31
		-	<b>1</b>	<b>acid</b>	0.32
		-	<b>24</b>	<b>water</b>	0.32
<b>Fe (II) chloride</b>	<b>3-4</b>	-	<b>1</b>	<b>water</b>	0.29
		-		<b>acid</b>	0.23
<b>Fe (III) sulfate</b>	<b>3-4</b>	-	<b>24</b>		0.08
		<b>2 %</b>			0.05

For 100 % Fe(II)-loaded zeolite, a maximum  $mg_{Cr}/mg_{Fe}$  ratio of 0.93 demonstrates full exchange with chromium:



After Cr exchange, the mole ratio Cr/Fe = 1.

Since  $Mr_{Cr} = 52.00$  and  $Mr_{Fe} = 55.845$ ,

$$\rightarrow \text{mass}(Cr)/\text{mass}(Fe) = 52.00/55.845 = 0.93 \quad \text{Equation 4.6}$$

For 100 % Mn(II)-loaded zeolite, the maximum  $mg_{Cr}/mg_{Mn}$  ratio is infinite:



After Cr exchange, the mole ratio Cr/Mn =  $1/0 = \infty$ .

These numbers provide good relative comparisons on uptake. It is possible that surface adsorption increases uptake in Fe(II) sulfate-exchanged zeolites over Fe(II) chloride-exchanged zeolites. However, attempts to remove surface species with acid did not reduce the relative chromium uptake, although the total mass of iron and thus chromium taken up was reduced.

EDS data were gathered for one Fe-loaded zeolite sample (68 % A and 32 % X) both before

and after chromate exposure, and after reduction under hydrogen gas flow at 400 °C for 2 hours. EDS measurements found that samples prepared with FeSO<sub>4</sub> exhibit sulfate surface contamination on the order of 1 %. The contaminant was distributed heterogeneously (Table 4.14).

*Table 4.14: Various EDS values for sulfur content as % of the measured elements at various spots on the surface of three hydrated air-exposed Fe-loaded zeolites comprised of 68 % A, 32 % X.*

Sample	Fe-loaded zeolite A	Cr-treated Fe zeolite A	H <sub>2</sub> -reduced Fe-loaded zeolite A
S % at various sites	0.78	3.55	0.87
	0.98	1.20	1.06
	1.08	3.79	1.12
	1.08	1.56	1.19
		2.62	1.23
			1.83
			0.97
			0.87
			0.19
			0.45
		0.15	
<b>S % max</b>	1.08	3.79	1.83
<b>S % min</b>	0.78	1.20	0.15
<b>S % deviation</b>	0.40	2.59	1.68

### *Mössbauer spectroscopy*

Air-exposed Fe zeolite X showed no Mössbauer signal after being treated with chromate solution, even after a repeat measurement. This usually occurs when too little iron or too much water is present in the material. In this case, XRF spectroscopy had already been employed to determine a suitable iron content, but high water content remains a possibility. Other factors that may lead to loss of spectra include elements in the sample that absorb gamma rays linearly rather than resonantly or loosely held iron in the structure, providing a very low recoil-free fraction; these might occur upon introduction of the element chromium and migration of iron ions.

One Cr-treated Fe-loaded natural zeolite containing clinoptilolite was studied more successfully using Mössbauer spectroscopy (Figure 4.15, Table 4.15). The spectrum was best fitted to one Lorentzian doublet with  $\chi^2 = 0.678002$  and distorted ratio of linewidths:  $w^-/w^+ = 0.86$ . This corresponds to one Fe(III) environment and could not be fitted to any Fe(II) peaks. Introducing a

singlets gave a poor fit and high symmetry species could not be justified physically. The loss of Fe(II) confirms that oxidation has taken place upon exposure to chromate solution. The asymmetry can arise from several origins including texture effects such as preferred orientation, impurity species, inherent properties of the crystal structure, or the Goldanskii-Karyagin effect, when the probability of emission or adsorption is anisotropic; this effect depends upon proximity of the Mössbauer active nucleus to neighbouring atoms(218).

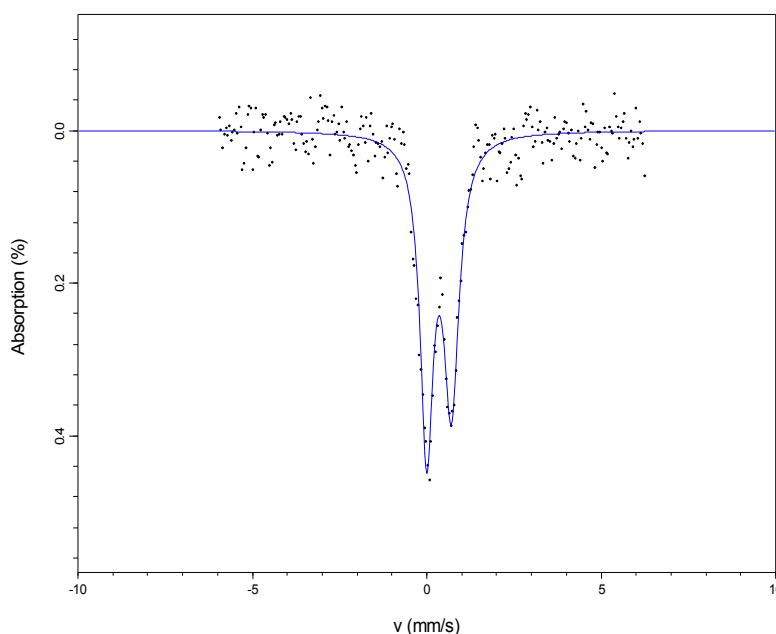


Figure 4.15: Mössbauer spectrum of hydrated air-exposed chromate-exposed Fe-loaded natural zeolite containing clinoptilolite phase.

Since the distortion was not observed in the Mössbauer spectrum of Fe-loaded natural zeolite prior to treatment with chromate solution, it may be safely assumed that neither the crystal structure, Goldanskii-Karyagin effect nor preferred orientation have led to this distortion: it is most likely that the introduction of Cr(III) ions has created an impurity that perturbs the linewidth ratio.

Table 4.15: Mössbauer parameters of hydrated air-exposed chromate-exposed Fe-loaded natural zeolite containing clinoptilolite phase,  $\chi^2 = 0.678002$ . Uncertainties are calculated using the covariance matrix. The uncertainty in the natural linewidth of Fe is  $\pm 0.02$  mm/s.

Species	Peak	Site population /%	IS /mm/s	QS /mm/s	Linewidth /mm/s	w-/w+
Octahedral Fe(III)	Doublet	100	0.35 (2)	0.71 (3)	0.27 (3)	0.86 (9)

The Mössbauer spectrum of Cr-treated 20 % Fe-loaded 80 % AlPO-5 was best fitted to one Lorentzian doublet with  $\chi^2 = 0.880385$  (Table 4.16). Since all the iron was present as Fe(III) before exposure to chromate solution, it is not surprising that no significant changes have occurred. Although all three parameters, isomer shift, quadrupole splitting and linewidth have decreased, these small changes are within error (see also Table 4.4)

Table 4.16: Mössbauer parameters of one hydrated air-exposed chromate-exposed uncalcined 20 % Fe-loaded AlPO containing 80 % AlPO-5 with berlinite impurity phase,  $\chi^2 = 0.880385$ . Uncertainties are calculated using the covariance matrix. The uncertainty in the natural linewidth of Fe is  $\pm 0.02$  mm/s: values quoted beyond 2 dp are included only to show precision uncertainties.

Species	Peak	Site population /%	IS /mm/s	QS /mm/s	Linewidth /mm/s
Octahedral Fe (III)	Doublet	100	0.398 (5)	0.658 (9)	0.228 (7)

### EPR Spectroscopy

EPR spectroscopy of one air-exposed Mn-loaded zeolite X and one air-exposed Fe-loaded zeolite X were studied after exposure to chromate solutions (Figure 4.16). The Mn-loaded sample recorded only a broad  $g \sim 2$  signal with no visible hyperfine structure, possibly due to migration and aggregation of ions into clusters under ion exchange reaction conditions. On the other hand, the Fe-loaded sample retains some structure, although the pattern is simplified: a small signal at  $g = 4.4$  and some poorly defined structure on the  $g \sim 2$  line are observed, possibly arising from Cr(III) ion contamination. It is possible that Cr(III) may be seen on the spectrum as lines at  $g = 4$ , but only if isolated sites with near axial symmetry exist.  $g = 4$  peaks were not observed in these samples.

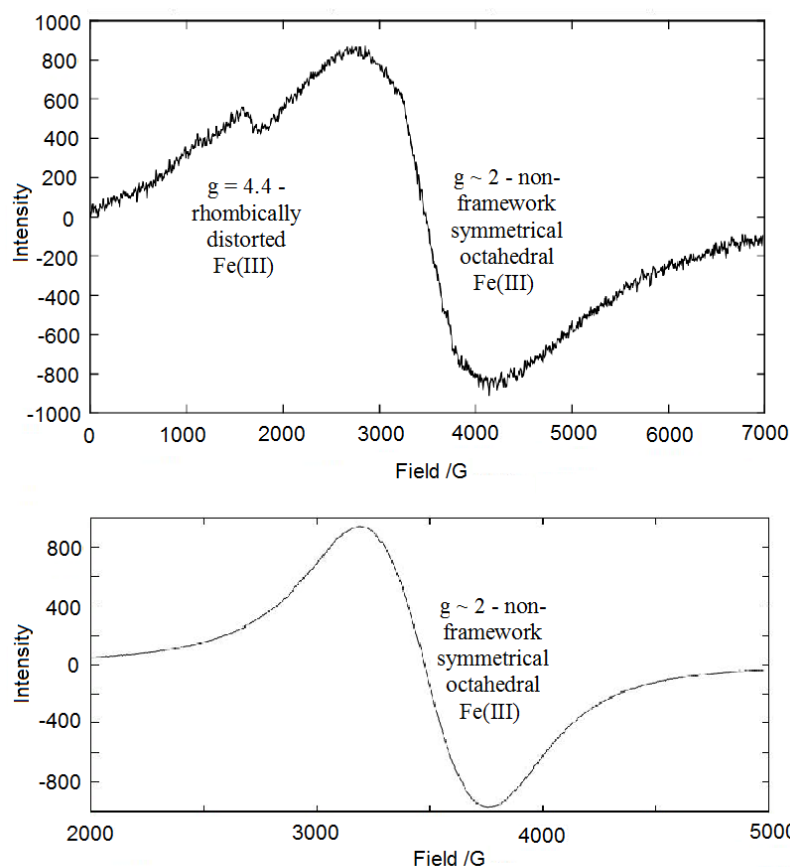


Figure 4.16: EPR spectra of hydrated air-exposed chromate-exposed samples; top: air-exposed Fe-loaded zeolite X,  $\nu = 9.795528$  GHz, and bottom: air-exposed Mn-loaded zeolite X,  $\nu = 9.794896$  GHz.

Fuks *et al.* report several lines arising from Cr(III) species: in particular lines at  $g = 1.97$ ,  $1.9$  and  $5$ , and note that Cr(III) cannot be treated as magnetically isolated ions. Antiferromagnetic exchange coupled clusters form and interactions are highly sensitive to surrounding ions, such as  $\text{PO}_4$  units(219).

EPR spectroscopy of chromate-exposed Fe-loaded natural clinoptilolite zeolite sample showed an overall loss in intensity compared with the precursor (Figure 4.9) and generally poor quality pattern. Both Fe species and contaminants have been lost (Figure 4.17). The observation of a low, broad  $g = 4.5$  peak suggests a more distorted environment. A broad, poor resolution peak at  $g = 3.0$  that may have been present in the parent material may be a residual contaminant or Fe environment.

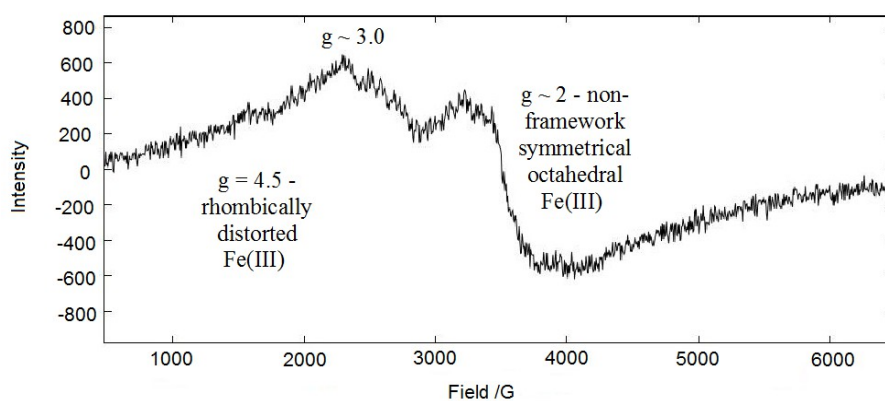


Figure 4.17: EPR spectrum of hydrated air-exposed chromate-exposed Fe-loaded natural zeolite containing clinoptilolite,  $\nu = 9.794582$  GHz.

EPR spectra of two 20 % Fe-loaded AlPO systems containing 80 % AlPO-5 phase were measured after exposure to chromate solution (calcined and uncalcined, Figure 4.18). The uncalcined sample, which should still contain some templates from the synthesis step, measured a broad  $g \sim 2$  signal, and a broad  $g \sim 4.5$  signal cut by a sharper  $g = 4.8$  peak. Ridges are observable at  $g = 2.8$ ,  $3.0$  and  $8.2$  that may be due to impurity Cr(III) ions. More interestingly, in the spectrum of the calcined, template-free sample, not only is the typical  $g = 4.4$  line observed and ridges seen at  $g = 2.8$ ,  $3.0$  and  $3.3$  that may be impurities, but also a sharp signal that cuts the  $g \sim 2$  line. This signal appears in a later spectrum of this sample (Figures 5.10 and 5.17) and, as such, it was concluded that the signal is real. There are several possible origins for this unusual feature, the most common being the presence of a free radical, usually the case in organic systems, a consequence of further kinds of exchange interaction, or superparamagnetism arising from clusters of Fe species with aligned spins. The exact  $g$  value can provide insight into the origin of this line. This line was measured between field =  $3500.528$  and  $3512.26$ , giving a centre point at  $g$ -value  $1.9959$  to 4 sf, very close to the ideal  $g = 2.0$  value. This signal will be discussed further in Chapter 5, where it is compared with similar samples.

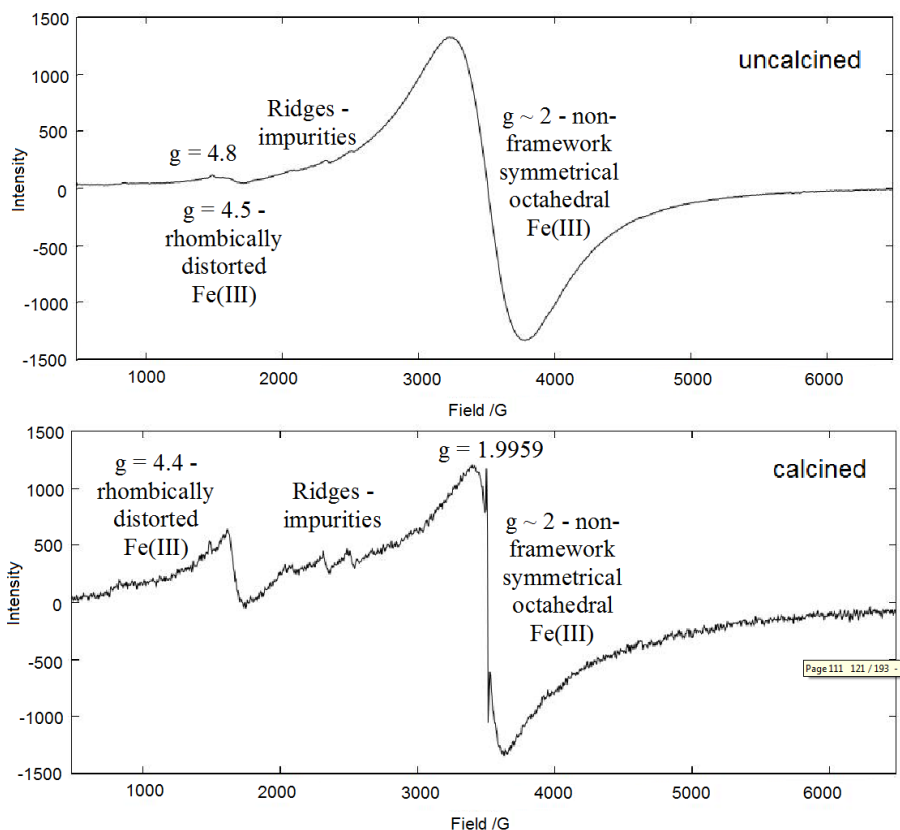


Figure 4.18: EPR spectra of hydrated air-exposed chromate-exposed 20 % Fe-loaded samples containing 80 % AlPO-5 with berlinite impurity phase, top: uncalcined,  $\nu = 9.793821$  GHz calcined,  $\nu = 9.794975$  GHz.

The EPR spectrum of 10 % Mn-loaded AlPO containing 23 % AlPO-5 measured only a broad  $g \sim 2$  signal, indicating strong exchange ion interactions, probably from clustering or oxidation of Mn(II) ions.

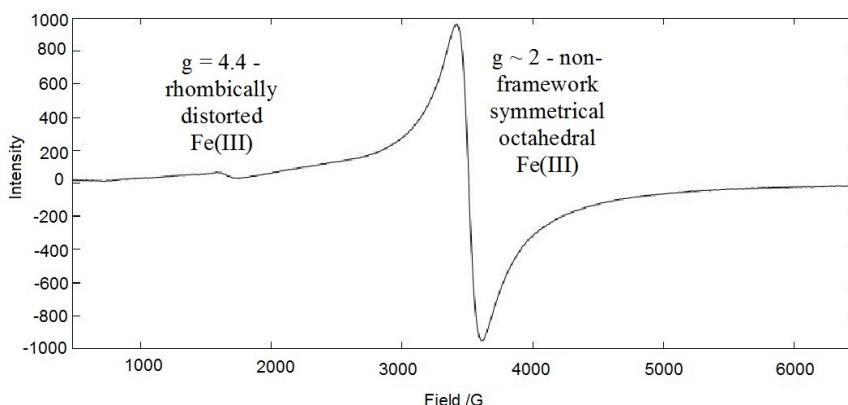


Figure 4.19: EPR spectrum of hydrated air-exposed chromate-exposed Fe-loaded LAU AlPO,  $\nu = 9.793496$  GHz.

EPR spectroscopy of a chromate-exposed calcined LAU Fe-containing AlPO gave a sharp  $g \sim 2$  signal and small peak at  $g = 4.4$  (Figure 4.19).XPS(77,179)

After chromate exchange, the Fe peaks in Fe-loaded zeolite X and AlPO-5 containing

sample were undetectable, *i.e.* the iron content was too low. Tables 4.17 and 4.18 give the average binding energies and chemical shifts of the Fe- or Mn-cations in samples following exposure to 0.02 M chromate solution.

*Table 4.17: Corrected Fe 2p B<sub>e</sub>s for samples of Fe-loaded zeolite X and chemical shifts away from element binding energies as provided in Table 4.8. Corrected 2p B<sub>e</sub>s from Table 4.9 (before chromate exposure) have been included for comparison.*

Sample	Average B <sub>e</sub> 2p <sub>3/2</sub> /eV		Average B <sub>e</sub> 2p <sub>1/2</sub> /eV		Chemical shift /eV	
	Before	After	Before	After	Before	After
Mesoporous Fe zeolite X	713	712 ± 0.1	726	726 ± 0.1	2	1-2
Non-air-exposed Fe zeolite X	714 ± 0.7	-	728 ± 1.5	-	3-4	-
Air-exposed Fe zeolite X	713 ± 0.5	712 ± 0.02	727 ± 0.6	726 ± 0.1	2-3	1-2

No data are listed for Fe-loaded AIPO samples containing AIPO-5, because the Fe 2p peaks were indistinguishable. Thus the concentration at the external surface is not sufficiently high to be detected *via* XPS. The 2p<sub>1/2</sub> peak belonging to air-exposed Fe-loaded zeolite X overlaps with an Sn peak (see Figure 4.20). Tin is present due to treating the chromate solution after mixing with the molecular sieve, to reduce Cr(VI) species to Cr(III) and thus render the liquid safe to transport and test. Presence in the solid, which should not have been Sn-treated, occurs *via* contamination.

*Table 4.18: Corrected Mn 2p B<sub>e</sub>s for samples of Mn-loaded zeolite X and AIPO containing 23 % AIPO-5 40 % berlinite and 37 % cristobalite impurity phases, and chemical shifts away from element binding energies as provided in Table 4.8. Corrected 2p B<sub>e</sub>s from Table 4.10 (before chromate exposure) have been included for comparison.*

Sample	Average B <sub>e</sub> 2p <sub>3/2</sub> /eV		Average B <sub>e</sub> 2p <sub>1/2</sub> /eV		Chemical shift /eV	
	Before	After	Before	After	Before	After
Mesoporous Mn zeolite X	646 ± 1.5	647	658 ± 1.7	660	4-5	5-7
Air-exposed Mn zeolite X	646 ± 1.8	648 ± 0.01	658 ± 1.8	660 ± 0.03	4-5	6-7
Mn-AIPO containing AIPO-5	644 ± 0.2	648 ± 0.1	656 ± 0.6	660 ± 0.4	2-3	6-7

There is no deviation on the mesoporous Mn-loaded zeolite X average B<sub>e</sub> as only one suitable measurement was obtained.

After treatment with chromate, the Fe or Mn binding energies are in close agreement, giving useful averages from which oxidation states may be estimated with confidence. A high chemical shift and notable increase in Mn binding energies after chromate exposure points to successful reduction of chromium by manganese species, probably Mn(IV). However, this is not observed for

Fe species, the shifts of which conversely decrease: a reduction of Fe(II) oxidation state disagrees with findings by Mössbauer spectroscopy and it is therefore, given the quality of the data, more suitable to conclude that this relates to a narrowing of the distribution of surface Fe environments and possible loss of surface species.

The surface concentration of ions in the original (non chromate exchanged) and final (chromate exchanged) Fe- and Mn-containing samples are given in Tables 4.19 and 4.20; data have been corrected by dividing through by the appropriate RSF. These numbers may be compared with the XRF spectroscopic values for  $\text{mg}_{\text{Fe}}/\text{g}_{\text{sieve}}$  given in Chapter 3, assuming the oxygen content at the surface is comparable to that in the bulk. With this assumption, ratios have been used to estimate  $\text{mg}_{\text{Fe}}/\text{g}_{\text{sieve}}$  values. However, it is likely that the oxygen at the surface is higher than the bulk due to the formation of surface oxides, and these numbers may be misleadingly low.

*Table 4.19:  $\text{Fe}_{\text{tot}}/\text{O}_{\text{tot}}$  ratios for samples of Fe-loaded zeolite X, both before (original) and after (final) chromate exposure, with corresponding  $\text{mg}_{\text{Fe}}/\text{g}_{\text{sieve}}$  estimates from these ratios.*

Sample	Original $\text{Fe}_{\text{tot}}/\text{O}_{\text{tot}}$	Original $\text{mg}_{\text{Fe}}/\text{g}_{\text{sieve}}$	Final $\text{Fe}_{\text{tot}}/\text{O}_{\text{tot}}$	Final $\text{mg}_{\text{Fe}}/\text{g}_{\text{sieve}}$
Mesoporous Fe zeolite X	0.12	206	0	88
Non-air-exposed Fe zeolite X	0.041	81	-	-
Air-exposed Fe zeolite X	0.083	151	0.089	160

These  $\text{Fe}_{\text{tot}}/\text{O}_{\text{tot}}$  ratios lead to  $\text{mg}_{\text{Fe}}/\text{g}_{\text{sieve}}$  values that are much higher than those determined by bulk analysis using XRF spectroscopy, and thus suggest that the surface is highly contaminated with additional Fe species. After exposure to chromate solution, the Fe 2p peaks of non-air-exposed Fe zeolite X could not be distinguished, which implies that the concentration of surface ions dropped below the level of detection. XPS is relatively insensitive and errors may be large.

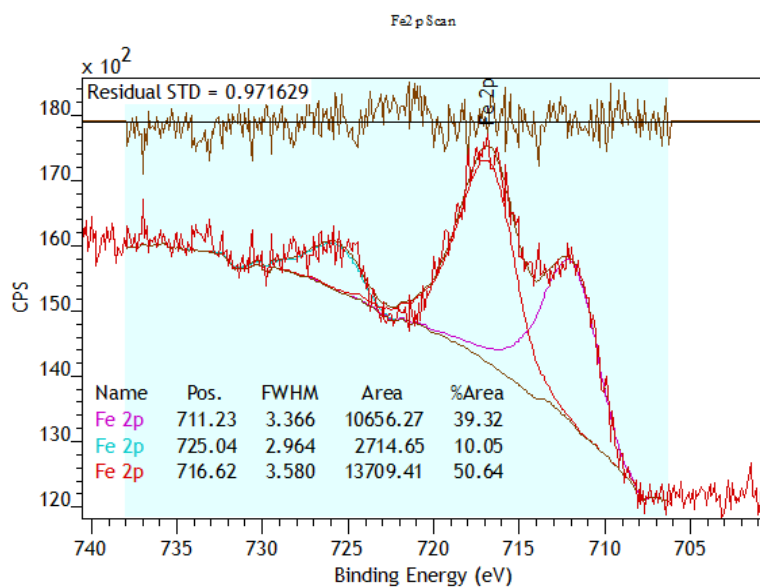
*Table 4.20:  $\text{Fe}_{\text{tot}}/\text{O}_{\text{tot}}$  ratios for samples of Mn-loaded zeolite X and AlPO containing 23 % AlPO-5, 40 % berlinite and 37 % cristobalite impurity phases, both before (original) and after (final) chromate exposure, with corresponding  $\text{mg}_{\text{Fe}}/\text{g}_{\text{sieve}}$  estimates from these ratios.*

Sample	Original $\text{Mn}_{\text{tot}}/\text{O}_{\text{tot}}$	Original $\text{mg}_{\text{Mn}}/\text{g}_{\text{sieve}}$	Final $\text{Mn}_{\text{tot}}/\text{O}_{\text{tot}}$	Final $\text{mg}_{\text{Mn}}/\text{g}_{\text{sieve}}$
Mesoporous Mn zeolite X	0.069	116	0.052	87
Mn zeolite X	0.060	100	0.070	117
Mn-AlPO-5	0.030	53	0.020	39

In agreement with the proposed mechanism, the surface concentration of ions relative to

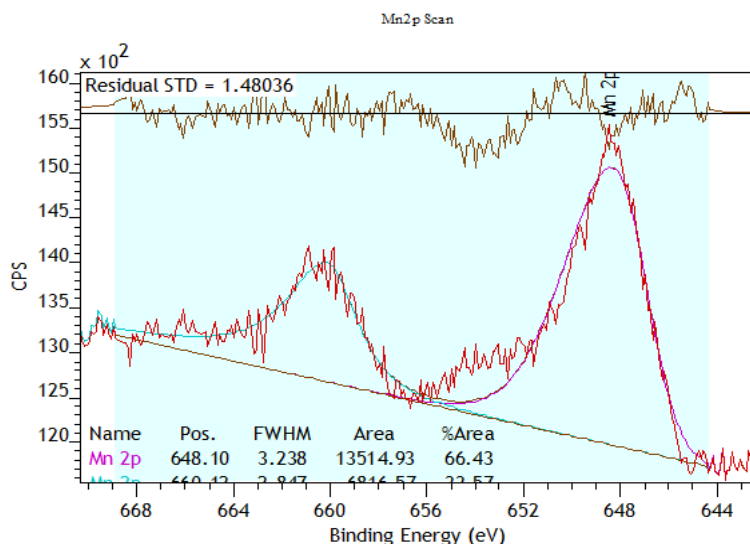
oxygen decreases in samples which should contain redox-active cations except for Mn-zeolite X, for which there is a small, just significant increase. The concentration of oxygen atoms at the surface may also be subject to change. Orange, air-exposed Fe-zeolite X, which was not expected to contain redox active ions at the surface, also measures an increase in surface species: this finding supports the hypothesis of ion migration to the sample surface prior to the reduction of Cr(VI). Fe and Mn loadings at the external surface are not appreciably different, unlike the bulk *via* XPS analysis.

Areas are affected by the quality of background modelling. A well-fitted LA(a,b,n) background function (a Lorentzian curve convoluted with a Gaussian) should give an area within 2 % accuracy (Figure 4.20), whilst the flat diagonal base line used to fit Mn 2p peaks gives an area within 5 % accuracy (Figure 4.21). This compares with 15 % accuracy if no background subtraction is modelled.



zX\_Fe\_006\_Crs#002

Figure 4.20: XPS spectrum of chromate-exposed hydrated air-exposed Fe-loaded zeolite X overlapping with Sn lines (red) with LA(a,b,n) background fitting.



zX\_Mn\_003\_Crs#002

Figure 4.21: XPS spectrum of chromate-exposed hydrated air-exposed Mn-loaded zeolite X with linear background fitting.

A 5 % error in measurement corresponds to a deviation of  $\sim \pm 0.007$  for the values used to obtain the ratios in [Tables 4.19](#) and [4.20](#). True errors will be larger due to variation in oxygen content.

### ***Summary***

Fe-loaded zeolites change from green to brown upon aerial exposure, indicating oxidation, but the difference is not detected by Mössbauer spectroscopy. This suggests the surface: bulk ratio is sufficiently low. Contaminant peaks in EPR spectroscopy may result from aggregated Cr(III) ions at the surface or in the bulk.

### **4.3. Looking at Cr sites**

Whilst Prakash *et al.* record a characteristic Cr(III) signal in their as-synthesised CrAPSO-5 sample, Cr(VI) is not EPR active. Chromium is in low concentrations in the tested samples and no  $g = 4$  chromium signal was observed *via* EPR spectroscopy(202).

Kiser and Manning extensively studied the oxidation state and site symmetry of chromium adsorbed by Fe(II)-loaded faujasite zeolite using XANES and EXAFS(125). XANES results suggested that Cr(VI) was largely reduced to Cr(III), but the retention of a weak absorption peak at 5994.5 eV was indicative of trace unreacted Cr(VI), which they quantified to  $\sim 1\%$ . Other differences were seen between this sample and a purely Cr(III) treated zeolite sample, in particular broadened peaks. EXAFS found chromium sites to belong to bridged octahedral species and the study concluded that the product was a  $\text{Cr}_x\text{Fe}_{1-x}(\text{OH})_3$  found upon the sample surface and inside the pore network.

### ***XPS***

Since Mössbauer spectroscopy would not be able to detect chromium sites, XPS was used as the primary investigative tool for these species. However, only two samples were measured for which Cr peaks were distinguishable by XPS. For all other samples, the surface chromium content was too low to give distinct peaks on the XPS spectra and therefore to fit (see [Figures 4.22](#) and [4.23](#)). Binding energies and chemical shifts are given in [Table 4.21](#).

Table 4.21: Corrected Cr 2p  $B_e$ s for samples of Fe-loaded zeolite X, and chemical shifts away from element binding energies as provided in Table 4.8.

Sample	Average $B_e$ 2p <sub>3/2</sub> /eV	Average $B_e$ 2p <sub>1/2</sub> /eV	Chemical shift /eV
Mesoporous Fe zeolite X	578 ± 0.03	588 ± 0.06	3-4
Air-exposed Fe zeolite X	578 ± 0.1	588 ± 0.01	3-4

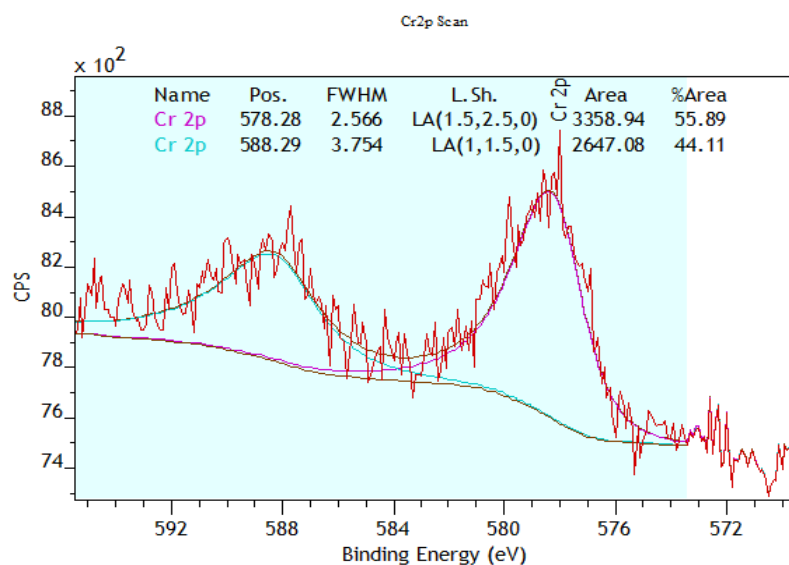


Figure 4.22: XPS spectrum of chromate-exposed hydrated 2% alginate templated Fe-loaded zeolite X. Chromium content is sufficient to give distinct peaks

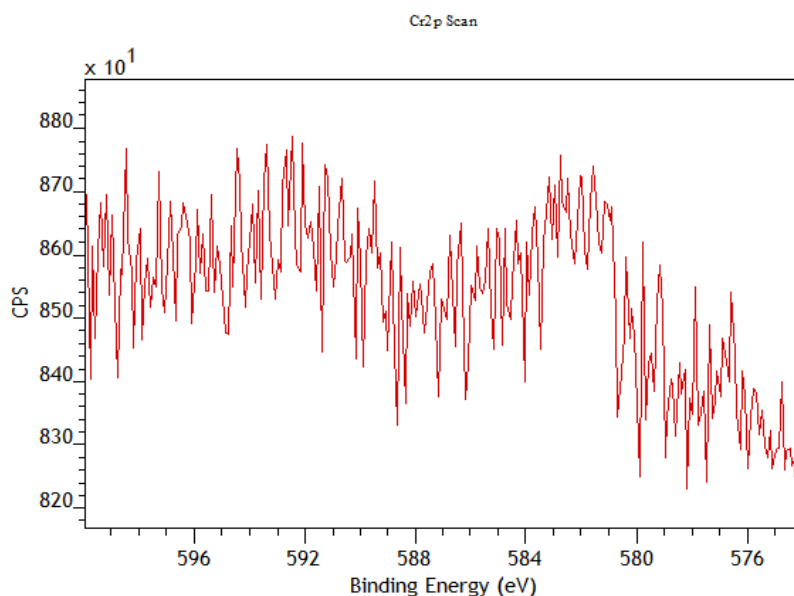


Figure 4.23: XPS spectrum of chromate-exposed hydrated alginate templated Mn-loaded zeolite X. Surface chromium content is too low to give distinct peaks.

Very small deviations in binding energies and relatively small ranges for chemical shifts suggest that the data are reliable and as such oxidation states may be estimated with some

confidence. The chemical shift implies that Cr(III) is the dominant species at the sample surface, but that Cr(VI) contamination may persist, in agreement with the findings by Kiser and Manning(125). On the other hand, Arias *et al.* report almost 70 % of chromium as Cr(VI)(209). Although chromium content has not been quantified here, the presence of both Cr(III) and Cr(VI) at the sample surface is consistent with the proposed ion exchange mechanism, wherein Cr(VI) initially binds to the surface before undergoing chemical reduction by exchangeable metal cations.

Table 4.22 gives the surface concentration of chromium in chromate exchanged samples relative to both the oxygen at the external surface and the iron for direct comparison of the exchange; data have been corrected by dividing through by the appropriate RSF.

*Table 4.22:  $Cr_{tot}/O_{tot}$  and  $Fe_{tot}/Cr_{tot}$  ratios for samples of Fe-loaded zeolite X, both before and after chromate exposure, with corresponding  $mg_{Fe}/g_{sieve}$  estimates from these ratios.*

Sample	$Cr_{tot}/O_{tot}$	$Fe_{tot}/Cr_{tot}$	$mg_{Cr}/g_{sieve}$
Mesoporous Fe zeolite X	0.049	0.91	78
Air-exposed Fe zeolite X	0.051	1.76	81

In the air-exposed non-mesoporous sample, which should contain residual non-redox active Fe(III), the Fe concentration remains higher as expected, giving a high  $Fe_{tot}/Cr_{tot}$  ratio in Table 4.22. A ratio close to 1 for mesoporous Fe-loaded zeolite X suggests that additional Cr uptake occurs largely at the external surface. Like with iron (page 112), the chromium loading in  $mg_{Cr}/g_{sieve}$  at the sample surface as recorded by XPS is much higher than that measured by XRF spectroscopy. The mesoporous sample, which gives a similar surface Cr concentration to the non-mesoporous, measured  $33.1 mg_{Cr}/g_{sieve}$  via XRF spectroscopy (Table 3.20), a little more than the non-mesoporous  $29.1 mg_{Cr}/g_{sieve}$  (Table 3.8). This suggests that uptake proceeds via initial surface adsorption.

The FWHM for chromium peaks are  $\sim 2.4$  eV (1.5-3.8 eV), which suggest a relatively narrow distribution of sites. Low data resolution makes fitting chromium peaks with two curves, Cr(III) and Cr(VI), inadvisable.

Although  $Mn_{tot}/Cr_{tot}$  measurements were not possible, EDS provided Mn/Cr ratios of 0.68 and 0.87 and suggested the material surfaces were heterogeneous in zeolites A and X. These numbers should be taken as a guideline only, since it is not unusual for discrepancies to appear between analytical techniques(220). However, it is likely that Mn ions are also over-represented at the sample surface, like those of Fe and Cr.

### ***UV-vis spectroscopy***

UV spectra of solid samples record broad, featureless bands below 600 nm, indicating the

presence of various Fe species, potentially ranging from isolated Fe(III) to large Fe<sub>2</sub>O<sub>3</sub> nanoparticles(197).

The effects of matrix absorption in solids outweighs the influences of coloured transition metals. As such, the only characteristic absorption detected is the peak at ~440 nm in an uncalcined 50 % Fe-loaded AIPO containing 61 % AIPO-5. This peak is not present in the calcined sample but is not removed by chromium exchange and it does not appear in other AIPO-5 samples. It is probably absorption due to template effects. On the other hand, no bands at 460 and 500 nm are detected on the spectra of any samples, which would be indicative of Fe<sub>2</sub>O<sub>3</sub> particles at the external surface, implying that these do not dominate(221).

### *pH*

A set of Fe-loaded zeolite X samples were exposed to chromate solution under different pH conditions. The initial solution (before combination with sodium dichromate and zeolite) was prepared at pHs between 5 and 13. The objective of these experiments was to determine whether there was a pH dependence upon chromium uptake. Besides an anomalous result at pH6 (not repeated through lack of identical starting material), a steadily decreasing Fe/Na ratio across the series is observed, indicating that Fe is preferentially leached under alkaline conditions (Figure 4.24 (a)). However, results suggested that chromium uptake remained consistent across the pH range, except for the final, pH 13 sample, which suggests a slightly elevated chromium uptake (Figure 4.24 (b)).

*Table 4.23: XRF spectroscopy data from calibrated fused beads of Fe-loaded zeolite X, Cr exposed at pH 5-13. The number marked in red is unusually high and represents dealumination and breakdown of the molecular sieve. This may be caused by contaminants or error in pH readings.*

<b>pH</b>	<b>Si/Al</b>	<b>Fe/Na</b>	<b>M/Si</b>	<b>mg<sub>Fe</sub>/g<sub>sieve</sub></b>	<b>mg<sub>Cr</sub>/g<sub>sieve</sub></b>	<b>mg<sub>Cr</sub>/mg<sub>Fe</sub></b>
<b>5</b>	1.50	1.10	0.22	78.9	11.1	0.14
<b>6</b>	79.65	2.24	0.03	18.7	10.5	0.56
<b>7</b>	1.50	1.10	0.22	78.7	10.9	0.14
<b>8</b>	1.51	1.01	0.23	80.4	11.0	0.14
<b>9</b>	1.51	0.99	0.23	79.5	11.1	0.14
<b>10</b>	1.53	0.94	0.23	80.7	10.8	0.13
<b>11</b>	1.50	0.94	0.23	80.9	10.7	0.13
<b>12</b>	1.53	0.74	0.22	77.5	10.3	0.13
<b>13</b>	1.50	0.40	0.23	76.2	16.4	0.21

Although XRD confirmed that crystallinity was not compromised in any of the samples

exposed to these conditions, the Si/Al ratio of the sample at pH 6 suggests some breakdown of the molecular sieve occurred and a high chromium loading is also noted. Lack of a general rise suggests the chromium value result may be a consequence of loss of other elements.

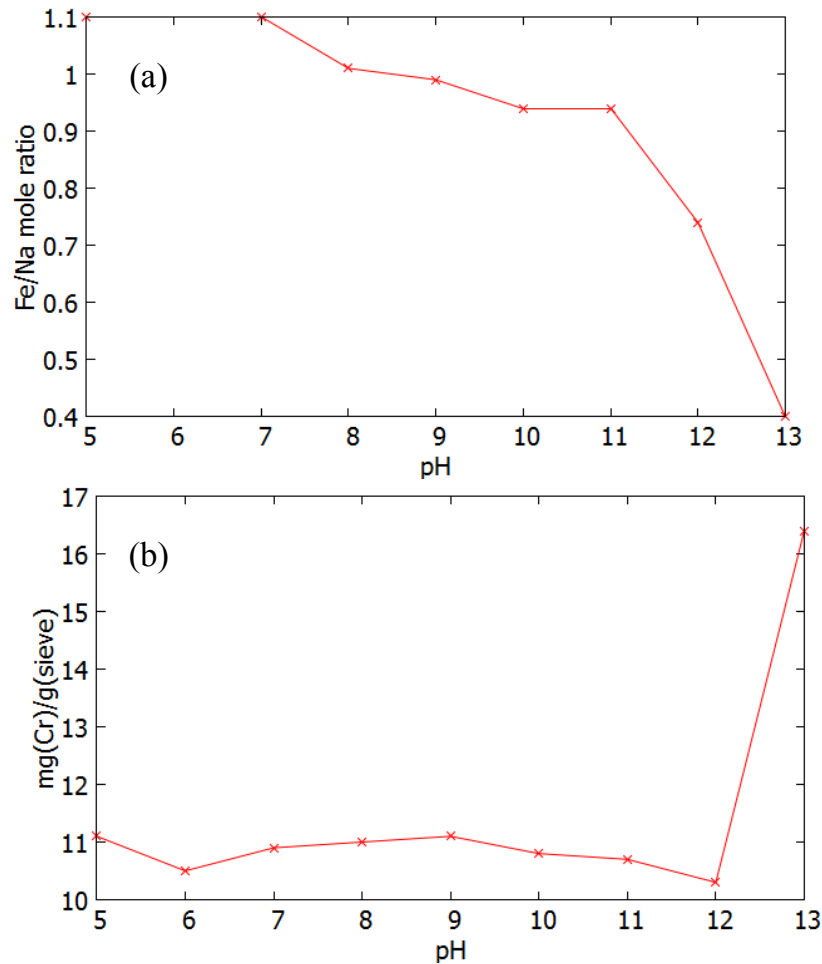


Figure 4.24: (a) Graph of Fe/Na mole ratio against pH 5-13; (b) graph of  $\text{mg}_{\text{Cr}}/\text{g}_{\text{sieve}}$  against pH 5-13 from calibrated fused beads of Cr-treated Fe-loaded zeolite X.

### Summary

Chromium uptake is pH independent. Surface loadings are not significantly high.

## Chapter 5: Effect of Modified Ions Upon Chromium Uptake

This chapter builds upon the foundation work in [Chapter 4](#) that explores the oxidation states and coordination environments of ions, chiefly iron ions, in selected molecular sieves. The chapter focusses upon the effects of air exposure on Fe ions and modifications to these ions designed to increase the chromium uptake capacity in selected systems that were identified in [Chapter 3](#) for potential remediation. Using primarily Mössbauer and EPR spectroscopies, the results of these modifications are explored and XRF spectroscopy is employed to examine the relationship with chromium uptake. Through these methods, attempts are made to elucidate the mechanism for chromium uptake.

### 5.1. Air Exposure

#### *Colour*

Fe(II) in zeolites has a fragile stability towards oxygen and heat, readily oxidising on exposure to air or dry oxygen or during dehydration(107,222). This is clearly visible from the green to orange colour transition observed in Fe-loaded zeolite X upon exposure to air. The same may also be observed for Fe-loaded zeolite A. The initial green colour (indicative of Fe(II) species) gradually changes to an orange colour (indicative of Fe(III) species). This reaction may be partially suppressed under an inert atmosphere. In order to prevent the supposed oxidation of redox-active to redox-inactive Fe ions, samples were stored in a desiccator containing drying beads in a glove box. The mechanism of the colour change was examined by mapping out the colour changes using Dulux colour charts. For fourteen days, a small quantity of two Fe-containing zeolite X samples was removed from the glove box and the colours noted regularly until the colour change was complete. Stored over the drying beads, the samples slowly dehydrated. It was discovered that the more hydrated the sample, the more rapid the oxidation. Results are presented in [Figures 5.1](#) and [5.2](#).

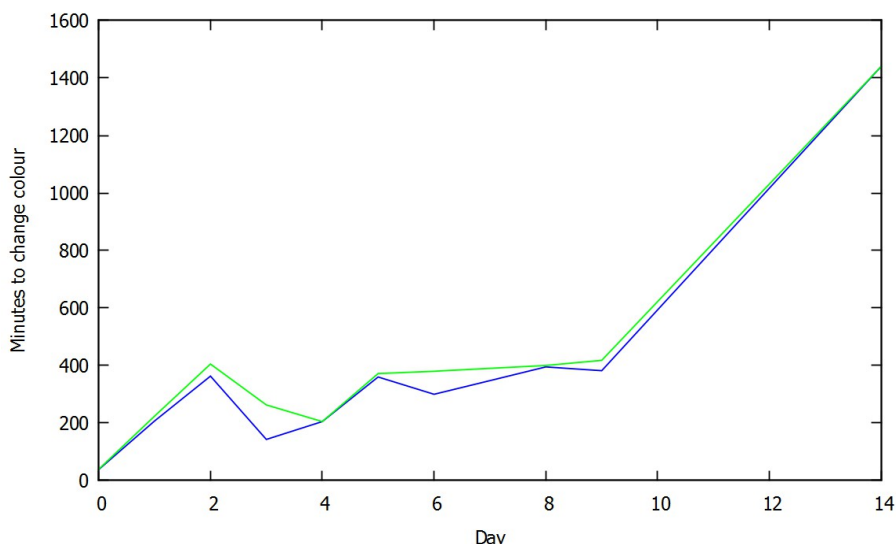


Figure 5.1: Graph of time taken in minutes for the full colour change to occur when Fe-loaded zeolite X is air-exposed against the number of days dried under inert atmosphere.

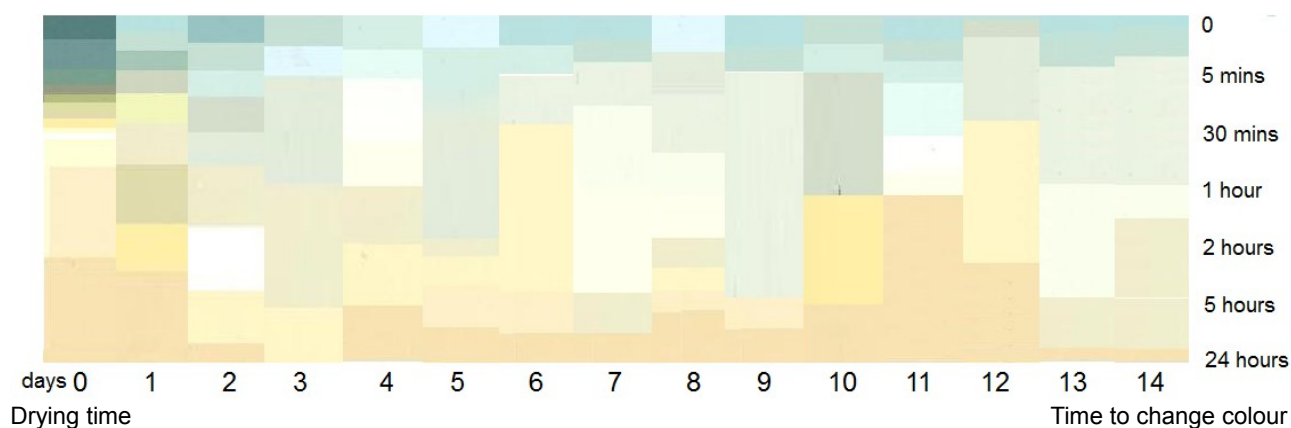


Figure 5.2: Chart of Fe-loaded zeolite X in Dulux colours. Drying time in number of days is compared with time to change colour once air exposed. Each bar represents the colours through which the sample cycled.

### ***Mössbauer Spectroscopy***

The green to orange colour change of Fe-loaded zeolite X was investigated by Mössbauer Spectroscopy of one green, non-air-exposed sample, which was prepared under glove box conditions and sealed into a Mössbauer disc with Araldite glue. The spectrum was fitted to two Lorentzian doublets corresponding to octahedral Fe(II) and Fe(III) with  $\chi^2 = 0.799808$  (Figure 5.3, Table 5.1). Inspection of hyperfine parameters given in Table 5.1 suggests that there is no change in site populations of octahedral Fe(III) and Fe(II) between the non-air-exposed sample (Figure 5.3) and orange air-exposed sample (Figure 4.1 (a)). Other hyperfine parameters also remain similar, with only a reduced Fe(II) linewidth of note. This implies that a narrower distribution of octahedral Fe(II) coordination environments exists in the non-air-exposed sample. It is possible that, upon air exposure, ions migrate through the zeolite structure, creating the observed colour change and

widening the distribution of Fe(II) sites. Mössbauer performed in Chapter 4 suggested that even before calcination, aerial oxidation of Fe(II) occurs in AlPO-5; Ojo *et al.*, Arias *et al.*, and Lee *et al.* meanwhile, observe the oxidation of Fe in both framework and extraframework positions, with accompanying partial iron extraction from the framework(197,209,223).

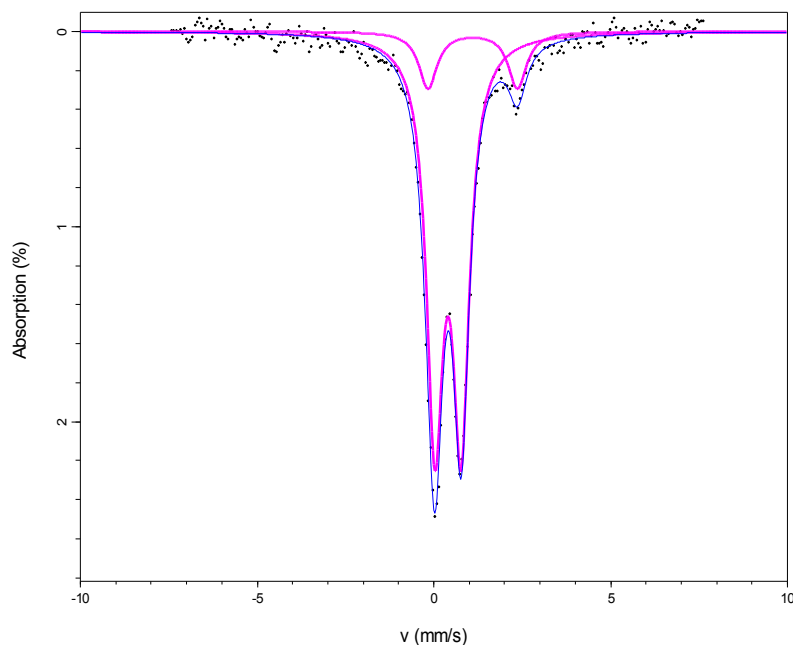


Figure 5.3: Mössbauer spectrum of non-air-exposed Fe-loaded zeolite X.

Table 5.1: Mössbauer parameters of non-air-exposed Fe-loaded zeolite X,  $\chi^2 = 0.799808$ . The air-exposed Fe-loaded zeolite X sample from Chapter 6 has been included for the purpose of comparison. Uncertainties are calculated using the covariance matrix. The uncertainty in the natural linewidth of Fe is  $\pm 0.02$  mm/s: values quoted beyond 2 dp are included only to show precision uncertainties.

Zeolite X	Species	Peak	Site population /%	IS /mm/s	QS /mm/s	Linewidth / mm/s
Non-air-exposed	Octahedral Fe (III)	Doublet	86 (2)	0.400 (6)	0.75 (1)	0.283 (8)
	Octahedral Fe (II)	Doublet	14 (2)	1.10 (4)	2.53 (8)	0.31 (6)
Air-exposed	Octahedral Fe (III)	Doublet	86 (2)	0.378 (8)	0.74 (1)	0.286 (9)
	Octahedral Fe (II)	Doublet	14 (4)	1.09 (9)	2.44 (18)	0.45 (12)

After 3 months of air exposure, the original Fe-loaded zeolite X sample (Figure 4.1 (a)) was remeasured using Mössbauer Spectroscopy to investigate whether any further oxidation occurred over time. The spectrum was fitted to two Lorentzian doublets, octahedral Fe(III) and Fe(II) of 90 % and 10 % of the spectral area respectively (Figure 5.4, Table 5.2). The  $\chi^2$  value was 0.68091. Although the proposed oxidation lies within error, the ready repeatability of 86 % Fe(III) value coupled with visible inspection of the plot supports the conclusion that a small amount of oxidation has occurred. The quality of the plot is good. The isomer shift parameter of octahedral Fe(II) is slightly lower, whilst its quadrupole splitting parameter is a little higher, indicating increasing

distortion and possibly a lowering of average coordination number for these species. These observations would be consistent with migration of Fe(II) species, coordinating weakly and irregularly to the zeolite framework.

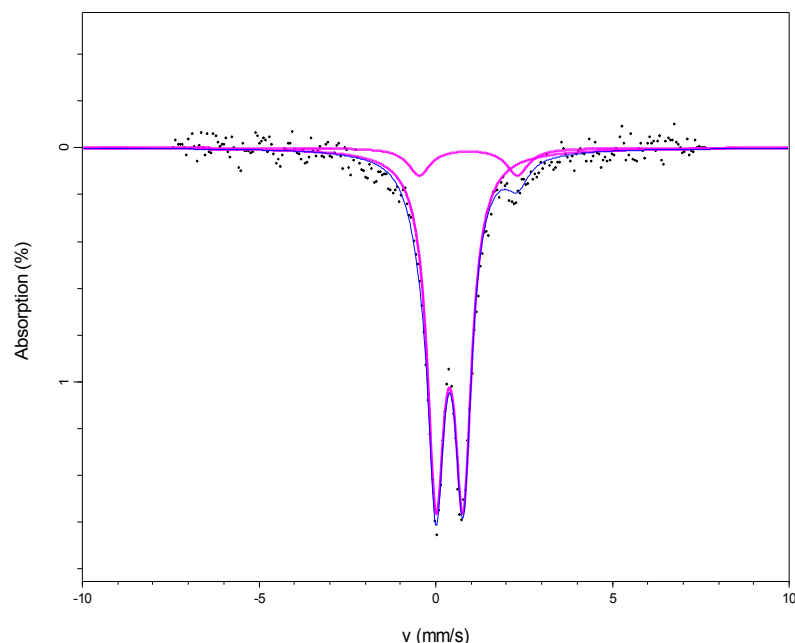


Figure 5.4: Mössbauer spectrum of hydrated air-exposed Fe-loaded zeolite X after 3 months further air exposure.

Table 5.2: Mössbauer parameters of hydrated air-exposed Fe-loaded zeolite X after 3 months further air exposure,  $\chi^2 = 0.68091$ . Fixed (unrefined) parameters are marked with \*. Uncertainties are calculated using the covariance matrix. The uncertainty in the natural linewidth of Fe is  $\pm 0.02$  mm/s: values quoted beyond 2 dp are included only to show precision uncertainties.

Species	Peak	Site population /%	IS /mm/s	QS /mm/s	Linewidth /mm/s
Octahedral Fe (III)	Doublet	90 (3)	0.389 (9)	0.77 (2)	0.29 (1)
Octahedral Fe (II)	Doublet	10 (3)	0.92 (11)	2.78 (2)	0.38*

### Summary

Dehydration delays the observed colour change/oxidation, but no increase in Fe(III) populations is observed *via* Mössbauer spectroscopy corresponding to Fe<sub>2</sub>O<sub>3</sub>. It is possible that changing recoil free fractions as ions migrate mask changing Fe(II)/Fe(III) populations.

## 5.2. Reduction

In order to generate a higher proportion of redox-active ions and thus enhance the ion-exchange potential of zeolite X and AlPO-5, post-synthetic reduction of Fe(III) to Fe(II) was attempted. Various methods have been proposed for the reduction of metal ions present in

microporous materials. Sodium borohydride was employed by Jung *et al.* to convert included Ni(II) cations into metallic nickel nanoparticles and by Lee *et al.* to produce Fe(0) in Fe(II)-loaded natural clinoptilolite zeolite sample(9,224). Csicsery used cadmium vapour to deliver the reduction of Co(II) ions in zeolite A whilst avoiding the structural jeopardy associated with decationisation(116). Reduction under hydrogen gas flow is a common, harsh method of metal ion reduction in microporous materials, producing both ions of a lower oxidation state and metal ions. A temperature range of 360-500 °C is typically reported and the reaction may additionally be performed under pressure(225,226). After hydrogen gas reduction of Fe(III) species in natural clinoptilolite zeolite sample at 360 °C, Morice and Rees observed some broadening in the Mössbauer spectrum, which they interpreted as the formation of Fe(0) metal aggregates(217). When aggregates become thousands of atoms large, they no longer fit within the pore channels and cause destruction of the structure or accumulate on the zeolite surface. Loss of crystallinity is not uncommon, even when only Fe(II) is produced(226). Higher temperatures are required to reduce Fe and Mn ions that are found in framework positions than those in extraframework positions and Xue *et al.* observed the reduction of only extraframework Fe(III) in ZSM-5 after 1 hour of hydrogen gas flow at 500 °C(67). Whilst some authors have discovered reversible Fe(II) ↔ Fe(III) oxidation-reduction relationships in zeolites, spontaneous oxidation to Fe(III) is still prevalent across this chemistry(227–229). Reduction to iron metal, however, is not reversible and “is always accompanied by complete destruction of the zeolite”(216).

It is also important to note that the site populations derived from Mössbauer spectroscopy may not be valid in samples where Fe(0) metal aggregates form. The comparability of site populations relies upon the similarity in environments between different oxidation states. As sites vary more widely (*e.g.* surrounded by other Fe(0) atoms rather than zeolite), site populations may no longer be assumed to accurately reflect fractional occupancies. A greater understanding could be obtained through acquisition of the recoil free fractions for each species: by measuring the samples at low temperatures, variations in site populations that arise from factors such as rigidity of position may be explored. Future studies may consider carrying out these investigations on samples with varying Fe environments.

TGA measurements of an H<sub>2</sub>-reduced Fe-zeolite X sample indicated 24 % of the mass was comprised of water, and thus the water content was not affected by the reduction process.

### ***Mössbauer Spectroscopy***

Mössbauer spectroscopy was performed on a series of Fe-loaded zeolite samples that were

exposed to reducing hydrogen gas flow for different lengths of time. Although this technique is very harsh, it was selected over solution techniques such as sodium borohydride because it avoids both the risk of mass loss through mixing and subsequent filtration, and simultaneous aerial or water exposure, which have been shown to drive the oxidation. Samples of Fe-loaded zeolite X were heated to 500 °C at 10 °C/min under a constant, steady flow of 90:10 N<sub>2</sub>:H<sub>2</sub> gas, before being held at this temperature for 1-24 hours and then rapidly cooled to room temperature still in the furnace. The same parent sample of Fe-loaded zeolite X was used for all reduction products and is compared with 1, 3, 6 and 12 hour reduced products in Figure 5.5 and Table 5.3. The spectra are fitted to two Lorentzian doublets, corresponding to octahedral Fe(II) and Fe(III), and in some cases one Lorentzian sextet, corresponding to Fe(0) metal.  $\chi^2$  values were 1.0946, 1.15177, 4.23134, 1.80165 and 1.17452 respectively. Site populations in Table 5.3 suggest that parent material, which is an alginate-templated Fe-loaded zeolite X, was more extensively oxidised than previous, non-templated samples. It is possible that the introduction of mesoporosity has increased surface loading of oxidised Fe(III) or enhanced aerial access and so oxidation. Narrow linewidths reflect a shortening of the excited state lifetime: this may arise from interactions between aggregated Fe species.

*Table 5.3: Mössbauer parameters of 2 % alginate templated Fe-loaded zeolite X, exposed to hydrogen gas flow at 500 °C for no, 1, 3, 6 and 12 hours,  $\chi^2 = 1.0946, 1.15177, 4.23134, 1.80165$  and  $1.17452$  respectively. Fixed (unrefined) parameters are marked with \*. Linewidths that fall below the natural linewidth of  $\alpha$ -iron are marked in red. Uncertainties are calculated using the covariance matrix. The uncertainty in the natural linewidth of Fe is  $\pm 0.02$  mm/s: values quoted beyond 2 dp are included only to show precision uncertainties.*

Reduction /hrs	Species	Peak	Site population /%	IS /mm/s	QS /mm/s	Linewidth /mm/s
<b>None</b>	Octahedral Fe (III)	Doublet	93 (1)	0.369 (4)	0.836 (7)	0.279 (5)
	Octahedral Fe (II)	Doublet	7 (1)	1.22 (3)	2.26 (5)	0.18 (4)
<b>1</b>	Octahedral Fe (III)	Doublet	78 (2)	0.360 (9)	0.90 (2)	0.34 (1)
	Octahedral Fe (II)	Doublet	23(2)	1.17(2)	2.28(5)	0.29 (3)
<b>3</b>	Octahedral Fe (III)	Doublet	71.5 (8)	0.389 (8)	0.91 (2)	0.336 (5)
	Octahedral Fe (II)	Doublet	20 (1)	1.01 (3)	2.31 (7)	0.38 (2)
	Fe (0) metal	Sextet	9 (1)	0	B ~ 33 T	0.16 (2)
<b>6</b>	Octahedral Fe (III)	Doublet	69 (1)	0.38 (2)	0.86 (3)	0.31 (1)
	Octahedral Fe (II)	Doublet	18 (2)	1.04 (7)	2.31 (1)	0.36 (4)
	Fe (0) metal	Sextet	13 (1)	0	B ~ 33 T	0.21*
<b>12</b>	Octahedral Fe (III)	Doublet	60 (2)	0.37 (3)	0.87 (7)	0.32 (2)
	Octahedral Fe (II)	Doublet	13 (3)	1.04 (20)	2.25 (40)	0.38 (9)
	Fe (0) metal	Sextet	27 (2)	0	B ~ 33 T	0.14 (2)

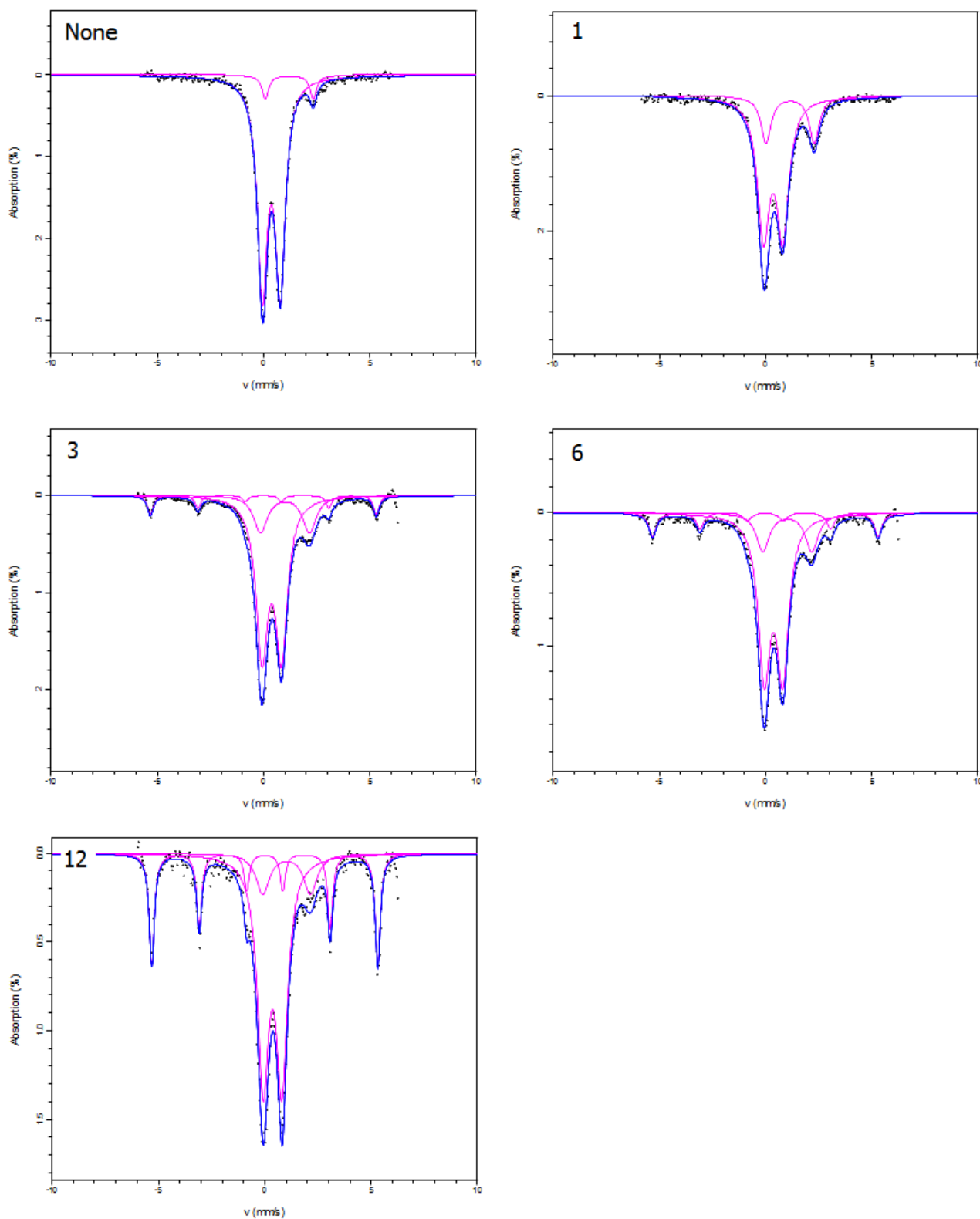


Figure 5.5: Mössbauer spectra of 2 % alginate templated Fe-loaded zeolite X, exposed to hydrogen gas flow at 500 °C for no, 1, 3, 6 and 12 hours respectively.

Looking at site populations in Table 5.3, a steady decrease in Fe(III) populations may be observed, along with a steady increase in Fe(0) populations after 3 hours of heating. Fe(II)

populations, on the other hand, initially increase and then begins to decrease; this behaviour suggests that the formation of Fe(0) occurs more rapidly than the formation of Fe(II), but that harsher conditions are required before the former process may be initiated.

Although they differ from previous samples, isomer shifts and quadrupole splitting parameters do not differ appreciably from the parent material, and are unlikely to be significant. It is important to note that the linewidths of some Fe(0) metal species fall below the natural linewidth of  $\alpha$ -Fe and thus do not reflect real values; values were left unfixed where the fit still appeared reasonable and may be used to assess the errors within values.

After 3 months of air exposure, the sample of alginate templated Fe-loaded zeolite X that was hydrogen reduced for 6 hours was remeasured using Mössbauer spectroscopy. The spectrum was fitted to two Lorentzian doublets corresponding to octahedral Fe(II) and Fe(III), and one Lorentzian sextet, corresponding to Fe(0) metal (Figure 5.6, Table 5.4). The  $\chi^2$  value was 2.93257. Inspection of site populations supports the supposition that reduction to Fe(0) is not reversible within the zeolite framework: whilst Fe(0) populations remain constant, a statistically significant decrease in Fe(II) site populations is observed, and corresponding Fe(III) population increases from gradual continuous oxidation. Isomer shift and quadrupole splitting parameters do not demonstrate any significant changes; broadening of the Fe(II) peaks was observed, but since the linewidth had to be fixed at a sensible value to prevent the fit from becoming unreasonable, the parameter cannot provide quantitative information.

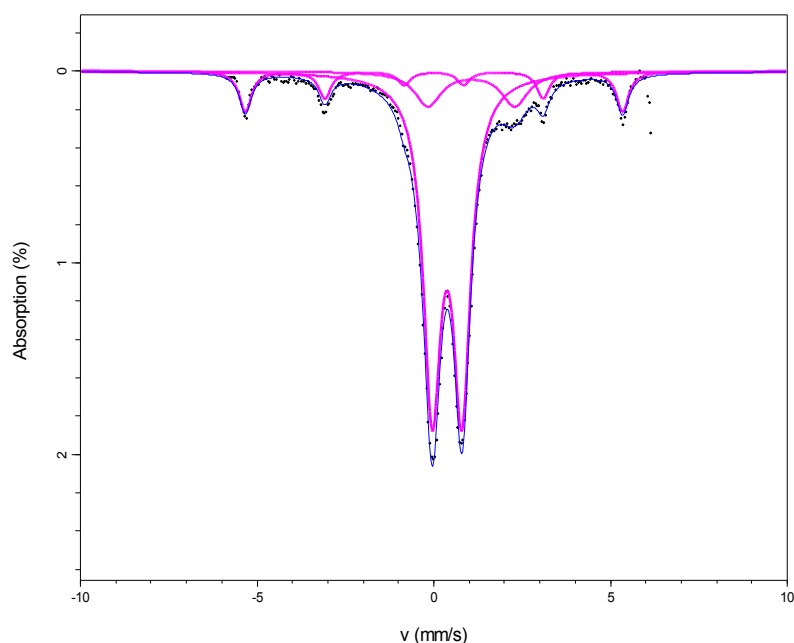


*Figure 5.6: Mössbauer spectrum of 6 hours 500 °C hydrogen reduced 2 % alginate templated Fe-loaded zeolite X after 3 months of further air exposure.*

*Table 5.4: Mössbauer parameters of 6 hours 500 °C hydrogen reduced 2 % alginate templated Fe-loaded zeolite X after 3 months of further air exposure,  $\chi^2 = 2.93257$ . Fixed (unrefined) parameters are marked with \*. Uncertainties are calculated using the covariance matrix. The uncertainty in the natural linewidth of Fe is  $\pm 0.02$  mm/s: values quoted beyond 2 dp are included only to show precision uncertainties.*

Species	Peak	Site population /%	IS /mm/s	QS /mm/s	Linewidth /mm/s
Octahedral Fe (III)	Doublet	75 (0.6)	0.374 (3)	0.841 (7)	0.301 (4)
Octahedral Fe (II)	Doublet	12 (0.7)	1.06 (4)	2.45 (8)	0.46*
Fe (0) metal	Sextet	13 (0.7)	0	B ~ 33 T	0.21*

This study suggests that although reduction under hydrogen gas flow can be quickly employed to maximise the proportion of low oxidation state Fe species, Fe(II) remain vulnerable to aerial oxidation, and only by converting ions to Fe(0) can stability be achieved. In Table 5.9, XRF spectroscopy is used to determine whether the presence of Fe(0) facilitates chromium uptake.

A similar hydrogen reduction study was performed on an Fe-loaded sample containing 70 % zeolite A and 30 % zeolite X (Table 3.5). One parent sample and samples reduced for 1, 2, 5, 12 and 24 hours were measured using Mössbauer spectroscopy and fitted to two Lorentzian doublets, corresponding to octahedral Fe(II) and Fe(III), and in some cases one Lorentzian sextet, corresponding to Fe(0) metal (Table 5.5).  $\chi^2$  values were 0.654635, 1.21819, 0.603153, 0.653543, 0.600623 and 0.541441 respectively. Although inspection of site populations suggests that some Fe(0) metal is evolved and Fe(II) populations increase, the trend is not as clear as in the Fe-loaded zeolite X samples treated similarly. In the samples heated for 5 and 24 hours, site populations indicate that mild oxidation has taken place. Such an unexpected result has been observed in other systems(230), although complications may arise under the experimental conditions: these samples were heated to 500 °C as rapidly as possible, rather than at a steady rate of 10 °C/min as for the zeolite X samples, and may have experienced inconsistent heating and cooling rates. In addition, the larger number of samples meant they were prepared over a longer time period, leading to (i) turning off the hydrogen gas flow between samples, such that flow rates may have differed and (ii) longer waiting times before measurement (since the Mössbauer measurement time exceeds the sample preparation time, *i.e.* days > hours). The mixed nature of the zeolite makes it difficult to understand the mechanisms taking place, and more than one reaction may be taking place.

Table 5.5: Mössbauer parameters of Fe-loaded zeolite comprised of 70 % and 30 % X, exposed to hydrogen gas flow at 500 °C for no, 1, 2, 5, 12 and 24 hours,  $\chi^2 = 0.654635, 1.21819, 0.603153, 0.653543, 0.600623$  and  $0.541441$  respectively. Fixed (unrefined) parameters are marked with \*. Site populations that do not fit the expected pattern are marked in red. Uncertainties are calculated using the covariance matrix. The uncertainty in the natural linewidth of Fe is  $\pm 0.02$  mm/s: values quoted beyond 2 dp are included only to show precision uncertainties.

Reduction /hrs	Species	Peak	Site population /%	IS /mm/s	QS /mm/s	Linewidth /mm/s
None	Octahedral Fe (III)	Doublet	81(5)	0.35 (2)	0.80 (3)	0.25 (2)
	Octahedral Fe (II)	Doublet	19 (6)	1.18 (7)	2.15 (14)	0.25 (10)
1	Octahedral Fe (III)	Doublet	86 (2)	0.373 (6)	0.812 (9)	0.294 (8)
	Octahedral Fe (II)	Doublet	14 (2)	1.03 (3)	2.61 (7)	0.30 (5)
2	Octahedral Fe (III)	Doublet	74 (4)	0.44 (2)	0.94 (3)	0.40 (3)
	Octahedral Fe (II)	Doublet	26 (4)	0.92 (3)	2.54 (5)	0.28 (4)
5	Octahedral Fe (III)	Doublet	92 (2)	0.346 (9)	0.94 (2)	0.35 (1)
	Octahedral Fe (II)	Doublet	8 (2)	1.17 (5)	2.27 (10)	0.21 (7)
12	Octahedral Fe (III)	Doublet	72 (4)	0.37 (1)	0.87 (3)	0.30 (2)
	Octahedral Fe (II)	Doublet	18 (5)	1.19 (10)	2.16 (20)	0.45 (15)
	Fe (0) metal	Sextet	10 (3)	0	B ~ 33 T	0.21*
24	Octahedral Fe (III)	Doublet	83 (3)	0.40 (1)	0.93 (2)	0.33 (2)
	Octahedral Fe (II)	Doublet	18 (4)	0.93 (6)	2.51 (11)	0.33 (9)

Mössbauer spectroscopy was also performed on two 6 hours hydrogen reduced air-exposed AIPO samples: one calcined 10 % Fe-loaded sample, consisting of 100 % berlinite phase, and one uncalcined 20 % Fe-loaded sample, that consists of 80 % AIPO-5 and 20 % berlinite. The berlinite phase was studied to allow for interpretation of the AIPO-5 phase in the mixed sample.

The spectrum of the 100 % berlinite AIPO was fitted to two Lorentzian doublets, corresponding to tetrahedral Fe(III) and octahedral Fe(II) (14 % and 79 % respectively), and one Lorentzian sextet, corresponding to Fe(0) metal (7 %), with  $\chi^2 = 1.74554$  (Figure 5.7 (1), Table 5.6). This sample is readily reducible. Tetrahedral Fe(III) environments correspond to successful inclusion of Fe ions into framework positions; as expected, these sites behave consistently with greater resistivity to reduction. However, whether Fe migrates to the framework upon hydrogen reduction or is already present, but invisible in the pre-reduction material, cannot be confirmed. Relatively narrow linewidths and quadrupole splitting parameters support the conclusion of distinct, relatively symmetric environments.

The spectrum of the 80 % AIPO-5 was fitted to one Lorentzian doublet, corresponding to octahedral Fe(II) (94 %), and one Lorentzian sextet, corresponding to Fe(0) metal (6 %), with  $\chi^2 = 1.1858$  (Figure 5.7 (2), Table 5.6). Again, this sample is readily reducible, with no Fe(III)

remaining and no ions detected in framework positions. There is therefore no evidence for the inclusion of Fe ions into AlPO-5 tetrahedral framework sites. Similar amounts of Fe(0) metal between the two samples suggests that differences in framework do not significantly affect the extent of reduction. Relatively narrow linewidths support the conclusion of distinct environments.

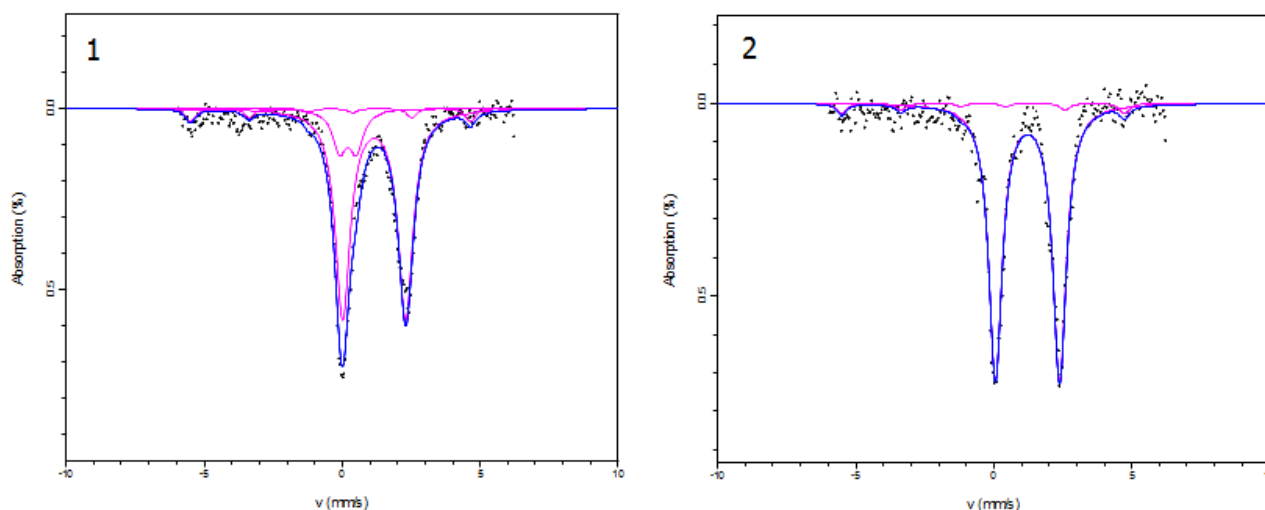


Figure 5.7: Mössbauer spectra of air-exposed 6 hours hydrogen reduced AlPO samples: (1) calcined 10 % Fe-loaded AlPO containing 100 % berlinite phase, and (2) uncalcined 20 % Fe-loaded AlPO containing 80 % AlPO-5 and 20 % berlinite phases.

Table 5.6: Mössbauer parameters of air-exposed 6 hours hydrogen reduced AlPO samples: (1) calcined 10 % Fe-loaded AlPO containing 100 % berlinite phase,  $\chi^2 = 1.74554$ , and (2) uncalcined 20 % Fe-loaded sample containing 80 % AlPO-5 and 20 % berlinite phases,  $\chi^2 = 1.1858$ . Fixed (unrefined) parameters are marked with \*. Uncertainties are calculated using the covariance matrix. The uncertainty in the natural linewidth of Fe is  $\pm 0.02$  mm/s: values quoted beyond 2 dp are included only to show precision uncertainties.

AlPO	Species	Peak	Site population /%	IS /mm/s	QS /mm/s	Linewidth /mm/s
(1) berlinite	Tetrahedral Fe (III)	Doublet	14 (2)	0.21 (5)	0.6*	0.30 (7)
	Octahedral Fe (II)	Doublet	79 (3)	1.165 (9)	2.29 (2)	0.32 (1)
	Fe (0) metal	Sextet	7 (2)	0	B ~ 33 T	0.21*
(2) 80 % AlPO-5	Octahedral Fe (II)	Doublet	94 (4)	1.227 (9)	2.33 (2)	0.29 (1)
	Fe (0) metal	Sextet	6 (4)	0	B ~ 33 T	0.21*

After 3 months of air exposure, the uncalcined 20 % Fe-loaded sample containing 80 % AlPO-5 was remeasured using Mössbauer spectroscopy to test its sensitivity towards oxidation. The spectrum was fitted to one Lorentzian doublet corresponding to octahedral Fe(II) with  $\chi^2 = 3.0351$  (Figure 5.8, Table 5.7). Interestingly, unlike in the zeolite samples, no Fe(II)  $\rightarrow$  Fe(III) oxidation took place upon aerial exposure, suggesting stability towards Fe(II) ions. On the other hand, Fe(0) populations were depleted. Although no Fe(0) metal is identified in the spectrum, this does not mean it is not present, merely that it cannot be clearly distinguished. Smaller populations of Fe(0) metal may persist. After three months, a small distortion in the linewidth ratio is observed. This

asymmetry can arise from texture effects such as preferred orientation, impurity species, inherent properties of the crystal structure, or the Goldanskii-Karyagin effect, when the probability of emission or adsorption is anisotropic(218). The effect may be due to the presence of oxidation product impurities or changes to the AlPO structure. Significant Fe-loading on the sample surface may dominate the Mössbauer spectrum.

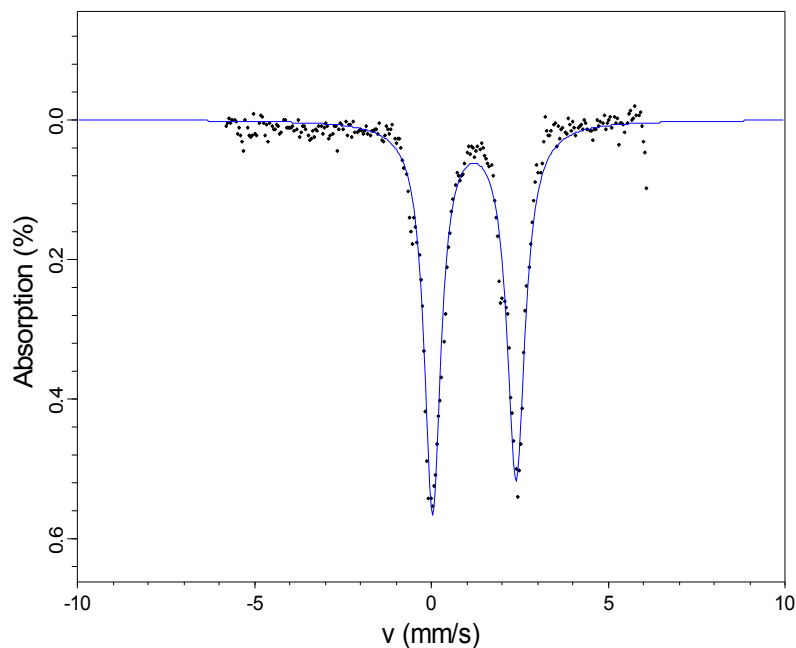


Figure 5.8: Mössbauer spectrum of air-exposed 6 hours hydrogen reduced uncalcined 20 % Fe-loaded AlPO containing 80 % AlPO-5 and 20 % berlinite phases after 3 months of further air exposure.

Table 5.7: Mössbauer parameters of air-exposed 6 hours hydrogen reduced uncalcined 20 % Fe-loaded sample containing 80 % AlPO-5 and 20 % berlinite phases after 3 months of further air exposure,  $\chi^2 = 3.0351$ . Fixed (unrefined) parameters are marked with \*. Uncertainties are calculated using the covariance matrix. The uncertainty in the natural linewidth of Fe is  $\pm 0.02$  mm/s: values quoted beyond 2 dp are included only to show precision uncertainties.

Species	Peak	Site population /%	IS /mm/s	QS /mm/s	Linewidth /mm/s	w-/w+
Octahedral Fe (II)	Doublet	100	1.220 (4)	2.360 (9)	0.21 (7)	0.91 (3)

One sample of the LAU framework AlPO reduced for 6 hours under hydrogen gas flow was examined using Mössbauer spectroscopy. The spectrum was fitted to two Lorentzian doublets corresponding to tetrahedral Fe(III) and octahedral Fe(II), 11 % and 89 % respectively, with  $\chi^2 = 0.963491$  (Figure 5.9, Table 5.8). The Fe ions in this sample seem to be readily reducible and the sample contains framework ions that are more difficult to reduce and may require longer reduction times or higher temperatures. No Fe(0) metal was detected. Narrow linewidths and relatively low quadrupole splitting parameters suggest that discrete Fe environments exist, with low distortion. The stability of Fe(II) species after prolonged aerial exposure was not examined.

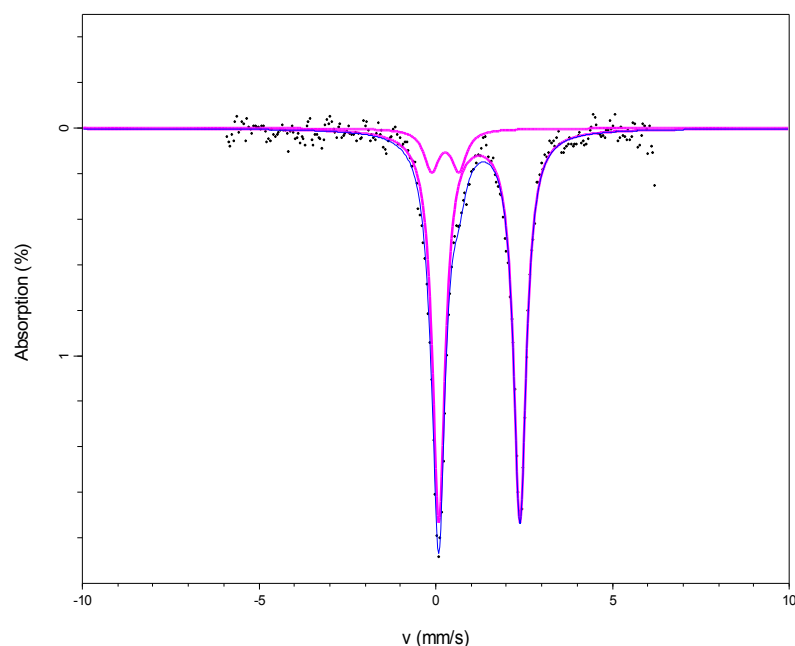


Figure 5.9: Mössbauer spectrum of 6 hours hydrogen reduced LAU AIPO.

Table 5.8: Mössbauer parameters of 6 hours hydrogen reduced Fe-loaded LAU AIPO,  $\chi^2 = 0.963491$ . Uncertainties are calculated using the covariance matrix. The uncertainty in the natural linewidth of Fe is  $\pm 0.02$  mm/s; values quoted beyond 2 dp are included only to show precision uncertainties.

Species	Peak	Site population /%	IS /mm/s	QS /mm/s	Linewidth /mm/s
Tetrahedral Fe (III)	Doublet	11 (2)	0.27 (5)	0.77 (9)	0.25 (7)
Octahedral Fe (II)	Doublet	89 (3)	1.235 (5)	2.295 (9)	0.219 (7)

### ***EPR Spectroscopy***

EPR spectroscopy was employed to complement the data gathered on hydrogen reduced samples by Mössbauer spectroscopy. Signals are interpreted as discussed in Chapter 4.

One 12 hour hydrogen gas reduced Fe-loaded zeolite X sample was measured, providing only a broad signal at  $g \sim 2$  and no additional features. This is almost certainly the result of Fe(III) depletion and clustering.

More interesting data were collected on the uncalcined 20 % Fe-loaded sample containing 80 % AIPO-5. After hydrogen reduction for 6 hours at 500 °C, a low intensity spectrum with several features is revealed (Figure 5.10), in contrast to its non-hydrogen reduced sample, which recorded a smooth curve with distinct  $g \sim 2$  signal and only a small, broad  $g = 4.4$  feature (page 92). The  $g \sim 2$  signal intensity is substantially decreased relative to the background as octahedral Fe(III) populations are reduced. The  $g = 4.4$  signal is retained, but changes in shape, becoming sharper and

more distinct, complicated by proximity to a  $g = 4.7$  signal of a different, sharper shape. Poor resolution ridges also appear both above and below  $g \sim 2$  which may be impurities. Most interesting, however, is the sharp peak cutting the  $g \sim 2$  signal. The exact  $g$  value can provide insight into the origin of this line. This line was measured between field = 3500.528 and 3512.26, giving a centre point at  $g$ -value 1.9956 to 4 sf. The similarity between this number and the  $g$ -value of 1.9959 recorded for the same 20 % Fe-loaded sample containing 80 % AlPO-5 after calcination but before hydrogen gas treatment suggests that it arises from the same origin (Figure 4.18). Thus it is unlikely that the peak is due to Fe(0) metal species which may have caused paramagnetism: instead, radicals produced by the breakdown of organic templates is more likely.

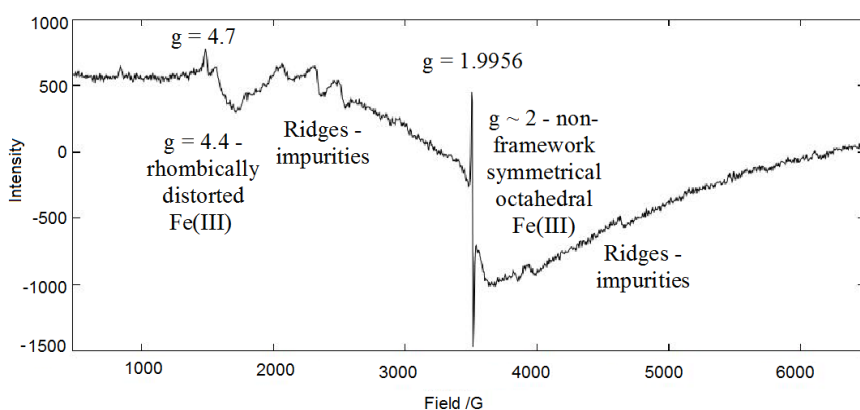


Figure 5.10: EPR spectrum of 6 hours hydrogen reduced uncalcined 20 % Fe-loaded sample of 80 % AlPO-5 and 20 % berlinite phases,  $\nu = 9.793758$  GHz.

The EPR spectrum of one calcined 10 % Mn-loaded sample containing 23 % AlPO-5 shows no interesting features after hydrogen reduction for 6 hours at 500 °C, only a broad  $g \sim 2$  signal arising from exchange interactions.

The 6 hour 500 °C hydrogen reduced LAU AlPO, however, provides a spectrum with a somewhat sharper  $g \sim 2$  signal and accompanying loss in intensity, probably as Fe(III) species are exchanged out (Figure 5.11). The presence of a broad  $g = 4.4$  signal is consistent with the tetrahedral framework sites observed in the Mössbauer spectrum (Figure 5.9, Table 5.8).

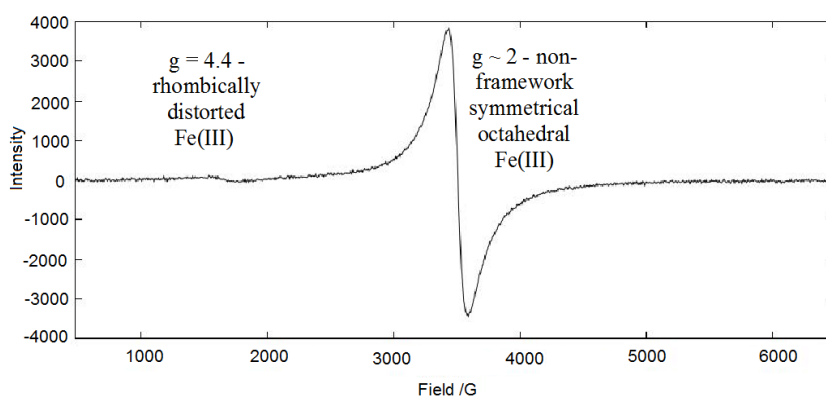


Figure 5.11: EPR spectrum of 6 hours hydrogen reduced Fe-loaded LAU AlPO,  $\nu = 9.795069$  GHz.

### XRD

The gradual breakdown of zeolites caused by metal or metal oxide aggregates in the pores is traditionally observed as a loss of crystallinity in diffraction patterns, *i.e.* a drop off in peak intensities as Si-O and Al-O links are severed, and then the formation of metal and metal oxide peaks. Since Mössbauer spectroscopy of hydrogen reduced Fe-loaded zeolite X samples detects the formation of Fe(0) metal aggregates after 3 hours of exposure, the formation of new peaks is predicted after this time. XRD patterns were obtained for alginate-templated Fe-loaded zeolite X samples exposed to hydrogen gas flow at 500 °C for up to 24 hours (Figure 5.12). In agreement with the Mössbauer spectroscopy, small peaks are seen at  $2\theta = 44.5$  and  $65.0$  after 3 hours of hydrogen gas exposure, although the  $2\theta = 44.5$  peak is first observed after just 1 hour. These peaks represent Fe(0) metal clusters forming in the sample, in agreement with the Mössbauer spectroscopy findings (Figure 5.5, Table 5.3). No iron oxide phases were detected. Zeolite peak intensity visibly decreases across the series, with the intensity of the first peak dropping down to  $\sim 1/4$  between the parent sample and 1 hour hydrogen reduced sample. After 24 hours of hydrogen gas exposure the structure breaks down and crystallinity is almost entirely destroyed. This indicates that the size of Fe(0) metal aggregates has exceeded the capacity of cavities within the zeolite pore network, causing the structure to rupture.

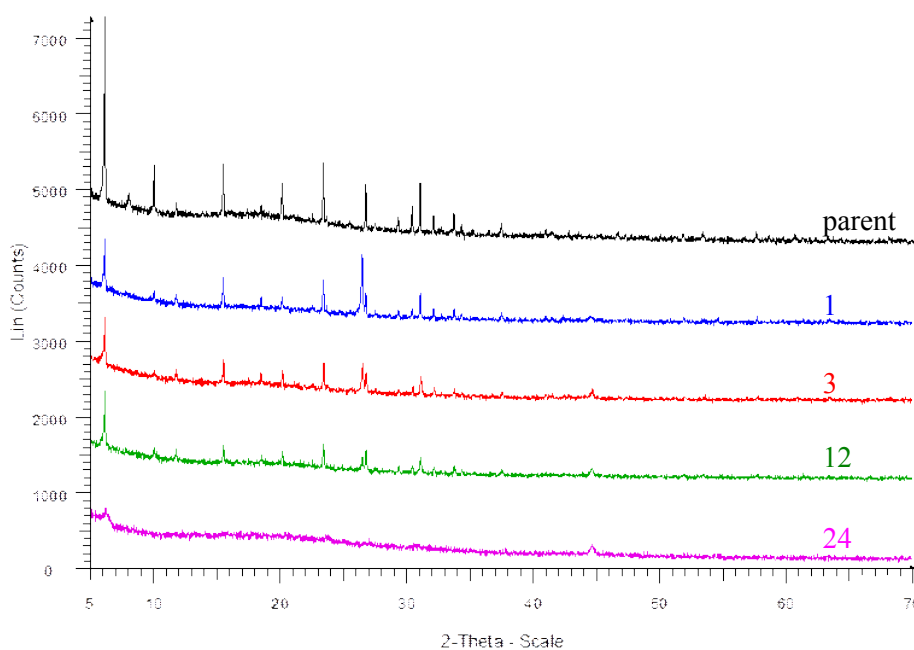


Figure 5.12: PXRD patterns of five samples of 2% alginate templated Fe-loaded zeolite X, original (black) and reduced under 500 °C hydrogen gas flow for 1 hour (blue), 3 hours (red), 12 hours (green) and 24 hours (pink).

PXRD of the mixed zeolite X and A sample also demonstrated structural breakdown after 24 hours of hydrogen gas exposure, but Fe(0) metal peaks are not observed (Figure 5.13).

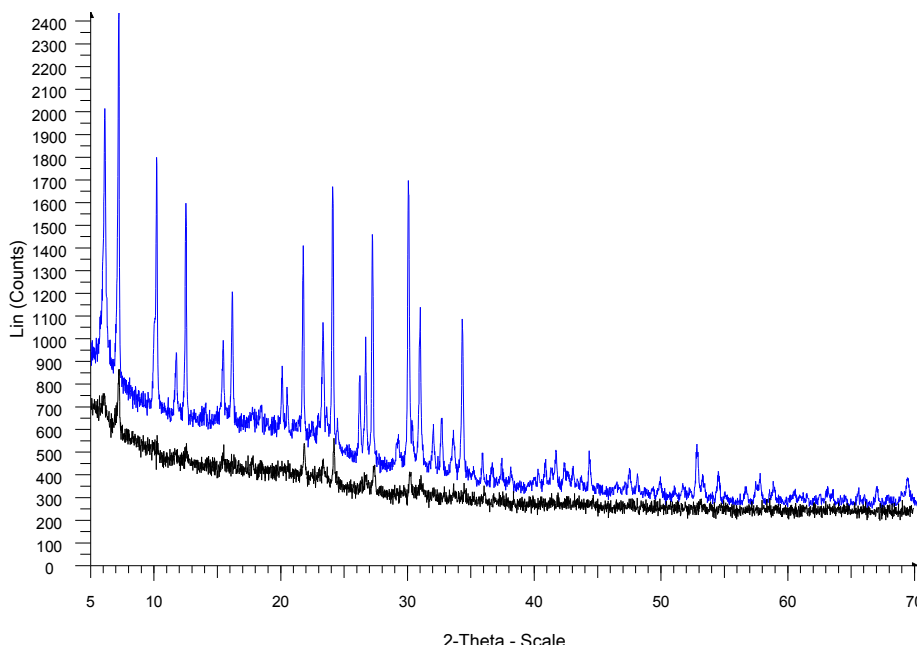


Figure 5.13: PXRD patterns of two samples of mixed phase zeolite comprising 70 % A and 30 % X, original (blue) compared with 24 hour 500 °C hydrogen gas reduced (black).

In the PXRD of 20 % Fe-loaded uncalcined sample containing 80 % AlPO-5, whilst the structure was not destroyed after 6 hours of hydrogen gas flow, some intensity was lost, peak splitting and some suggestion of emerging preferred orientation observed (Figure 5.14).

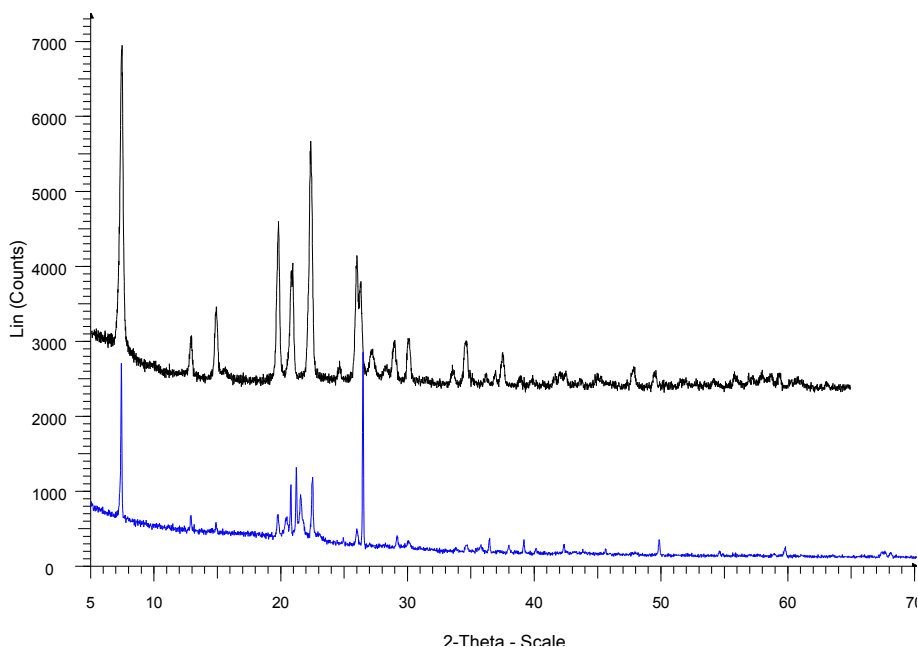


Figure 5.14: PXRD patterns of two samples of uncalcined 20 % Fe-loaded AlPO containing 80 % AlPO-5 and 20 % berlinite impurity, original (black) and 6 hours 500 °C hydrogen reduced (blue).

SEM imaging may also be used to detect the formation of Fe(0) metal and oxide aggregates, but in these samples could not distinguish Fe particles from other inter-crystal impurities.

### *XRF Spectroscopy*

XRF spectroscopy was performed on several Fe-loaded zeolite X samples (Table 5.9) and several Fe/Mn-loaded AIPO samples (Table 5.10) that had been heated under hydrogen gas flow for a number of hours and then later exposed to chromate solution.

*Table 5.9: XRF spectroscopy data from calibrated fused beads of 500 °C hydrogen gas reduced 2 % alginate templated Fe-loaded zeolite X samples.*

<b>H<sub>2</sub> reduced Fe-loaded zeolite X</b>	<b>Si/Al</b>	<b>Fe/Na</b>	<b>Fe/Si</b>	<b>mg<sub>Fe</sub>/g<sub>sieve</sub></b>	<b>mg<sub>Cr</sub>/g<sub>sieve</sub></b>
<b>0 hours</b>	1.59	1.11	0.27	95.7	10.7
<b>1 hour</b>	1.58	0.95	0.28	95.1	16.8
<b>3 hours</b>	1.58	0.93	0.28	94.3	16.4
<b>6 hours</b>	1.57	1.07	0.28	96.6	10.9
<b>12 hours</b>	1.58	1.00	0.28	96.7	5.6
<b>24 hours</b>	1.68	1.01	0.28	97.0	21.3

Table 5.9 indicates a variation in chromium uptake across the series of hydrogen gas exposure times, whilst overall Fe populations remain steady across the series. Thus chromium uptake must not be governed by a simple adsorption mechanism and is dependent upon oxidation state. Although Fe(II) populations are mostly higher in the hydrogen reduced compounds than the non hydrogen reduced compounds, chromate uptake was not as high as 29.1 mg<sub>Cr</sub>/mg<sub>sieve</sub>, reported in Table 3.8. This may be partially due to natural variation between samples. If the adsorption-reduction mechanism is taking place and the sieves select for positively charged hydrated Cr(III) ions, greater Fe(0) and Fe(II) populations should increase uptake. This should lead to a steady increase in chromium uptake across the series, which is not observed. It may therefore be assumed that Fe(0) does not readily oxidise and that Fe(II) species are required for the reduction. Fe(II) populations initially increase with hydrogen gas exposure time and then start to decrease at a slower rate as Fe(0) metal is evolved after 3 hours. This mechanism predicts the highest uptakes around 1-3 hours, *i.e.* the trend that is observed except for an unexpectedly high uptake of 21 mg<sub>Cr</sub>/mg<sub>sieve</sub> after 24 hours of hydrogen gas exposure. A high Si/Al ratio, and loss of crystallinity seen in the XRD pattern (Figure 5.12), suggest that by 24 hours the zeolite structure breaks down as large Fe aggregates form; the remaining solid may be rich in chromium.

*Table 5.10: XRF spectroscopy data from calibrated fused beads of 500 °C hydrogen gas reduced uncalcined AlPO samples. The 20 % Fe-loaded AlPO comprises of 80 % AlPO-5 and 20 % berlinite impurity phase, whilst the 10 % Mn-loaded AlPO comprises 23 % AlPO-5, 40 % berlinite and 37 % cristobalite phases. M = Fe or Mn.*

Sieve		Al/P	M/P	mg <sub>M</sub> /g <sub>sieve</sub>	mg <sub>Cr</sub> /g <sub>sieve</sub>
<b>Uncalcined 20 % Fe AlPO-5</b>	<b>Pre-Cr treatment</b>	0.98	0.09	37.7	0.6
	<b>Post Cr-treatment</b>	1.00	0.09	34.5	1.0
<b>Uncalcined 10 % Mn AlPO-5</b>	<b>Pre-Cr treatment</b>	1.09	0.12	44.7	0.5
	<b>Post Cr-treatment</b>	1.12	0.11	39.2	4.5

Table 5.10 suggests that although relative chromium uptakes are still lower in the AlPO systems than the zeolite systems, chromium uptakes in Fe-loaded systems are consistently increased by hydrogen gas exposure for 6 hours and reduction of almost all Fe(III) species to Fe(II), except those identified in framework positions (Figure 5.7 (1), Table 5.6 and Figure 5.9, Table 5.8). Uncalcined 20 % Fe-loaded sample containing 80 % AlPO-5 increased its chromium uptake from 0.6 to 1.0 mg<sub>Cr</sub>/mg<sub>sieve</sub> and the uncalcined 10 % Mn-loaded sample containing 23 % AlPO-5 increased from 3.3 to 4.4 mg<sub>Cr</sub>/mg<sub>sieve</sub>. This suggests that Mn species may also be in higher oxidation states prior to hydrogen gas exposure. Results highlight both the importance of redox-active species and the effectiveness of the target mechanism, but also the importance of structure in directing uptake of species and facilitating reduction under hydrogen gas flow.

### **Summary**

Heating under H<sub>2</sub> provides fine control over oxidation state. In Fe-loaded zeolite X, Fe(III) steadily decreases upon hydrogen gas exposure, whilst Fe(II) initially decreases then increases as Fe(0) aggregates over 1000 atoms form, causing the breakdown of the molecular sieves. In mixed zeolite X and A systems, oxidation occurs for some systems. Impurities provide a distinct sharp EPR signal.

### **5.3. Changes Upon Chromate Exposure**

Mössbauer and EPR spectroscopy measurements of chromate-exposed samples was used to determine whether the oxidation states of Fe populations had been affected by exposure.

#### ***Mössbauer Spectroscopy***

The Mössbauer spectrum of one chromium exposed Fe-loaded 12 hours 500 °C hydrogen

gas exposed zeolite X sample was fitted to two Lorentzian doublets corresponding to octahedral Fe(III) and Fe(II), 95 % and 6 % respectively, with  $\chi^2 = 0.857686$  (Figure 5.15, Table 5.11). This extent of Fe(III) population increase suggests that Fe(II) has indeed been oxidised by chromate solution. There is no evidence to support the loss of Fe(III) species or introduction of Cr(III) species. A significant increase in the Fe(II) quadrupole splitting parameter, however, suggests that remaining Fe(II) coordination environments are highly distorted: this may be a result of ion migration through the zeolite framework.

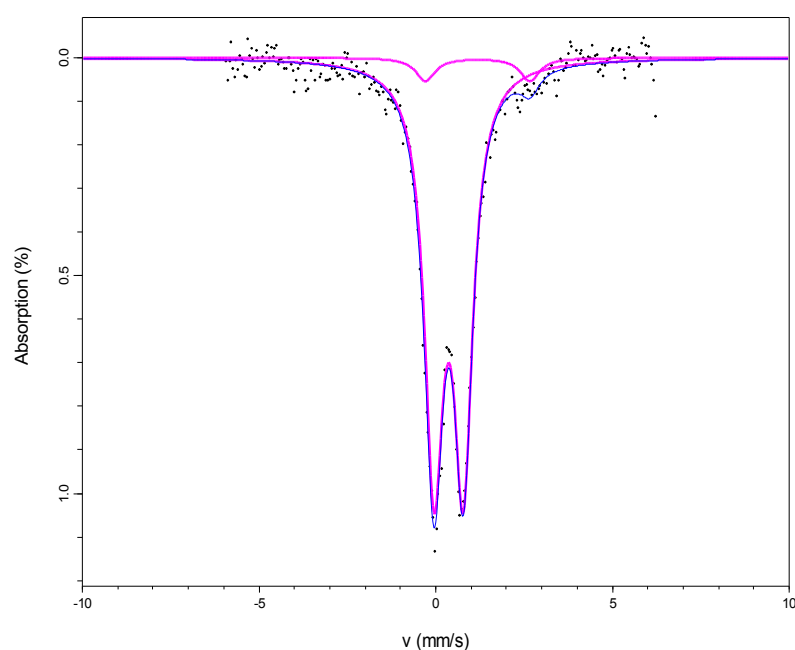


Figure 5.15: Mössbauer spectrum of 12 hours 500 °C hydrogen reduced Fe-loaded zeolite X after chromate exposure.

Table 5.11: Mössbauer parameters of 12 hours 500 °C hydrogen reduced Fe-loaded zeolite X after chromate exposure,  $\chi^2 = 0.857686$ , with non-chromate-exposed 12 hours 500 °C hydrogen reduced Fe-loaded 2 % alginate templated zeolite X (Figure 5.5, Table 5.3) included for comparison. Linewidths that fall below the natural linewidth of  $\alpha$ -iron are marked in red. Uncertainties are calculated using the covariance matrix. The uncertainty in the natural linewidth of Fe is  $\pm 0.02$  mm/s: values quoted beyond 2 dp are included only to show precision uncertainties.

Zeolite	Species	Peak	Site population /%	IS /mm/s	QS /mm/s	Linewidth / mm/s
Chromate-exposed	Octahedral Fe (III)	Doublet	95 (2)	0.365 (8)	0.83 (1)	0.32 (1)
	Octahedral Fe (II)	Doublet	6 (3)	1.18 (14)	2.95 (26)	0.33 (21)
Non-chromate-exposed	Octahedral Fe (III)	Doublet	60 (2)	0.37 (3)	0.87 (7)	0.32 (2)
	Octahedral Fe (II)	Doublet	13 (3)	1.04 (20)	2.25 (40)	0.38 (9)
	Fe (0) metal	Sextet	27 (2)	0	B ~ 33 T	0.14 (2)

Mössbauer spectra were recorded for one uncalcined 20 % Fe-loaded 6 hours 500 °C hydrogen gas exposed sample containing 80 % AlPO-5 (Figure 5.16, Table 5.12). The spectrum for the uncalcined, 20 % Fe-loaded sample was fitted to one Lorentzian doublet corresponding to

octahedral Fe(II), with  $\chi^2 = 0.835924$  (Figure 5.16, Table 5.7). Although no Fe(0) metal is identified, this does not mean it is not present, merely that it cannot be clearly distinguished. Smaller populations of Fe(0) metal may persist. Fe(II) ions are appreciably more stable than in zeolite X, but do not undergo chemical reaction during chromate uptake. This may account for lower chromate uptakes in AIPO systems. Further distortion in the linewidth ratio occurs upon chromate exposure, as observed earlier upon reduction (Figure 5.8, Table 4.15). This may be due to the presence of oxidation product impurities or changes to the AIPO structure.

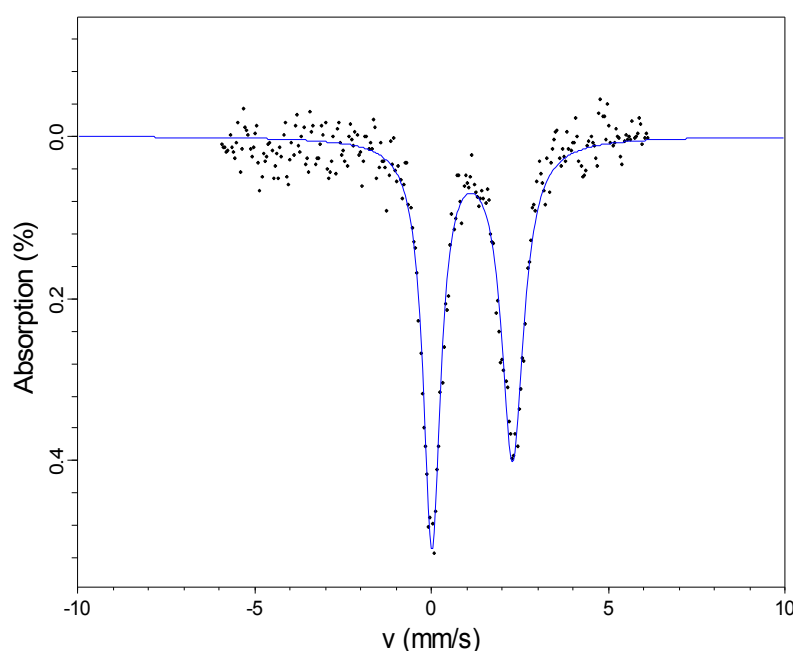


Figure 5.16: Mössbauer spectrum of air-exposed 6 hours 500 °C hydrogen reduced uncalcined 20 % Fe-loaded AIPO containing 80 % AIPO-5 and 20 % berlinite phases after chromate exposure.

Table 5.12: Mössbauer parameters of air-exposed 6 hours 500 °C hydrogen reduced uncalcined 20 % Fe-loaded sample containing 80 % AIPO-5 and 20 % berlinite phases after chromate exposure,  $\chi^2 = 0.835924$ , with non-chromate-exposed air-exposed 6 hours 500 °C hydrogen reduced uncalcined 20 % Fe-loaded sample containing 80 % AIPO-5 and 20 % berlinite phases included for comparison (Figure 5.8, Table 5.7). Uncertainties are calculated using the covariance matrix. The uncertainty in the natural linewidth of Fe is  $\pm 0.02$  mm/s: values quoted beyond 2 dp are included only to show precision uncertainties.

AIPO	Species	Peak	Site population /%	IS /mm/s	QS /mm/s	Linewidth /mm/s	w-/w+
Chromate-exposed	Octahedral Fe (II)	Doublet	100	1.16 (1)	2.28 (2)	0.38 (3)	0.79 (6)
Non-chromate-exposed	Octahedral Fe (II)	Doublet	100	1.220 (4)	2.360 (9)	0.21 (7)	0.91 (3)

### *EPR Spectroscopy*

EPR spectroscopy of chromate-exposed Fe-loaded hydrogen reduced samples was used to

examine the changes to oxidation states and coordination environments. Fe-loaded zeolite sample reduced for 12 hours under hydrogen gas flow was not tested, since there were no interesting features on the non-chromate-exposed sample.

The uncalcined 20 % Fe-loaded AIPO containing 80 % AIPO-5 reduced for 6 hours at 500 °C under hydrogen gas flow was chromate-exposed overnight and then examined using EPR spectroscopy (Figure 5.17). The  $g \sim 2$  signal intensity remains low, suggesting that no large production of Fe(III) ions has occurred. The signal is dominated by the sharp peak seen elsewhere (Figures 4.18 and 5.10). This line was measured between field = 3506.393 and 3512.26, giving a centre point at  $g$ -value 1.9940 to 4 sf. Although a little lower than the other two acquired  $g$ -values for such a peak, one in calcined and one in pre-chromate hydrogen gas treated 20 % Fe-loaded sample containing AIPO-5, this number remains similar. Given that this sample is synthesised from the pre-chromate hydrogen gas treated 20 % Fe-loaded sample containing AIPO-5, it seems likely that the difference is due to measurement error and the peak arises from the same cause: probably trapped radicals produced by the breakdown of organic templates. The typical  $g = 4.4$  signal indicates rhombically distorted octahedral Fe(III) ions, and sits close to a sharp  $g = 4.7$  signal the same shape as another signal at  $g = 8.2$ ; these are likely to arise from an impurity phase. Although the spectrum is complicated by many signals, two distinct ridges of the same shape are seen at  $g = 3.0$  and 2.8, that have been observed elsewhere in this work (Figures 4.18 and 5.10) and attributed to impurity phases. It is possible that these ridges share the same origin as the sharp  $g \sim 2$  signal.

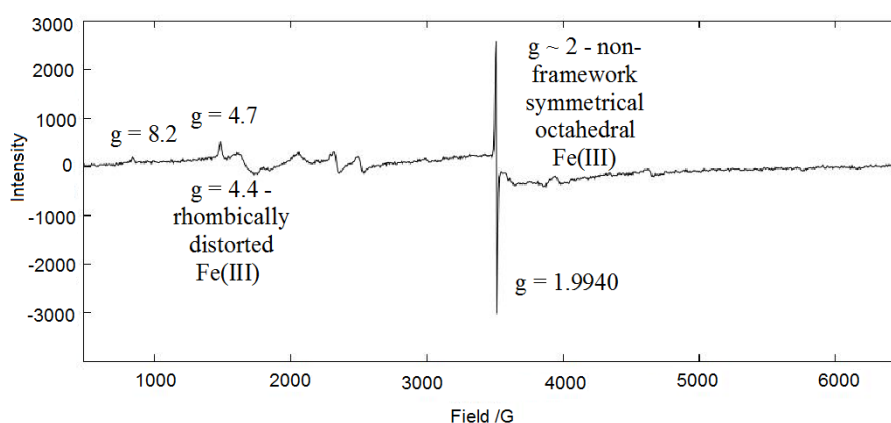


Figure 5.17: EPR spectrum of chromate-exposed uncalcined  $H_2$  reduced 20 % Fe-loaded AIPO containing 80 % AIPO-5 and 20 % berlinite impurity,  $\nu = 9.793981$  GHz.

In the Fe-loaded 6 hour hydrogen reduced LAU AIPO, the EPR spectrum does not look appreciably different after chromate exposure than before. This would correspond to very little loss in Fe species.

***Summary***

Distortion of the AlPO-5 linewidth ratio occurs upon chromate exposure. Fe(0) populations are stable and inactive in zeolite X, yet unstable in AlPO-5.

## Chapter 6: Suitability for Application and Recycling

This chapter looks at the viability of materials explored in previous chapters for effective chromate remediation. The order in which metals are preferentially taken up by zeolite X systems is examined and numbers compared for direct competition between chromate and other metals. Further, attempts have been made to assess the extent of chromium uptake from solutions with concentrations that reflect real levels of contamination, and to compare the extent of uptake to regulatory standards. Finally, the chapter focusses on methods for chromium extraction from molecular sieves after uptake, discussing the potential for molecular sieve recycling and the extent to which the target reduction mechanism has been successful, rendering Cr(III) products. The effect of chromium extraction methods upon oxidation state is also considered.

The ideal material for Cr(VI) remediation would possess a high cation exchange capacity but, under a different set of conditions, low cation retention capacity, facilitating the release of chromium ions. Too high a cation retention capacity and release of Cr(III) for recycling will become difficult; too low a cation retention capacity and Cr(III) will readily exchange out of the molecular sieve in favour of other species. A wide range of exchange and retention capacities exist within the scope of molecular sieves, not just for chromium, but all ions: zeolite P, for example, exhibits a higher Cr(III) cation retention capacity than some commercial exchangers(90). Meanwhile, zeolite A was found to desorb small amounts of Fe(III), Mn(II) and Cu(II) 24 hours after uptake(175).

### 6.1. Competitive Ions

In order to assess the suitability of the preferred system, Fe-loaded zeolite X, XRF spectroscopy was employed to determine the capacity and preferences of the sieve for metals that might compete in industrial waste water solutions. Selectivity is usually governed by the pore sizes in zeolite frameworks, surface area and the availability of different sites. Zeolite X and A have been demonstrated to select for slightly larger Zn(II) over Cd(II) (4.30 and 4.26 Å hydrated radii respectively); it has been suggested that, when in direct competition, smaller ions occupy sites located at the zeolite surface(96). If this suggestion truly reflects the ion exchange and uptake mechanism, and assuming no other factors, zeolite X should demonstrate a higher selectivity for Cr(III) than both Zn(II) and Cd(II), with a hydrated radius of 4.61 Å. However, other factors complicate the mechanism: whilst zeolites have been reported to simultaneously take up Cr(VI)

with other cationic ions, usually Cd(II), which originates in many of the same waste streams, in one study, Cr(III) hydroxide precipitates compromised cooperative cadmium uptake(5,82). Although mixed waste uptake solutions are common and generally useful, too much competition can inhibit the uptake of priority pollutants. Clinoptilolite, although exhibiting good selectivity for caesium in radioactive waste immobilisation, suffers from Ag(I) and Ba(II) competition(82).

In the first test, a mixed metal solution was prepared containing ten metal ions that were considered common heavy metal contaminants in industrial waste water streams, particularly those with harmful effects. Michalev and Petrov, who focus upon the uptake of Cu(II), Pb(II), Cd(II), Zn(II), Cr(III), Ni(II), Co(II) and Mn(II) heavy metal ions by synthetic zeolite, classify heavy metals into three risk categories: high, for mercury, cadmium, lead, arsenic, selenium, zinc and titanium; medium, for cobalt, nickel, molybdenum, copper and chromium; and relatively low, for barium, manganese, vanadium, strontium and aluminium(80). The metals selected for these experiments were Cd(II), Co(II), Cu(II), Fe(III), Mn(II), Ni(II), Pb(II), Sn(II), Zn(II) and of course Cr(VI). Metal ion salts were dissolved into the same solution in equal concentrations of 0.02 M, presumed to be an excess. Two zeolite X samples, one loaded with Fe and one with Mn were exposed to this solution overnight, before being filtered off and prepared as fused beads for XRF spectroscopic analysis. Because of the large number of metals introduced, and their small, unknown uptakes by the zeolite, these measurements were not compared with a specially prepared calibration standard, and instead numbers are measured against in-built XRF S8 Tiger standards. Data are provided in Table 6.1 as milligrams of metal per gram of sieve for ease of direct comparison.  $\text{mg}_{\text{Na}}/\text{g}_{\text{sieve}}$  are also compared, as it is speculated that some of the ion exchange occurs not between Fe/Mn ions in the sieve and metals in solutions, but through further loss of Na ions. Mole percentages are given underneath so that the numbers of adsorbed ions may also be compared.

*Table 6.1: XRF spectroscopy data from uncalibrated fused beads of Fe- and Mn-loaded zeolite X containing a mixture of metal ions in  $\text{mg}_M/\text{g}_{\text{sieve}}$  and mole percentages (italics).*

Sieve	Si/Al	$\text{mg}_{\text{Na}}/\text{g}_{\text{sieve}}$	$\text{mg}_{\text{Fe}}/\text{g}_{\text{sieve}}$	$\text{mg}_{\text{Mn}}/\text{g}_{\text{sieve}}$	$\text{mg}_{\text{Cd}}/\text{g}_{\text{sieve}}$	$\text{mg}_{\text{Co}}/\text{g}_{\text{sieve}}$	$\text{mg}_{\text{Cu}}/\text{g}_{\text{sieve}}$	$\text{mg}_{\text{Ni}}/\text{g}_{\text{sieve}}$	$\text{mg}_{\text{Pb}}/\text{g}_{\text{sieve}}$	$\text{mg}_{\text{Sn}}/\text{g}_{\text{sieve}}$	$\text{mg}_{\text{Zn}}/\text{g}_{\text{sieve}}$	$\text{mg}_{\text{Cr}}/\text{g}_{\text{sieve}}$
Fe-zeolite X	1.54	32.78	95.36	1.65	2.46	1.55	1.46	2.55	18.42	10.79	2.60	2.15
		<i>39.8</i>	<i>47.7</i>	<i>0.8</i>	<i>1.3</i>	<i>0.7</i>	<i>1.1</i>	<i>1.2</i>	<i>2.5</i>	<i>2.5</i>	<i>1.1</i>	<i>1.2</i>
Mn-zeolite X	1.60	25.17	7.55	83.90	6.74	3.10	5.85	5.26	4.14	9.80	5.56	4.54
		<i>32.9</i>	<i>4.1</i>	<i>45.9</i>	<i>1.8</i>	<i>1.6</i>	<i>2.8</i>	<i>2.7</i>	<i>0.6</i>	<i>2.5</i>	<i>2.6</i>	<i>2.6</i>

The order of preferential uptake differs between Fe- and Mn-loaded zeolite X. For Fe-loaded zeolite X, the order of ion uptake by weight is:

$$\text{Pb} > \text{Sn} > \text{Zn} \sim \text{Ni} \sim \text{Cd} > \text{Cr} > \text{Mn} \sim \text{Co} \sim \text{Cu}$$

And by mole:



It is important to note that the extent of Fe-uptake cannot be assessed in this system, due to its presence in the sieve before exposure to the mixed metal ion solution.

Similarly, for Mn-loaded zeolite X, the order of ion uptake by weight is:



And by mole:



In this system, the extent of Mn-uptake cannot be assessed, due to its presence in the sieve before exposure to the mixed metal ion solution.

The order of uptake is not the same between the two systems, suggesting that redox activity also significantly affects uptake; for example, the uptake of lead is high compared with other metals in Fe-loaded zeolite X, whilst relatively low in Mn-loaded zeolite X, as well as quantitatively smaller. Despite the reports by Izidoro *et al.*, Zn(II) uptake was only observably higher than Cd(II) uptake in Mn-loaded zeolite *via* mole percentages(96).

Crucially, chromium appears low down the lists for uptake by weight in both Fe- and Mn-loaded zeolite X. Although mole percentages give better results, it is still not the dominantly selected ion in either system. It is possible that the two-step reduction-ion exchange mechanism kinetically hinders its selectivity. More than double the amount of chromium is taken up in the Mn-loaded than Fe-loaded system, suggesting that chromium does better in competition when in a Mn(II) environment. However, uptake is still lower than when competition-free (Table 3.8).

Uptake values were not always significantly different between competing ions, such that comparisons must be made with caution. Since it is impossible to be certain the extent to which differences in values reflect selectivities of the systems or fluctuations in uptake, further tests were done to assess the competition between some of these ions in binary systems, competing with Cr(VI) for uptake by the preferred system, Fe-loaded zeolite X. Fe, Mn and Co ions were excluded: Fe ions pose little toxicity risk and uptake cannot be assessed in an Fe-loaded zeolite, and Mn and Co ions are not appreciably taken up by Fe-loaded zeolite X in comparison to Cr(VI). In addition, this list is anything but exhaustive, and already excludes some metals, such as arsenic (which also forms an anion), which are of especial environmental concern. A Cr(VI) only system was compared. All metals were prepared at 0.02 M concentrations. XRF spectroscopy of fused beads of samples exposed to binary and Cr(VI) systems were measured. Due to small, unknown uptake values, these

measurements were not compared with a specially prepared calibration standard, and instead numbers are measured against in-built XRF S8 Tiger standards. Data are provided in Table 6.2.

*Table 6.2: XRF spectroscopy data from uncalibrated fused beads of Fe-loaded zeolite X exposed to solutions containing chromate and other metals.*

Exchange ions	Si/Al	Fe/Na	Fe/Si	mg <sub>Fe</sub> /g <sub>sieve</sub>	mg <sub>M</sub> /g <sub>sieve</sub>	mg <sub>Cr</sub> /g <sub>sieve</sub>	M/Cr
<b>Cr</b>	1.51	0.84	0.24	81.1	-	29.0	-
<b>Cd and Cr</b>	1.50	1.22	0.24	76.8	37.9	30.0	0.58
<b>Cu and Cr</b>	1.50	1.17	0.25	83.6	22.8	28.2	0.66
<b>Ni and Cr</b>	1.51	1.22	0.25	83.0	23.6	33.6	0.62
<b>Pb and Cr</b>	1.52	0.97	0.21	60.5	141.3	22.5	1.58
<b>Sn and Cr</b>	1.55	0.97	0.21	65.6	70.0	29.9	1.03
<b>Zn and Cr</b>	1.52	0.99	0.25	83.0	18.1	29.0	0.50

The order of ion uptake by weight is:

$$\text{Pb} > \text{Sn} > \text{Cd} > \text{Ni} \sim \text{Cu} > \text{Zn}$$

And by mole:

$$\text{Pb} > \text{Sn} > \text{Cu} > \text{Ni} > \text{Cd} > \text{Zn}$$

These data suggest that the most highly adsorbed ions by Fe-loaded zeolite X are repeatedly measured as lead and tin. With M/Cr ratios greater than 1, they are also the greatest chromium competitors, where other ions are less readily taken up, with M/Cr ratios less than 1. However, it is noticeable that chromium uptake levels are not appreciably affected by the uptake of other ions, averaging 28.9 mg<sub>Cr</sub>/g<sub>sieve</sub>, indistinguishable the 29.0 mg<sub>Cr</sub>/g<sub>sieve</sub> uptake recorded in the absence of competitive ions (Table 3.8). Only in competition with lead is the uptake of chromium affected (reduced to 22.5 mg<sub>Cr</sub>/g<sub>sieve</sub>).

In conclusion, Fe-loaded zeolite X readily takes up chromium, and functions well as a binary mixed waste sequester, taking up other ions without loss of chromium capacity, except for lead, with which it competes. At high concentrations of mixed ion solutions and a larger selection of competitive species, all ion uptakes are affected and only small amounts of each metal are taken up into the zeolite. The identification of competitive ions may be of value in the later extraction of chromium from molecular sieves.

### **Summary**

Uptake of chromium alongside competitive ions demonstrate the potential for mixed ion uptake systems, including mixed anion/cations.

## 6.2. Extent of Removal

Since all previous treatments with chromate solution were in excess, an experiment was devised to study chromate uptake from solutions at more realistic concentrations. The purpose of this was to determine whether the proposed systems could be useful industrially in the application of chromate remediation. A good system should lower the chromium content of waste water below standard safety limits when prepared at concentrations comparable to observed industrial levels. Hawley *et al.* state that natural levels of chromate contamination in water are around 10 µg/l, whilst the World Health Organisation quotes 50 µg/l as an acceptable maximum concentration(18). In contaminated areas, chromate in water may reach hazardous levels between 300 and 500 µg/l. Tests were carried out on “simulated waste water” solutions with concentrations between 50 and 500 µg/l at 50 µg/l intervals with the aim of reducing the chromate concentration below the WHO acceptable level.

Work from earlier chapters has suggested that promising systems include (i) Fe-loaded zeolite X, (ii) H<sub>2</sub> reduced Fe-loaded zeolite X, and (iii) H<sub>2</sub> reduced Fe-loaded AlPO-5 (Tables 3.8, 5.9 and 5.10). Data suggests that 3 hours of Fe-loaded zeolite X exposure and 6 hours of Fe-loaded AlPO-5 exposure produces optimal systems, however, both hydrogen reduced systems were exposed together for 6 hours to allow for direct comparability. All three systems were exposed to the “simulated waste water” solutions to test their applicability. Results are presented in Table 6.3 for both liquid ICP and solid XRF spectroscopic measurements. Liquid XRF results were also measured: tin was added to solutions at a ratio of 200:1 mole of chromium originally present in order to reduce harmful Cr(VI) to less harmful Cr(III) and provide an exact ratio against which the chromium content could be compared. The XRF spectrometer measures mass percentages down to parts per million, more or less accurately depending upon the element. The theoretical maximum chromium percentage corresponds to Sn/Cr = 200, *i.e.* all the chromium moles are present in solution. A good threshold at which to expect detection might be 0.001 % (10 ppm). This level of detail should be adequate to detect chromium loadings close to the maximum theoretical values, even in liquids, for which the concentration is lower than in the solids. However, the spectrometer proved unable to detect chromium in liquids, and solid detection occurred only for AlPO samples, for which a systematic zero error exists. The errors associated with measurement are larger than the measured values.

ICP results were more useful. Lower detection of chromium implies loss of Cr species *via* uptake into molecular sieves. Slight dilution during solid washing means that concentrations may fluctuate in liquid samples.

*Table 6.3: XRF spectroscopy data of Cr content in calibrated fused beads and ICP data of Cr content in liquid samples of (i) Fe-loaded zeolite X, (ii) 6 hours hydrogen gas reduced Fe-loaded zeolite X and (iii) 6 hours hydrogen reduced sample containing AIPO-5 phase after exposure to “simulated waste water” containing realistic concentrations of chromium.*

Concentration of Cr/ $\mu\text{g/l}$	Sample	ICP Liquid		XRF Solid	
		Chromium content $\mu\text{g/l}$ (ppb)	Iron content $\mu\text{g/l}$ (ppb)	Theoretical maximum Cr %	Chromium % of theoretical
50	Fe-loaded zeolite X	0.63	10940	0.25	-
	6 hours H <sub>2</sub> reduced Fe-loaded zeolite X	4.72	778.4	0.25	-
	6 hours H <sub>2</sub> reduced Fe-loaded AIPO-5	4.76	1397	0.25	0.11
100	Fe-loaded zeolite X	5.28	12240	0.50	-
	6 hours H <sub>2</sub> reduced Fe-loaded zeolite X	3.22	14520	0.50	-
	6 hours H <sub>2</sub> reduced Fe-loaded AIPO-5	0.66	448.9	0.50	0.11
150	Fe-loaded zeolite X	4.91	13780	0.75	-
	6 hours H <sub>2</sub> reduced Fe-loaded zeolite X	< 0.1	10430	0.75	-
	6 hours H <sub>2</sub> reduced Fe-loaded AIPO-5	< 0.1	35.19	0.75	0.10
200	Fe-loaded zeolite X	7.74	12270	1.00	-
	6 hours H <sub>2</sub> reduced Fe-loaded zeolite X	3.72	22260	1.00	-
	6 hours H <sub>2</sub> reduced Fe-loaded AIPO-5	1.57	68.43	1.00	0.15
250	Fe-loaded zeolite X	7.09	13230	1.25	-
	6 hours H <sub>2</sub> reduced Fe-loaded zeolite X	18.33	1275	1.25	-
	6 hours H <sub>2</sub> reduced Fe-loaded AIPO-5	4.28	406.6	1.25	0.12
300	Fe-loaded zeolite X	17.84	15230	1.50	-
	6 hours H <sub>2</sub> reduced Fe-loaded zeolite X	0.31	13640	1.50	-
	6 hours H <sub>2</sub> reduced Fe-loaded AIPO-5	3.77	567.7	1.50	0.10
350	Fe-loaded zeolite X	4.41	10080	1.75	-
	6 hours H <sub>2</sub> reduced Fe-loaded zeolite X	16.01	1430	1.75	-
	6 hours H <sub>2</sub> reduced Fe-loaded AIPO-5	8.03	84.81	1.75	0.10
400	Fe-loaded zeolite X	16.20	13580	2.00	-
	6 hours H <sub>2</sub> reduced Fe-loaded zeolite X	20.13	4697	2.00	-
	6 hours H <sub>2</sub> reduced Fe-loaded AIPO-5	3.20	159.2	2.00	0.13
450	Fe-loaded zeolite X	1.20	21580	2.25	-
	6 hours H <sub>2</sub> reduced Fe-loaded zeolite X	25.95	4500	2.25	-
	6 hours H <sub>2</sub> reduced Fe-loaded AIPO-5	6.74	1594	2.25	0.12
500	Fe-loaded zeolite X	52.98	19540	2.50	-
	6 hours H <sub>2</sub> reduced Fe-loaded zeolite X	67.31	3198	2.50	-
	6 hours H <sub>2</sub> reduced Fe-loaded AIPO-5	71.68	14.44	2.50	0.12

ICP results show that 0.5 g of Fe-loaded zeolites and AlPOs in 25 cm<sup>3</sup> solution is sufficient to extract chromium to below the WHO limit 50 µg/l up to initial concentrations of 450 µg/l. At 500 µg/l, values for all three systems lie > 50 µg/l, and a second cycle or larger sieve volumes would be required. Large leaching of Fe suggests that ion exchange and surface species loss occur simultaneously. Whilst it varies widely, this is naturally higher for zeolite samples with higher initial Fe-loadings than the AlPO system. Although the WHO limit for iron is significantly higher than that of chromium (0.3 mg/l), many of these numbers do fall above the guideline limit. This implies that lower initial Fe-loadings or subsequent solution treatment with a Na-loaded molecular sieve to regenerate an Fe-loaded catalyst (that would then need to be reduced under H<sub>2</sub> gas to become active) would need to be implemented industrially.

XRF spectroscopic plots were inspected. Much lower intensity peaks in the liquid compared with solid samples were observed, as predicted (Figure 6.1). Tentatively assigned Cr peaks can be seen in many of the spectra belonging to solid samples, in particular in the hydrogen reduced Fe-loaded zeolite X, whilst no evidence for any such peaks may be detected in liquid samples. This is in agreement with the ICP data. In one uncalibrated measurement of hydrogen reduced Fe-loaded zeolite X, 0.01 % Mn was detected and the Mn peak seen beside one of the possible Cr peaks. This Mn peak is of a comparable order of magnitude to the possible Cr peak (Figure 6.1).

Evidence supports the conclusion that chromium has been adsorbed by the solid, and the systems explored here are suitable chromium adsorbers at realistic concentrations of chromium wastewater contamination, although the problem of extensive Fe leaching must be considered carefully.

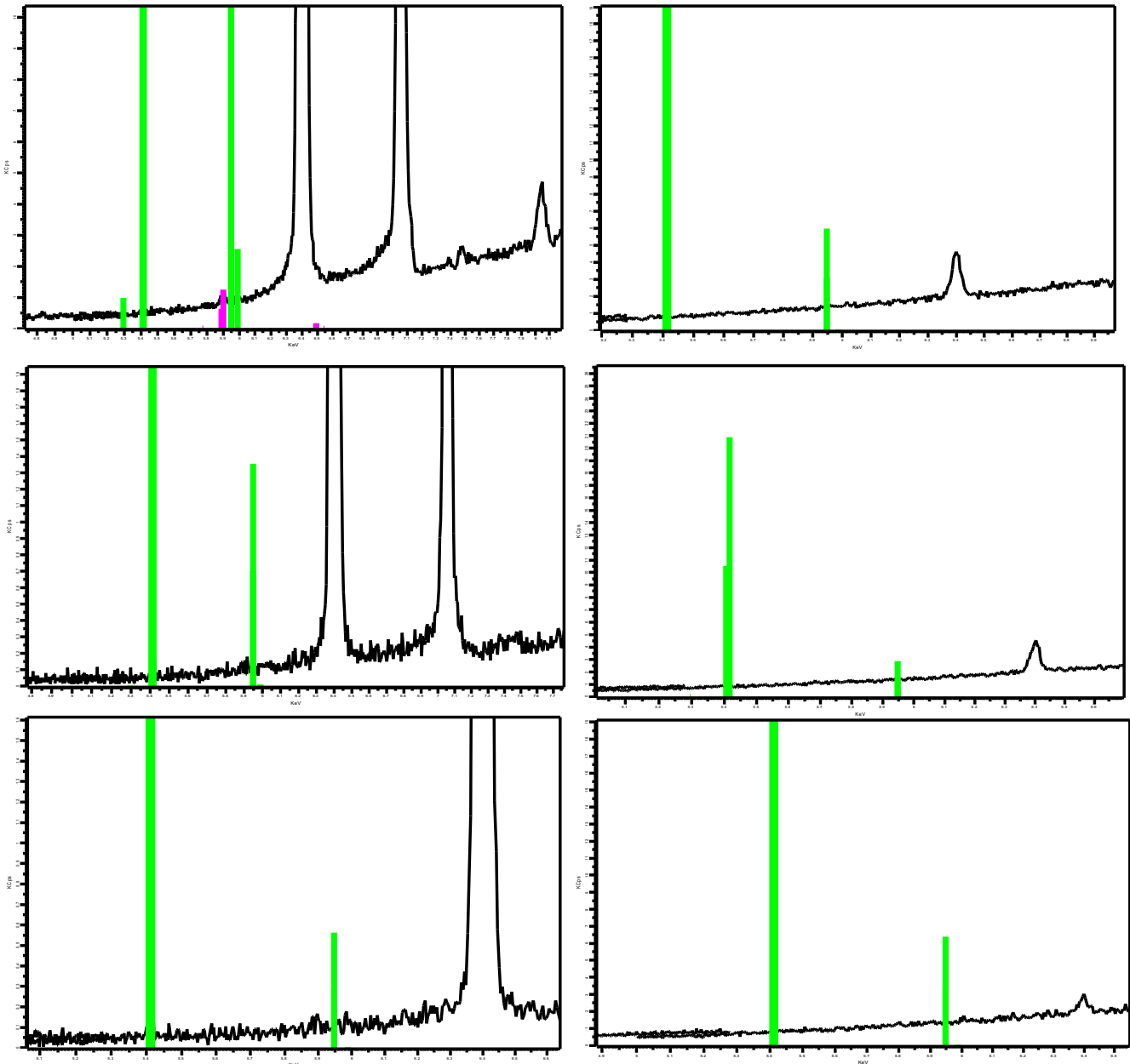


Figure 6.1: XRF spectroscopy images with solids left and liquids right. Top: 6 hours hydrogen reduced Fe-loaded zeolite X sample prepared at 500 °C and exposed to 500 µg/l chromate solution; middle: Fe-loaded zeolite X exposed to 100 µg/l chromate solution; bottom: 6 hours hydrogen reduced 20 % Fe-loaded AlPO-5-containing sample exposed to 200 µg/l chromate solution. Green lines indicate expected peak positions for chromium; pink lines indicate expected peak positions for manganese.

### Summary

6.2 Three Fe-loaded systems: zeolite X, hydrogen reduced zeolite X and hydrogen reduced AlPO-5 were shown to reduce the chromium content of wastewaters below the WHO recommended limit of 50 µg/l up to concentrations of 450 µg/l. Surface contamination of chromium species may be limiting factor for CEC. Iron is appreciably sequestered, providing the problem of a secondary waste stream.

### 6.3. Chromium Extraction and Recovery

In order for molecular sieves to prove useful in chromium remediation, extraction after the sieves have been exposed to chromium and removed it from solution is essential. Ideally, chromium extraction would be accompanied by the regeneration of the molecular sieve to allow for its recycling. On the other hand, the process by which chromium is removed has the potential to modify Cr ions; re-oxidation to Cr(VI) should be avoided at all costs, and procedures that might reduce any Cr(VI) ions that remain would be optimal.

Three pathways for recovering chromium from molecular sieves are ion exchange with competitive ions, complexing with ligands, and acid treatment, a harsher method which carries the disadvantage of compromising the sieve structure. Dealumination proceeds under even only very mildly acidic conditions and Fe(II) species may be oxidised or extracted(81,231,232). After prolonged treatment below pH 4, aluminium will be entirely removed from the framework, leaving behind an amorphous silica gel(64,76). Even where zeolite structures remain intact, steady loss of aluminium during the regeneration steps reduces the number of functional cycles across which the molecular sieve may be applied.

Lead has already been identified as an ion that competes with chromium for uptake by Fe-loaded zeolite X during initial exposure (Section 6.1.). However, the environmental toxicity of lead makes it unacceptable for this purpose. The ideal competitive ion should completely out-compete chromium when exposed to chromium-loaded materials, extracting all of it from the molecular sieve so that the structure may be regenerated without risk of contaminating other waters with trace chromium. Chromium recycling and sieve functionality for further cycles should also be maintained. To this end, other salts were explored. In particular, sodium and potassium were selected, which would allow for one-step regeneration of a parent alkali metal molecular sieve, the starting material for repeated Fe-loading and reuse. Zinc is also compared as a baseline, which did not compete well against chromium in a binary system (Section 6.1.). Two other metals were selected, silver and barium: these ions present a toxicity-cost compromise, but ion exchange studies have shown Ag(I) and Ba(II) compete in some highly selective sequestration systems such as Cs(I) uptake by clinoptilolite(82). The high selectivity of zeolite A for Ag(I) makes Ag(I) a promising proposition.

Table 6.4 summarises the data from XRF spectroscopic measurements of fused beads prepared from chromate-exposed Fe-loaded zeolite X samples which were subsequently submerged overnight in a 0.02 M solution of a candidate competitive ion or complexing agent. Data have been calibrated to accurately measure the chromium, iron, aluminium and silicon values. The extent of

uptake of competitive ions was not of interest. As predicted, Ag(I) ions extracted the greatest quantities of chromium from solution, Ba(II) was relatively successful and Zn(II) fared relatively poorly.  $\text{mg}_{\text{Fe}}/\text{g}_{\text{sieve}}$  measurements suggest that the extraction of Fe ions remaining in the system is concurrent with loss of Cr ions. A high Fe/Na value in the K(I) extraction system suggests that K(I) selectively exchanges with remaining Na(I) ions, rather than Cr or Fe.

Complexing agents EDTA and sodium citrate were similarly combined with chromate-exposed Fe-loaded zeolite X (Table 6.4). Hawley *et al.* report the successful regeneration of Cr(VI)-bound anion resins and Na-loaded zeolites *via* washing with sodium hydroxide solution or complexing agents such as EDTA, allowing for six cycles of regeneration and reuse(5). In complexing systems, an ion, here sodium, that is part of the complex is exchanged for a transition metal to which the complex binds more readily, promoting the ion exchange of Na(I) into the zeolite and Cr(III) out. This has the advantage of regenerating the Na-loaded zeolite at the same time as collecting chromium for recycling. Both EDTA and sodium citrate were effective chromium extractors. Although appreciable levels of chromium remain unextracted, altering conditions such as temperature, agitation, number of washes with the complexing agent and exposure time to it may yield a more complete extraction. This experiment may only be employed as a baseline.

PXRD of ion-exchanged and complexed samples identifies no loss of zeolite crystallinity in any of these samples.

Table 6.4: XRF spectroscopy data from calibrated fused beads of chromate-exposed Fe-loaded zeolite X after exposure to a competitive ion (Na(I), K(I), Zn(II), Ba(II) or Ag(I)) or complexing agent (Na citrate or EDTA) solution.

Removal technique		Si/Al	Fe/Na	Fe/Si	$\text{mg}_{\text{Fe}}/\text{g}_{\text{sieve}}$	$\text{mg}_{\text{Cr}}/\text{g}_{\text{sieve}}$
Metal ion exchange	Na	1.59	0.37	0.14	21.5	17.5
	K	1.60	4.47	0.13	26.0	15.8
	Zn	1.59	0.30	0.14	25.4	18.1
	Ba	1.51	0.62	0.11	20.3	6.48
	Ag	1.48	0.49	0.11	20.0	3.66
Complexing	EDTA	1.59	0.047	0.06	9.44	6.33
	Na citrate	1.50	0.28	0.12	20.8	7.10

Acid treatment was also applied for chromium recovery. This method avoids the problem of contaminated/mixed ion product solutions containing chromium, but has the disadvantage of risking the integrity of the molecular sieve. If the sieve is severely compromised, it will not be recyclable, and the solution will be contaminated with dissolved aluminosilicates. Initially, solutions were prepared with a pH between 4.5 and 0 at pH = 0.5 unit intervals, and mixed with sodium dichromate to a 0.02 M concentration and before overnight exposure to the molecular sieves. After solid

samples had been filtered and washed, they were examined using XRF spectroscopy (as calibrated fused beads), PXRD and UV-vis spectroscopy; solution samples were also examined by UV-vis spectroscopy.

PXRD patterns suggest a linear progression in amorphous character with increasing acidity. The structure is maintained at pH 4.5-2, but a loss in intensity of the peaks is observed with decreasing pH. At pH 2, only the most intense peaks are visible over the background, and at pH 1.5 only a few indications of peaks remain. Below pH 1.5 there is no indication of crystallinity: dealumination and structural breakdown of the zeolite has occurred (Figure 6.2). Furthermore, the retrieved masses of solids decrease noticeably from pH 1.5 and below. Insufficient mass of the samples prepared at pHs 1.0, 0.5 and 0 were recovered to make into fused beads and, as such, these samples have not been analysed with XRF spectroscopy (Table 6.5).

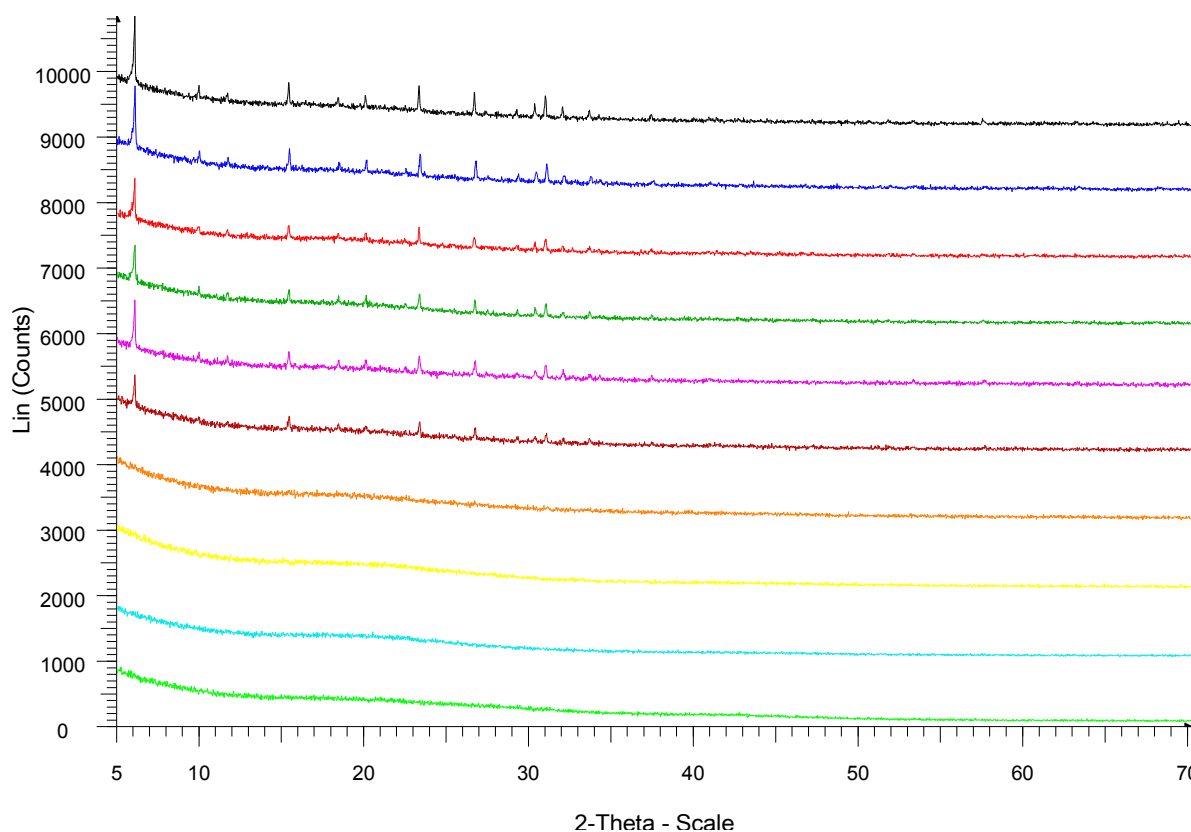


Figure 6.2: PXRD patterns of ten samples of acid-washed chromate-exposed Fe-loaded zeolite X; top to bottom: acid pH = 4.5-0: 4.5 (black), 4.0 (blue), 3.5 (red), 3.0 (green), 2.5 (pink), 2.0 (burgundy), 1.5 (orange), 1.0 (yellow), 0.5 (turquoise), 0 (lime).

XRF spectroscopic analysis suggests that high levels of chromium remain in the molecular sieve post acid treatment. We already know from earlier work (Table 4.23) that uptake is not pH dependent, and these numbers would also indicate that chromium is not readily extracted using acid. Although there is variation in the values of  $\text{mg}_{\text{Cr}}/\text{g}_{\text{sieve}}$ , the range is consistent with error between

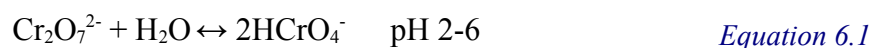
different samples and no pattern is observable down the series. More importantly, at pH 2, a slightly higher Si/Al ratio is noted, and at pH 1.5 the number rises to 4.47, an unrealistic representation of zeolite X and clear indication that dealumination is taking place.

*Table 6.5: XRF spectroscopy data from calibrated fused beads of chromate-exposed Fe-loaded zeolite X after treatment with acidic solutions between pH 4.5 and 1.5. A lower Cr loading indicates a higher level of extraction.*

Acid pH	Si/Al	Fe/Na	Fe/Si	mg <sub>Fe</sub> /g <sub>sieve</sub>	mg <sub>Cr</sub> /g <sub>sieve</sub>
4.5	1.58	1.13	0.28	95.7	28.3
4	1.61	1.16	0.28	95.9	28.5
3.5	1.58	0.94	0.27	92.6	27.6
3	1.59	1.11	0.28	96.2	23.4
2.5	1.59	1.46	0.28	95.4	27.6
2	1.77	3.23	0.29	105.4	32.3
1.5	4.47	7.21	0.24	112.3	26.9

In the UV-vis spectra of the acid solutions after exposure to samples of chromium-containing Fe-loaded zeolite X, only the dominant transition metal ion, Fe(III), is easily identified by comparison against the standards. Figure 6.3 shows the spectra of the solution at pH 1.5 and four standards: Fe(III), Fe(II), Cr(VI) and Cr(III). The Fe(II) standard is converted to Fe(III) under these pH conditions: Fe(II) bands appear near the infra red region ~1000 nm and do not contribute(204). Thus no deductions about iron oxidation state can be made from these spectra. Since samples did not appreciably differ across the pH series, only this one sample is shown. The pH 1.5 sample was selected because it is close to the centre of the series and represents the crossover between sieve retention and sieve breakdown under acidic conditions.

Across the pH range, Cr(VI) standards vary little, reflecting the equilibrium between chromate and dichromate species (Figure 6.4).



Formation of the chlorochromate ion,  $\text{CrO}_3\text{Cl}^-$ , which occurs under hydrochloric acid, may also compete(233).

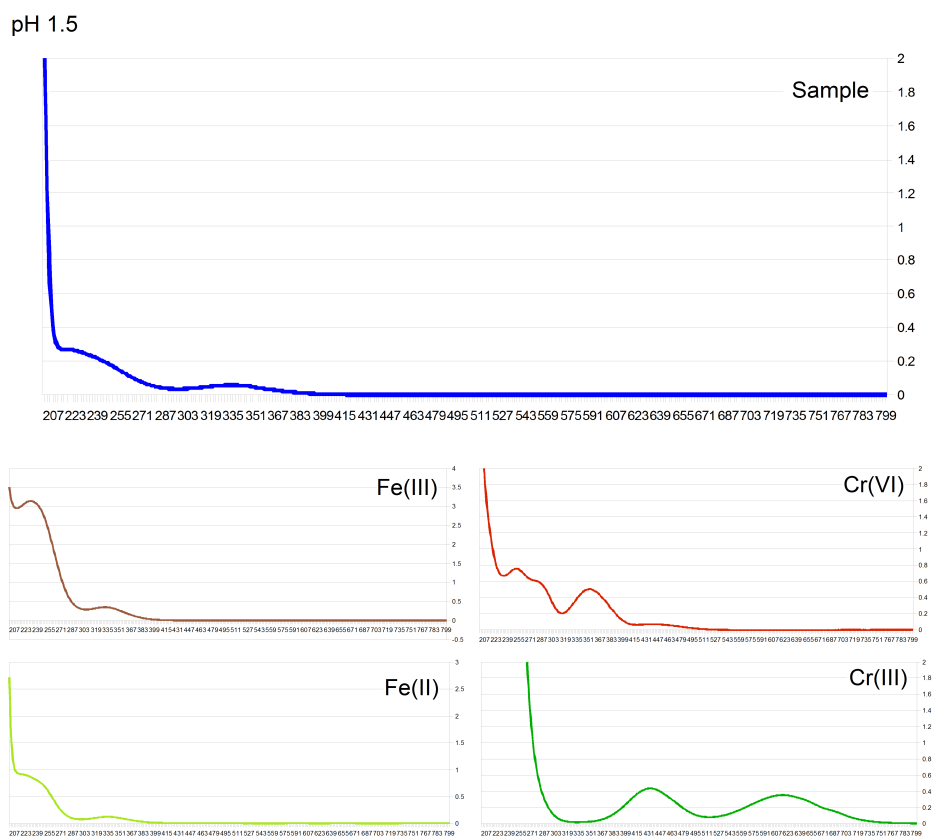


Figure 6.3: Four UV-vis spectra at pH 1.5: top (large) sample of solution after exposure to chromate-exposed Fe-loaded zeolite X; middle left: Fe(III) solution; middle right: Cr(VI) solution; bottom left: Fe(II) solution; bottom right: Cr(III) solution, for comparison.

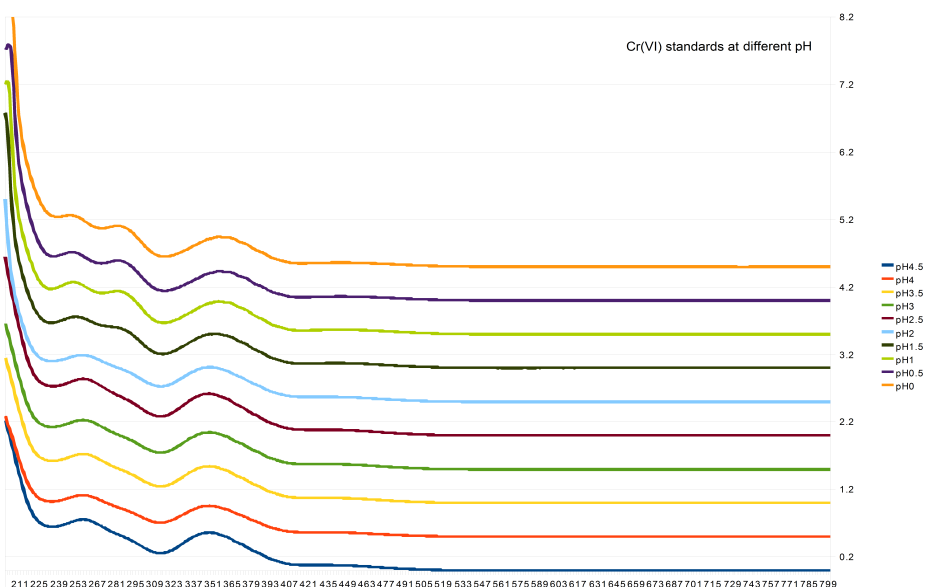


Figure 6.4: UV-vis spectra of chromate-containing solutions prepared at pH 4.5 to 0 (top to bottom).

Although Cr(VI) is strongly oxidising under acidic conditions, and should in time convert to Cr(III), there was no evidence to support the formation of Cr(III); in particular, the characteristic

band at 622 nm was absent and close inspection found two minor peaks at ~590 nm and ~640 nm, with a dip at the 622 nm region (Figure 6.5)(209).

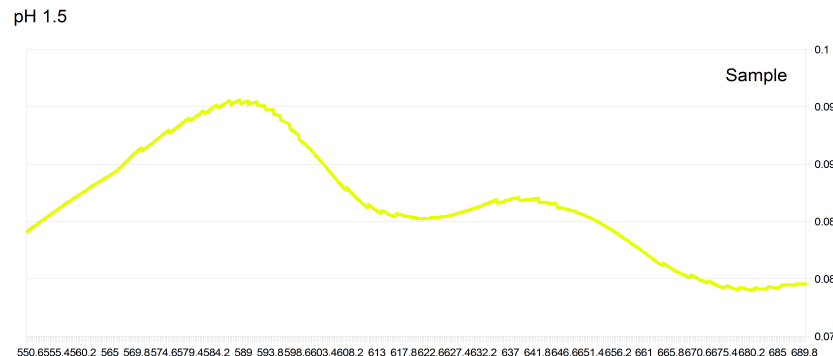


Figure 6.5: UV-vis spectrum of pH 1.5 solution after mixing with chromate-exposed Fe-loaded zeolite X in the narrow 550.6-689.8 nm wavelength range.

UV-vis spectroscopy of solid materials did not provide useful results. The spectra showed broad, featureless bands below 600 nm; Lee *et al.* interpret this as an indication of various Fe species ranging from isolated Fe(III) to larger nanoscale Fe<sub>2</sub>O<sub>3</sub> particles(197). Chromium content is low compared with that of Fe or Mn, and spectra do not differ between before and after chromium exposure. As it is impossible to prepare standards with control over metal oxidation state in the correct matrix, close comparisons could not be made.

In addition to compromising the sieve structure, chromium extraction by acid treatment is less successful than ion exchange or complexing methods. Figure 6.6 summarises this conclusion.

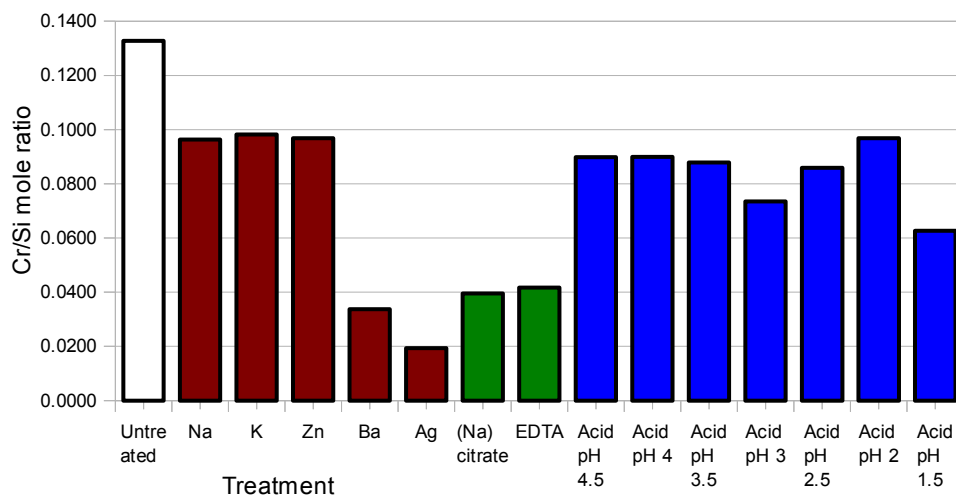


Figure 6.6: Graph of chromate-exposed Fe-loaded zeolite X after mixing with nothing (white), competing ions (red), complexing agents (green) or acidic (blue) solutions for the purpose of chromium extraction. y axis is in arbitrary units for the mole ratio of Cr/Si; a lower ratio corresponds to a higher chromium extraction.

It is possible that acid treatment for a shorter exposure time could reduce breakdown of the molecular sieve. However, it is also possible that breakdown of the molecular sieve is required to

extract chromium using acid treatment. In order to investigate this possibility, a further series of acid-treated samples were prepared around pH 1.5, where dealumination takes place. PXRD showed complete loss of crystal structure for all samples. XRF spectroscopic results from calibrated fused beads are presented in Table 6.6.

*Table 6.6: XRF spectroscopy data from calibrated fused beads of chromate-exposed Fe-loaded zeolite X after treatment with acidic solutions between pH 1.77 and 1.47. A lower chromium loading indicates a higher level of extraction.*

Acid pH	Si/Al	Fe/Na	M/Si	mg <sub>Fe</sub> /g <sub>sieve</sub>	mg <sub>Cr</sub> /g <sub>sieve</sub>
1.77	5.69	6.71	0.18	91.4	23.0
1.69	12.17	7.35	0.12	65.9	17.0
1.63	21.97	4.72	0.08	49.0	16.9
1.57	46.58	4.03	0.06	35.3	16.6
1.52	53.67	3.54	0.06	35.2	15.1
1.47	1.52	1.03	0.22	79.5	10.7

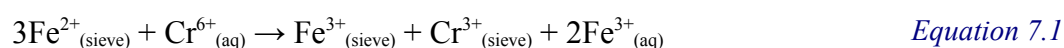
Dealumination proceeds steadily down to pH 1.52, below which a higher Si/Al ratio suggests substantial loss of aluminium in the remaining solid material, and it may be assumed that most of the molecular sieve and its guest ions have dissolved into solution. Values for mg<sub>Cr</sub>/g<sub>sieve</sub> steadily decrease with increased acidity. As the amorphous silica gel forms, chromium is released. This suggests that acid treatment is only successful for the extraction of chromium upon complete destruction of the host molecular sieve.

### ***Summary***

Systems demonstrated that simultaneous recycling and reduction of Cr is viable. Cr(III) may be recovered using acid, complexing agents or ion exchange to put to variable future applications. Acidic treatment initially destroys zeolite sieves and subsequently leaches chromium.

## Chapter 7: Summary and Conclusions

This thesis set out to identify and optimise systems for chromate remediation. Molecular sieves loaded with redox-active metal ions were exposed to chromate solution, uptake was monitored by XRF spectroscopy and characterisation was attempted to identify whether uptake proceeds by the proposed mechanism.



This target mechanism is considered to be three-step: (i) Cr(VI) ions adhere to the sieve surface, (ii) Cr(VI) is reduced to Cr(III) by redox-active metal ions and (iii) Cr(III) ions exchange into the molecular sieve. This mechanism addresses two key factors: the need to selectively collect chromium to allow for recycling and the need to reduce toxic Cr(VI) to less harmful, reusable Cr(III). It is therefore important to ascertain its possibility. In the case where reduction does not take place upon chromium uptake (*i.e.* only step (i) proceeds), any retrieval method for extracting chromium from the sieve would carry the additional responsibility of simultaneously reducing it to Cr(III).

Two factors may be manipulated to drive the target mechanism and optimise conditions for chromate remediation: the morphology and in particular porosity of the molecular sieve to select for Cr(III) adsorption and retention, and the oxidation states and availability of metal ions that perform the reduction. These factors have been explored across the chapters of this thesis.

Chapter 3 is concerned with structure, testing the chromium uptake of Fe- and Mn-loaded molecular sieves, attempting phase pure synthesis of promising impure systems and modifying the porosity of some structures through templating.

AIPO-5, AIPO-Fe23 and the LAU-zeotype AIPO were found to be contaminated with other competing phases, sometimes identifiable through SEM or XRD, as was the natural zeolite tuff containing chiefly clinoptilolite. Although zeolite A was synthesised phase pure, in most samples competition with high Si/Al zeolite X persisted. AIPO-Fe23 investigations focussed upon attempts to identify better conditions or heating methods for synthesising the target phase: higher pressure and a narrow temperature range  $150\text{ }^{\circ}\text{C} < T < 200\text{ }^{\circ}\text{C}$  were identified. In general, chromium uptakes in uncharged AIPO-5 systems were lower than those for aluminosilicate zeolites. High Si/Al zeolite X showed the highest chromium uptake (Table 7.1). This is dependent upon the identity of the

redox-active metal ion, where  $\text{Fe} > \text{Fe-Mn} > \text{Mn} > \text{Na}$  ( $29.1 > 16.3 > 0.5 > 0 \text{ mg}_{\text{Cr}}/\text{mg}_{\text{sieve}}$ ).

Synthesis of a hierarchially porous ZSM-5 zeolite was attempted, and zeolite X and AIPO-5 were templated *via* introduction of CTAB, gelatin, agar and alginate at the synthesis stage. TEM images and XRF spectroscopic measurements showed that zeolite X was successfully templated with alginate, creating mesoporosity that increased chromium uptake in the order  $2\% > 1\% > 4\%$  alginate.

*Table 7.1: Summary of XRF spectroscopy data from chromate-exposed calibrated fused beads of Fe- and Mn-loaded molecular sieves systems explored in Chapter 3.*

Sieve	$\text{mg}_{\text{Cr}}/\text{mg}_{\text{Fe-sieve}}$	$\text{mg}_{\text{Cr}}/\text{mg}_{\text{Mn-sieve}}$
<b>AIPO-5</b>	0.6	3.3
<b>AIPO-Fe23</b>	0.7	0.8
<b>LAU AIPO</b>	0.5	0.8
<b>Clinoptilolite</b>	13.5	0.6
<b>Zeolite A</b>	20.3	0
<b>Zeolite X</b>	29.1	0.5
<b>Hp ZSM-5 zeolite</b>	7.19	0
<b>Alginate zeolite X</b>	33.1	4.3

Chapter 4 explores the mechanism for chromium uptake by first assigning Fe and Mn oxidation states and coordination environments and then examining any changes to these upon chromium uptake by the host molecular sieves. The metals found in molecular sieves may be framework ions (for AIPOs, where metals are introduced at the synthesis stage), or extraframework ions within the pore channels, or adsorbed onto the external surface. It was discovered *via* Mössbauer spectroscopy that the majority of iron ions were oxidised to Fe(III) in molecular sieves, occupying octahedral extraframework positions. Broad Mössbauer spectroscopy and XPS linewidths suggested a distribution of Fe ion environments, consistent with coordination to extraframework water molecules. Upon chromate exposure, further oxidation of Fe(II) to Fe(III) occurs. XPS data were not of sufficient quality to determine Fe or Cr oxidation states, but Mn-loaded samples show evidence of an increase in oxidation state upon chromate exposure *via* a significant shift to higher binding energies. Fe(III)-loading of zeolite X generated samples with high Fe contents, but lower Cr uptakes and an accompanying loss of zeolite crystallinity. Dehydration decreases the number of Fe sites, indicating a distribution of water-coordinated environments, despite sulfate surface species. EDS measurements showed that samples prepared with  $\text{FeSO}_4$  exhibit heterogeneously distributed sulfate surface contamination on the order of 1%. Fe(II)-Fe(III)

transitions are not detected in Mössbauer spectroscopy in parallel with green-brown colour changes, suggesting surface: bulk ratio is sufficiently low. Low uptakes into non-redox active Fe(III)-loaded AIPO-5 systems indicates ion exchange is crucial. Chromium uptake was not affected by pH between 5 and 13, but washing samples with acid or water beforehand to remove surface Fe species decreased chromium uptakes.

In [Chapter 5](#), the effect of modifying ions upon chromium uptake was explored. Dehydration of non-air-exposed Fe-loaded zeolite X samples showed that water performs a role in the colour change oxidative process. Exposing Fe-loaded molecular sieves to heat and hydrogen gas successfully reduced Fe(III) ions; the extent of reduction increased with increasing length of exposure. In Fe-loaded zeolite X, Fe(0) was introduced after 3 hours and, in some AIPO systems, after 6 hours. XRD shows that, after 24 hours of hydrogen gas exposure, large metal aggregates form, the structure breaks down and crystallinity is almost entirely destroyed. AIPO Fe(III) ions are more readily reduced, such that no Fe(III) remains in most systems. Some tetrahedral framework Fe(III) ions were observed, but not in samples containing AIPO-5 phases. In Fe-loaded zeolite X, chromium uptake correlates with Fe(II) content only, which initially increases upon reduction and then decreases as Fe(0) metal evolves. Reduction to Fe(0) is not reversible in Fe(0)-metal-containing zeolite X, whilst Fe(0) in AIPOs appears to disappear after chromium treatment. Although relative chromium uptakes are still lower amongst AIPOs than zeolites, chromium uptakes in Fe-loaded systems are consistently increased by hydrogen gas exposure. Measurements of samples after 3 months of air exposure provided evidence that slow aerial oxidation takes place, even after reduction.

[Chapter 6](#) addresses the suitability of selected systems for application in chromate remediation and recycling. It addresses three key concepts: the extent of chromium removal from simulated waste waters with real contaminant level chromium concentrations, the effect of competitive ions upon chromium uptake and methods for extracting chromium from the sieves. Fe-loaded zeolite X, hydrogen reduced Fe-loaded zeolite X and a hydrogen reduced Fe-loaded sample consisting mostly of AIPO-5 were selected for further investigation. These systems were able to reduce the chromium content of wastewater below the WHO recommended limit of 50 µg/l up to concentrations of 450 µg/l, although iron was leached appreciably. Although chromium competed badly in mixed systems containing many contaminant metal ions, binary competition with one other metal ion did not lead to any significant decrease in chromium uptake except in the case of a Pb-Cr solution; these tests outline the potential for mixed waste remediation solutions involving chromate anions and other cations with molecular sieves. The toxicity of lead, however, makes it unacceptable for ion exchanging with chromium to extract it from molecular sieves, but other ions

were identified, showing the potential for many extraction routes. Similarly, complexing agents EDTA and Na citrate proved effective at chromium extraction, with the added bonus of recovering a Na-loaded zeolite for recycling the sieve. Acid extraction was less successful, and chromium release low when above the pH where the molecular sieve was destroyed. Acidic treatment extracts chromium, but only after destroying the zeolite.

The evidence gathered across the chapters of this thesis may be used to determine the mechanism of chromium uptake. Where chromium adheres to the external surface, uptake should be driven by mesoporosity, a larger quantity of surface iron and more absorbing forms of Fe, *e.g.* Fe(III). Little or no loss of Fe species upon chromate exposure should be observed, and the chromium adsorbed should be Cr(VI) at the surface and surface only. Mesoporosity, introduced by templating zeolite X with alginate, leads to an increased uptake of chromium as predicted, whilst reducing the number of surface Fe species by washing with water or acid reduces chromium uptake. The presence of counter ions (sulfates) observed at the sample surface provide evidence that surface concentrated Fe species are present. However, it is not the case that higher Fe(III) loadings than Fe(II) loadings increase uptake, and Fe concentrations unambiguously decrease upon chromium loading; this points to the conclusion that adsorption is not operating as the sole mechanism.

Where adsorption is followed by reduction of Cr(VI) to Cr(III), Fe(II) and possibly Fe(0) metal species drive the reaction, especially where Fe(II) is found at the sample surface. Since reducing the number of surface species reduces the chromium uptake, that evidence also supports this mechanism. XRF spectroscopy of hydrogen gas reduced Fe-loaded zeolite X samples shows that Fe(II), but not Fe(0) nor Fe(III), increases chromium uptake, supporting the conclusion of a reduction reaction. Oxidation to Fe(III) upon chromate exposure is observed *via* Mössbauer spectroscopy, suggesting that high proportions of chromium retained as Cr(VI) are unlikely. EPR spectra that show loss of Fe signals upon chromate treatment that may be interpreted as migrating Fe species. Whilst little or no chromium uptake would be consistent with this mechanism operating alone, surface adhesion is almost certainly necessary before reduction takes place.

Mesoporosity, a large quantity of iron in the sieve and prior reduction of Cr(VI) to Cr(III) facilitate ion exchange of Cr(III) into the molecular sieve and Fe(III) or Mn(IV) out. The sizeable loss of Fe species observed is only consistent with this step taking place and implies that all three mechanistic steps occur, as intended. The migration of iron species to the sample surface and presence of chromium inside as well as on the surface of molecular sieves (where XPS and EDS struggle to detect it) also provide support for this conclusion. As a stepwise mechanism, it is likely that not every step goes to completion, counter ion surface contamination facilitates uptake of Cr(VI) that is not all reduced and ion exchanged into the sieve, and some Cr(III) species will be

desorbed before ion exchange occurs. A thorough investigation of the equilibrium position of each step would provide useful conclusions on the limitations of these systems.

Further work on this project could include a greater range of molecular sieves for chromate remediation, employing higher resolution techniques to measure chromium contents in liquids and solids produced from simulated waste water tests, such as ICP. This would provide information about the industrial potential of these materials and build the foundation for further exploration of metal ions and complexing agents that might regenerate the molecular sieves and excrete chromium fully and selectively. After the identification of good extraction methods, repeated cycles of extraction and regeneration would provide information about the longevity of molecular sieves and direct research on upscaling the method for industrial application. Additionally, further attempts at AlPO-Fe<sub>23</sub> phase pure synthesis should be explored.

## Appendix I

Pourbaix thermodynamic diagram for (i) iron, (ii) manganese and (iii) chromium as taken from *Atlas of Electrochemical Equilibria in Aqueous Solutions*(126).

(i)

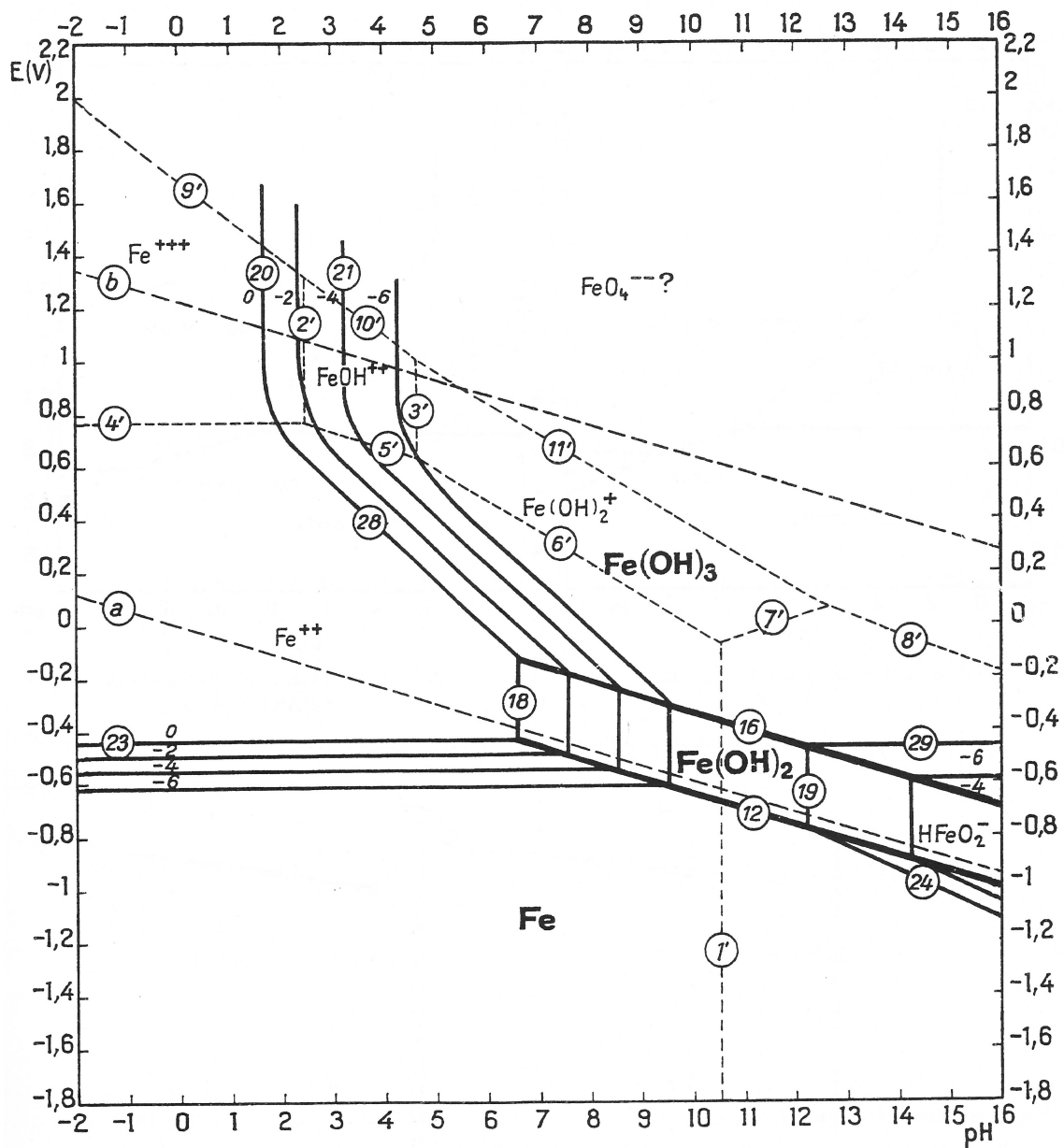
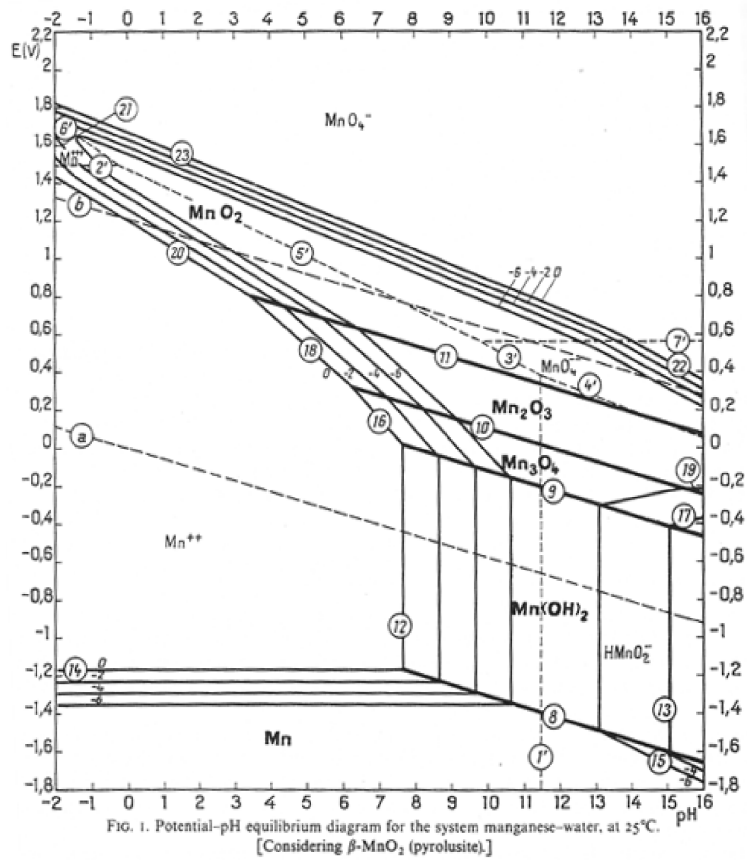
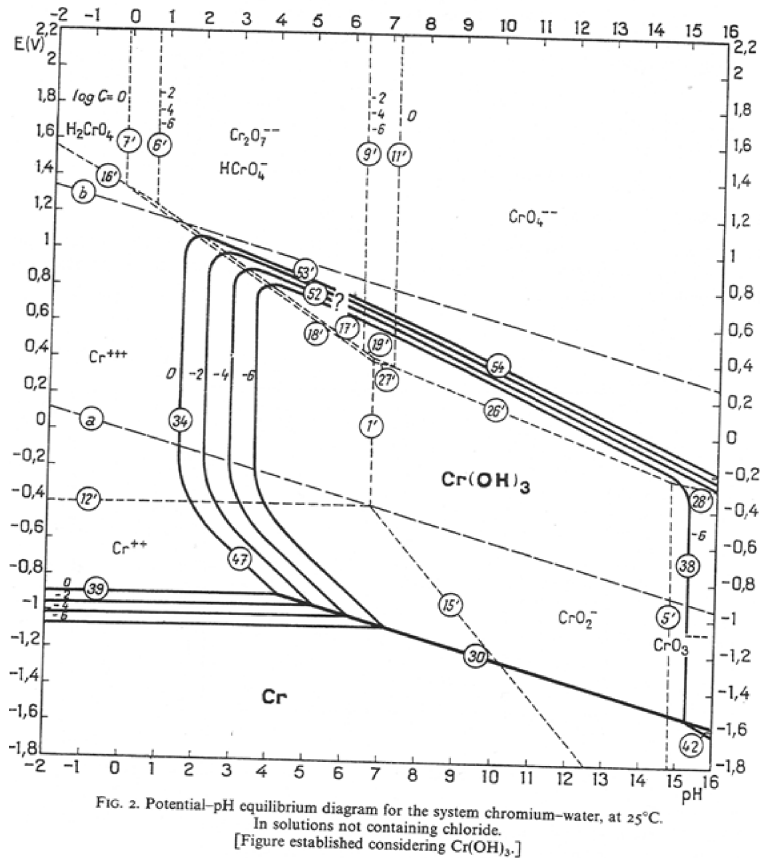


FIG. 5. Potential-pH equilibrium diagram for the system iron-water, at 25°C [considering as solid substances only Fe, Fe(OH)<sub>2</sub> and Fe(OH)<sub>3</sub>].

(ii)



(iii)



## Appendix II

Since ions are often loaded in excess, such that the amount measured by XRF spectroscopy is greater than the amount required to charge balance in the formula, XRF spectroscopic values of elemental weight %s were used to calculate the  $\text{mg}_{\text{Cr}}/\text{g}_{\text{sieve}}$ . Oxygen and hydrogen (that are XRF inactive) are calculated from (a) TGA mass % of water and (b) assuming a formula balancing quantity of additional oxygen, specific to the molecular sieve framework.

Fused bead data is collected in oxides mass % ( $F_{\text{ox.mass}} \times 100$ ), which may be transformed to give elemental mole % ( $F_{\text{mole}} \times 100$ ) and elemental mass % ( $F_{\text{el.mass}} \times 100$ ).

$$F_{\text{mol}} = \frac{m_{\text{el}} \cdot F_{\text{ox.mass}}}{Mr_{\text{oxide}}}$$

$$F_{\text{el.mass}} = F_{\text{mol}} \cdot Mr_{\text{el}} = \frac{m_{\text{el}} \cdot Mr_{\text{el}} \cdot F_{\text{ox.mass}}}{Mr_{\text{oxide}}}$$

where  $m$  = multiplicity (number per formula unit)

$Mr$  = molecular mass

$F$  = fraction

### Zeolites

The calculation for  $\text{mg}_{\text{Cr}}/\text{g}_{\text{zeo}}$  must take into account oxygen in the framework and extra-framework water. Zeolites were found to be 25% water by TGA.

$$F_{\text{mol}}(\text{O}) = 2 \cdot (F_{\text{mol}}(\text{Al}) + F_{\text{mol}}(\text{Si}))$$

$$g_{\text{Cr}}/g_{\text{zeo}} = \frac{F_{\text{mass}}(\text{Cr}) \cdot 0.75}{(F_{\text{mol}}(\text{O}) \cdot 16) + 1}$$

$$\text{mg}_{\text{Cr}}/g_{\text{zeo}} = 1000 \cdot g_{\text{Cr}}/g_{\text{zeo}}$$

### AIPOs

The calculation for  $\text{mg}_{\text{Cr}}/\text{g}_{\text{alp}}$  must take into account oxygen in the framework and extra-framework water. AIPO-5 phases were found to contain 8% water by TGA.

$$F_{\text{mol}}(\text{O}) = 4 \cdot F_{\text{mol}}(\text{Al})$$

$$g_{\text{Cr}}/g_{\text{alp}} = \frac{F_{\text{mass}}(\text{Cr}) \cdot 0.92}{(F_{\text{mol}}(\text{O}) \cdot 16) + 1}$$

$$\text{mg}_{\text{Cr}}/g_{\text{alp}} = 1000 \cdot g_{\text{Cr}}/g_{\text{alp}}$$

After calculations, numbers may be accurate to ~ 5%.

## Bibliography

1. Chen H, Arocena JM, Li J, Thring RW, Zhou J. "Mobility and Storage Sinks for Chromium and Other Metals in Soils Impacted by Leather Cannery Wastes." *Journal of Environmental Monitoring*. (2012); **14** 12; 3240–8.
2. Li Z, Jones HK, Bowman RS, Helferich R. "Enhanced Reduction of Chromate and PCE by Pelletized Surfactant-Modified Zeolite/Zerovalent Iron." *Environmental Science & Technology*. (1999); **33** 23; 4326–30.
3. Lazaridis N, Jekel M, Zouboulis I. "Removal of Cr(VI), Mo(VI), and V(V) Ions from Single Metal Aqueous Solutions by Sorption or Nanofiltration." *Separation Science and Technology*. (2003); **38** 10; 2201–19.
4. Choudhary VR, Jana SK, Kiran BP. "Alkylation of Benzene by Benzyl Chloride over H-ZSM-5 Zeolite with its Framework Al Completely or Partially Substituted by Fe or Ga." *Catalysis Letters*. (1999); **59**; 217–9.
5. Hawley EL, Deeb RA, Kavanaugh MC, Jacobs J. "Treatment Technologies for Chromium(VI)." *CRC Press LLC*; (2004); p.273-308.
6. Ketir W, Rekhila G, Trari M, Amrane A. "Preparation, Characterization and Application of CuCrO<sub>2</sub>/ZnO Photocatalysts for the Reduction of Cr(VI)." *Journal of Environmental Sciences. The Research Centre for Eco-Environmental Sciences, Chinese Academy of Sciences*; (2012); **24** 12; 2173–9.
7. Mohan D, Pittman Jr C. "Activated Carbons and Low Cost Adsorbents for Remediation of Tri- and Hexavalent Chromium from Water." *Journal of Hazardous Materials*. (2006); **B137**; 762–811.
8. Feng YC, Meng Y, Li FX, Lv ZP, Xue JW. "Synthesis of Mesoporous LTA Zeolites with Large BET Areas." *Journal of Porous Materials*. (2012); (in press).
9. Figueiredo H, Cristina Quintelas. "Tailored Zeolites for the Removal of Metal Oxyanions: Overcoming Intrinsic Limitations of Zeolites." *Journal of Hazardous Materials. Elsevier B.V.*; (2014); **274** ; 287–99.
10. Mohan D, Singh K, Singh V. "Removal of Hexavalent Chromium from Aqueous Solution Carbon, Using Low Cost Activated Carbons Derived from Agricultural Waste Materials and Activated Fabric Cloth." *Industrial & Engineering Chemistry Research*. (2005); **44**; 1027–295.
11. Mohan D, Singh K, Singh V. "Trivalent Chromium Removal from Wastewater Using Low Cost Activated Carbons Derived from Agricultural Waste Materials and Activated Carbon Fabric." *Journal of Hazardous Materials*. (2006); **135**; 280–95.
12. Kimbrough D, Cohen Y, Winer A, Creelman L, Mabuni C. "Critical Assessment of Chromium in the Environment." *Crit Rev Environ Sci Technol*. (1999); **29** 1; 1–46.
13. "International Agency for Research on Cancer, Chromium, Nickel and Welding. IARC Monographs on the Evaluation of Carcinogenic Risks to Humans." IARC Scientific Publications. Lyon; 1990.

14. Richard FC, Bourg AC. "Aqueous Geochemistry of Chromium: A Review." *Water Research*. (1991); **25** 7; 807–16.
15. Fuller J. "California Regional Water Quality Control Board (CRWQCB) Waste Discharge Requirements for the City of Fortuna Wastewater Treatment Facility." *The Community Clean Water Institute*; (2003).
16. Saeed M, Li L, Moradi Gharehtapeh A. "Effect of Alternative Electrolytes on Enhanced Electrokinetic Remediation of Hexavalent Chromium in Clayey Soil." *International Journal of Environmental Research*. (2013); **7** 1; 39–50.
17. Alberto C, Reyes R, Yolanda L, Fiallo V. "Application of Illite- and Kaolinite-Rich Clays in the Synthesis of Zeolites for Wastewater Treatment." *Earth and Environmental Sciences*. (2010); **15**; 363–74.
18. Lee S, Lee K, Park J. "Simultaneous Removal of Cd and Cr(VI) Using Fe-Loaded Zeolite." *Journal of Environmental Engineering*. (2006); **132**; 445–50.
19. "An Updated Thintri Market Study, Chrome Plating Alternatives: Thermal Spray, Electroless Plating, and Others." (2009).
20. Almeida E, Fedrizzi L, Diamantino T. "Oxidising Alternative Species to Chromium VI in Zinc-Galvanised Steel Surface Treatment. Part 2 - An Electrochemical Study." *Surface and Coatings Technology*. **1998** 105; 1–2, 5, 97–101.
21. Barrera-Díaz CE, Lugo-Lugo V, Bilyeu B. "A Review of Chemical, Electrochemical and Biological Methods for Aqueous Cr(VI) Reduction." *Journal of Hazardous Materials. Elsevier B.V.*; (2012); **223-224**; 1–12.
22. Thornton EC, Amonette JE. "Hydrogen Sulfide Gas Treatment of Cr(VI)-Contaminated Sediment Samples from a Plating-Waste Disposal Site Implications for in-Situ Remediation." *Environmental Science & Technology. American Chemical Society*; (1999); **33** 22; 4096–101.
23. Fruchter J, Cole C, Williams M, Vermeul V, Szecsody J, Istok J, Humphrey M. "Creation of a Subsurface Permeable Treatment Zone for Aqueous Chromate Contamination Using In Situ Redox Manipulation." *Groundwater Monitoring and Remediation*. (2000); **66**; 66–77.
24. Ponder SM, Darab JG, Mallouk TE. "Remediation of Cr(VI) and Pb(II) Aqueous Solutions Using Supported, Nanoscale Zero-valent Iron." *Environmental Science & Technology. American Chemical Society*; (2000); **34** 12; 2564–9.
25. Haq R, Shakoori A. "Microbiological Treatment of Industrial Wastes Containing Toxic Chromium Involving Successive use of Bacteria, Yeast and Algae." *World Journal of Microbiology and Biotechnology. Kluwer Academic Publishers*; (1998); **14** 4; 583–5.
26. McLean J, Beveridge T, Phipps D. "Chromate Removal from Contaminated Groundwater Using Indigenous Bacteria." In-Situ and On-Site Bioremediation Fifth International Symposium, Battelle Press, Columbus, Ohio; (1999); p. 121–6.
27. Cervantes C, Ji G, Ramirez J, Silver S. "Resistance to Arsenic Compounds in Microorganisms." *Microbiology Reviews*. (1994); **15** ; 355–67.
28. Xu C, Cheng D, Gao B, Yin Z, Yue Q, Zhao X. "Preparation and Characterization of  $\beta$ -FeOOH-Coated Sand and its Adsorption of Cr(VI) from Aqueous Solutions." *Frontiers of Environmental Science & Engineering in China*. (2011); **6** 4; 455–62.
29. Evanko CR, Dzombak DA. "Remediation of Metals-Contaminated Soils and Groundwater." *Ground-Water Remediation Technologies Analysis Center*. (1997); TE-97-01.

30. Ai Z, Cheng Y, Zhang L, Qiu J. "Efficient Removal of Cr(VI) from Aqueous Solution with Fe@Fe<sub>2</sub>O<sub>3</sub> Core-Shell Nanowires." *Environmental Science & Technology*. (2008); **42** 18; 6955–60.
31. Liu S, Xie J, Fang C, Cao G, Zhu T, Zhao X. "Self-Assembly of a CoFe<sub>2</sub>O<sub>4</sub>/Graphene Sandwich by a Controllable and General Route: Towards a High-Performance Anode for Li-Ion Batteries." *Journal of Materials Chemistry*. (2012); **22** 37; 19738.
32. Davis R, Olson R. "The Geochemistry of Chromium Migration and Remediation in the Subsurface." *Ground Water*. (1995); **33** 5; 759–68.
33. (USEPA). "Record of Decision for the Kysor Industrial Corp. Superfund Site." U.S. Environmental Protection Agency (USEPA). Cadillac, MI; 1989.
34. Aggarwal D, Goyal M, Bansal RC. "Adsorption of Chromium by Activated Carbon from Aqueous Solution." *Carbon*. (1999); **37** 12; 1989–97.
35. Bailey SE, Olin TJ, Bricka RM, Adrian DD. "A Review of Potentially Low-Cost Sorbents for Heavy Metals." *Water Research*. (1999); **33** 11; 2469–79.
36. Kratochvil D, Pimentel P, Volesky B. "Removal of Trivalent and Hexavalent Chromium by Seaweed Biosorbent." *Environmental Science & Technology*. (1998); **32** 18; 2693–8.
37. Babel S, Kurniawan TA. "Cr(VI) Removal from Synthetic Wastewater Using Coconut Shell Charcoal and Commercial Activated Carbon Modified with Oxidizing Agents and/or Chitosan." *Chemosphere*. (2004); **54** 7; 951–67.
38. Gao H, Liu Y, Zeng G, Xu W, Li T, Xia W. "Characterization of Cr(VI) Removal from Aqueous Solutions by a Surplus Agricultural Waste-Rice Straw." *Journal of Hazardous Materials*. (2008); **150** 2; 446–52.
39. Orhan Y, Buyukgungor H. "The Removal of Heavy Metals by Using Agricultural Wastes." *Water Science and Technology*. (1993); **28**; 247–55.
40. L Dupont EG. "Removal of Hexavalent Chromium with a Lignocellulosic Substrate Extracted from Wheat Bran." *Environmental Science & Technology*. (2003); **37** 18; 4235–41.
41. Silva B, Figueiredo H, Soares O, Pereira M, Figueiredo J, Lewandowska A, Bañares M, Neves I, Tavares T. "Evaluation of Ion Exchange-Modified Y and ZSM-5 Zeolites in Cr(VI) Biosorption and Catalytic Oxidation of Ethyl Acetate." *Applied Catalysis B: Environmental*. (2012); **117-118**; 406–13.
42. Liu J, Liu B, Wang Y-Y, Shi Q-Z. "A 2-Fold Interpenetrated 3D Cd(II) Architecture with Helical Structure Containing 1D Cadmium–Oxygen Chain." *Inorganic Chemistry Communications Elsevier B.V.*; (2013); **27**; 111–3.
43. Wang S, Alekseev E V, Diwu J, Casey WH, Phillips BL, Depmeier W, Albrecht-Schmitt TE. "NDTB-1: A Supertetrahedral Cationic Framework That Removes TcO<sub>4</sub><sup>-</sup> from Solution." *Angewandte Chemie*. (2010); **122** 6; 1075–8.
44. Pöllmann H, Auer S. "Cr<sup>6+</sup>-Containing Phases in the System at 23°C." *Journal of Solid State Chemistry*. (2012); **185**; 82–8.
45. Kim J, Tratnyek PG. "Rapid Dechlorination of Polychlorinated Dibenzo-p-dioxins by Bimetallic and Nanosized Zerovalent Iron." *Environmental Science & Technology*. (2008); **42** 11; 4106–12.
46. Goswamee RL, Sengupta P, Bhattacharyya KG, Dutta DK. "Adsorption of Cr(VI) in Layered Double Hydroxides." *Applied Clay Science*. (1998); **13** 1; 21–34.

47. Kovanda F, Kováčsová E, Koloušek D. "Removal of Anions from Solution by Calcined Hydrotalcite and Regeneration of Used Sorbent in Repeated Calcination-Rehydration-Anion Exchange Processes." *Collection of Czechoslovak Chemical Communications*. (1999); **64.9**; 1517–28.
48. Wang S, Hseu R, Chang R, Chiang P, Chen J, Tzou Y. "Adsorption and Thermal Desorption of Cr(VI) on Li/Al Layered Double Hydroxide." *Colloids and Surfaces A: Physicochemical and Engineering Aspects*. (2006); **277** 1-3; 8–14.
49. Lotsch B, Millange F, Walton RI, O'Hare D. "Separation of Nucleoside Monophosphates using Preferential Anion Exchange Intercalation in Layered Double Hydroxides." *Solid State Sciences*. (2001); **3** 8; 883–6.
50. Khan AI, O'Hare D. "Intercalation Chemistry of Layered Double Hydroxides: Recent Developments and Applications." *Journal of Materials Chemistry*. (2002); **12** 11; 3191–8.
51. Newman SP, Jones W. "Comparative Study of Some Layered Hydroxide Salts Containing Exchangeable Interlayer Anions." *Journal of Solid State Chemistry*. (1999); **148** 1; 26–40.
52. Miyata S. "Anion-Exchange Properties of Hydrotalcite-Like Compounds." *Clays and Clay Minerals*. (1983); **31** 4; 305–11.
53. Brindley G, Kikkawa S. "Thermal Behaviour of Hydrotalcite and of Anion-Exchanged Forms of Hydrotalcite." *Clays and Clay Minerals*. (1980); **28** 2; 87–91.
54. Depe C, Metoui F El, Forano C, Roy D, Dupuis J, Besse J. "Polymerization of Silicates in Layered Double Hydroxides." *Chemistry of Materials*. (1996); **8**; 952–60.
55. Yun SK, Constantino VR, Pinnavaia TJ. "Synthesis and Properties of Silicate-Intercalated Layered Double Hydroxides Formed By Intragallery Hydrolysis Of Tetraethylorthosilicate." *Clay and Clay Minerals*. (1995); **43** 4; 503–10.
56. Park I, Kuroda K, Kato C. "Preparation of a Layered Double Hydroxide-Porphyrin Intercalation Compound." *Chemistry Letters. Chemical Society of Japan*; 11; 2057–8.
57. Bonnet S, Forano C, Roy A De, Besse JP. "Synthesis of Hybrid Organo - Mineral Materials: Anionic Tetraphenylporphyrins in Layered Double Hydroxides." *Chemistry of Materials*. (1996); **8**; 1962–8.
58. Robins DS, Dutta PK. "Examination of Fatty Acid Exchanged Layered Double Hydroxides as Supports for Photochemical Assemblies." *Langmuir*. (1996); **12** 2; 402–8.
59. Hwang S-H, Han Y-S, Choy J-H. "Intercalation of Functional Organic Molecules with Pharmaceutical, Cosmeceutical and Nutraceutical Functions into Layered Double Hydroxides and Zinc Basic Salts." *Bulletin-Korean Chemical Society*. (2001); **22.9**; 1019–22.
60. Whilton NT, Vickers PJ, Mann S. "Bioinorganic Clays: Synthesis and Characterization of Amino- and Polyamino Acid Intercalated Layered Double Hydroxides." *Journal of Materials Chemistry*. (1997); **7** 8; 1623–9.
61. Chetia M, Goswamee RL, Banerjee S, Chatterjee S, Singh L, Srivastava RB, Sarma HP. "Arsenic Removal from Water Using Calcined Mg–Al Layered Double Hydroxide." *Clean Technologies and Environmental Policy*. (2011); **14** 1; 21–7.
62. Cronstedt A. "Observation and Description of an Unknown Kind of Rock to be Named Zeolites." *Kongl Vetenskaps Acad Handl Stockh*. (1756); **17**; 120–3.
63. Davis ME, Lobo RF. "Zeolite and Molecular Sieve Synthesis." *Chemistry of Materials*. (1992); **11** 9; 756–68.

64. Hey MH. "Studies on the Zeolites Part I. General Review." *Mineralogical Magazine*. (1930); **22**; 422–37.
65. Hill J-R, Sauer J. "Molecular Mechanics Potential for Silica and Zeolite Catalysts Based on ab Initio Calculations 2. Aluminosilicates." *Journal of Physical Chemistry*. (1995); **99**; 9536–50.
66. Hernandez-Ramirez O, Holmes SM. "Novel and Modified Materials for Wastewater Treatment Applications." *J Mater Chem*. (2008); **18**; 2751–61.
67. Xue Z, Ma J, Hao W, Bai X, Kang Y, Liu J, Li R. "Synthesis and Characterization of Ordered Mesoporous Zeolite LTA with High Ion Exchange Ability." *Journal of Materials Chemistry*. (2012); **22** 6; 2532.
68. Kuzniatsova T, Kim Y, Shqau K, Dutta PK, Verweij H. "Zeta Potential Measurements of Zeolite Y: Application in Homogeneous Deposition of Particle Coatings." *Microporous and Mesoporous Materials*. (2007); **103** 1-3; 102–7.
69. Nikolakis V. "Understanding Interactions in Zeolite Colloidal Suspensions: A Review." *Current Opinion in Colloid & Interface Science*. (2005); **10** 5-6; 203–10.
70. Mafra L, Alejandro Vidal-Moya J, Blasco T. "Annual Reports on NMR Spectroscopy: Volume 77. 4. Structural Characterization of Zeolites by Advanced Solid State NMR Spectroscopic Methods." *Elsevier Ltd*; (2012); p.259-287.
71. Aramburo LR, Liu Y, Tylliszczak T, de Groot FM, Andrews JC, Weckhuysen BM. "3D Nanoscale Chemical Imaging of the Distribution of Aluminum Coordination Environments in Zeolites with Soft X-Ray Microscopy." *Chemphyschem Communications*. (2013); (in press).
72. Martínez C, Pérez-Pariente J, editors. "Zeolites and Ordered Porous Solids: Fundamentals and Applications." Valencia, Spain: *FEZA*; (2011).
73. Smith J V. "Topochemistry of Zeolites and Related Materials: 1. Topology and Geometry." *Chemical Reviews*. (1988); **88**; 149–82.
74. Willhammar T. "Structural Study of Zeolites Utilizing Novel Electron Crystallographic Methods." (2013).
75. Smart LE, Moore EA. "Solid State Chemistry: An Introduction, Third Edition, 7. Zeolites and Related Structures." *Taylor & Francis CRC Press*; (2005); p.259-291.
76. Kim J, Keane M. "Ion Exchange of Divalent Cobalt and Iron with Na-Y Zeolite: Binary and Ternary Exchange Equilibria." *Journal of Colloid and Interface Science*. (2000); **232** 1; 126–32.
77. Xing S, Zhao D, Yang W, Ma Z, Wu Y, Gao Y, Chen W, Han J. "Fabrication of Magnetic Core–Shell Nanocomposites With Superior performance for Water Treatment." *Journal of Materials Chemistry A*. (2013); **1** 5; 1694.
78. Egashira R, Tanabe S, Habaki H. "Removal of Heavy Metals from Model Mine Wastewater by Adsorption Using Mongolian Natural Zeolites." *Journal of Chemical Engineering of Japan*. (2013); **46** 1; 50–5.
79. Misaelides P. "Application of Natural Zeolites in Environmental Remediation: A Short Review." *Microporous and Mesoporous Materials. Elsevier Inc.*; (2011); **144** 1-3; 15–8.
80. Michalev T, Petrov I. "The Removal of Heavy Metal Ions by Synthetic Zeolites: A Review." *НАУЧНИ ТРУДОВЕ НА РУСЕНСКИЯ УНИВЕРСИТЕТ*. (2012); **51** 9.1; 79–84.
81. Chávez-Rivas F, Rodríguez-Fuentes G, Berlier G, Rodríguez-Iznaga I, Petranovskii V,

- Zamorano-Ulloa R, Coluccia S. "Evidence for Controlled Insertion of Fe ions in the Framework of Clinoptilolite Natural Zeolites." *Microporous and Mesoporous Materials*. Elsevier Inc.; (2013); **167**; 76–81.
82. Chmielewska E, Lesny J. "Selective Ion Exchange onto Slovakian Natural Zeolites in Aqueous Solutions." *Journal of Radioanalytical and Nuclear Chemistry*. (2012); **293** 2; 535–43.
83. Diale P, Muzenda E. "A Study of South African Natural Zeolites Properties and Applications." WCECS JZ, editor. San Francisco, USA: *IAENG*; (2011).
84. Erdem E, Karapinar N, Donat R. "The Removal of Heavy Metal Cations by Natural Zeolites." *Journal of Colloid and Interface Science*. (2004); **280** 2; 309–14.
85. Babel S, Kurniawan TA. "Low-Cost Adsorbents for Heavy Metals Uptake from Contaminated Water: a Review." *Journal of Hazardous Materials*. (2003); **97**; 219–43.
86. Cabrera-Lafaurie W, Román FR, Hernández-Maldonado AJ. "Removal of Salicylic Acid and Carbamazepine from Aqueous Solution with Y-Zeolites Modified with Extraframework Transition Metal and Surfactant Cations: Equilibrium and Fixed-Bed Adsorption." *Journal of Environmental Chemical Engineering*. (2014); **2** 2; 899–906.
87. Lee K-M, Lim Y-H, Park C-J, Jo Y-M. "Adsorption of Low-Level CO<sub>2</sub> Using Modified Zeolites and Activated Carbon." *Industrial & Engineering Chemistry Research*. (2012); **51** 3; 1355–63.
88. Melo CR, Riella HG, Kuhnen NC, Angioletto E, Melo AR, Bernardin AM, da Rocha MR, da Silva L. "Synthesis of 4A Zeolites from Kaolin for Obtaining 5A Zeolites Through Ionic Exchange for Adsorption of Arsenic." *Materials Science and Engineering: B. Elsevier B.V.*; (2012); **177** 4; 345–9.
89. EL-Mekkawi DM, Selim MM. "Removal of Pb<sup>2+</sup> from Water by Using Na-Y Zeolites Prepared from Egyptian Kaolins Collected from Different Sources." *Journal of Environmental Chemical Engineering. Elsevier B.V.*; (2014); **2** 1; 723–30.
90. Covarrubias C, Garcia R, Arriagada R, Ynez J, Garland M. "Cr(III) Exchange on Zeolites Obtained from Kaolin and Natural Mordenite." *Microporous and Mesoporous Materials*. (2006); **88** ; 220–31.
91. Muller U, Bull I. "Process for the Preparation of Zeolites Having B-CHA Structure." EP 2325143 A2, 2011.
92. Rakić V, Rac V, Stošić D, Gajinov S, Rajić N. "Zeolites as Adsorbents of Atmospheric and Water Pollutants." Proceedings of the 4th Slovenian-Croatian Symposium on Zeolites. p. 97–100.
93. Jacobs PA, Beyer HK, Valyon J. "Properties of the End Members in the Pentasil-Family of Zeolites: Characterization as Adsorbents." *Zeolites*. (1981); **1** 3; 161–8.
94. Kubota Y, Itabashi K, Inagaki S, Nishita Y, Komatsu R, Tsuboi Y, Shinoda S, Okubo T. "Effective Fabrication of Catalysts from Large-pore, Multi-dimensional Zeolites Synthesized without Using Organic Structure-directing Agents." *Chemistry of Materials*. (2014); 1–37.
95. Lohse U, Altrichter B, Donath R, Fricke R, Jancke K, Parlitz B, Schreiber E. "Synthesis of Zeolite Beta." *Journal of the Chemical Society Faraday Transactions*. (1996); **92** 1; 159–65.
96. Izidoro JDC, Fungaro D, Abbott JE, Wang S. "Synthesis of Zeolites X and A from Fly Ashes for Cadmium and Zinc Removal from Aqueous Solutions in Single and Binary ion Systems." *Fuel. Elsevier Ltd*; (2012); August; 1–8.

97. Daou TJ, Boltz M, Tzani L, Michelin L, Louis B. "Gas-Phase Chlorination of Aromatics Over FAU- and EMT-Type Zeolites." *Catalysis Communications. Elsevier B.V.*; (2013); **39**; 10–3.
98. Colella C, Wise WS. "The IZA Handbook of Natural Zeolites: A Tool of Knowledge on the Most Important Family of Porous Minerals." *Microporous and Mesoporous Materials. Elsevier Inc.*; (2014); **189**; 4–10.
99. Riley P, Seff K. "Crystal Structures of Dehydrated Partially Cobalt(II)-Exchanged Zeolite A and its Carbon Monoxide Adduct." *Inorganic Chemistry*. (1974); **13** 6; 1355–60.
100. Thuadaj P, Nuntiya A. "A Comparative Study Using Two Methods to Produce Zeolites from Fly Ash and Amorphous Silica from Rice Husk Ash." TIChE International Conference. (2011); p. 1–2.
101. Chauhan Y, Talib M. "A Novel and Green Approach of Synthesis and Characterization of Nano-Adsorbents (Zeolites) from Coal Fly Ash: a Review." *Scientific Reviews and Chemical Communications*. (2012); **2** 1; 12–9.
102. Dodson J, Cooper E, Hunt A, Matharu A, Cole J, Minihan A, Clark J, Macquarrie D. "Alkali Silicates and Structured Mesoporous Silicas from Biomass Power Station Wastes: the Emergence of Bio-MCMs." *Green Chemistry*. (2013); **15** 5; 1203.
103. Ojha K, Pradhan NC, Samanta AN. "Zeolite from Fly Ash: Synthesis and Characterization." *Bulletin of Materials Science*. (2004); **27** 6; 555–64.
104. Mora AJ, Fitch AN, Cole M, Goyal R, Jones RH, Jobic H, Carr SW. "The Structure of Calcined Aluminophosphate ALPO<sub>4-5</sub> Determined by High Resolution X-Ray and Neutron Powder Diffraction." *Journal of Materials Chemistry*. (1996); **6** 210; 1831–5.
105. De Man J, Jacobs W, Gilson J, van Santen R. "Modeling of Structure and Vibrational Spectra of AlPO<sub>4-5</sub> and its Silica Analog SSZ-24." *Zeolites*. (1992); **12** 7; 826–36.
106. Li L, Chen M, Grace J, Tazaki K, Shiraki K, Asada R, Watanabe H. "Remediation of Acid Rock Drainage by Regenerable Natural Clinoptilolite." *Water, Air, and Soil Pollution*. (2007); **18**; 11–27.
107. Brukner A, Lohse U, Mehner H. "The Incorporation of Iron Ions in AlPO<sub>4-5</sub> Molecular Sieves After Microwave Synthesis Studied by EPR and Mossbauer Spectroscopy." *Microporous and Mesoporous Materials*. (1998); **20**; 207–15.
108. Lin S, Li J, Sharma RP, Yu J, Xu R. "Fabrication of SAPO-34 Crystals with Different Morphologies by Microwave Heating." *Topics in Catalysis*. (2010); **53** 19-20; 1304–10.
109. Parnham ER, Morris RE. "1-Alkyl-3-Methyl Imidazolium Bromide Ionic Liquids in the Ionothermal Synthesis of Aluminium Phosphate Molecular Sieves." *Chemistry of Materials*. (2006); **18** ; 4882–7.
110. Korzenski MB, Schimek GL, Kolis JW, Long GJ. "Hydrothermal Synthesis, Structure, and Characterization of a Mixed-Valent Iron (II/III) Phosphate, NaFe<sub>3.67</sub>(PO<sub>4</sub>): A New Variation of the Alluaudite Structure Type." *Journal of Solid State Chemistry*. (1998); **139**; 152–60.
111. Breck D. "Zeolite Molecular Sieves, Structure, Chemistry and Use." New York: *John Wiley & Sons*; (1974); p.23, 449, 553, 168.
112. Ristic A, Novak Tušar N, Arcon I, Zabukovec Logar N, Thibault-Starzyk F, Czyzniewska J, Kaucic V. "Large-Pore FAPO-36: Synthesis and Characterisation." *Chemistry of Materials*. (2003); **15**; 3643–9.
113. Nagase T, Ikeda T, Hiyoshi N, Abe C, Hanaoka T. "Structural Changes in-LIT Zeolites Related

- to Cation-Exchange Treatments Under Aqueous and Non-Aqueous Conditions.” *Microporous and Mesoporous Materials*. Elsevier Inc.; (2014); **190**; 92–8.
114. Sherry H. “Cation Exchange on Zeolites in Molecular Sieve Zeolites.” Gould RF, editor. Washington: *American Chemical Society*; (1971); p.350–378.
115. Banu M, Hye Lee Y, Magesh G, Sung Lee J. “Isopropylation of Naphthalene by Isopropanol over Conventional and Zn, Fe Modified USY Zeolites.” *Catalysis Science & Technology*. (2013); (in press).
116. Csicsery SM. “Shape-Selective Catalysis in Zeolites.” *Zeolites*. (1984); **4** 2; 116–26.
117. Zhou L, Xu J, Chen C, Wang F, Li X. “Synthesis of Fe, Co, and Mn Substituted AlPO-5 Molecular Sieves and their Catalytic Activities in the Selective Oxidation of Cyclohexane.” *Journal of Porous Materials*. (2006); **15** 1; 7–12.
118. Gómez-Hortigüela L, Pérez-Pariente J, García R, Chebude Y, Díaz I. “Natural Zeolites from Ethiopia for Elimination of Fluoride from Drinking Water.” *Separation and Purification Technology*. Elsevier B.V.; (2013); **120**; 224–9.
119. Mendoza-Barrón J, Jacobo-Azuara A, Leyva-Ramos R, Berber-Mendoza MS, Guerrero-Coronado RM, Fuentes-Rubio L, Martínez-Rosales JM. “Adsorption of Arsenic (V) from a Water Solution onto a Surfactant-Modified Zeolite.” *Adsorption*. (2010); **17** 3; 489–96.
120. Zhang P, Avudzeaga DM, Bowman RS. “Removal of Perchlorate from Contaminated Waters Using Surfactant-Modified Zeolite.” *Journal of Environmental Quality*. (2007); **36** 4; 1069–75.
121. Guan H, Bestland E, Zhu C, Zhu H, Albertsdottir D, Hutson J, Simmons CT, Ginic-Markovic M, Tao X, Ellis A V. “Variation in Performance of Surfactant Loading and Resulting Nitrate Removal Among Four Selected Natural Zeolites.” *Journal of Hazardous Materials*. Elsevier B.V.; (2010); **183** 1-3; 616–21.
122. Wingenfelder U, Furrer G, Schulin R. “Sorption of Antimonate by HDTMA-Modified Zeolite.” *Microporous and Mesoporous Materials*. (2006); **95** 1-3; 265–71.
123. Ma H-L, Zhang Y, Hu Q-H, Yan D, Yu Z-Z, Zhai M. “Chemical Reduction and Removal of Cr(VI) from Acidic Aqueous Solution by Ethylenediamine-Reduced Graphene Oxide.” *Journal of Materials Chemistry*. (2012); **22** 13; 5914.
124. Yokoi T, Tatsumi T, Yoshitake H. “Fe(3+) Coordinated to Amino-Functionalized MCM-41: an Adsorbent for the Toxic Oxyanions with High Capacity, Resistibility to Inhibiting Anions, and Reusability after a Simple Treatment.” *Journal of Colloid and Interface Science*. (2004); **274** 2; 451–7.
125. Kiser J, Manning B. “Reduction and Immobilization of Chromium(VI) by Iron(II)-Treated Faujasite.” *Journal of Hazardous Materials*. (2010); **174**; 167–74.
126. Pourbaix M. “Atlas of Electrochemical Equilibria in Aqueous Solutions.” Houston, Texas: *National Association of Corrosion Engineers*; (1974); p.259,262,289,290,309,313.
127. Yang Y, Burke N, Zhang J, Huang S, Lim S, Zhu Y. “Influence of Charge Compensating Cations on Propane Adsorption in X Zeolites: Experimental Measurement and Mathematical Modeling.” *RSC Advances*. (2014); 1–22.
128. Colella C. “Recent Advances in Natural Zeolite Applications Based on External Surface Interaction with Cations and Molecules.” International Zeolite Conference. *Elsevier B.V.*; (2007); p. 2063–73.

129. Sano M, Yamatera H. "Ions and Molecules in Solution." N.Tanaka, H. Ohtaki and RT, editor. Amsterdam: *Elsevier*; (1982); p.109.
130. Li YY, Wan MM, Zhu JH. "Cleaning Carcinogenic Nitrosamines with Zeolites." *Environmental Chemistry Letters*. (2013); **12** 1; 139–52.
131. Morrow C. "The Metallation of Zeolites with Manganese Oxide for Adsorption of Lead (II) and Copper (II) in Polluted Waters." (2011); .
132. Ames L. "Removal of Cesium by Sorption from Aqueous Solutions." United States; 30, 1962. p. 262.
133. Blanchard G, Maunaye M, Martin G. "Removal of Heavy Metals from Waters by Means of Natural Zeolites." *Water Research*. (1984); **18** 12; 1501–7.
134. Zamzow M, Eichbaum B, Sandgren K, Shanks D. "Removal of Heavy Metals and Other Cations from Wastewater Using Zeolites." *Separation Science and Technology*. (1990); **25** 13-15; 1555–69.
135. Kazantseva L. "Effect of an Amorphous Precursor Macrostructure on the Size of NaA and NaX Zeolites." *Bulletin of the Russian Academy of Sciences: Physics*. (2012); **76** 10; 1136–8.
136. Beale AM, Sankar G, Catlow CR, Anderson P, Green TL. "Towards an Understanding of the Oxidation State of Cobalt and Manganese Ions in Framework Substituted Microporous Aluminophosphate Redox Catalysts: An Electron Paramagnetic Resonance and X-Ray Absorption Spectroscopy Investigation." *Physical Chemistry Chemical Physics*. (2005); **7** 8; 1856–60.
137. Yang W, Song Y, Mu Y, Zhai S, Fu Y, An Q, Zhai B, Song X. "Synthesis and Crystal Morphology Control of AlPO<sub>4</sub>-5 Molecular Sieves by Microwave Irradiation." *Solid State Sciences. Elsevier Ltd*; (2014); (in press).
138. Azzolina Jury F, Polaert I, Estel L, Pierella LB. "Synthesis and Characterization of MEL and FAU Zeolites Doped with Transition Metals for their Application to the Fine Chemistry under Microwave Irradiation." *Applied Catalysis A. Elsevier B.V.*; (2013); **453** 2010; 92–101.
139. Li H, Jin J, Wu W, Chen C, Li L, Li Y, Zhao W, Gu J, Chen G, Shi J. "Synthesis of a Hierarchically Macro-/Mesoporous Zeolite Based on a Micro-Emulsion Mechanism." *Journal of Materials Chemistry*. (2011); **21** 48; 19395.
140. Corbin D, Whitney J, Fulz W, Stucky G, Eddy M, Cheetham A. "Synthesis of Open-Framework Transition-Metal Phosphates Using Organometallic Precursors in Acidic Media. Preparation and Structural Characterization of Fe<sub>5</sub>P<sub>4</sub>O<sub>20</sub>H<sub>10</sub> and NaFe<sub>3</sub>P<sub>3</sub>O<sub>12</sub>." *Inorganic Chemistry Communications*. (1986); **25** 14; 2279–80.
141. Chauhan N, Das J, Jasra R, Parikh P, Murthy Z. "Synthesis of Small-Sized ZSM-5 Zeolites Employing Mixed Structure Directing Agents." *Materials Letters. Elsevier B.V.*; (2012); **74**; 115–7.
142. Misaelides P, Nikashina V, Godelitsas A, Gembitskii P, Kats E. "Sorption of As (V)-Anions from Aqueous Solutions by Organo-Modified Natural Zeolitic Materials." *Journal of Radioanalytical and Nuclear Chemistry*. (1998); **227** 1; 183–6.
143. Misaelides P, Zamboulis D, Sarridis P, Warchoł J, Godelitsas A. "Chromium (VI) Uptake by Polyhexamethylene-Guanidine-Modified Natural Zeolitic Materials." *Microporous and Mesoporous Materials*. (2008); **108** 1-3; 162–7.
144. Nikashina V, Kats E, Serova I, Gembitski PA. "Uranium Sorption by Organozeolites and Ferromagnetic Organozeolites from Waste Water of Special Laundry." *In Combined and*

- Hybrid Adsorbents*. (2006); 85–92.
145. Wang J, Song J, Yin C, Ji Y, Zou Y, Xiao F-S. “Tetramethylguanidine-Templated Synthesis of Aluminophosphate-Based Microporous Crystals with AFI-Type Structure.” *Microporous and Mesoporous Materials*. Elsevier Inc.; (2009); **117** 3; 561–9.
  146. Walsh D, Kulak A, Aoki K, Ikoma T, Tanaka J, Mann S. “Preparation of Higher-Order Zeolite Materials by Using Dextran Templating.” *Angewandte Chemie (International ed in English)*. (2004); **43** 48; 6691–5.
  147. He N-Y, Cao J-M, Bao S-L, Xu Q-H. “Room-Temperature Synthesis of an Fe-Containing Mesoporous Molecular Sieve.” *Materials Letters*. (1997); **31** 1-2; 133–6.
  148. Zhu Y, Hua Z, Zhou J, Wang L, Zhao J, Gong Y, Wu W, Ruan M, Shi J. “Hierarchical Mesoporous Zeolites: Direct Self-Assembly Synthesis in a Conventional Surfactant Solution by Kinetic Control over the Zeolite Seed Formation.” *Chemistry*. (2011); **17** 51; 14618–27.
  149. Zhua Y, Huaa Z, Zhoua X, Songa Y, Gong Y, Zhoub J, Zhaoc J, Shi J. “CTAB-Templated Mesoporous TS-1 Zeolites as Active Catalysts in Desulfurization Process: the Decreased Hydrophobicity is More Favourable in Thiophene Oxidation.” *RSC Advances*. (2012); (in press).
  150. Xu J, Luan Z, He H, Zhou W, Kevan L. “A Reliable Synthesis of Cubic Mesoporous MCM-48 Molecular Sieve.” *Chemistry of Materials*. (1998); **10**; 3690–8.
  151. Meng X, Xiao F-S. “Green Routes for Synthesis of Zeolites.” *Chemical reviews*. (2014); **114** 2; 1521–43.
  152. Shen K, Qian W, Wang N, Zhang J, Wei F. “Direct Synthesis of c-Axis Oriented ZSM-5 Nanoneedles from Acid-Treated Kaolin Clay.” *Journal of Materials Chemistry A*. (2013); **1** 10; 3272.
  153. Bedard R. “Zeolites in Industrial Separation and Catalysis.” Weinheim: *Wiley-VCH*; (2002); p.72-73.
  154. Tatsumi T. “Handbook of Porous Solids.” Weinheim: *Wiley-VCH*; (2010); p.913-920.
  155. Plank C, Rosinski E. “US Patent 3.257.310.” 3.257.310, 1966.
  156. Kerr G. “Method for Preparing Highly Silaceous Zeolite-Type Materials and Materials Resulting Therefrom.” *Journal of Physical Chemistry*. (1967); **71**; 4155–6.
  157. Wolf P, Hammond C, Conrad S, Hermans I. “Post-Synthetic Preparation of Sn-, Ti- and Zr-Beta: a Facile Route to Water Tolerant, Highly Active Lewis Acidic Zeolites.” *Dalton transactions (Cambridge, England : 2003)*. (2014); **43** 11; 4514–9.
  158. Fodor D, Pacosová L, Krumeich F, van Bokhoven JA. “Facile Synthesis of Nano-Sized Hollow Single Crystal Zeolites Under Mild Conditions.” *Chem Comm*. (2013); 207890; 1–3.
  159. Díaz U. “Layered Materials with Catalytic Applications: Pillared and Delaminated Zeolites from MWW Precursors.” *ISRN Chemical Engineering*. (2012); **2012**; 1–35.
  160. Ikhsan J, Johnson I, Wells J. “A Comparative Study of the Adsorption of Transition Metals on Kaolinite.” *Journal of Colloid and Interface Science*. (1998); **217** 2; 403–10.
  161. Thompson R, Franklin K, Lechert H, Staelin P. “Verified Syntheses of Zeolitic Materials.” Robson H, editor. *Elsevier Science B.V.*; (2001); p.150-151, 179-180.
  162. Girnus I, Jancke K, Vetter R, Caro J. “Large ALP04-5 Crystals by Microwave Heating.” *Zeolites*. (1995); **2449**; 15:33–9.

163. Peng L, Li J, Yu J, Li G, Fang Q, Xu R. "Solvothermal Synthesis, Structure and Mössbauer Spectroscopy of a New Mixed-Valence Iron Aluminophosphate  $[\text{FeII}(\text{H}_2\text{O})_2\text{Fe}_{0.8}\text{IIIAl}_{1.2}(\text{PO}_4)_3] \cdot \text{H}_3\text{O}$ ." *Comptes Rendus Chimie*. (2005); **8** 3-4; 541–7.
164. Guo Y, Shao L, Song X, Li J. "Synthesis, Characterization and Template Removal of an iron-Containing Aluminophosphate Molecular Sieve with LAU Topology." *Microporous and Mesoporous Materials*. Elsevier Inc.; (2013); **165**; 14–9.
165. Kokotailo G, Fyfe C. "Zeolite Structure Analysis with Powder X-Ray Diffraction and Solid-State NMR Techniques." *The Rigaku Journal*. (1995); **12** 1; 3–10.
166. Toby BH. "R Factors in Rietveld Analysis: How Good is Good Enough?" *Powder Diffraction*. (2012); **21** 01; 67–70.
167. Scardi P, Mccusker LB, Dreele RB Von, Cox DE, Loue D. "Rietveld Refinement Guidelines." *Journal of Applied Crystallography*. (1999); **32**; 36–50.
168. Thompson EM. "Energy Dispersive X-Ray Spectrometry (EDXRF), AMC Technical Brief 21." 2005.
169. Slater C. "Synthesis and Characterisation of Amorphous Bioceramics." *University of Birmingham*; (2011); *PhD Thesis*.
170. Fairley N. "Introduction to XPS and AES, CasaXPS Manual 2.3.15." 1.2 ed. *Casa Software Ltd*; (2009).
171. Dowsing R, Gibson J. "Electron Spin Resonance of High Spin d5 Systems." *Journal of Chemistry and Physics*. (1969); **50**; 294.
172. Maddock AG. "Mossbauer Spectroscopy: Principles and Applications of the Techniques." *Elsevier, Horwood Chemical Science Series*; (1997); p.Chapter 5.
173. Dyar MD. "Mossbauer Spectroscopy" [Internet]. *Geochemical Instrumentation and Analysis*. (2012); [cited 2012 Jan 1]. Available from: [http://serc.carleton.edu/research\\_education/geochemsheets/techniques/mossbauer.html](http://serc.carleton.edu/research_education/geochemsheets/techniques/mossbauer.html)
174. Forder S. "The Use of Mossbauer Spectroscopy in Metallurgy." *ISLAME, Madrid, AIP Conf Proc*. (2005); **765**; 307–16.
175. Vlahović M, Mazaj M, Logar NZ, Jaćimović Ž. "Simultaneous Removal of  $\text{Fe}^{3+}$ ,  $\text{Mn}^{2+}$  and  $\text{Cu}^{2+}$  from Aqueous Solutions by Natural and Synthetic Zeolites." *Proceedings of the 5th Serbian-Croatian-Slovenian Symposium on Zeolites*. p. 151–4.
176. Lagarec K, Rancourt D. "Recoil Mossbauer Spectral Analysis Software for Windows." Department of Physics, University of Ottawa: *The Mossbauer Group*; (1998).
177. Miglierini M, Petridis D. "Mössbauer Spectroscopy in Materials Science." *Springer. Springer Science & Business Media*; (1999); **66**.
178. Wilson W, Swartzendruber L. "A Flexible Least Squares Routine for General Mossbauer Effect Spectra Fitting." *Computer Physics Communications*. (1974); **7**; 151–62.
179. Joshi P, Awate A, Shiralkar V. "Partial Isomorphous Substitution of  $\text{Fe}^{3+}$  in the LTL Framework." *Journal of Physical Chemistry*. (1993); **97**; 9749–53.
180. Chandwadkar A, Bhat R, Ratnasamy P. "Synthesis of Iron-Silicate Analogs of Zeolite Mordenite." *Zeolites*. (1991); **11**; 42–7.
181. Breck D, Eversole W, Milton R, Reed T, Thomas T. "Crystalline Zeolites. I. The Properties of a New Synthetic Zeolite, Type A." *Journal of the American Chemical Society. American Chemical Society*; (1956); **78** 23; 5963–72.

182. Meier W, Olson D, Baerlocher H. "Atlas of Zeolite Structure Types." 4th ed. London: *Elsevier*; (1996).
183. Concepcion-Rosabal B, Balmaceda-Era J, Rodriguez-Fuentes G. "Characterization of Fe<sup>2+</sup>-Containing Natural Clinoptilolite and its Interaction with Saccharides." *Microporous and Mesoporous Materials*. (2000); **38**; 161–6.
184. Ates A, Reitzmann A, Hardacre C, Yalcin H. "Abatement of Nitrous Oxide Over Natural and Iron Modified Natural Zeolites." *Applied Catalysis A. Elsevier B.V.*; (2011); **407** 1-2; 67–75.
185. Koyama K, Takeuchi Y. "Clinoptilolite: the Distribution of Potassium Atoms and its Role in Thermal Stability." *Zeitschrift für Kristallographie-Crystalline Materials*. (1977); **145** 1-6; 216–39.
186. Cho K, Cho H, de Menorval L, Ryoo R. "Generation of Mesoporosity in LTA Zeolites by Organosilane Surfactant for Rapid Molecular Transport in Catalytic Application." *Chemistry of Materials*. (2009); **21**; 5664–73.
187. Ruiz-salvador AR, Sastre G, Lewis DW, Catlow CRA. "Space Group Symmetry and Al-O-P Bond Angles in AlPO<sub>4</sub>-5." *Journal of Chemical Materials*. (1996); **6** 11; 1837–42.
188. Mooney RC. "The Crystal Structure of Aluminium Phosphate and Gallium Phosphate, Low-Cristobalite Type." *Acta Crystallographica* 9. (1956); **9**; 728–34.
189. Da-Yong T, Ji-Yang L, Wen-Fu Y, Xue-Jing C, Ji-Hong Y, Ru-Ren X. "Morphology Control of AlPO<sub>4</sub>-5 Molecular Sieve in Mixed-solvents System Under Microwave Irradiation." *Chemical Journal of Chinese Universities*. (2008); **12**; 033.
190. Sankar G, Thomas JM, Catlow CRA. "Combining X-Ray Absorption with X-Ray Diffraction for the Structural Elucidation of Catalysts." *Topics in Catalysis*. (2000); **10**; 255–64.
191. Kan Q, Wu Z, Xu R, Liu X. "Catalysis of Zeolite Molecular Sieves Containing Iron for Ethylbenzene Dehydrogenation." *Journal of Molecular Catalysis*. (1992); **74**; 223–31.
192. Cardile C, Tapp N, Milestone N. "Synthesis and Characterization of an Iron-Substituted Aluminophosphate Molecular Sieve." *Zeolites*. (1990); **10** 550; 90–4.
193. Guo Y, Song X, Li J, Li Y, Han Y, Yu J, Xu R. "Syntheses and Characterizations of Heteroatom-Containing Open-Framework Aluminophosphates." *Dalton Transactions*. (2011); **40** 36; 9289–94.
194. Schulke U. "Preparation and Crystal Structure of Ammonium Cyclooctaphosphate Trihydrate: (NH<sub>4</sub>)<sub>8</sub>P<sub>8</sub>O<sub>24</sub>.32O." *Zeitschrift für anorganische und allgemeine Chemie*. (1993); **619**; 374–80.
195. Shi J, Li J, Wu E. "Adsorption of Hydrogen and Deuterium in MnO<sub>2</sub> Modified NaX Zeolites." *Microporous and Mesoporous Materials. Elsevier Inc.*; (2012); **152** November; 219–23.
196. Zenonos C, Sankar G, Cora F, Lewis DW, Pankhurst QA, Catlow CRA, Thomas JM. "On the Nature of Iron Species in Iron Substituted Aluminophosphates." *Physical Chemistry Chemical Physics*. (2002); **4**; 5421–9.
197. Lee JK, Kim YJ, Lee H-J, Kim SH, Cho SJ, Nam I-S, Hong SB. "Iron-Substituted TNU-9, TNU-10, and IM-5 Zeolites and their Steam-Activated Analogs as Catalysts for Direct N<sub>2</sub>O Decomposition." *Journal of Catalysis. Elsevier Inc.*; (2011); **284** 1; 23–33.
198. Das J, Satyanaryana CV, Chakrabarty DK. "Substitution of Al in the AlPO<sub>4</sub>-5 and AlPO<sub>4</sub>-II Frameworks by Si and Fe: A Study by Mossbauer, Magic-Angle-Spinning Nuclear Magnetic Resonance and Electron Paramagnetic Resonance Spectroscopies and Chemical Probes." *J*

- Chem Soc Faraday Trans.* (1992); **88** 21; 3255–61.
199. Meagher A, Nair V, Szostak R. “A Mossbauer Study of ZSM-5-Type Ferrisilicates.” *Zeolites*. (1988); **8**; 3–11.
200. Tabor E, Sobalik Z. “Mossbauer Spectroscopy Study of the Iron Active Sites in Zeolites for N<sub>2</sub>O Decomposition.” (2011); (in press).
201. Hidouri M, Lajmi B, Wattiaux A, Fournés L, Darriet J, Amara MB. “Characterization by X-ray Diffraction, Magnetic Susceptibility and Mössbauer Spectroscopy of a New Alluaudite-Like Phosphate: Na<sub>4</sub>CaFe<sub>4</sub>(PO<sub>4</sub>)<sub>6</sub>.” *Journal of Solid State Chemistry*. (2004); **177** 1; 55–60.
202. Prakash A, Hartmann M, Zhu Z, Kevan L. “Incorporation of Transition Metal Ions into MeAPO/MeAPSO Molecular Sieves.” *The Journal of Physical Chemistry B*. (2000); **104** 7; 1610–6.
203. Zenonos C, Sankar G, Cora F, Lewis DW, Pankhurst QA, Catlow CRA, Thomas JM. “On the Nature of Iron Species in Iron Substituted Aluminophosphates.” *Physical Chemistry Chemical Physics*. (2002); **4** 21; 5421–9.
204. Perez-Ramirez J, Santhosh Kumar M, Bruckner A. “Reduction of N<sub>2</sub>O with CO Over FeMFI Zeolites: Influence of the Preparation Method on the Iron Species and Catalytic Behavior.” *Journal of Catalysis*. (2004); **223** 1; 13–27.
205. Fletcher-Wood R, Gorin C, Forder S, Bingham P, Hriljac J. “Mössbauer Spectroscopy for Optimising Systems for Environmental Remediation.” *Hyperfine Interactions*. (2013); **226** 1-3; 499–508.
206. Bingham P, Parker JM, Searle T, Williams JM, Smith I. “Novel Structural Behaviour of Iron in Alkali-Alkaline-Earth-Silica Glasses.” *Comptes Rendus Chimie*. (2002); **5** 11; 787–96.
207. Bradley D, Copperthwaite R, Cotton S, Sales K, Gibson J. “Three-Co-Ordinated Transition-metal Compounds Part III. Electron Spin Resonance Studies on Tris(bis(trimethylsilylamido)derivatives of Titanium, Chromium, and Iron.” *JCS Dalton*. (1973); 191–4.
208. Levi Z, Raitsimring A, Goldfarb D. “ESR and Electron Spin-Echo Studies of MnAlPO<sub>5</sub>.” *Journal of Physical Chemistry*. (1991); **95** 7; 7830–8.
209. Arias D, Escalante D, Lopez CM, Machado FJ, Mkndez B, Moronta D, Pinto M, Sazo V, Agudelo MR De. “On the Nature of Acid Sites in Substituted Aluminophosphate Molecular Sieves with the AEL Topology.” *Journal of Molecular Catalysis A*. (122AD); 97; 175–86.
210. Arieli D, Delabie A, Vaughan D, Strohmaier K, Goldfarb D. “Isomorphous Substitution of Mn(II) into Aluminophosphate Zeotypes: A Combined High-Field ENDOR and DFT Study.” *The Journal of Physical Chemistry B*. (2002); **106** 30; 7509–19.
211. De Biasi RS, Simoes A. “ESR in Mn-Doped Cristobalite AlPO<sub>4</sub>.” *Journal of Physics: Condensed Matter* *1*. (1989); **34**; 5915.
212. Dowsing R, Gibson J, Goodgame D, Goodgame M, Hayward P. “Determination of Stereochemistry of Manganese(II) Complexes by Electron Spin Resonance.” *Nature Publishing Group*. (1968); **219**; 1037–8.
213. Subrahmanyam C, Viswanathan B, Varadarajan T. “Synthesis, Characterization and Catalytic Activity of Mesoporous Trivalent Iron Substituted Aluminophosphates.” *Journal of Molecular Catalysis A: Chemical*. (2004); **223** 1-2; 149–53.
214. Catana G, Pelgrims J, Schoonheydt RA. “Electron Spin Resonance Study of the Incorporation

- of Iron in Ferrisilicate and FAPO-5." *Zeolites*. (1995); **15** ; 475–80.
215. Prasad S. "Characterization of Iron in Fe-VP14 and its Thermally Transformed Product, FAPO-8." *Microporous Materials*. (1997); **12**; 123–30.
216. Inamura K, Iwamoto R, Iino A, Takyu T. "Reduction and Sulfidation Properties of Iron Species in Iron-Supported Y-Zeolite by Temperature-Programmed Reduction and Sulfiding." *Journal of Catalysis*. (1993); **142**; 274–88.
217. Rees L, Morice J. "Mossbauer Studies of  $^{57}\text{Fe}$  in Zeolites." *Transactions of the Faraday Society*. (1968); **64**; 1388–95.
218. Sobkowiak A, Ericsson T, Edström K, Gustafsson T, Björefors F, Häggström L. "A Mössbauer Spectroscopy Study of Polyol Synthesized Tavorite  $\text{LiFeSO}_4\text{F}$ ." *Hyperfine Interactions*. (2013); **226** 1-3; 229–36.
219. Fuks H, Kaczmarek SM, Bosacka M. "EPR and IR Investigations of some Chromium (III) Phosphate (V) Compounds." *Reviews on Advanced Materials Science*. (2010); **23**; 57–63.
220. Van Bokhoven JA, Lamberti C. "Structure of Aluminum, Iron, and Other Heteroatoms in Zeolites by X-ray Absorption Spectroscopy." *Coordination Chemistry Reviews. Elsevier B.V.*; (2014); (in press).
221. Zhang X, Shen Q, He C, Ma C, Cheng J, Hao Z. " $\text{N}_2\text{O}$  Catalytic Reduction by  $\text{NH}_3$  Over Fe-Zeolites: Effective Removal and Active Site." *Catalysis Communications. Elsevier B.V.*; (2012); **18**; 151–5.
222. Garten R, Delgass W, Boudart M. "A Mossbauer Spectroscopic Study of the Reversible Oxidation of Ferrous Ions in Zeolite Y." *Journal of Catalysis*. (1970); **18**; 90–107.
223. Ojo A, Dwyer J, Parish R. "Zeolites: Facts, Figures, Future Part A - Proceedings of the 8th International Zeolite Conference." *Studies in Surface Science and Catalysis. Elsevier*; (1989); p.227-236.
224. Jung J-S, Chae W-S, McIntyre RA, Seip CT, Wiley JB, O'Connor CJ. "Preparation and Characterisation of Ni Nanoparticles in an MCM Mesoporous Material." *Materials Research Bulletin*. (1999); **34** 9; 1353–60.
225. Huang Y-Y, Anderson J. "On the Reduction of Supported Iron Catalysts Studied by Mossbauer Spectroscopy." *Journal of Catalysis*. (1975); **40**; 143–53.
226. Maurelli S, Vishnuvarthan M, Chiesa M, Berlier G, Doorslaer S Van. "Elucidating the Nature and Reactivity of Ti Ions Incorporated in the." *Journal of the American Chemical Society*. (2011); **133** 73; 7340–3.
227. Delgass W, Garten R, Boudart M. "Dehydration and Adsorbate Interactions of Fe-Y Zeolite by Mossbauer Spectroscopy." *Journal of Physical Chemistry*. (1969); **611** 16; 2970–9.
228. Garten R, Delgass W, Boudart M. "A Mossbauer Spectroscopic Study of the Reversible Oxidation of Ferrous Ions in Y Zeolite." *Journal of Catalysis*. (1970); **18**; 90–107.
229. Dubkov K. "Evolution of Iron States and Formation of  $\alpha$ -Sites upon Activation of FeZSM-5 Zeolites." *Journal of Catalysis*. (2002); **207** 2; 341–52.
230. Berry FJ, Hongzhang D, Jobson S, Dongbai L, Liwu L. "Oxidation of Iron in Titania-supported Iron-Ruthenium under Reducing Conditions: In Situ Evidence from  $^{57}\text{Fe}$  Mossbauer Spectroscopy." *Journal of the Chemical Society, Chemical Communications*. (1987); 3; 186.
231. Stumm W, Lee G. "Ind. Eng. Chem." (1961); **53**; 143.

232. Nikashina V, Zvereva L, Olshanova K, Potapova M. "Study of the Selectivity of Different Types of Zeolites Towards some Non-Ferrous Metals." *Journal of Chromotography A*. (1976); **120** 1; 155–8.
233. Albert Cotton F, Wilkinson G. "Advanced Inorganic Chemistry, Fifth Edition." *John Wiley & Sons, Wiley Interscience*; (1988).